

**A STUDY ON SPRAYED FIBER REINFORCED POLYMER COMPOSITES  
FOR STRENGTHENING OF REINFORCED CONCRETE MEMBERS**

**BY**

**QUDEER HUSSAIN**

**A DISSERTATION SUBMITTED IN PARTIAL FULFILLMENT OF  
THE REQUIREMENTS FOR THE DOCTOR OF PHILOSOPHY IN  
ENGINEERING  
SIRINDHORN INTERNATIONAL INSTITUTE OF TECHNOLOGY  
THAMMASAT UNIVERSITY  
ACADEMIC YEAR 2015**

**A STUDY ON SPRAYED FIBER REINFORCED POLYMER COMPOSITES  
FOR STRENGTHENING OF REINFORCED CONCRETE MEMBERS**

**BY**

**QUDEER HUSSAIN**

**A DISSERTATION SUBMITTED IN PARTIAL FULFILLMENT OF  
THE REQUIREMENTS FOR THE DOCTOR OF PHILOSOPHY IN  
ENGINEERING  
SIRINDHORN INTERNATIONAL INSTITUTE OF TECHNOLOGY  
THAMMASAT UNIVERSITY  
ACADEMIC YEAR 2015**



A STUDY ON SPRAYED FIBER REINFORCED POLYMER COMPOSITES FOR  
STRENGTHENING OF REINFORCED CONCRETE MEMBERS

A Dissertation Presented

By

QUDEER HUSSAIN

Submitted to

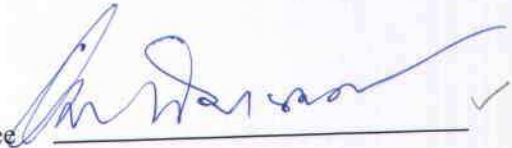
Sirindhorn International Institute of Technology

Thammasat University

In partial fulfillment of the requirements for the degree of  
DOCTOR OF PHILOSOPHY IN ENGINEERING

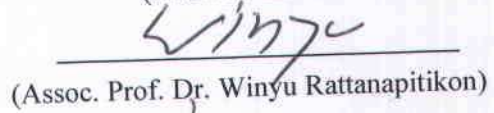
Approved as to style and content by

Advisor and Chairperson of Thesis Committee



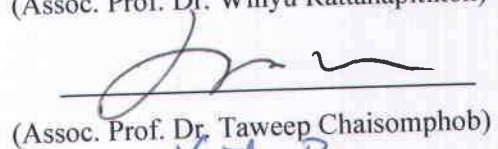
(Prof. Dr. Amorn Pimanmas)

Co-Advisor



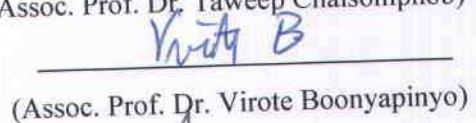
(Assoc. Prof. Dr. Winyu Rattanapitikon)

Committee Member and  
Chairperson of Examination Committee



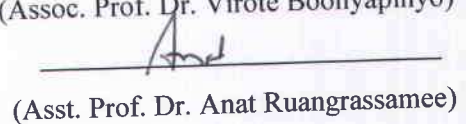
(Assoc. Prof. Dr. Taweep Chaisomphob)

Committee Member



(Assoc. Prof. Dr. Virote Boonyapinyo)

Committee Member



(Asst. Prof. Dr. Anat Ruangrassamee)

External Examiner: Prof. Dr. Hamed M.M.S Hadhond

OCTOBER 2015

## Acknowledgements

First and foremost I want to thank my advisor Amorn Pimanmas. It has been an honor to be his Ph.D. student. He has taught me, both consciously and unconsciously, how good experimental physics is done. I appreciate all his contributions of time, ideas, and funding to make my Ph.D. experience productive and stimulating. The joy and enthusiasm he has for his research was contagious and motivational for me, even during tough times in the Ph.D. pursuit. I am also thankful for the excellent example he has provided as a successful researcher and professor. Thank you.

To my doctoral dissertation committee: Dr. Winyu Rattanapitikon, Dr. Taweeep Chaisomphob, Dr. Virote Boonyapinyo, and Dr. Anat Ruangrassamee. I appreciate the support during my dissertation research, and general advice you provided about academic writing, and publishing. I look forward to our continued collaboration in publishing, research, and more.

I gratefully acknowledge the funding sources that made my Ph.D. work possible. I was funded by the EXAT and TRF research projects and my work was also supported by the SIIT and AIT research projects. My sincere thanks also goes to Ms. Varaporn Sumtanon, for offering me the spraying facilities in Channakorn Engineering Co. Ltd., Thailand.

To the staff and students at SIIT and AIT Lab, I am grateful for the chance to visit and be a part of the lab. Thank you for welcoming me as a friend and helping to develop the ideas in this thesis. I am incredibly grateful for Ms. Por and Ms. Mini who stood by to support me along the way and provided support and friendship that I needed. Thank you for helping me during my PhD journey. I am indebted to all my friends (Tahir, Irshad, Adnan, Joy, Bank, and Soknath) who have supported me over the last few years. I have enjoyed many useful and entertaining discussions with my friends and co-workers (lalin, Seyha, Arslan, Ice and Bas).

I would like to thank my family for all their love and encouragement. For my parents who raised me with a love of science and supported me in all my pursuits.

Lastly, There is nothing more precious than, the support of a Mom who really cares. Thanks Mom (Ami Jee).

## **Abstract**

### **A STUDY ON SPRAYED FIBER REINFORCED POLYMER COMPOSITES FOR STRENGTHENING OF REINFORCED CONCRETE MEMBERS**

by

Qudeer Hussain

B.Eng, Civil Engineering, UET Taxila, Pakistan, 2007

M.Eng, Civil Engineering, UET Taxila, Pakistan, 2010

Extensive research is currently being conducted concerning the use of uni-directional fiber reinforced plastic (FRP) wraps or laminates in the strengthening and rehabilitation of reinforced concrete (RC) members. These unidirectional FRP(s) include carbon, glass, aramid, polyethylene terephthalate (PET) and polyethylene naphthalates (PEN). As strengthening materials, they offer some advantages over conventional steel and concrete jacketing such as low weight, high strength and excellent resistance to corrosion. Over the last few decades, a new method of strengthening reinforced concrete members by Sprayed Fibre Reinforced Polymer (shortly as SFRP) composites has been introduced. This method further simplifies the application procedure to apply fiber using a spraying process. The salient features of SFRP are quick and easy application as well as the uniform tensile properties in all directions.

This thesis reports extensive usage of sprayed fiber reinforced plastic (SFRP) strengthening system on RC members using glass and carbon fibers embedded in a polyester matrix. In the first step, small scale circular and square columns strengthened with different thicknesses of SFRP were tested under uniaxial compression to investigate the increase in the ultimate strength and ductility. It was found that substantial increases in ultimate load carrying capacity, member stiffness and ductility

can be achieved with SFRP confinement for both circular and square sections. The efficiency of SFRP for providing the external confinement and the resulting increase in strength and ductility is greater in circular columns than in square columns. The obtained experimental results were used to assess the performance of existing strength models developed for unidirectional FRP. It was found that almost all existing models are conservative to predict the experimental compressive strength of SFRP-confined concrete. New strength models are proposed based on the obtained experimental data for both circular and square SFRP-confined columns and a good correlation was found between experimental and analytical values.

The second phase aims to investigate the effectiveness of externally bonded SFRP in shear strengthening of RC deep beams under quasi-static loading. Given that bond between SFRP and concrete surface is the critical link, different anchoring systems i.e. Through Bolts (TB), Mechanical Expansion Bolts (MB), and Epoxy Chemical Bolts (EB) were proposed and used to enhance the bond between concrete surface and SFRP. The proposed anchoring systems are found to be effective to prevent the de-lamination of SFRP. Test results indicated that SFRP was capable of enhancing the ultimate load and deflection of RC deep beams provided that adequate anchoring system is installed. The performance of SFRP strengthening depends on several key variables such as SFRP material, thickness, strengthening configuration, strength of concrete, type of anchoring system and length of the anchor bolt.

The third step aims to evaluate a possible use of the SFRP technique to elevate the shear strength of RC deep beams with web openings. Towards this goal, an extensive experimental program has been conducted. Both circular and square openings of different sizes were investigated. Two types of concrete (i.e., low and high strength) were used to cast the specimens. The deep beams with openings were strengthened with a variety of SFRP thicknesses and strengthening configurations. The externally bonded SFRP was remarkably effective to increase the ultimate load of the RC deep beams with both the square and circular openings and both low- and high-strength concrete beams. Also, SFRP applied on 3 sides (U-shaped) was more effective than 2-sided SFRP in shear strengthening. The efficiency of the SGFRP strengthening and MB anchoring system was lower for the high-strength concrete specimens as compared with the low-strength specimens.

Then, in a fourth step, the research work was primarily focused on the development of two-dimensional nonlinear finite element analysis for RC deep beams (with and without openings) strengthened with SFRP. In the finite element analysis, realistic material constitutive laws were utilized which were capable of accounting for the non-linear behavior of materials. The finite element analysis was performed using computer software WCOMD. The calculated finite element results are found to be in good agreement with the experimental results and to capture the structural response of both un-strengthened and SFRP strengthened RC deep beams. A comparison between the finite element results and experimental data proved the validity of the finite element models. Further, the finite element models were utilized to investigate the behavior of RC deep beams strengthened with different directions of SFRP strips and web openings located at different locations. The finite element results showed that there is considerable decrease in the ultimate load carrying capacity when openings are induced in shear span. The SFRP strengthening is found effective to enhance load carrying capacity of RC deep beams with openings irrespective of openings locations and shape. The vertical SFRP strips are found to be more effective than horizontal ones.

At the end of this study, an experimental program was conducted to investigate the behavior of large scale non-ductile RC columns (representing reinforcement detailing of those structures which were designed against gravity loads only or constructed prior to the development of modern seismic codes) strengthened using SFRP. Three types of RC columns (i.e. shear, flexure-shear and flexure dominated) were strengthened using SFRP jackets and tested under lateral cyclic loading. A constant axial load was also applied along with lateral cyclic loading. In SFRP, two types of fiber materials (i.e. glass and carbon) were used for strengthening of RC columns. The results of SFRP strengthened RC columns were compared with control or un-strengthened RC columns. SFRP strengthening is found effective for all types of investigated columns (i.e. shear, flexure-shear and flexure dominated) to increase strength and ductility. Both types of SFRP (i.e., glass and carbon) jackets greatly improved the behavior of strengthened RC columns in terms of strength and ductility.

## Table of Contents

Chapter	Title	Page
	Signature Page	i
	Acknowledgements	ii
	Abstract	iii
	Table of Contents	vi
	List of Figures	x
	List of Tables	xvii
1	Introduction	1
	1.1. Overview	1
	1.2. Problem description	1
	1.3. Seismic strengthening using concrete jackets	1
	1.4. Seismic strengthening using steel plates	2
	1.5. Seismic strengthening using fiber reinforced polymers	3
	1.6. Objectives of study	4
	1.7. Dissertation outline	5
2	Literature Review	6
	2.1 Introduction	6
	2.2 SFRP strengthening of unreinforced concrete beams	6
	2.3 SFRP strengthening of reinforced concrete beams	8
	2.4 Anchorage systems for SFRP beams	11
	2.5 SFRP strengthening of columns	14
3	Materials	18
	3.1. Concrete materials	18
	3.1.1 Cement	18
	3.1.2 Water	18
	3.1.3 Fine aggregates (sand)	18
	3.1.4 Coarse aggregates (gravel)	18
	3.1.5 Reinforcing steel bars	19
	3.2. SFRP system	19
	3.2.1 Glass fiber roving	19
	3.2.2 Carbon fiber roving	20
	3.2.3 Resin and catalyst	20
4	SFRP Application Process	22
	4.1 Introduction	22
	4.2 SFEP application process	22
5	SFRP Material Properties	28
	5.1 Sprayed SFRP properties	28
	5.1.1 Density	82
	5.1.2 Fiber volume fraction	28
	5.1.3 Tensile properties of SFRP composite	82
6	SFRP Strengthening of Small-size Concrete Columns	33
	6.1 Introduction	33



	6.2	Experimental program	34
	6.3	Specimen preparation	35
	6.4	Concrete properties	37
	6.5	SFRP strengthening	37
	6.6	Thickness of SFRP	39
	6.7	Instrumentation	40
	6.7.1	Circular columns	40
	6.7.2	Square columns	41
	6.8	Test procedure	41
	6.9	Results and discussions	43
	6.9.1	Overall behavior and stress-strain response	43
	6.10	Failure modes	46
	6.10.1	Circular columns	46
	6.10.2	Square columns	47
7		Strength models for SFRP confined concrete columns	48
	7.1	Introduction	48
	7.2	Existing models	48
	7.3	Assessment of existing models	51
	7.4	Proposed strength models	54
8		SFRP Strengthening of RC Deep Beams	57
	8.1	Introduction	57
	8.2	Description of the test specimens	58
	8.3	Test matrix	59
	8.4	Application of SFRP	60
	8.5	Concrete properties	62
	8.6	Instrumentation and loading setup	63
	8.7	Anchoring systems – Literature review	64
	8.7.1	SFRP slits	65
	8.7.2	Proposed anchoring systems	66
	8.7.2.1	TB anchoring system	67
	8.7.2.2	MB anchoring system	67
	8.7.2.3	EB anchoring system	68
	8.8	Test results and discussions	68
	8.8.1	Failure modes	70
	8.8.2	Load carrying capacity and mid span deflections	73
	8.8.2.1	Beam group 1	79
	8.8.2.1.1	Effect of SFRP slits	79
	8.8.2.2	Beam group 2	79
	8.8.2.2.1	Effectiveness of the anchoring systems	79
	8.8.2.2.2	Effect of SGFRP thickness	80
	8.8.2.2.3	Effect of anchor bolt length	81
	8.8.2.2.4	Effect of anchor bolt spacing	81
	8.8.2.3	Beam group 3	82
	8.8.2.3.1	Effect of SCFRP thickness	82
	8.8.2.3.2	Effect of SFRP material	82
	8.8.2.4	Beam group 4	83
	8.8.2.4.1	Effect of SGFRP thickness	83

	8.8.2.4.2	Effect of SGFRP strengthening configuration	84
9		SFRP Strengthening of RC Deep Beams with Openings	85
	9.1	Introduction	85
	9.2	Experimental program	86
	9.2.1	Description of the test specimens and test matrix	86
	9.2.2	SGFRP strengthening	89
	9.2.3	Material properties	91
	9.2.4	Test setup and instrumentation	91
	9.3	MB Anchoring system	92
	9.4	Experimental results and discussions	93
	9.4.1	Cracking behavior	93
	9.4.2	Failure modes	97
	9.4.3	Load carrying capacity and mid span deflection	99
	9.4.3.1	Specimens in group A	102
	9.4.3.2	Specimens in group B	102
	9.4.3.3	Specimens in group C	103
	9.4.3.4	Specimens in group D	103
	9.4.3.5	Specimens in group E	104
	9.4.3.6	Specimens in group F	104
	9.4.4	Effectiveness of the MB anchoring system	105
	9.4.5	Effect of the opening size and shape	105
	9.4.6	Effect of the SGFRP strengthening configuration	108
	9.4.7	Effect of concrete strength	109
	9.4.8	Stiffness of the SGFRP beams with openings	111
10		Analytical Analysis of SFRP Strengthened RC Deep Beams	114
	10.1	Introduction	114
	10.2	Finite element modeling	114
	10.3	Constitutive models of concrete and reinforcing bars	115
	10.3.1	Cracked concrete model	115
	10.3.1.1	Combined tension compression model	116
	10.3.1.2	Shear stress transfer model	118
	10.4	Model of reinforcing steel bar	118
	10.5	Constitutive model of SFRP	120
	10.6	Finite element simulation of test results	120
	10.6.1	Load capacity and deflection behavior	122
	10.6.2	Cracking pattern	127
	10.7	Discussion on finite element analysis results	129
	10.7.1	Finite element models of un-strengthened beams	129
	10.7.2	Finite element models for glass strengthened beams	129
	10.7.3	Finite element models for carbon strengthened beams	130
	10.7.4	Finite element models for glass beams (HS)	130
	10.8	Effect of SFRP strips	131
	10.8.1	Effect of direction	134
	10.8.2	Effect of vertical SFRP strip width and spacing	135
	10.8.3	Effect of position of horizontal SFRP strips	136
11		Analytical Analysis of SFRP Beams with openings	139
	11.1	Introduction	139

	11.2	Finite element modeling	139
	11.3	Finite element simulation of test results	141
	11.3.1	Load capacity and deflection behavior	145
	11.3.2	Cracking pattern	161
	11.4	Discussion on finite element results	165
	11.4.1	Finite element models of un-strengthened beams	165
	11.4.2	Finite element models for strengthened beams	166
	11.4.2.1	Group A	166
	11.4.2.2	Group B	166
	11.4.2.3	Group C	167
	11.4.2.4	Group D	167
	11.4.2.5	Group E	167
	11.4.2.6	Group F	168
	11.4.2.7	Strengthening configurations	168
	11.5	Effect of openings size and location	168
	11.6	Finite element analysis results	176
	11.6.1	Effect of openings location	176
	11.6.2	Effect of SGFRP strengthening	181
12		SFRP Strengthening of Large Sized RC Columns	187
	12.1	Introduction	187
	12.2	Experimental program	188
	12.3	Strengthening of RC columns	190
	12.4	Instrumentation and testing procedure	194
	12.5	Results and discussion	197
	12.5.1	Shear dominated RC columns	203
	12.5.2	Flexure-shear dominated RC columns	205
	12.5.3	Flexure dominated RC columns	207
	12.6	Ductility	210
	12.7	Development of strain in steel bars	210
	12.8	Stiffness	218
	12.9	Cumulative dissipated energy	220
	12.10	Effect of aspect ratio	222
	12.11	Effect of SFRP material	224
	12.12	Bulging of concrete	224
	12.13	Observed failure modes	225
13		Conclusions and Recommendations	227
	13.1	Conclusions	228
	13.2	Recommendations for future research work	229
		References	231

## List of Figures

<b>Figures</b>	<b>Page</b>
1-1: Concrete jacketing	2
1-2: Steel jacketing	3
1-3: Application of Carbon FRP to the box girder [14]	4
2-1: SFRP application to beam specimens	7
2-2: SFRP spray application on beams	8
2-3: Failure of beams showing de-bonding of SFRP	9
2-4: SFRP strengthened RC beams	10
2-5: Application of SFRP on girders	11
2-6: SFRP application in notched beams	12
2-7: Anchoring system for corners	12
2-8: Anchoring system for RC beam	13
2-9: Anchoring system	14
2-10: Failure of SFRP strengthened RC column	15
2-11: Glass fiber reinforced polymer spraying process	16
2-12: Typical failure of SFRP strengthened column	17
3-1: Glass fiber roving	19
3-2: Carbon fiber roving	20
4-1: FRP spray equipment	23
4-2: FRP Chopper/Spray unit	23
4-3: SFRP application details	24
4-4: Cutting blade	24
4-5: Spraying chopped fibers	25
4-6: Ribbed aluminum roller	26
4-7: A aluminum roller is used to obtain uniform thickness of SFRP	26
4-8: A aluminum roller is used to obtain uniform thickness of SFRP	27
5-1: Detailing of SFRP tensile strip	29
5-2: Spray process to prepare SFRP sheets	30
5-3: SGFRP sheets	30
5-4: Loading setup to test SFRP tensile strips	31
5-5: Typical failure of SFRP tensile strip	32
6-1: Test specimen	36
6-2: Preparation of circular columns	36
6-3: Column specimens with rough surface	37
6-4: Arrangement for SFRP spray process	38
6-5: SFRP application process	38
6-6: SFRP strengthened square columns	39
6-7: SFRP strengthened circular columns	39

6-8: Instrumentation for circular specimens	41
6-9: Instrumentation for square specimens	41
6-10: Typical square test specimens	42
6-11: Test setup	43
6-12: Stress-strain curves of circular specimens	44
6-13: Stress-strain curves of square specimens	45
6-14: Typical failure modes of SFRP confined circular columns	47
6-15: Typical failure modes of SFRP confined square columns	47
7-1: Performance of existing strength models for circular columns	52
7-2: Performance of existing strength models for square columns	53
7-3: Strengthening ratio versus confinement ratio	55
7-4: Theoretical strengthening ratio versus experimental	56
8-1: Detailing of RC Deep beam (units are in mm)	59
8-2: SFRP configurations	60
8-3: Roughened Concrete surface of beam	61
8-4: Spraying process of FRP	61
8-5: Concrete casting	63
8-6: Test setup	64
8-7: Details of SFRP slits	66
8-8: TB anchoring system	67
8-9: MB anchoring system	67
8-10: EB anchoring system	67
8-11: Failure mode of Beam BN-LS-CB	71
8-12: Failure mode of Beam BN-HS-CB	71
8-13: Failure mode of beam BN-LS-5GA	71
8-14: Failure mode of beam BN-LS-5GA-S	71
8-15: Failure mode of beam BN-LS-5GA-EB	72
8-16: Failure mode of Beam BN-LS-5GA-EB1	72
8-17: Failure mode of Beam BN-LS-5GA-MB2	72
8-18: Failure mode of Beam BN-LS-3CA-MB	72
8-19: Typical failure mode of beam with SFRP configuration A	73
8-20: Failure mode of beam	73
8-21: Typical concrete crushing failure under loading region	73
8-22: Load deflection curves of RC deep beams (effect of SFRP slits)	74
8-23: Load deflection curves of RC deep beams systems	74
8-24: Load deflection curves of RC deep beams SGFRP thickness	75
8-25: Load deflection curves of RC deep beams length of bolts	75
8-26: Load deflection curves of RC deep beams	76
8-27: Load deflection curves of RC deep beams SCFRP thickness	76
8-28: Load deflection curves of RC deep beams	77
8-29: Load deflection curves of RC high strength deep beams (group 4)	77

8-30: Comparison of normalized ultimate loads (Groups 1-3)	78
8-31: Comparison of normalized ultimate loads (Group 4)	78
9-1: Group A, B, E and F beam detailing	87
9-2: Group C and D beam detailing	87
9-3: Concrete casting	89
9-4: SGFRP strengthening configurations	90
9-5: Roughened surface of concrete beam	90
9-6: SFRP strengthening process of RC deep beams with openings	91
9-7: Loading set up	92
9-8: MB Anchoring system	92
9-9: Failure mode of Beam specimen - Control LS-S18	94
9-10: Failure mode of Beam specimen - Control LS-S12	94
9-11: Failure mode of Beam specimen - Control LS-C16	94
9-12: Failure mode of Beam specimen - Control LS-C10	95
9-13: Initiation of diagonal cracks in SFRP beams with square openings	95
9-14: Initiation of diagonal cracks in SFRP beams	95
9-15: Failure mode of SGFRP strengthened beam	97
9-16: Typical failure mode of SFRP strengthened beam	98
9-17: Typical failure mode of SFRP strengthened beam	98
9-18: Typical failure mode of SFRP strengthened beam	98
9-19: Failure mode of SGFRP strengthened beam	99
9-20: Load deflection curves of beams - Group A	99
9-21: Load deflection curves of beams - Group B	100
9-22: Load deflection curves of beams - Group C	100
9-23: Load deflection curves of beams - Group D	101
9-24: Load deflection curves of beams - Group E	101
9-25: Load deflection curves of beams - Group F	102
9-26: Effect of the openings size and shape (control beams)	106
9-27: Effect of the openings size and shape SGFRP beams	107
9-28: Effect of the openings size and shape SGFRP beams	107
9-29: Effect of the SGFRP-strengthening configuration	109
9-30: Expected versus actual load increase	111
9-31: Stiffness calculation	112
10-1: Reinforced concrete planar element	116
10-2: Compression-tension model for normal stress	117
10-3: Shear stress transfer model	118
10-4: Model of steel bar	119
10-5: SFRP stress strain model	120
10-6: Finite element model of control beam FEM-LS-CB	121
10-7: Finite element model of SFRP beam	121
10-8: Finite element model of SFRP beam	121

10-9: Experimental versus finite element model	122
10-10: Experimental vs. finite element model	123
10-11: Experimental vs. finite element model	123
10-12: Experimental vs. finite element model	124
10-13: Experimental vs. finite element model	124
10-14: Experimental vs. finite element model	125
10-15: Experimental vs. finite element model	125
10-16: Experimental vs. finite element	126
10-17: Experimental vs. finite element model	126
10-18: Cracking pattern of FEM-LS-CB	128
10-19: Cracking pattern of BN-LS-CB	128
10-20: Cracking pattern of FEM-HS-CB	128
10-21: Cracking pattern of BN-HS-CB	128
10-22: Specimen FEM-LS-V01	131
10-23: Specimen FEM-LS-V02	131
10-24: Specimen FEM-LS-H01	132
10-25: Specimen FEM-LS-H02	132
10-26: Finite element model FEM-LS-V01	133
10-27: Finite element model FEM-LS-V02	133
10-28: Finite element model FEM-LS-H01	133
10-29: Finite element model FEM-LS-H02	133
10-30: Effect of SFRP strip direction	135
10-31: Effect of SFRP strip width and spacing	136
10-32: Effect of SFRP strip position	137
10-33: Cracking pattern of FEM-LS-V01	138
10-34: Cracking pattern of FEM-LS-V02	138
10-35: Cracking pattern of FEM-LS-H01	138
10-36: Finite element model FEM-LS-H02	138
11-1: FEM-Con-LS-S18 and FEM-Con-HS-S18	141
11-2: FEM-Con-LS-S12 and FEM-Con-HS-S12	141
11-3: FEM-Con-LS-C16	142
11-4: FEM-Con-LS-C10	142
11-5: FEM-LS-5A-S18	142
11-6: FEM-LS-3A-S12	143
11-7: FEM-LS-3A-S12 and FEM-LS-5A-S12	143
11-8: FEM-LS-3A-C10, FEM-LS-5A-C10	143
11-9: FEM-LS-5B-S18 and FEM-HS-5B-S18	144
11-10: FEM-LS-5B-S12	144
11-11: FEM-LS-5B-S12	144
11-12: FEM-LS-5B-S12	145
11-13: Control LS-S18 vs. FEM-Con- LS-S18	146

11-14: LS-5A-S18 vs. FEM-LS-5A-S18	146
11-15: LS-3B-S18 vs. FEM-LS-3B-S18	147
11-16: LS-5B-S18 vs. FEM-LS-5B-S18	147
11-17: Control LS-S12 vs. FEM-Con-LS-S12	148
11-18: LS-3A-S12 vs. FEM-LS-3A-S12	148
11-19: LS-5A-S12 vs. FEM-LS-5A-S12	149
11-20: LS-5B-S12 vs. FEM-LS-5B-S12	149
11-21: LS-5C-S12 vs. FEM-LS-5C-S12	150
11-22: Control LS-C16 vs. FEM-Con-LS-C16	150
11-23: LS-3A-C16 vs. FEM-LS-3A-C16	151
11-24: LS-5A-C16 vs. FEM-LS-5A-C16	151
11-25: LS-5B-C16 vs. FEM-LS-5B-C16	152
11-26: LS-5C-C16 vs. FEM-LS-5C-C16	152
11-27: Control LS-C10 vs. FEM-Con-LS-C10	153
11-28: LS-3A-C10 vs. FEM-LS-3A-C10	153
11-29: LS-5A-C10 vs. FEM-LS-5A-C10	154
11-30: LS-5B-C10 vs. FEM-LS-5B-C10	154
11-31: LS-5C-C10 vs. FEM-LS-5C-C10	155
11-32: Control HS-S18 vs. FEM-Con-HS-S18	155
11-33: HS-3A-S18 vs. FEM-HS-3A-S18	156
11-34: HS-5A-S18 vs. FEM-HS-5A-S18	156
11-35: HS-5B-S18 vs. FEM-HS-5B-S18	157
11-36: HS-5C-S12 vs. FEM-HS-5C-S12	157
11-37: Control HS-S12 vs. FEM-Con-HS-S12	158
11-38: HS-3A-S12 vs. FEM-HS-3A-S12	158
11-39: HS-5A-S12 vs. FEM-HS-5A-S12	159
11-40: FEM-Con- LS-S18	161
11-41: Control LS-S18	161
11-42: FEM-Con-LS-S12	162
11-43: Control LS-S12	162
11-44: FEM-Con-LS-C16	163
11-45: Control LS-C16	163
11-46: FEM-Con-LS-C10	164
11-47: Control LS-C10	164
11-48: Beam N-C	169
11-49: Beam N-S-B	170
11-50: Beam N-S-T	170
11-51: Beam N-S-C	171
11-52: Beam N-R-B	171
11-53: Beam N-R-T	172
11-54: Beam N-R-C	172



11-55: Finite element model N-C	174
11-56: Finite element model N-S-B	174
11-57: Finite element model N-S-T	174
11-58: Finite element model N-S-C	175
11-59: Finite element model N-R-B	175
11-60: Finite element model N-R-T	175
11-61: Finite element model N-R-C	176
11-62: RC deep beams without opening and with square openings	177
11-63: RC deep beams without opening and with rectangular openings	178
11-64: Comparison of ultimate load	178
11-65: Finite element model N-R-C	179
11-66: Finite element model N-S-B	179
11-67: Finite element model N-S-T	179
11-68: Finite element model N-S-C	179
11-69: Finite element model N-R-B	180
11-70: Finite element model N-R-T	180
11-71: Finite element model N-R-C	180
11-72: Square openings located at bottom	183
11-73: Square openings located at top	183
11-74: Square openings located at center	184
11-75: Rectangular openings located at bottom	184
11-76: Rectangular openings located at top	185
11-77: Rectangular openings located at center	185
11-78: Comparison of ultimate load (Square openings)	186
11-79: Comparison of ultimate load (Rectangular openings)	186
12-1: Detailing of RC columns (units in mm)	189
12-2: Details of SFRP strengthening	191
12-3: Roughened concrete surface of column	191
12-4: SFRP application process	192
12-5: Surface preparation using ribbed aluminum roller	192
12-6: SFRP cutting process	193
12-7: SFRP strengthened RC Columns	193
12-8: Details of strain gauges	195
12-9: Details of LVDTs installation	195
12-10: Loading setup	196
12-11: Lateral loading protocol	196
12-12: Load-displacement hysteretic response of column SD-CON [99]	198
12-13: Load-displacement hysteretic response of column SD-CARB	198
12-14: Load-displacement hysteretic response of column SD-GLAS	199
12-15: Load-displacement hysteretic response of column FSD-CON	199
12-16: Load-displacement hysteretic response of column FSD-CARB	200

12-17: Load-displacement hysteretic response of column FD-CON	200
12-18: Load-displacement hysteretic response of column FD-CARB	201
12-19: Load-displacement hysteretic response of column SD-GLAS	201
12-20: Shear dominated RC columns	202
12-21: Flexure-shear dominated RC columns	202
12-22: Flexure dominated RC columns	203
12-23: Failure mode of column SD-CON at 3.5% lateral drift	204
12-24: Failure mode of column SD-GLAS at 9% lateral drift	205
12-25: Failure mode of column FSD-CON at 4% lateral drift	206
12-26: Failure mode of column FSD-CARB at 9% lateral drift	207
12-27: Failure mode of column FD-CON at 4.5% lateral drift	208
12-28: Failure mode of column FD-GLAS at 9% lateral drift	209
12-29: Strain in longitudinal reinforcement (SD-CARB)	211
12-30: Strain in longitudinal reinforcement (SD-GLAS)	212
12-31: Strain in longitudinal reinforcement (FSD-CARB)	212
12-32: Strain in longitudinal reinforcement (FD-CARB)	213
12-33: Strain in longitudinal reinforcement (FD-GLAS)	213
12-34: Strain in Transverse reinforcement (SD-CARB)	214
12-35: Strain in Transverse reinforcement (SD-GLAS)	214
12-36: Strain in Transverse reinforcement (FSD-CARB)	215
12-37: Strain in Transverse reinforcement (FD-CARB)	215
12-38: Strain in Transverse reinforcement (FD-GLAS)	216
12-39: Strain distribution along longitudinal reinforcement	217
12-40: Stiffness degradation curves of shear dominated RC columns	218
12-41: Stiffness degradation curves	219
12-42: Stiffness degradation curves of flexure dominated RC columns	219
12-43: Cumulative dissipated energy of shear dominated RC columns	220
12-44: Cumulative dissipated energy	221
12-45: Cumulative dissipated energy of flexure dominated RC columns	221
12-46: Comparison of maximum lateral load	223
12-47: Comparison of ductility	223
12-48: Rupture of FRP strap	225

## List of Tables

<b>Tables</b>	<b>Page</b>
3-1: Mechanical properties of fibers	20
3-2: Mechanical properties of resin and catalyst	21
5-1: Mechanical properties of SFRP	29
6-1: Test program of column specimens	35
6-2: Concrete mix composition (per cubic meter)	37
6-3: Target and actual SFRP thickness	40
6-4: Test results	45
7-1: Existing strength models	50
7-2: Existing strength models	51
7-3: Performance of existing strength models	53
7-4: Statistical performance of existing strength models	54
7-5: Summary of experimental and predicted results	56
8-1: Summary of test matrix	62
8-2: Concrete strengths and mix proportions	63
8-3: Experimental results	69
9-1: Test matrix	88
9-2: Experimental test results	96
9-13: Stiffness of the RC deep beams with openings	113
10-1: Summary of experimental program and FEM	115
10-2: Summary of experimental and finite element results	127
10-3: Summary of finite element analysis results	132
11-1: Summary of experimental program and FEM	140
11-2: Summary of experimental and finite element results	160
11-3: Details of finite element models	173
11-4: Details of finite element models	177
11-5: Summary of finite element analysis	182
12-1: Details of test specimens	189
12-2: Summary of test results	197

# **Chapter 1**

## **Introduction**

### **1.1. Overview**

The research work presented here in this thesis deals with the seismic strengthening or rehabilitation of existing reinforced concrete members using externally bonded Sprayed Fiber Reinforced Polymer (SFRP) composites. By applying SFRP coating to the external surface(s) of reinforced concrete (RC) members to provide supplementary reinforcement, it is likely to enhance the ultimate load carrying capacity, ductility, stiffness and energy absorption capacity of the RC members.

### **1.2. Problem description**

The strengthening of reinforced concrete (RC) structures is frequently required because of excessive loading as a result of changes in use, modifications to design codes, improper maintenance or exposure to environmental effects, such as corrosion and seismic activity [1]. Recent earthquakes all around the world i.e., 1989 Loma Prieta, 1994 Northridge Earthquake, 1995 Kobe earthquake in Japan and 2005 Kashmir earthquake in Pakistan have caused collapse, or severe damage to a large number of RC structures that were not designed for seismic forces. The destruction of infrastructure at large scales was resulted into casualties and economic loss. One obvious solution to this problem is to simply demolish the deficient structures and replace them with new ones. Unfortunately, the economics of today's world make this solution impractical. The only remaining alternative then, is to improve the load carrying capacity of those structures which were designed before the development of current seismic codes to modern standards using most applicable and cheap methods.

### **1.3. Seismic strengthening using concrete jackets**

The seismic strengthening of RC member using concrete jacketing has been successfully used in the last few decades [2]. Concrete jacketing is the addition of a concrete shell surrounding a member that is reinforced to improve the strength and ductility of the element [3, 4] as shown in Figure 1-1.

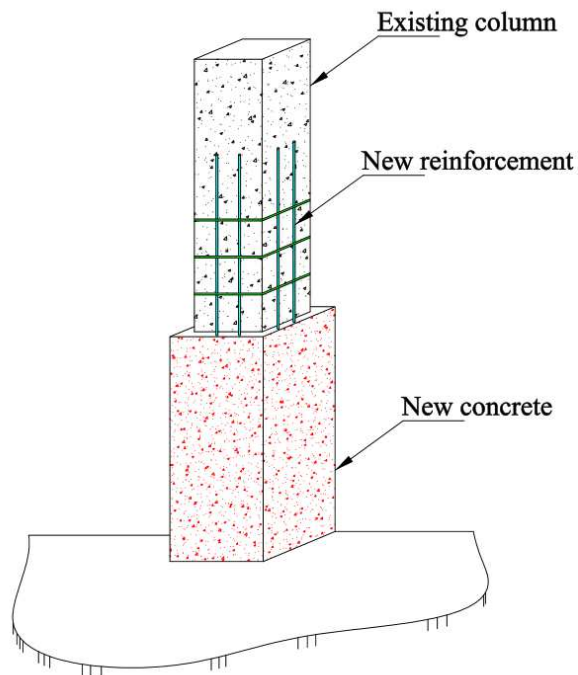
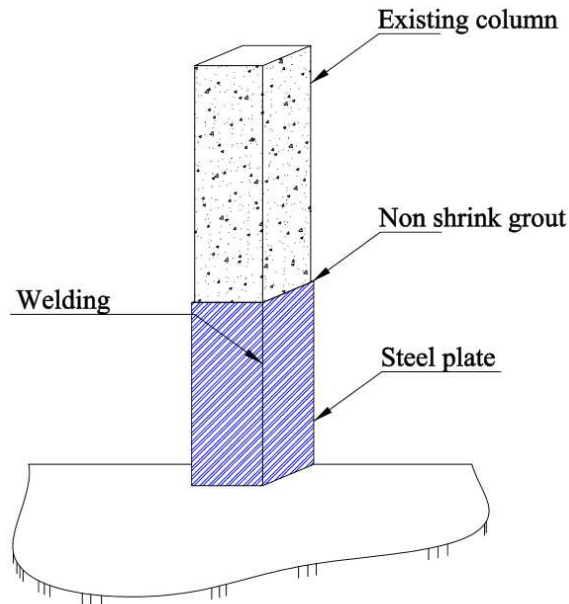


Figure 1-1: Concrete jacketing

However use of concreting jacketing involves some disadvantages such as increase in volume and weight, artful detailing and laborious work to install at the site.

#### 1.4. Seismic strengthening using steel plates

The use of externally bonded steel elements such as steel plates (Figure 1-2), angles and strips has been widely used to strengthened reinforced concrete members [5, 6]. The use of steel jacketing does not increase the weight of the structure significantly and saves construction time when compared with reinforced concrete jacket. The steel elements can be pre-fabricated, and are more rapidly installed at site and less disruptive to building occupants [7].



**Figure 1-2: Steel jacketing**

Despite of successful application of steel jacketing in seismic strengthening, this technique involves some disadvantages such as high weight of steel plates causing problem during installation and corrosion problems during the service life.

### **1.5. Seismic strengthening using fiber reinforced polymers**

Externally bonded unidirectional fiber reinforced polymers (FRP) systems have been used to strengthen and retrofit existing concrete structures (Figure 3-1) around the world since the mid-1980s [8]. FRP is a composite material made up of two distinct, independent elements. The primary structural element is the fibers, which are encapsulated by a matrix composed of some type of polymer [9]. Externally bonded FRP systems were developed as alternatives to traditional external reinforcing techniques such as steel plate bonding and steel or concrete column jacketing. These unidirectional FRP(s) include carbon FRP [10], glass FRP [11], aramid FRP [12], polyethylene terephthalate (PET) FRP and polyethylene naphthalates (PEN) FRP [13]. As strengthening materials, they offer some advantages over conventional steel and concrete such as low weight, high strength and excellent resistance to corrosion. The higher costs associated with these FRP materials is typically offset by savings in labour when compared to the difficulty of steel plate jacketing.



**Figure 1-3: Application of Carbon FRP to the box girder [14]**

Up to now, the bulk of research into FRP strengthening has revolved around the use of unidirectional fiber fabrics which are epoxy bonded to the concrete surface(s). These unidirectional fibers are here referred to as “*conventional unidirectional FRP*” in this study. In contrast to the conventional unidirectional FRP, strengthening of concrete members with Sprayed Fiber Reinforced Polymer (SFRP) composites was first studied at the University of British Columbia [15]. Further this technique was evaluated in details for the strengthening or retrofitting of un-reinforced and reinforced concrete shallow beams [9, 16-19]. However, no research activities are found in literature on the development of material models, and strengthening of RC members such as RC deep beams with and without web openings and RC columns.

### **1.6. Objectives of study**

The scope of this research was to investigate the effectiveness of the Sprayed Fiber Reinforced Polymer (SFRP) composites as a seismic strengthening and repair method for reinforced concrete members such as RC deep beams and RC columns. In this study, glass and or carbon fibers are sprayed using un-saturated polyester resin on the concrete surface of RC members representing detailing of existing structures in low seismicity regions such as Thailand. The main research parameters included were fiber material, fiber length, thickness of fiber, strengthening orientation and strength of concrete. In the first step, small scale circular and square unreinforced concrete columns strengthened using SFRP were tested under monotonic axial loading to investigate the

stress-strain response of SFRP confined concrete. Further, the efficiency of externally bonded SFRP composites was investigated to enhance the ultimate load carrying capacity of reinforced concrete deep beams with and without web openings. Different anchoring systems to prevent the delamination of SFRP from concrete surface were also proposed and investigated. Finally, seismic strengthening of large scale reinforced concrete columns were performed using SFRP composites. SFRP strengthened RC columns were tested under reverse cyclic loading with constant axial load.

### **1.7. Dissertation outline**

This thesis dissertation is composed of thirteen chapters. A comprehensive literature review on existing studies conducted on seismic strengthening of RC member using SFRP is presented in chapter 2. The important experimental and numerical studies on RC members such as beams and columns are described.

Material properties of different materials such as steel, cement, aggregates, glass and carbon fiber roving and un-saturated polyester resin are presented in Chapter 3. The sprayed fiber reinforced polymer composites process is discussed in chapter 4. The mechanical properties of SFRP composites which are determined essentially following ASTM standards are given in Chapter 5.

A detailed experimental study conducted on SFRP strengthening of un-reinforced concrete columns is presented in chapter 6, whereas analytical study on these SFRP strengthened columns is discussed in Chapter 7. Existing strength models developed for uni-directional FRPs and newly proposed strengthened models to predict the compressive strength of SFRP confined concrete are also summarized in Chapter 7.

An experimental program to evaluate the efficiency of externally bonded SFRP to enhance strength and ductility of reinforced concrete deep beams without openings and with web openings is described in chapters 8 and 9, respectively. Chapter 10 and 11 describes a finite element analysis aiming to develop nonlinear finite element analysis for RC deep beams strengthened with SFRP.

In chapter 12, an experimental study performed on seismic strengthening of large scale RC columns is presented. Finally, chapter 13 presents the conclusions of present research work along with proposal for future research areas.



## **Chapter 2**

### **Literature Review**

#### **2.1 Introduction**

As mentioned in Chapter 1, the research work conducted throughout this thesis involved the use of Sprayed Fiber Reinforced Polymer (SFRP) composites for the strengthening or retrofitting of un-reinforced and reinforced concrete members. Since SFRP is a new strengthening technique compared to externally bonded unidirectional FRP fabrics, there has been limited research performed using this approach. Further the available research is mostly performed on shallow reinforced concrete beams or girders. This chapter will discuss the results obtained by researchers around the world on strengthening or retrofitting of reinforced concrete and masonry members using SFRP composites.

To the best of author's knowledge, the effectiveness of externally bonded SFRP as a means of shear strengthening of RC deep beams and seismic strengthening of large scale RC columns has not been investigated and this research project is the first of its kind.

#### **2.2 SFRP strengthening of unreinforced concrete beams**

The very first study on strengthening of un-reinforced small scale concrete beams using externally bonded SFRP composites dates back to 1996 [15]. In this study unreinforced concrete beams were strengthened using glass SFRP. Beams were sprayed on tensions side with a 3 mm thick coating of randomly distributed glass fibers at an estimated fiber content of 8% by volume. Few concrete beams were notched in the center to simulate service induced damage. The beams were tested under third-points loading. Authors reported that visually, premature de-bonding of the SFRP coating did not occur and SFRP coating developed a strong bond with concrete surface. Beams with SFRP coatings were found to possess a superior load carrying capacity and were found to absorb fracture energies far in excess of those absorbed by beams without SFRP coating [15].

The second study reported in the literature was carried out by Lee et al. [20]. In this study, authors investigated experimentally the structural enhancement of SFRP for repair and strengthening of plain concrete beams. They also examined how parameters

such as coating thickness and fiber materials affect the load capacity and ductility of the plain concrete beams. Substantial increases in the load capacity and energy absorption capability were observed after application of SFRP [20].

Most recently, Kwon et al. [21] tested unreinforced concrete beams strengthened with SFRP composites. The dimensions of the beams were 150 x 150 x 300 mm and SFRP was applied to the specimens' bottom surfaces (Figure 2-1). The research parameters investigated were concrete strength, fiber length in SFRP composite and fiber volume ratio. Most of the un-strengthened flexural specimens failed in a brittle manner. The strengthened specimens showed significant changes in the slopes of their load deflection curves at the deflections where the corresponding un-strengthened specimens failed. In this study, two types of failure modes were observed: delaminating and rupturing. The delaminating failure of SFRP was caused by sudden crack propagation along the interface between the concrete surface and SFRP.



**Figure 2-1: SFRP application to beam specimens**

### 2.3 SFRP strengthening of reinforced concrete beams

The first attempt to use SFRP composites for shear strengthening of shallow reinforced concrete beams is reported by Boyd, [9]. In this study, influence of various types of SFRP strengthening schemes was investigated to enhance the shear strength of shallow RC beams (Figure 2-2). The three schemes of SFRP strengthening were A, C and D (A = SFRP applied onto the two side faces only; C = SFRP applied onto the side and the bottom faces; D = SFRP applied over all faces of the beam). The results showed that strengthening scheme C and D were more effective than scheme A. In terms of the failure modes, all beams strengthened with schemes A and C failed by de-bonding of SFRP (Figure 2-3), whereas specimens with scheme D failed by rupture of SFRP. However, in their experiment, no anchoring system has been employed to fix the SFRP to the beam surface.

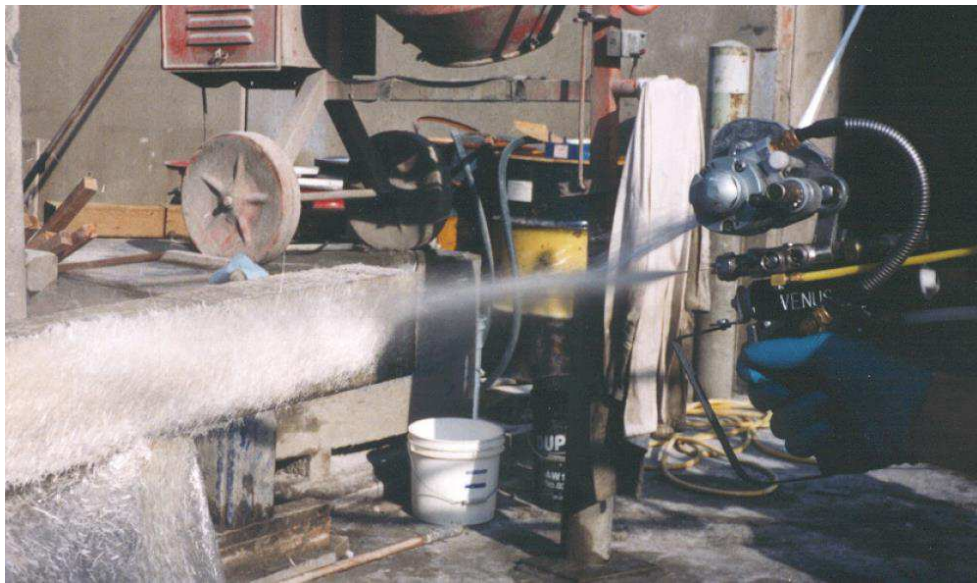
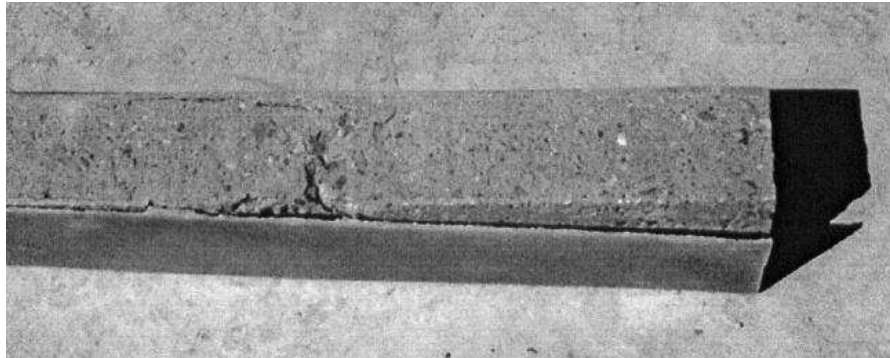


Figure 2-2: SFRP spray application on beams



**Figure 2-3: Failure of beams showing de-bonding of SFRP**

Lee and Hausmann (2004) [16] investigated the strength and ductility aspects of damaged and undamaged RC beams retrofitted with SFRP coating and to assess the feasibility of using SFRP coating for repair/strengthening of RC beams (Figure 2-4). The dimension of RC beams was 100x100x450 mm. Some of the RC specimens were pre-cracked to model deteriorated concrete structures. The concrete surface receiving SFRP coating was sandblasted to remove any debris and etches so that a high quality of bond between the concrete surface and SFRP coating can be assured. The parameters under this investigation include coating thickness, fiber volume fraction, fiber material, and fiber length, pre-cracked and un-cracked specimens. The findings of the experimental study can be summarized as follows: 1) Coating thickness has a significant influence on the peak load, ductility and energy absorption capacity of RC beams. 2) A more ductile failure with a significant increase in energy absorption capacity was observed with a thicker coating. 3) An appropriate fiber length near 26 mm will maximize the increase in load carrying and energy absorption capacities of RC beams. 4) Moderate volume fraction of fibers (up to 30%) is desirable for increasing the ductility and energy absorption of RC beams. 5) Carbon fibers lead to higher increase in load carry ability and lower increase in energy absorption for both damaged and undamaged RC beams due to their brittle characteristics compared to glass fibers.



**Figure 2-4: SFRP strengthened RC beams**

Ross et al. 2004 [23] performed experimental and analytical study on bridge girders and channel beams with and without SFRP composites (Figure 2-5). The channel beam bridge girder sections tested were once a part of the Neil Bridge on Vancouver Island in British Columbia, Canada. The SFRP used in this investigation were a mixture of chopped fiber glass strand and polyester resin applied using special spray equipment to a concrete surface that had been primed with a vinylester resin. Results show that the use of SFRP as a retrofit material increased the flexural stiffness of the reinforced concrete channel beam bridge girders [23].



**Figure 2-5: Application of SFRP on girders**

Cristina TC and Junichiro N (2000) evaluated the performance of reinforced concrete beams strengthened with SFRP composites. In this study, different resin systems such as Vinyl ester resin, Vinyl ester resin (R806), 50% Vinyl ester resin (R806) and 50% polyester resin (bb 100) and the polyester resin (bb 100) were investigated. The authors concluded that SFRP spray process of strengthening and rehabilitation is a very promising technique, and continued research will undoubtedly lead to its use in reality [24].

#### **2.4 Anchorage systems for SFRP strengthened concrete beams**

As it can be seen that almost all above mentioned studies reported pre-mature de-bonding of SFRP from the concrete surface. This is mainly because of weak resin system. Further a number of research efforts has been conducted in the past to prevent the delamination or de-bonding of SFRP from concrete surface. Few studies are summarized below;

The effectiveness of anchorage used to enhance the bonding capacity between the SFRP coating and the application face was first investigated by Lee 2004 [22]. A series of three point bending tests were carried out on notched un-reinforced concrete specimens retrofitted with SFRP layers and anchors. Anchorage was introduced using SFRP slits at 100 mm and 200 mm spacing as shown in Figure 2-6. A substantial

increase in ultimate load carrying capacity of beams were observed after SFRP strengthening. Further it was found that anchorage in the form of SFRP slits is very useful to enhance the bond between concrete surface and SFRP and load carrying capacity.



Figure 2-6: SFRP application in notched beams

Kanakubo et al. (2010) [25] proposed different anchoring methods to anchor SFRP at the meeting corner of beam and slab such as SFRP slits (No.1), slits and bolts (No.2), bolts (No.3), and bolts and steel blocks (No.4) as shown in the Figure 2-7. The authors reported that SFRP slits are effective for anchoring SFRP to concrete. Further, test results indicated a possible occurrence of cracks in SFRP nearby the anchor bolts in methods No.2 to No.4.

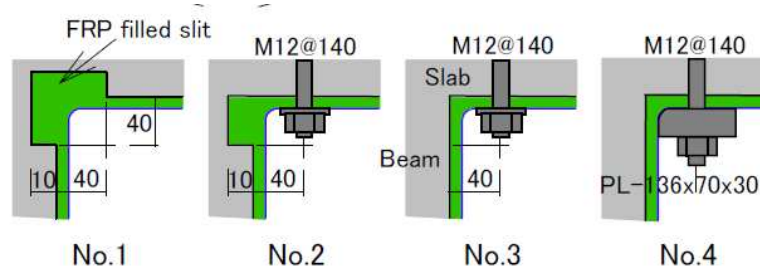


Figure 2-7: Anchoring system for corners

Soleimani (2006) [18] investigated the performance of SFRP for shear strengthening of RC shallow beams. In their research, an anchoring technique using through bolts and nuts with a roughened concrete surface was introduced to enhance the bond between concrete surface and the SFRP (Figure 2-8). Prior to the SFRP application, the concrete surface was roughened by a sandblasting method and through the use of a pneumatic chisel. Author concluded that roughening the concrete surface with a pneumatic chisel and the application of through bolt anchoring system was an effective means to increase the concrete-SFRP bond.



**Figure 2-8: Anchoring system for RC beam**

Recently, Kwon et al. [21] investigated the performance of different anchoring techniques such as U-shaped strips and shear keys to improve the interfacial bond resistance between the concrete surface and SFRP (Figure 2-9). It was found that, applying a U-shaped FRP strip in the center of the specimen more effectively controlled the deformation of the specimen under a flexural load, compared to applying U-shaped strips at both the ends. By applying shear keys at the bottom of the specimen, the flexural performance was improved by increasing the bond resistance between the concrete surface and applied SFRP.



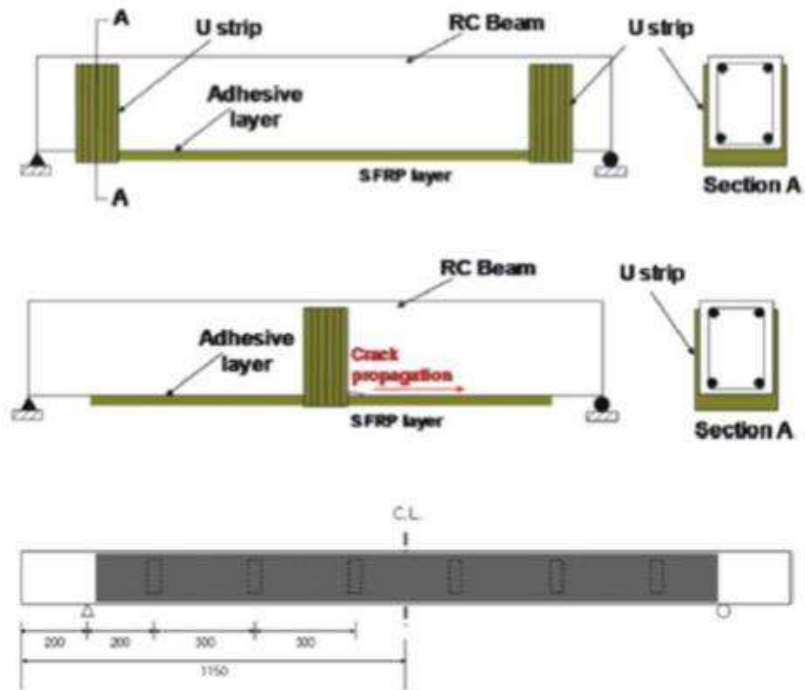


Figure 2-9: Anchoring system

## 2.5 SFRP strengthening of columns

Tests on circular reinforced concrete columns strengthened with SFRP demonstrated that the random distribution of fibres resulted in the increased toughness against crack propagation, in both directions i.e. parallel to the direction of compression and circumferentially as the concrete dilated [26]. Typical failure of SFRP strengthened column is shown in Figure 2-10.



**Figure 2-10: Failure of SFRP strengthened RC column**

Shaheen and Shrive (2007) has conducted an experimental investigation to access strength and strain increases imparted by SFRP technique of plain and steel reinforced masonry columns under concentric and eccentric loading. In this study twenty four columns were constructed and two thicknesses of SFRP where attempted (Figure 2-11). Based on test results, authors concluded that nevertheless, with only minor increases in strength, large increases in strain capacity were achieved with both the plain and reinforced columns under concentric axial compression [27].



**Figure 2-11: Glass fiber reinforced polymer spraying process**

Kwon et al. [21] investigated compressive response of small scale un-reinforced concrete columns strengthened using externally bonded SFRP. The test variables were fiber length, fiber volume ratio, and concrete compressive strength. The authors' reported that in general, the reinforced compressive specimens showed higher load carrying capacities and larger strain values at failure than unreinforced specimens, because of the confining effects of SFRP. Typical failure of SFRP strengthened column is shown in Figure 2-12.



**Figure 2-12: Typical failure of SFRP strengthened column**

In addition to the experimental investigations, there are few studies on finite element analysis of SFRP strengthened members. Lee et al. 2005 [28] conducted numerical studies on damaged reinforced concrete beams and bridge superstructures coated with SFRP to evaluate the retrofit and strengthening performance of SFRP. A computational model was developed by implementing a damage constitutive model in a finite element code to predict the performance of SFRP retrofitted concrete structures during service. Numerical simulations based on the model were compared with experimental data to assess the predictive capability of the proposed model [28].

## **Chapter 3**

### **Materials**

#### **3.1. Concrete materials**

This chapter deals with general properties and characteristics of the different material components used to prepare concrete throughout in this research work. However specific concrete mix proportions and compressive strength of the concrete is described in each experimental program.

##### **3.1.1 Cement**

Throughout this research work, a single brand of cement was used to prepare concrete. Cement was manufactured by Siam Cement Group Co. Ltd., Thailand. The cement is classified as Type 1, Normal Portland Cement. Fresh cement was used in the batching and mixing operations to avoid possible detrimental effects or inconsistencies in test results.

##### **3.1.2 Water**

All mixing water was taken directly from the City of Rangsit, drinking water supply.

##### **3.1.3 Fine aggregates (sand)**

Saturated Surface Dry (SSD) clean river sand with a fineness modulus of approximately 2.55 was used in all concrete mixtures. The concrete sand was purchased from Rung Sin Co. Ltd., Thailand, and has a relative density of 2.75.

##### **3.1.4 Coarse aggregates (gravel)**

Throughout this research program, crushed gravels with a maximum size of 19 mm were used in all mixes. The coarse aggregates were also obtained from Rung Sin Co. Ltd., Thailand. The relative density and SSD absorption values were 2.71 and 1.24%, respectively. The dry rodded density of gravels was 1555 kg/m<sup>3</sup>.

### 3.1.5 Reinforcing steel bars

All types of reinforcing steel bars (i.e. Deformed and round bars) used in this research program was also obtained from Rung Sin Co. Ltd., Thailand.

## 3.2. SFRP system

This section deals with the general description and characteristics of the SFRP composite. The SFRP composite include glass fiber roving, carbon fiber roving, unsaturated polyester resin and catalyst.

### 3.2.1 Glass fiber roving

The fibers used for the sprayed glass fiber reinforced polymer (SGFRP) composite was a glass-fiber roving coated with a silicone-based chemicals that enhance the bonding with the resin. The glass-fiber roving was manufactured by Jushi Group Co., LTD under the product name “*ER13-2400-180*” (Figure 3-1). The mechanical properties of the glass fiber roving provided by the manufacturer are listed in Table 3-1.



**Figure 3-1: Glass fiber roving**

### 3.2.2 Carbon fiber roving

The fibers used for the sprayed carbon fiber reinforced polymer (SCFRP) composite was a carbon-fiber roving (Figure 3-2). Carbon fibre roving was manufactured by Zoltek Companies, Inc., under the product name “*Panex35 continuous tow*”. The mechanical properties of the carbon fiber roving provided by the manufacturer are listed in Table 3-1.



Figure 3-2: Carbon fiber roving

Table 3-1: Mechanical properties of fibers

Properties	Fibre material		Units
	Glass	Carbon	
Diameter	13	7.2	$\mu\text{m}$
Tensile strength	2000	4137	MPa
Elastic modulus	80	242	GPa
Elongation at break	4.8	-	%

### 3.2.3 Resin and catalyst

The primary resin used for both SFRP was polyester resin manufactured by QualiPoly Chemical Corporation in Taiwan under the product name “*QL-724I*”. The catalyst which was used to initiate the curing of resin was “*ButanoxM-60*”, manufactured by Keum Jung AkzoNobel Peroxides Ltd. in China. The mechanical properties of resin and catalyst provided by manufactures are listed in Table 3-2.

**Table 3-2: Mechanical properties of resin and catalyst**

Properties	Resin		Units
	QL-7241	ButanoxM-60	
Density	1.08	1.17	g/cm <sup>3</sup>
Tensile strength	74	-	MPa
Tensile modulus	3700	-	MPa
Elongation at failure	2.4	-	%



## Chapter 4

### SFRP Application Process

#### 4.1 Introduction

Traditionally, unidirectional FRP(s) are externally applied on the concrete surface through resin which acts as a binding agent to bond fibers with concrete surface. Xiao (2004) [29] presented two types of FRP jacketing, namely in-situ fabricated jacketing and pre-fabricated jacketing. The first application involves hand or automated machine placement of epoxy saturated FRP or tows on concrete surface. On the other hand, in the second technique, preformed FRP laminates are applied to the concrete surface. Since in this study, sprayed FRP system is used only, the application process of SFRP technique is discussed next.

#### 4.2 Sprayed fiber reinforced polymer composites (SFRP) application process

Throughout this research program, the FRP spraying process was performed by means of UltraMax chopper/saturator unit manufactured by Magnum Venus Plastech (Figure 4-1). This is portable spraying equipment which can be easily used on site. Basically this spraying equipment is comprised of three main parts, a resin pump which pumps un-saturated polyester resin from container, a catalyst pump which pumps catalyst from bottle and shopper/spray unit as shown in Figure 4-2. Further, to run spraying equipment compressed air source (minimum capacity of 0.5 m<sup>3</sup>/minute) is used.

The resin and the catalyst are separately transported into the spray gun. They do not come into contact until they reach the mixing nozzle at the front of the gun. The catalyst content can be changed, but it is usually between 1 to 3% of the final mixture. This proportion will affect the time for curing the SFRP composite and is related to the temperature of the environment.



**Figure 4-1: FRP spray equipment**



**Figure 4-2: FRP Chopper/Spray unit**

At the nozzle, there are inlets for air and the solvent. Air powers the copper unit and the solvent is used to flush the resin and catalyst at the end of each period of operation. The glass or carbon fibers in the form of roving are brought to the chopper unit (Figure 4-3). One of the rollers inside the chopper unit has evenly spaced cutting blades (Figure 4-4) which cut the fiber into a pre-specified length (i.e. 13 mm, 26 and 52 mm). By changing this roller (i.e. the number of blades on the roller) the length of the chopped fibers can be changed. These chopped glass or carbon fibers are forced out by air flow (Figure 4-5). The rotation of rollers inside the chopper unit also helps a smooth flow of fibers (Figure 4-2).

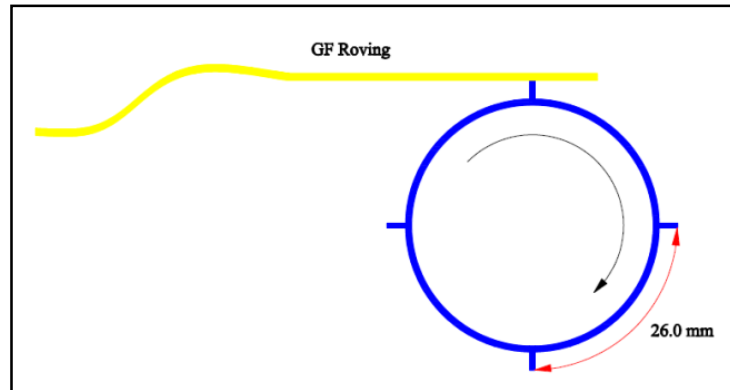


**Figure 4-3: SFRP application details**



**Figure 4-4: Cutting blade**

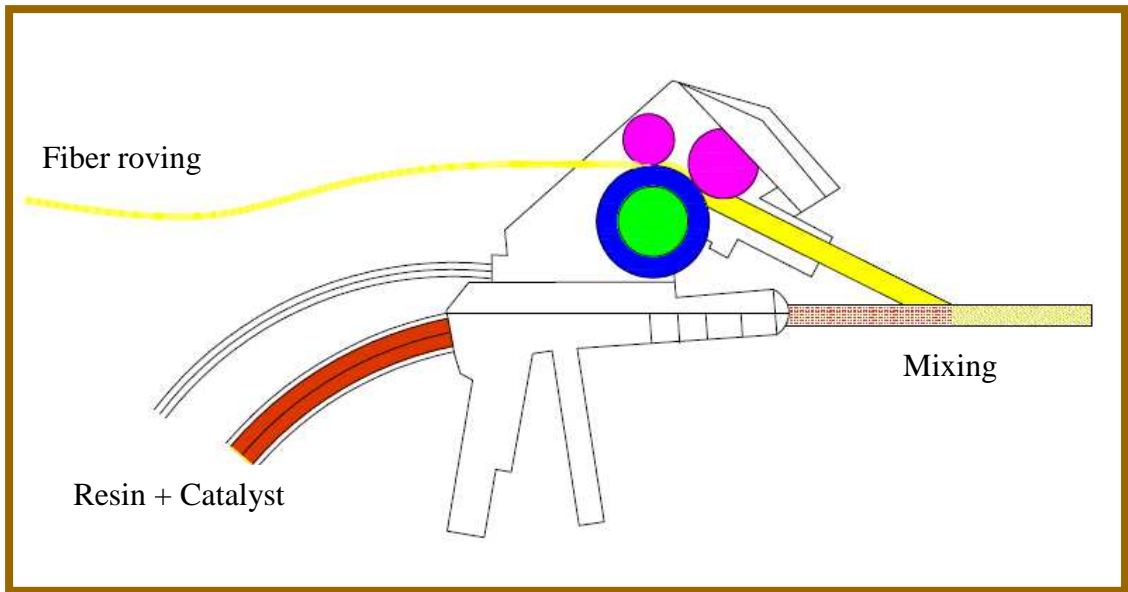


**Figure 4-5: Spraying chopped fibers**

The gun sprays the mixture of resin and catalyst with the chopped fiber on the concrete surface. After the SFRP is applied, an aluminum ribbed roller is used to remove any entrapped air and to obtain a uniform thickness of the SFRP (Figures 4-6 to 4-8). The final product is randomly distributed fibers encapsulated by a catalyzed resin. Although the operation of the SFRP spraying equipment is quite simple and straight forward, being able to produce uniform thickness of placement needs practice.



**Figure 4-6: Ribbed aluminum roller**



**Figure 4-7: A ribbed aluminum roller is used to obtain uniform thickness of SFRP on cylinders**



**Figure 4-8: A ribbed aluminum roller is used to obtain uniform thickness of SFRP on beams**

## Chapter 5

### SFRP Material Properties

#### 5.1 Sprayed SFRP properties

In this research program Sprayed Glass Fiber Reinforced Polymer Composites (SGFRP) and Sprayed Carbon Fiber Reinforced Polymer Composites (SCFRP) were used as the main material for strengthening RC members. SFRP was sprayed by skilled labor throughout the research program and as a result the quality and properties of SFRP composites were consistent. Boyd (2000) [16] investigated the effect of fibre length on the strengthening of RC beams and concluded that a fibre length of around 23 mm is appropriate to maximize the tensile strength and load carrying capacity of strengthened beams. Based on his results and discussion, two fiber lengths 13 mm and 26 mm were chosen to be used in this study. The properties of these SFRP materials are discussed below.

##### 5.1.1 Density

In this study, two different types of fiber lengths (i.e. 13 and 26 mm) were used for chopped fibers in SGFRP composite and only a single fiber length of 26 mm was used for chopped fibers in SCFRP composite. The density of different SFRP composites was determined using ASTM standard methods D792 [30]. The average test results are summarized in Table 5-1.

##### 5.1.2 Fiber volume fraction

The fiber volume fraction of both SGFRP and SCFRP composites was essentially determined using ASTM standards D2584 [31]. The average test results are summarized in Table 5-1.

##### 5.1.3 Tensile properties of SFRP composite

Boyd (200) [9] has determined the tensile properties of SFRP strips following the ASTM standard D638 [32] with a little modification in the size of tested strips. In the present study, the same method and similar strip size were used to determine the tensile strength of SFRP; however, the length of tensile strip was adjusted to fit the requirements of loading machine (Figure 5-1). For each SGFRP and SCFRP, a total of

10 tensile strips were cut from the sprayed sheets with five pieces for each thickness (i.e., 3 and 5 mm). The SGFRP and SCFRP sheets were prepared by spraying fibres onto a planar surface (Figures 5-2 and 5-3). The tensile strips were tested under the direct tension using a displacement-controlled loading machine (Figure 5-4). The applied load and the elongation were recorded by means of the data acquisition unit of the Universal Testing Machine (UTM). The typical failure of SGFRP tensile strip is shown in Figure 5-5. The average test values are reported in Table 5-1.

**Table 5-1: Mechanical properties of SFRP**

Properties	Units	SGFRP		SCFRP
		13 mm	26 mm	26 mm
Density	g/cm <sup>3</sup>		1.47	1.20
Fiber volume fraction	%	35-45	30-40	60-70
Tensile strength	MPa	85	92	104
Modulus of elasticity	MPa	10200	10600	9300
Fracturing strain	%	1.35	1.30	1.15

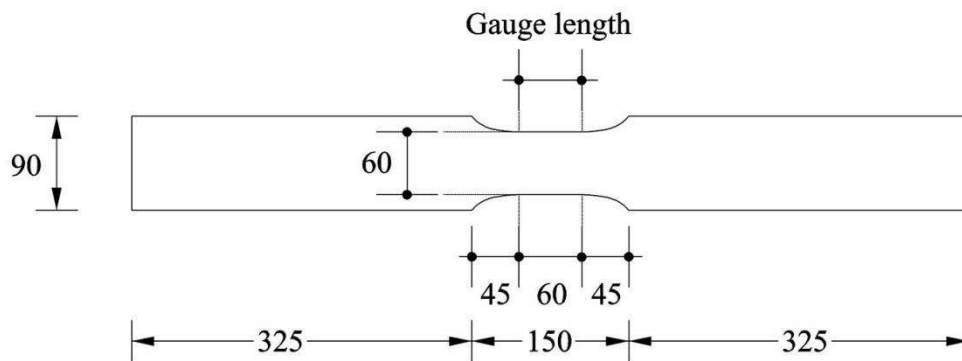


**Figure 5-1: Detailing of SFRP tensile strip**





**Figure 5-2: Spray process to prepare SFRP sheets**



**Figure 5-3: SGFRP sheets**



Figure 5-4: Loading setup to test SFRP tensile strips



**Figure 5-5: Typical failure of SFRP tensile strip**

## Chapter 6

### SFRP Strengthening of Small-size Concrete Columns

#### 6.1 Introduction

Column wrapping with conventional unidirectional FRP composites is a popular alternative for improving the seismic resistance of columns [33]. In the present literature, extensive research efforts have been conducted to experimentally investigate the axial behavior of concrete confined with externally bonded unidirectional FRPs such as glass, carbon, aramid, polyethylene naphthalate and polyethylene terephthalate. The improvement to the concrete properties was apparent with increased strength and ductility correlating to increases to the thickness of the FRP composites. Further, extensive laboratory researches have been conducted to obtain reliable strength as well as stress-strain models to predict compressive strength and stress-strain behavior of FRP-confined concrete. Saadatmanesh et al. 1994 [34] performed an experimental program on concrete columns confined by FRP and developed an analytical model based on the stress-strain model of concrete confined by reinforcing bars as proposed by Mander et al. 1988 [35]. The developed model was capable of predicting the strength and deformability of FRP-confined concrete. Samaan et al. 1998 [36] proposed a model to predict the stress-strain response of FRP-confined circular concrete sections. His model was found to correlate well with experimental results. An experimental program conducted by Rochette and Labossiere 2000 [12] to investigate the effect of Carbon FRP and Aramid FRP confinement on the behavior of square and rectangular columns reveals that confinement could increase the strength and ductility of concrete columns. Hosotani et al. 1998 [37] proposed an empirical stress-strain model for circular and square FRP-confined concrete columns. Shehata et al.[38] performed an experimental study on FRP-confined circular, square and rectangular concrete columns and proposed equations to predict the ultimate strength and strain of confined concrete for each cross sectional type. A new stress-strain model for FRP-confined concrete that can predict not only the ultimate strength, but also the ultimate strain has also been proposed. Youssef et al. 2007 [39] conducted an experimental and analytical study to examine the influence of radius of cross sectional corners on the strength of square columns confined with FRP. Dai et al. 2011 [13] performed a study on the behaviour of concrete confined

by PET and PEN fibers. He concluded that the stress-strain model proposed by Jiang and Teng [40] could be applied to predict the compressive strength of concrete confined by PET and PEN fibers but may overestimate the ultimate axial strain. A modified model was developed based on the stress-strain model proposed by Jiang and Teng [40], which could provide a better prediction of the ultimate strength, strain and the stress-strain behavior of PET- and PEN-confined concrete.

The research work presented in “Chapter 6” is mainly conducted to investigate the effectiveness of externally bonded SFRP to improve the strength and ductility of confined concrete. Small scale circular and square un-reinforced concrete columns strengthened with different thickness of SFRP are tested under uniaxial compression to investigate the increase in the ultimate strength and ductility.

## **6.2 Experimental program**

The entire experimental program comprised the testing of 12 circular and 12 square columns (Table 6-1). Two specimens for each cross sectional type were un-strengthened and served as the reference specimen. The specimen notations are given to represent the cross section type (C for Circular and S for Square), SFRP thickness (in mm) and fiber length (in mm). For example, in the specimen notation C-6-26, the first letter C denotes circular section, the second number is the SFRP thickness, i.e., 6 mm, and the last number represents the length of SFRP fibers, i.e., 26 mm.

**Table 6-1: Test program of column specimens**

Specimen	Cross section	Nominal dimensions Diameter/Width x Height (mm)	SFRP thickness (mm)	Fiber length (mm)	Number of Specimen
C-0-0	Circular	100 x 200	-	-	2
C-3-13	Circular	100 x 200	3	13	2
C-3-26	Circular	100 x 200	3	26	2
C-6-13	Circular	100 x 200	6	13	2
C-6-26	Circular	100 x 200	6	26	2
C-9-26	Circular	100 x 200	9	26	2
S-0-0	Square	100 x 200	-	-	2
S-3-13	Square	100 x 200	3	13	2
S-3-26	Square	100 x 200	3	26	2
S-6-13	Square	100 x 200	6	13	2
S-6-26	Square	100 x 200	6	26	2
S-9-26	Square	100 x 200	9	26	2

### 6.3 Specimen preparation

The dimension (diameter of circular section or width of square section) of the specimen was 100 mm, whereas the height of both circular and square specimens was 200 mm, i.e., the height-to-depth ( $h/d$ ) ratio is set to 2.0 as shown in Figure 6-1. The corners of the square section were rounded off to attain the radius ( $R_c$ ) of 20 mm to avoid the premature rupture of SFRP at the corners (Figure 6-1). The casting of specimens were performed using steel molds as shown in Figure 6-2. Soleimani and Banthia [18] investigated the effect of surface roughness on the enhancement of bond between SFRP and concrete surface. Test results indicated that roughening the concrete surface by a pneumatic chisel is an effective means to increase the bonding between concrete and SFRP. In the present study, the column surfaces were roughened using a chisel and hammer prior to the application of SFRP (Figure 6-3).

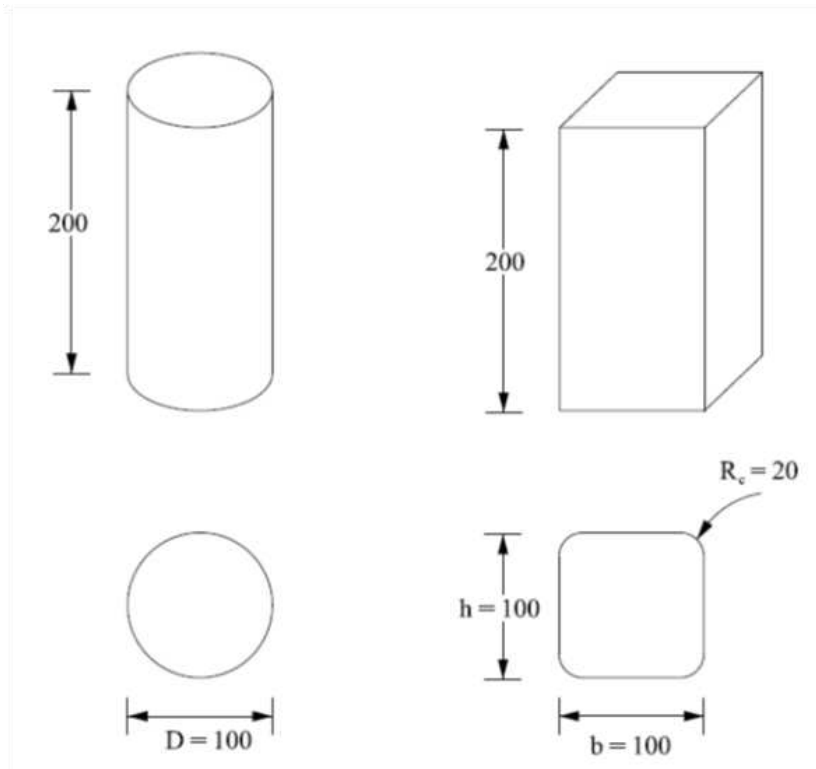


Figure 6-1: Test specimen; circular column (left) and square column (right)-dimensions are in mm



Figure 6-2: Preparation of circular columns



**Figure 6-3: Column specimens with rough surface**

#### **6.4 Concrete properties**

All test specimens were prepared using the same batch of concrete mix of Type 1 Portland cement as specified in ASTM C150 [41] and natural aggregates with the maximum size of 13 mm. The target un-confined compressive strength at 28 days was 20 MPa. The mix composition of the concrete is given in Table 6-2. However, the actual average compressive strength of concrete at the testing age (around 35-45 days) was slightly higher than the target strength as shown in Table 6-3.

**Table 6-2: Concrete mix composition (per cubic meter)**

Components	Quantity
Cement	265.00 kg
Water	172.25 kg
Sand	689.00 kg
Gravel	1086.50 kg
Water-to-Cement ratio (W/C)	0.65

#### **6.5 SFRP strengthening**

Prior to the spraying, an arrangement of iron stand and steel plates welded with rods are installed at both ends of the specimens for continuous rotation of the specimens during spraying process (Figure 6-4). SFRP was applied to the specimens by spraying glass fibers simultaneously with resin onto the specimen surface (Figure 6-5). SFRP strengthened circular and square columns are shown in Figures 6-6 and 6-7.





**Figure 6-4: Arrangement for SFRP spray process**



**Figure 6-5: SFRP application process**



**Figure 6-6: SFRP strengthened square columns**



**Figure 6-7: SFRP strengthened circular columns**

## **6.6 Thickness of SFRP**

The actual thickness of SFRP obtained in the spray process is dependent on the experience of skilled workmen, and may deviate from the desired thickness. The target thickness was 3 mm, 6 mm and 9 mm for both circular and square columns. After performing the tests, the actual thickness of SFRP shells for each specimen was determined using an ultrasonic thickness meter. These SFRP shells were obtained by removing concrete and the internal surface of shells was cleaned with a wire brush. The thickness was measured at different locations around the circular and square SFRP shells and the average values are reported in Table 6-3.

**Table 6-3: Target and actual SFRP thickness**

Specimen	Compressive strength	Target thickness (mm)	Actual thickness (mm)
C-0-0	23.40	-	-
C-3-13	23.40	3.00	3.50
C-3-26	23.40	3.00	3.50
C-6-13	23.40	6.00	6.00
C-6-26	23.40	6.00	6.00
C-9-26	23.40	9.00	9.50
S-0-0	24.50	-	-
S-3-13	24.50	3.00	3.25
S-3-26	24.50	3.00	3.25
S-6-13	24.50	6.00	5.50
S-6-26	24.50	6.00	5.50
S-9-26	24.50	9.00	8.50

## 6.7 Instrumentation

### 6.7.1 Circular columns

Each circular column specimen was instrumented with four strain gauges (gauge length = 67 mm) at the mid height of the specimen. Two of the four strain gauges were attached in the horizontal position at the opposite side (i.e., 180 degree apart) around the perimeter to record the transverse strain of SFRP whereas the remaining two gauges were attached vertically at the opposite location to record the axial strain in SFRP. In addition, three vertical linear variable displacement transducers (LVDTs) were installed at 120 degree apart around the perimeter to measure the axial strains and three horizontal LVDTs were placed 120 degree apart horizontally at the mid height to record the average transverse dilation of the specimens (Figure 6-8).

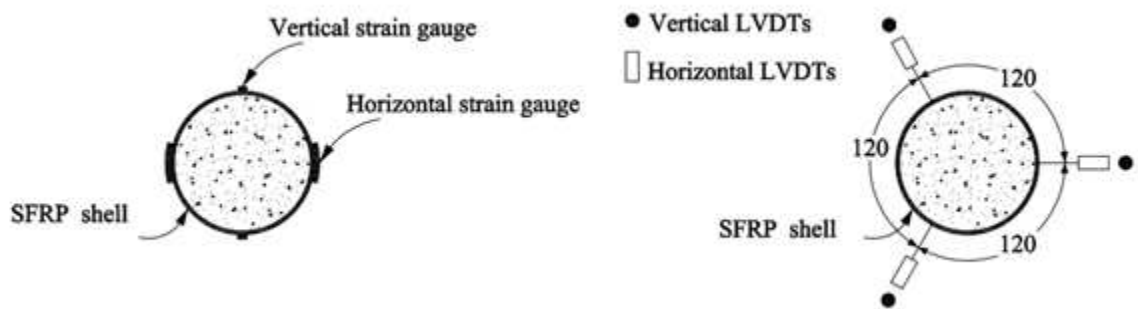


Figure 6-8: Instrumentation for circular specimens

### 6.7.2 Square columns

Each square column was instrumented with six strain gauges (gauge length = 67 mm) attached at the mid height. Four of the six strain gauges were attached horizontally at each corner to measure the transverse strain whereas the remaining two strain gauges were fixed vertically at two opposite sides (180 degree apart) to record the axial strain in SFRP. In addition to the strain gauges, six linear variable differential transducers (LVDTs) were instrumented to the specimen. Three LVDTs were placed vertically at each of three sides to measure the average axial strains whereas the remaining three LVDTs were provided horizontally at each of the three sides to record the lateral deformation (Figure 6-9). To ensure the safety of instruments, all LVDTs were removed prior to the final failure of specimens.

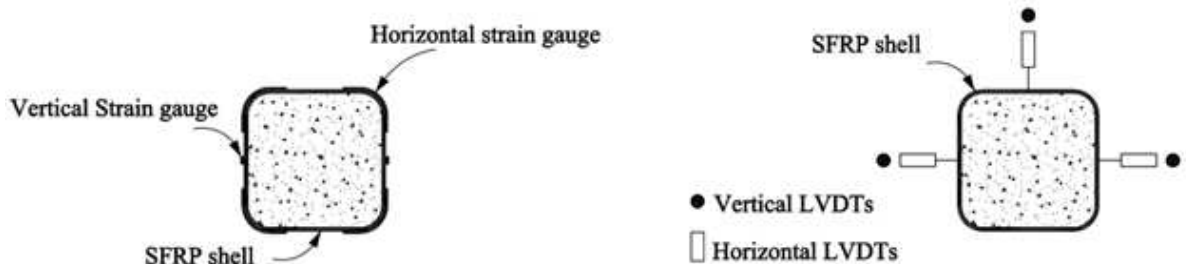


Figure 6-9: Instrumentation for square specimens

## 6.8 Test procedure

All circular and square specimens were tested under monotonic uniaxial compression up to failure in a Universal Testing Machine of 2000 kN capacity. The load was applied at a constant rate of 4 kN/sec and strains were measured at the load interval of 120 kN by an electronic data logger. Prior to the testing, some arrangements

were made to accurately measure the data and to avoid any possibility of premature failure. These arrangements included; 1) all SFRP-confined and unconfined specimens were capped with sulfur mortar pad at both ends to ensure a full contact surface, which results in a uniform distribution of load over the entire cross sectional area. 2) the sulfur mortar cap was trimmed off over the SFRP shell to avoid the possibility of transmitting the axial load onto the fiber shell area. 3) both ends of all strengthened specimens were additionally wrapped with two 25 mm wide strips of Carbon Fiber Reinforced Polymer (CFRP) sheets to avoid premature failure of SFRP shells at the ends. 4) In addition to the sulfur mortar capping, steel plates of 5 mm thickness were placed at both ends to ensure the application of load over the confined concrete area and to avoid any accidental axial load transfer onto the fiber shell especially when the specimen undergoes a large deformation near the failure (Figure 6-10). Test setup is shown in Figure 6-11.



**Figure 6-10: Typical square test specimens**



Figure 6-11: Test setup

## 6.9 Results and discussions

### 6.9.1 Overall behavior and stress-strain response

The stress-strain responses of all circular and square SFRP-confined columns under uniaxial monotonic loading are shown in Figures 6-12 and 6-13. Average values of tested compressive strength and strains are given in Table 6-4. It can be seen that the confinement from SFRP jacketing is effective to increase the ultimate strength and strain of both circular and square specimens. For all SFRP-confined specimens, the increase in the ultimate strength and strain is observed to vary with the increase in SFRP thickness. The specimen C-3-26 (3 mm thick SFRP) failed at 156% and 301% higher compressive strength and axial strain, respectively, compared to the control specimen. When the thickness of SFRP was increased to 6 mm as in the specimen C-6-26, the compressive strength and strain were increased by 259% and 536%, respectively. The highest increase in compressive strength and strain was 370% and 659%, respectively, recorded for the specimen C-9-26 with 9 mm thick SFRP.

However, in case of square column specimens, the increase in compressive strength and strain is generally less than those recorded for circular specimens. The specimen S-3-26 (3 mm thick SFRP) exhibited a 107% and 203% increase in compressive strength and strain, respectively whereas the increase in compressive strength and strain of specimen S-6-26 (6 mm thick SFRP) was 216% and 308% compared to the un-strengthened specimen. Similar to the circular column, the highest increase was 337% and 414% for compressive strength and strain, respectively, which was recorded for the specimen S-9-26 with 9 mm SFRP thickness. In addition, it is evident from these experimental results (Table 6-4) that the increase in strength and deformability of SFRP-confined concrete is significant for both fiber lengths i.e., 13 and 26 mm. However, SFRP with fiber length of 26 mm was found to be more effective to enhance both compressive strength and strain as compared with the fiber length of 13 mm.

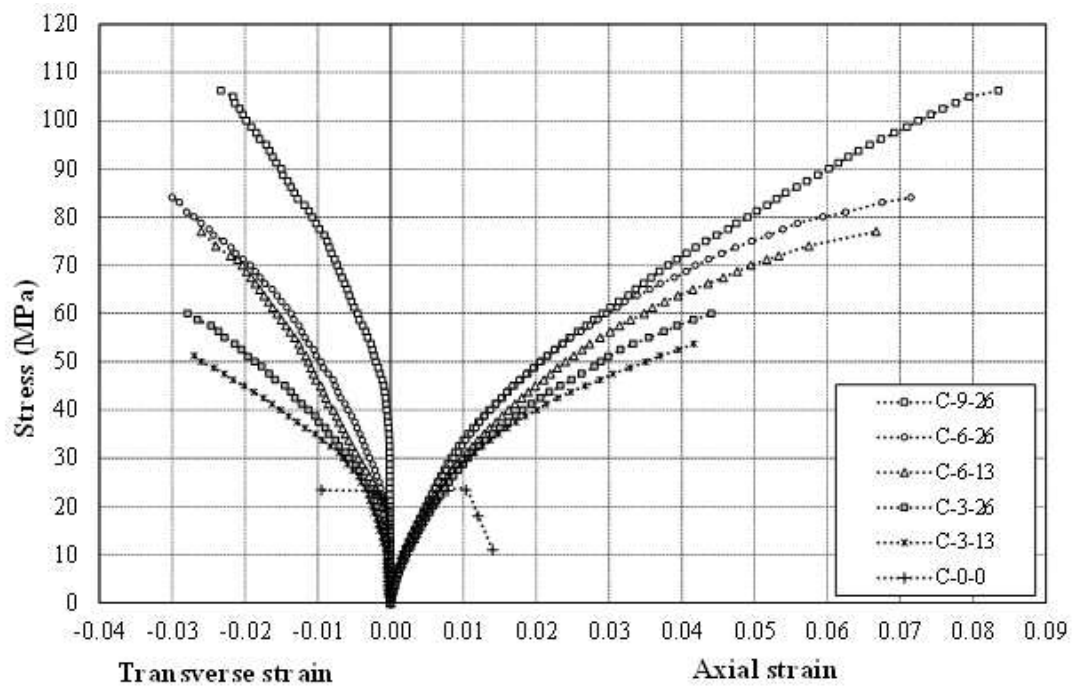


Figure 6-12: Stress-strain curves of circular specimens

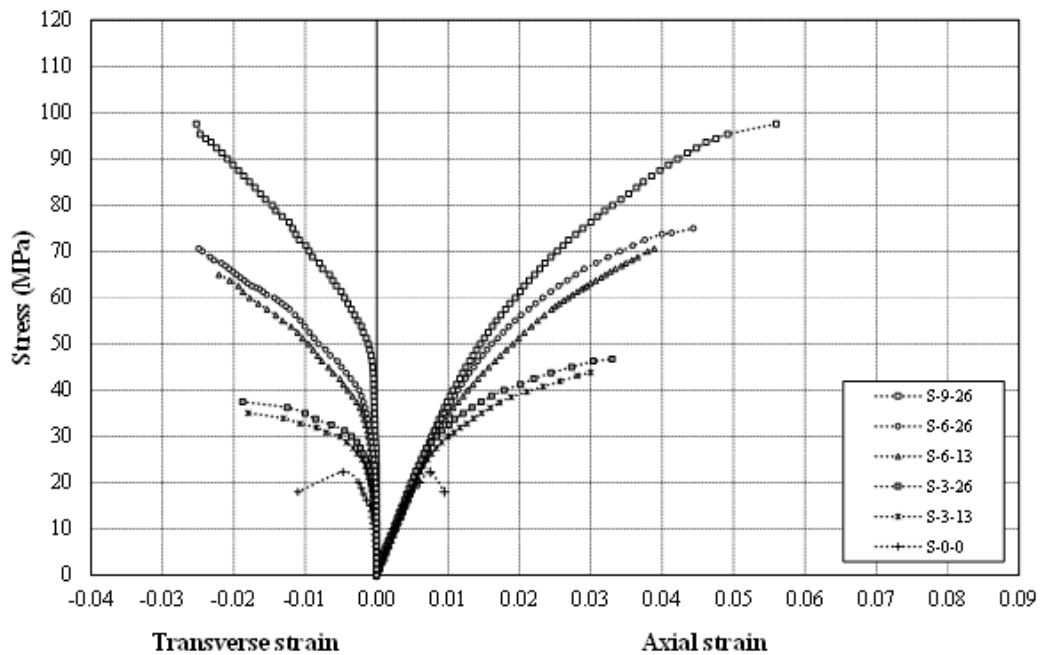


Figure 6-13: Stress-strain curves of square specimens

Table 6-4: Test results

Specimen	$f'_{co}$ (MPa)	$f'_{cc}$ (MPa)	$f'_{cc}/f'_{co}$	$\epsilon_{cc}$	$\epsilon_{cc}/\epsilon_{co}$
C-0-0	23.40	-	1.0	1.10	
C-3-13	23.40	53.71	2.30	4.16	3.78
C-3-26	23.40	59.95	2.56	4.41	4.01
C-6-13	23.40	77.00	3.29	6.67	6.06
C-6-26	23.40	84.00	3.59	7.00	6.36
C-9-26	23.40	110.00	4.70	8.35	7.59
S-0-0	24.50	-	1.0	1.09	1.00
S-3-13	24.50	46.21	1.89	3.00	2.75
S-3-26	24.50	46.71	1.91	3.30	3.03
S-6-13	24.50	70.57	2.88	3.90	3.58
S-6-26	24.50	74.94	3.06	4.45	4.08
S-9-26	24.50	97.50	3.98	5.60	5.14

The typical axial stress – axial strain and axial stress - transverse strain curves of SFRP-confined and unconfined specimens are shown in Figures 6-12 and 6-13. As can be seen, irrespective of the cross section shape and confinement level, the typical axial stress-strain curve of SFRP-confined concrete is essentially tri-linear, that is, it is composed of three parts. The first part of the curve is described by a linear line similar to the curve of the unconfined concrete. The second part is a transitional part, where



both axial stress-axial strain and axial stress-transverse strain curves of the confined concrete are softened and exhibited a non-linear behavior accompanied by a large increase in strain. In the third part, the stress-strain curves of confined concrete increase linearly again, but with a much lower elastic modulus compared to the first part, until a sudden failure occurs due to the rupture of the SFRP shell. This observed tri-linear behavior of SFRP confined concrete has also been reported for unidirectional FRP-confined concrete [42].

## **6.10 Failure modes**

### **6.10.1 Circular columns**

All SFRP-confined circular specimens failed by the rupture of SFRP shell caused by the hoop tension associated with the lateral expansion. The failure of the confined specimens resulting from the rupture of SFRP shell was suddenly brittle and characterized by a large explosive sound. Prior to the final rupture, intermittent snapping sounds indicating progressive fracturing of fibers could be clearly observed in all confined circular specimens.

The typical failure of SFRP-confined circular specimens is shown in Figure 6-14. The failure is characterized by a fully or partly vertical splitting rupture of SFRP shells. This failure mode indicates that the hoop tension in the SFRP shell which is caused by the transverse strain due to the lateral expansion of the specimen exceeds the composite strength. Figure 6-14(a) shows a fully vertical rupture of SFRP shell in specimen C-9-26 with the rupture traversing the entire height including the CFRP sheets. In case of other specimens with less SFRP thickness, i.e., specimens C-6-26 and C-3-26, the vertical rupture did not propagate across the full height, as shown in Figure 6-14(b) and (c), respectively. A possible reason is that the propagation of vertical rupture was restrained by CFRP sheets provided at both ends of the specimen. The confinement from CFRP sheet could arrest the propagation of SFRP rupture if the thickness of SFRP shell was not large. However, when the thickness of SFRP shell was increased as in the specimen C-9-26, the restraint from CFRP sheet was not adequate to inhibit the rupture propagation, thus the vertical splitting rupture spread through the entire height.

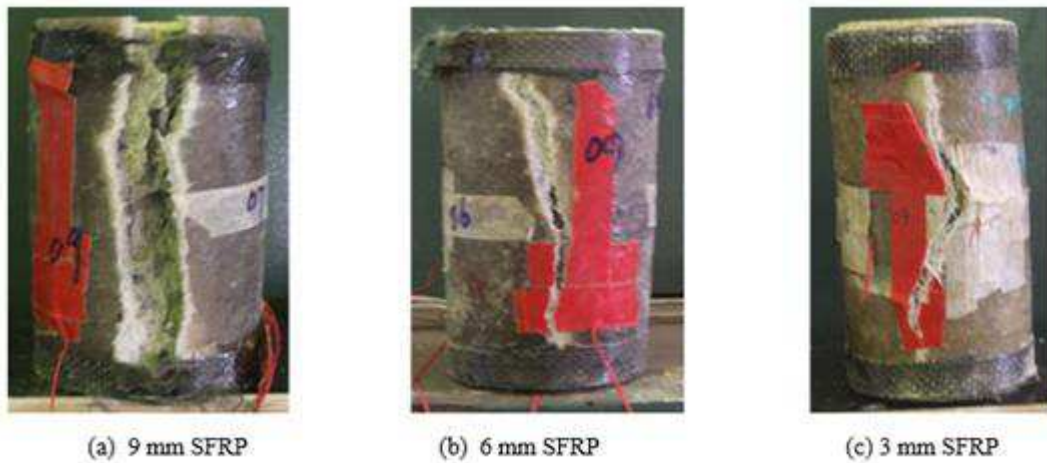


Figure 6-14: Typical failure modes of SFRP confined circular columns

### 6.10.2 Square columns

The typical failure of SFRP-confined square specimens also occurred due to the rupture of SFRP shell. Similar to the case of circular specimens, the failure of square specimens was sudden and explosive. When the final failure was approaching, some snapping sounds could be heard too. In almost all square specimens, the rupture of SFRP shell started near one of the corners of the section due to the stress concentration except in one specimen where the rupture of SFRP shell occurred at the column face (Figure 6-15). The rupture of confining fibers at the corners due to stress concentration has also been reported for FRP-confined square columns too [39].

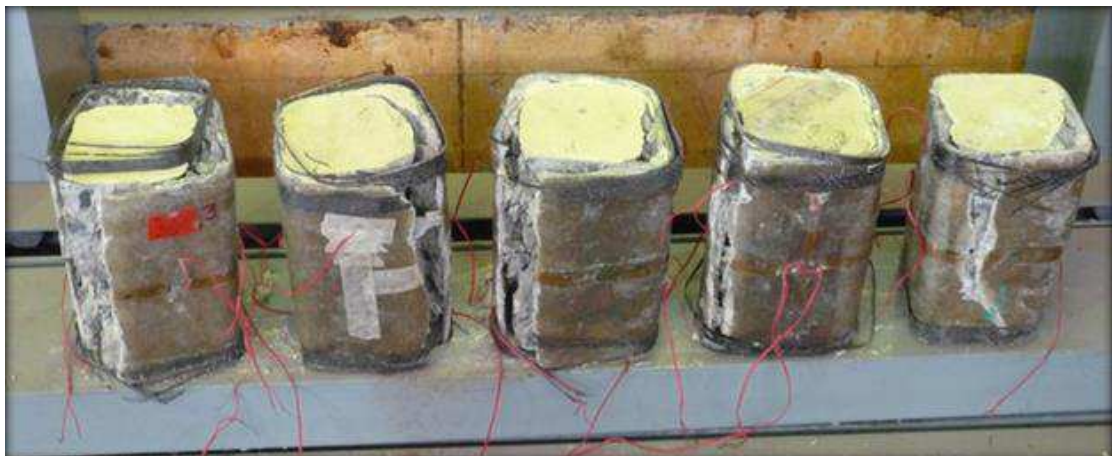


Figure 6-15: Typical failure modes of SFRP confined square columns

## Chapter 7

### Strength models for SFRP confined concrete columns

#### 7.1 Introduction

In this chapter, experimental results of both circular and square columns strengthened using SFRP composites (as discussed in chapter 6) are used to assess the performance of existing strength models developed for conventional unidirectional FRP. It was found that almost all existing models are conservative to predict the experimental compressive strength of SFRP-confined concrete. Finally, new strength models for SFRP-confined circular and square sections are proposed.

#### 7.2 Existing models

In the past 20 years, extensive analytical researches have been conducted on the development of models to predict compressive strength of circular and square column specimens confined by unidirectional FRP [10-12]. Currently, there are several strength models to predict the ultimate compressive strength of FRP-confined concrete. Based on the experimental results (presented in Chapter 6), the performance of existing strength models developed for the unidirectional FRP is assessed to examine its applicability to the SFRP confinement. Some of these models which are collected from literature are summarized in Table 7-1 and Table 7-2 for circular and square columns, respectively. Almost all of these models which are developed for FRP-confined concrete can be expressed in the following form:

$$\frac{f'_{cc}}{f'_{co}} = 1 + k_1 \frac{f_l}{f'_{co}} \quad (1)$$

where  $f'_{cc}$  and  $f'_{co}$  are compressive strength of confined and unconfined concrete, respectively,  $k_1$  is the confinement effectiveness coefficient and  $f_l$  is the lateral confining pressure. This form of the equation was originally proposed by Richart et al. 1928 [43] with  $k_1 = 4.1$  for concrete actively confined by fluid pressure. Later, Fardis and Khalili 1981 [44] reported that that the model proposed by Richart et al.

1928 [43] could be used for FRP-confined concrete. The lateral confining pressure  $f_l$  can be related to the strength and amount of FRP in the following way:

*For circular columns*

$$f_l = \frac{2f_{FRP} t}{D} \quad (2)$$

Where  $f_{FRP}$  is the tensile strength of the FRP in the hoop direction,  $t$  is the thickness of the FRP and  $D$  is the diameter of core concrete i.e., confined circular concrete section.

*For square columns*

$$f_l' = \frac{2f_{FRP} t}{D} k_s \quad (3)$$

where  $k_s$  is the shape factor which is defined as the ratio of the effective confinement area to the total cross sectional area of concrete [45]. The shape factor  $k_s$  can be determined by the following expression given by ACI318 [45]:

$$k_s = 1 - \left( (b - 2R_c)^2 + (h - 2R_c)^2 / 3A_g \right) \quad (4)$$

where  $A_g$  is the gross sectional area of concrete and can be determined by the following expression [45].

$$A_g = bh - (4 - \pi)R_c^2 \quad (5)$$

$D$  is the diameter of an equivalent circular column. In the ACI strength model for square sections [45].

The equivalent circular column is defined as a column which has the same FRP volumetric ratio as that of the original rectangular column. Following this definition, the diameter of the equivalent circular column can be expressed by the following equation;

$$D = \frac{2bh}{b + h} \quad (6)$$

Where  $b$  and  $h$  are width and depth of square or rectangular section.

**Table 7-1: Existing strength models for FRP-confined circular columns**

Sr. No	Model	Equation for $\frac{f'_{cc}}{f'_{co}}$
1	Karbhari and Gao [11]	$\frac{f'_{cc}}{f'_{co}} = 1 + 2.1 \left( \frac{f_l}{f'_{co}} \right)^{0.87}$
2	Samaan et al. [36]	$\frac{f'_{cc}}{f'_{co}} = 1 + 6.0 \left( \frac{f_l^{0.7}}{f'_{co}} \right)$
3	Fardis and Khalili [44]	$\frac{f'_{cc}}{f'_{co}} = 1 + 2.05 \left( \frac{f_l}{f'_{co}} \right)$
4	Miyauchi et al. 1997 [46]	$\frac{f'_{cc}}{f'_{co}} = 1 + 3.5 \left( \frac{f_l}{f'_{co}} \right)$
5	Saafi et al. [47]	$\frac{f'_{cc}}{f'_{co}} = 1 + 2.2 \left( \frac{f_l}{f'_{co}} \right)^{0.84}$
6	Toutanji [48]	$\frac{f'_{cc}}{f'_{co}} = 1 + 3.5 \left( \frac{f_l}{f'_{co}} \right)^{0.85}$
7	Ilki and Kumbasar [49]	$\frac{f'_{cc}}{f'_{co}} = 1 + 2.227 \left( \frac{f_l}{f'_{co}} \right)$
8	Lam and Teng [50]	$\frac{f'_{cc}}{f'_{co}} = 1 + 2.0 \left( \frac{f_l}{f'_{co}} \right)$
9	Riad et al. [51]	$\frac{f'_{cc}}{f'_{co}} = 1 + 1.60 \left( \frac{f_l}{f'_{co}} \right)$
10	Spoelstra and Monti [52]	$\frac{f'_{cc}}{f'_{co}} = 0.2 + 3.0 \left( \frac{f_l}{f'_{co}} \right)^{0.50}$
11	Mirmiran and Shahawy [53]	$\frac{f'_{cc}}{f'_{co}} = 1 + 4.269 \left( \frac{f_l^{0.587}}{f'_{co}} \right)$

*Note: Unit in MPa*

**Table 7-2: Existing strength models for FRP-confined square columns**

Sr. No	Model	Equation for $\frac{f'_{cc}}{f'_{co}}$
1	Shehata et al. [38]	$\frac{f'_{cc}}{f'_{co}} = 1 + 0.85 \frac{f'_l}{f'_{co}}$
2	American Concrete Institute [45]	$\frac{f'_{cc}}{f'_{co}} = -1.254 + 2.254 \sqrt{1 + \frac{7.94 f'_l}{f'_{co}}} - 2 \frac{f'_l}{f'_{co}}$
3	Campione and Miraglia [54]	$\frac{f'_{cc}}{f'_{co}} = 1 + 2 \frac{f'_l}{f'_{co}}$
4	Kumutha et al. [55]	$\frac{f'_{cc}}{f'_{co}} = 1 + 0.93 \frac{f'_l}{f'_{co}}$
5	Al-Salloum [56]	$\frac{f'_{cc}}{f'_{co}} = 1 + 3.14 \left( \frac{b}{D} \right) \frac{f'_l}{f'_{co}}$
6	Mirmiran et al. [53]	$\frac{f'_{cc}}{f'_{co}} = 1 + 6.0 \left( \frac{2r}{D} \right) \frac{f'_l}{f'_{co}}^{0.7}$
7	Lam and Teng [57]	$\frac{f'_{cc}}{f'_{co}} = 1 + 3.30 \frac{f'_l}{f'_{co}}$
8	Restrepo and De [58]	$\frac{f'_{cc}}{f'_{co}} = \alpha_1 \alpha_2$

Note: Unit in MPa.

### 7.3 Assessment of existing models

The present experimental results (Table 6-4) are employed to access the applicability of existing strength models (Tables 7-1 and 7-2) to the case of SFRP-confined circular and square columns. The comparison of various existing strength models with experimental results obtained in this study are given in Figures 7-1 and 7-2. The experimental strength ratio  $f'_{cc}/f'_{co}$  is plotted against the theoretical strength ratio proposed by various existing models. The performance of the existing models is evaluated in terms of statistical mean values, standard deviation and coefficient of variation as summarized in Tables 7-3 and 7-4. It can be seen that almost all existing models are conservative to predict the experimental compressive strength of SFRP-

confined concrete. Among these selected models, the predictions of test results by models proposed by Fardis and Khalili [44], Miyauchi et al. [46] and Toutanji [48] are relatively close to the experimental results for circular specimens. Whereas, in case of square specimens, the theoretical prediction by Shehata et al.'s model [38] is comparatively close to the experimental results.

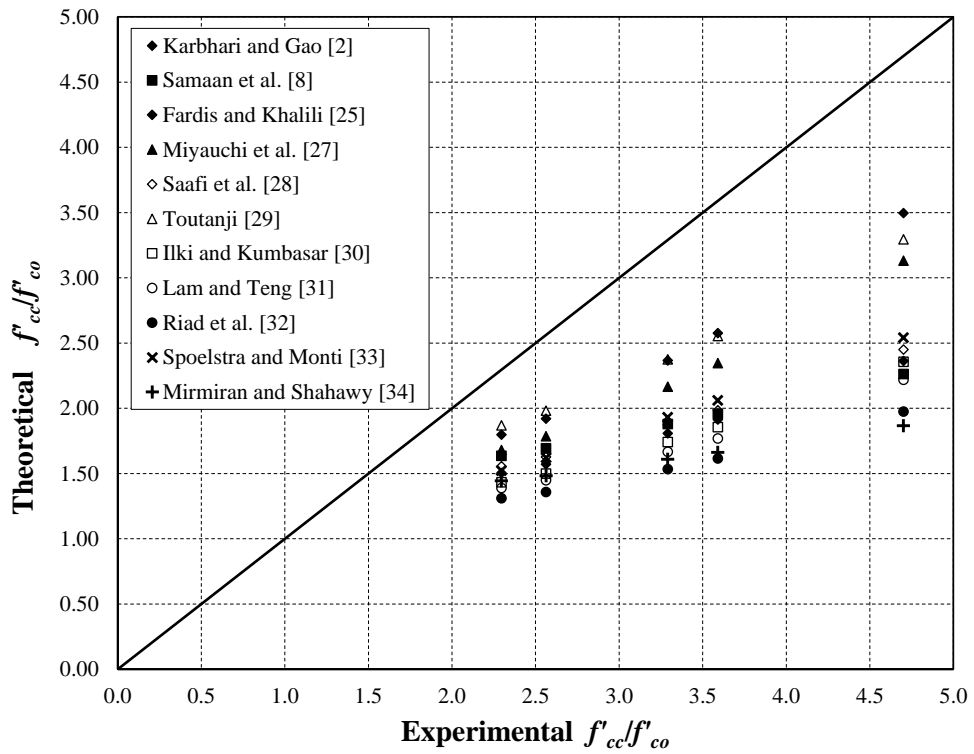


Figure 7-1: Performance of existing strength models for circular columns

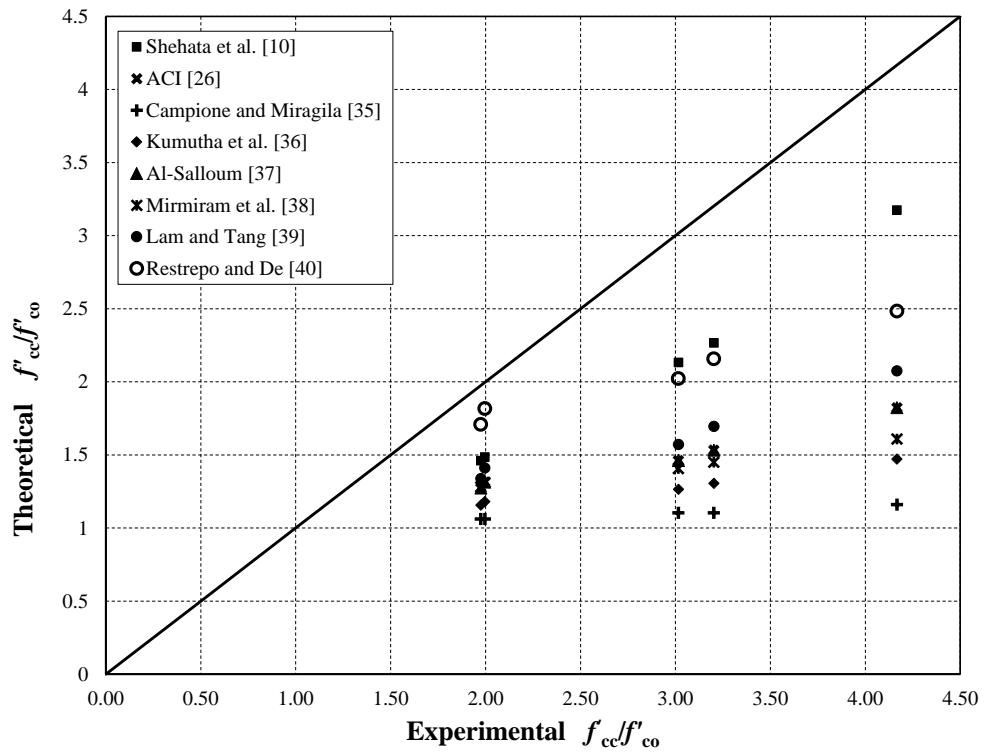


Figure 7-2: Performance of existing strength models for square columns

Table 7-3: Performance of existing strength models against test data of circular columns

Model	Average	Standard deviation	Coefficient of variation
Karbhari and Gao [11]	0.57	0.06	10.5
Samaan et al. [36]	0.59	0.09	15.3
Fardis and Khalili [44]	0.53	0.05	9.4
Miyauchi et al. [46]	0.68	0.03	4.4
Saafi et al. [47]	0.59	0.06	10.2
Toutanji [48]	0.74	0.05	6.8
Ilki and Kumbasar [49]	0.55	0.05	9.1
Lam and Teng [50]	0.53	0.06	11.3
Riad et al. [51]	1.91	0.64	33.5
Spoelstra and Monti [52]	0.60	0.05	8.3
Mirmiran and Shahawy [53]	0.51	0.09	17.6



**Table 7-4: Statistical performance of existing strength models against test data of square columns**

Model	Average	Standard deviation	Coefficient of variation
Shehata et al. [38]	0.75	0.03	4.0
American Concrete Institute [45]	0.80	0.14	17.5
Campione and Miraglia [54]	0.43	0.12	27.9
Kumutha et al. [55]	0.49	0.12	24.5
Al-Salloum [56]	0.56	0.11	19.6
Mirmiran et al. [53]	0.54	0.13	24.1
Lam and Teng [57]	0.60	0.10	16.7
Restrepo and De [58]	0.77	0.14	18.2

#### 7.4 Proposed strength models

The relationship between the strength ratio  $f'_{cc} / f'_{co}$  and the confinement ratio  $f_l / f'_{co}$  for both circular and square SFRP-confined specimens is plotted as shown in Figure 7-3. As can be seen, there exists a linear relationship between the compressive strength of SFRP-confined concrete and the lateral confining pressure. Based on these relations, new linear compressive strength models for circular and square sections confined with SFRP are proposed to predict the compressive strength of SFRP-confined concrete. The new models are based on linear equation as originally proposed by Richart et al. [44] with modified values of confinement effectiveness coefficient  $k_l$  as follows:

*For circular columns*

$$\frac{f'_{cc}}{f'_{co}} = 1 + 6.40 \frac{f_l}{f'_{co}} \quad (7)$$

*For square columns*

$$\frac{f'_{cc}}{f'_{co}} = 1 + 5.90 \frac{f_l}{f'_{co}} \quad (8)$$

In equations 7 and 8, the lateral confining pressure  $f_l$  and  $f'_l$  can be determined from equations 2 and 3 for circular and square section, respectively. The terms  $f_{FRP}$  in equations 2 and 3 is SFRP tensile strength which can be obtained by

testing flat coupons in accordance with the ASTM D638 [32]. The compressive strengths computed from the proposed equations 7 and 8 are plotted against experimental results in Figure 7-4 and summarized in Table 7-5. A good correlation is obtained for both circular and square columns. However, the proposed equations slightly yield lower values of compressive strength as compared to experimental results, thus the proposed models are on the conservative side.

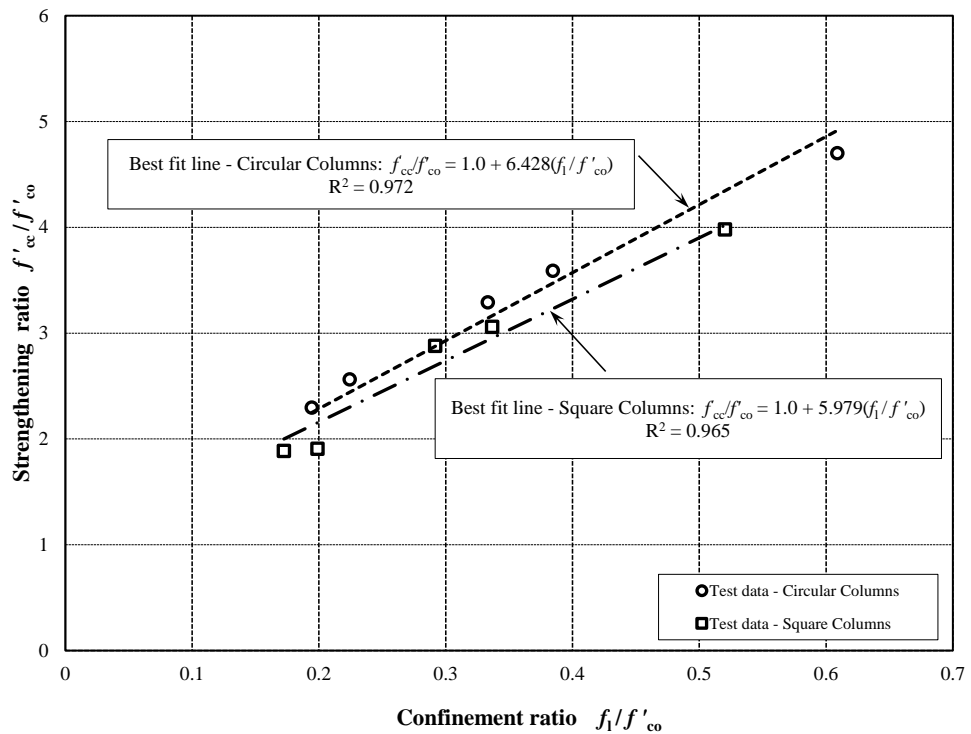


Figure 7-3: Strengthening ratio versus confinement ratio

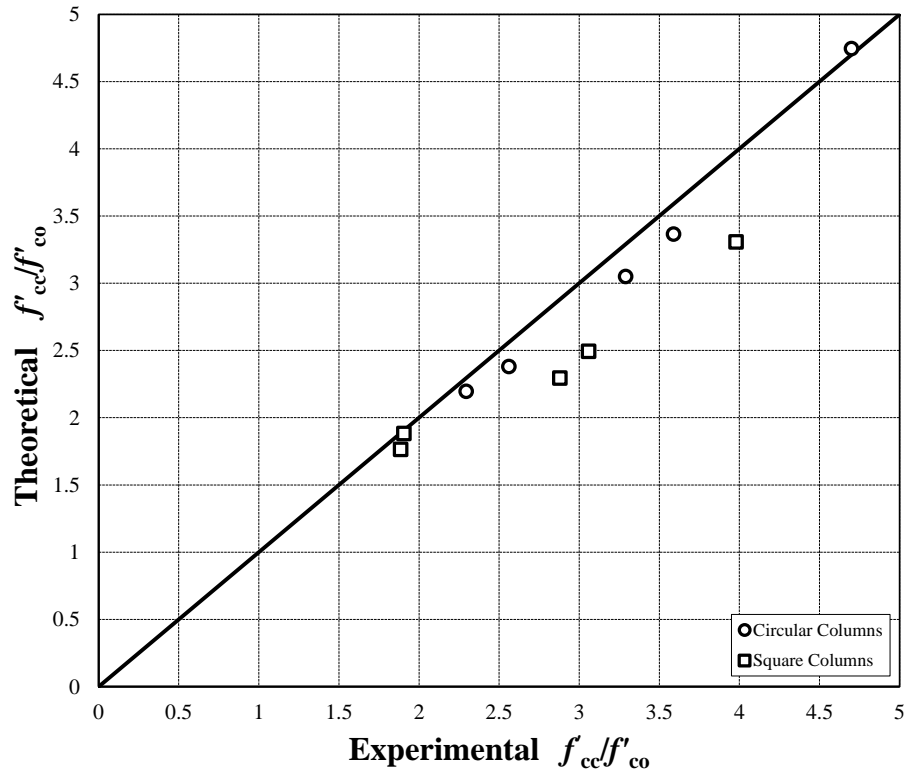


Figure 7-4: Theoretical strengthening ratio versus experimental strengthening ratio

Table 7-5: Summary of experimental and predicted theoretical results

Specimen	Experimental results			Theoretical results				$f'_{cc(Th)}/f'_{cc(Exp)}$
	$f'_{co}$	$f'_{cc}$	$f'_{cc}/f'_{co}$	$f_i$	$f_i/f'_{co}$	$f'_{cc}$	$f'_{cc}/f'_{co}$	
C-3-13	23.40	53.71	2.30	4.55	0.19	51.4	2.20	0.96
C-3-26	23.40	59.95	2.56	5.25	0.22	55.7	2.38	0.93
C-6-13	23.40	77.00	3.29	7.80	0.33	71.4	3.05	0.93
C-6-26	23.40	84.00	3.59	9.00	0.38	78.8	3.37	0.94
C-9-26	23.40	110.00	4.70	14.25	0.61	111.0	4.74	1.01
S-3-13	24.50	46.21	1.89	3.66	0.15	46.11	1.88	1.00
S-3-26	24.50	46.71	1.91	3.17	0.13	43.23	1.76	0.93
S-6-13	24.50	70.57	2.88	6.20	0.25	61.08	2.49	0.87
S-6-26	24.50	74.94	3.06	5.37	0.22	56.20	2.29	0.75
S-9-26	24.50	97.50	3.98	9.58	0.39	81.03	3.31	0.83

## Chapter 8

### SFRP Strengthening of RC Deep Beams

#### 8.1 Introduction

One of the important structural element in RC frame structures is deep beam which is the beam that has a large depth compared to the span length. Deep beams are commonly used as short span members in many applications such as transferred girder in tall buildings, footing, beam ledge, corbel, etc. Many experiments have been carried out to assess the flexural and shear responses of shallow RC beams strengthened externally with unidirectional FRP laminates and sheets [59-63] with the aims to examine the performances at both serviceability and ultimate limit state. In addition, extensive studies have documented attempts to strengthen RC deep beams without web openings [64, 65] and with web openings [66] using externally bonded unidirectional FRP. RC beams may be strengthened with externally bonded FRP using side bonding, U-jacketing or complete wrapping. The failure of almost all RC beams strengthened with side bonded FRPs and U-wrapped FRP was the de-bonding of FRP [67]; making the mobilisation of the full FRP tensile strength impossible in this case [67, 68]. In the past, some attempts have been reported to prevent the de-lamination or de-bonding of FRP from concrete surface using various materials, configurations, wrapping techniques and mechanical anchors [69-72]. The SFRP technique was also effective to increase the shear strength of shallow RC beams. Boyd (2000) [9] investigated the influence of various types of SFRP strengthening schemes on the shear strength of shallow RC beams. The three schemes of SFRP strengthening were A, C and D (A = SFRP applied onto the two side faces only; C = SFRP applied onto the side and the bottom faces; D = SFRP applied over all faces of the beam). The results showed that strengthening scheme C and D were more effective than scheme A. In terms of the failure modes, all beams strengthened with schemes A and C failed by de-bonding of SFRP, whereas specimens with scheme D failed by rupture of SFRP. However, in their experiment, no anchoring system has been employed to fix the SFRP to the beam surface. Soleimani and Banthia (2012) [18] investigated the performance of SFRP for shear strengthening of RC beams. In their research, an anchoring technique using through bolts and nuts with a roughened concrete surface were introduced to enhance

the bond between concrete surface and the SFRP. Prior to the SFRP application, the concrete surface was roughened by a sandblasting method and through the use of a pneumatic chisel. Their studies concluded that roughening the concrete surface with a pneumatic chisel and the application of through bolt anchoring system was an effective means to increase the concrete-SFRP bond.

An extensive review of existing studies on SFRP strengthening reveals that so far no research effort is conducted on the shear strengthening of RC deep beams using SFRP and there was limited research data on the prevention of the de-bonding of SFRP from concrete surface using mechanical anchors. Therefore, the present study (Chapter 8) mainly focused on shear strengthening of RC deep beams using SFRP and the evaluation of newly proposed anchoring systems to prevent delamination of SFRP from concrete surface. The proposed anchoring systems are relatively easy to install and can be applied to the variety of FRP composites. Two types of concrete (i.e., low and high strength) were used to cast the specimens. The specimens were strengthened with different SFRP materials (glass and carbon), SFRP thicknesses and strengthening configurations. The efficiency of the proposed anchoring systems is evaluated in terms of the prevention of SFRP delamination from concrete surface.

## **8.2 Description of the test specimens**

In the experimental program, RC deep beam specimens were cast and strengthened by SFRP technique. Beams were designed in such a way to cause shear failure prior to any flexural distress. A schematic representation of the specimen and reinforcement details is illustrated in Figure 8-1. All beams were 900 mm long, having a rectangular cross section of 100 x 300 mm and the effective span length of 750 mm. The flexural reinforcement consisted of 2 No. 13 (deformed bars with a yield strength of 410 MPa) with the cross sectional area ( $A_b$ ) of 129 mm<sup>2</sup>. Vertical and horizontal web reinforcements of No. 6 (round bars with a yield strength of 313 MPa) with the cross sectional area of 28.3 mm<sup>2</sup> were provided at 120 mm center-to-center spacing. At beam supports, closely spaced vertical and horizontal stirrups were provided to avoid local premature failure. Vertical web reinforcements were provided in the form of stirrups and horizontal web reinforcements were provided in the form of straight steel bars,

placed at both side faces of beam. Clear concrete cover of 15 mm was provided on all beam faces.

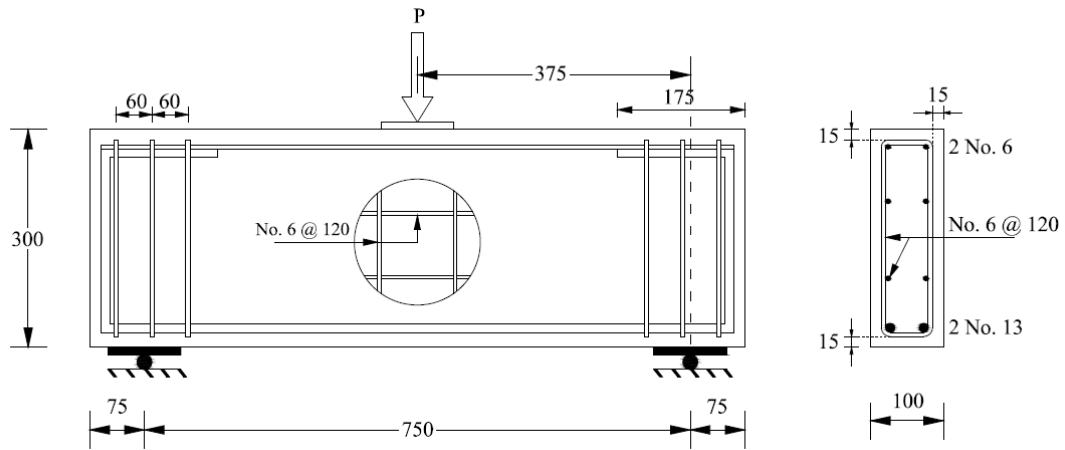


Figure 8-1: Detailing of RC Deep beam (units are in mm)

### 8.3 Test matrix

The experimental program consisted of 17 RC deep beam specimens. The entire test matrix (Table 8-1) is divided into four groups based on anchoring systems, fibre material and strength of concrete. Group 1 contained three beams, including one control specimen and two strengthened specimens. Group 2 and 3 were composed of six and two beams respectively and their results could be compared with beams in group 1. Group 4 had six beams that included one control beam. The key study parameters included SFRP fibre material (glass or carbon), SFRP thickness, concrete strength, SFRP configuration and anchoring systems. Two different SFRP configurations were considered in the experiment. In the SFRP configuration A, the sprayed fibres are applied onto the two side faces of the beam only whereas for SFRP configuration B, they are applied at both side and bottom faces (Figure 8-2). Beam notations were assigned to identify the experimental variables and anchoring systems (Table 8-1). For example, a beam designation *BN-LS-3GA-EB* stands for BN: RC deep beams, LS: Low strength concrete, 3GA: 3mm thick glass fibre (SGFRP) with strengthening configuration A, and EB: Epoxy bolts (EB) anchoring system. In the beam notation, number 1 and 2 may be appended to indicate other different details such as embedment length of anchor bolt, horizontal spacing etc. Details of each specimen are explained in Table 8-1.

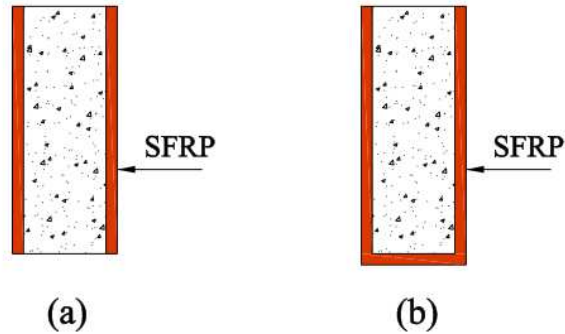


Figure 8-2: SFRP configurations; (a) SFRP configuration A, (b) SFRP configuration B

#### 8.4 Application of SFRP

Prior to the application of SFRP, beams' concrete surface that will receive SFRP was roughened uniformly using hammer and chisel to improve the bond between SFRP and concrete (Figure 8-3). The roughened surface was washed with high water pressure to remove any dust and loose debris. Two types of SFRP materials were applied onto the prepared surfaces, namely sprayed glass fibre-reinforced polymer (SGFRP) and sprayed carbon fibre-reinforced polymer (SCFRP). Lee and Hausmann (2004) [22] investigated the effect of fibre length on the strengthening of RC beams and concluded that a fibre length of around 23 mm is appropriate to maximise the tensile strength and load carrying capacity of strengthened beams. Throughout this study, a fibre length of 26 mm was used for SFRP. The spraying process was performed by means of UltraMax chopper/ saturator unit manufactured by Magnum Venus Plastech (Figure 8-4). Once the fibre was sprayed, aluminium ribbed rollers were used to remove any entrapped airs and to obtain a uniform thickness of sprayed fibre.



**Figure 8-3: Roughened Concrete surface of beam**



**Figure 8-4: Spraying process of FRP**



**Table 8-1: Summary of test matrix**

Beam	Fibre	SFRP	SFRP	Anchors	Horizontal	Vertical	Embedment
Group	Designation		thickness	configuration	spacing of	spacing of	length of
			(mm)		anchors	anchors	anchors
					(mm)	(mm)	(mm)
1	BN-LS-CB	-	-	-	-	-	-
	BN-LS-5GA	Glass	5	A	-	-	-
	BN-LS-5GA-S	Glass	5	A	Slits	-	-
2	BN-LS-5GA-EB	Glass	5	A	EB	120	90
	BN-LS-5GA-EB1	Glass	5	A	EB	120	90
	BN-LS-3GA-MB	Glass	3	A	MB	120	90
	BN-LS-5GA-MB1	Glass	5	A	MB	120	90
	BN-LS-5GA-MB2	Glass	5	A	MB	180	90
	BN-LS-5GA-TB	Glass	5	A	TB	120	90
3	BN-LS-3CA-MB	Carbon	3	A	MB	120	90
	BN-LS-5CA-MB	Carbon	5	A	MB	120	90
4	BN-HS-CB	-	-	-	-	-	-
	BN-HS-3GA-MB	Glass	3	A	MB	120	90
	BN-HS-4GA-EB	Glass	4	A	EB	120	90
	BN-HS-5GA-MB	Glass	5	A	MB	120	90
	BN-HS-5GB-MB	Glass	5	B	MB	120	90
	BN-HS-7GB-MB	Glass	7	B	MB	120	90

### 8.5 Concrete properties

Two types of concrete representing low-strength (LS) and high-strength (HS) concrete were used to cast the specimens. The specimens in groups 1-3 were cast from low strength (LS) concrete and the specimens in group 4 were made from high strength (HS) concrete. The target compressive strengths at 28 days for the low and high strength concrete were 20 MPa and 45 MPa, respectively. The concrete mix proportions are given in Table 8-2. All specimens were cast in the vertical position to reproduce the real construction condition (Figure 8-5). The actual concrete strengths at the testing days (around 35-45 days after casting) were slightly higher than the target design strengths. For each type of concrete, six cylinders (300 mm in height and 150 mm in diameter) were cast in steel moulds using the standard procedure[73]. The compressive strength was determined by testing these standard cylindrical specimens in accordance with [74]. The average tested compressive strength of concrete at the testing day was 21.45 MPa with the standard deviation of 0.65 for low strength concrete and 46.20 MPa

with the standard deviation of 1.40 for high strength concrete. Since all specimens in groups 1-3 and group 4 were cast from the same batch of low strength (LS) and high strength (HS) concrete, a uniform concrete compressive strength could be assumed for both strengthened and un-strengthened (control) beams.

**Table 8-2: Concrete strengths and mix proportions**

Mix components	28 day's target compressive strength	
	20	45
Water (kg/m <sup>3</sup> )	180	183
Cement(kg/m <sup>3</sup> )	360	420
Fine aggregate (kg/m <sup>3</sup> )	760	686
Coarse aggregates (kg/m <sup>3</sup> )	1015	1082

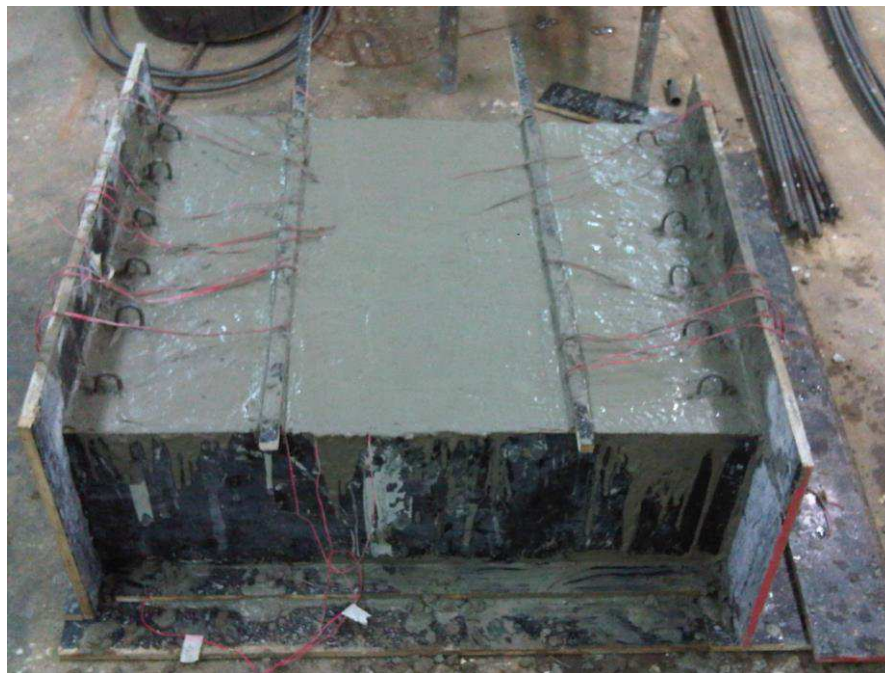


**Figure 8-5: Concrete casting**

### **8.6 Instrumentation and loading setup**

The specimens were tested under a concentrated load applied at the mid span in a simply supported arrangement. The length of the beam measured from support to support was 750 mm. The shear span length was 375 mm (Figure 8-6). A load is applied monotonically through a hydraulic jack of 600 kN capacity at a constant rate of 140 N per second until failure occurred. The applied load was recorded by a calibrated load cell placed under the loading piston of the hydraulic jack. Linear variable differential

transducers (LVDT) were placed under the beam at the mid span to measure vertical deflection. During the test, the initiation and propagation of cracks were visually inspected and recorded by photographs. Test setup is shown in Figure 8-6.

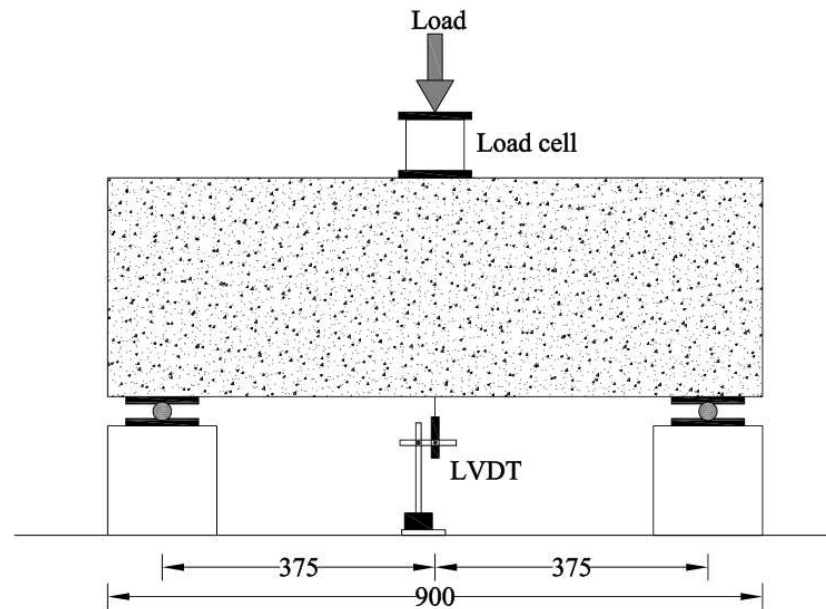


Figure 8-6: Test setup

### 8.7 Anchoring systems – Literature review

In recent years, the use of unidirectional FRP has become a popular technique for strengthening and retrofitting purpose. However, FRP exhibited a premature debonding failure prior to the development of the full tensile strength [75-77] has enlisted different methods which were successfully applied to prevent the FRP debonding such as mechanical anchors, near-surface mounted (MSN) installation, wrapping of FRP strips in different shapes, use of protruding fibre and anchor bolts, using comb-shaped anchors and mechanical-interlocking anchorage systems. Similarly, for SFRP strengthened members, the debonding failure could be observed especially when the fibre was applied onto the sides and/or bottom faces only [9]. Soleimani and Banthia (2012) [18] evaluated the performance of three different techniques to enhance the SFRP-concrete bond. The results showed that the use of pneumatic chisel for roughening the concrete surface and the through threaded bolts with steel plates and nuts was the most effective to improve the SFRP-concrete bond. Kanakubo *et al.* 2005 [25] proposed different methods to anchor SFRP at the meeting corner of beam and

slab such as SFRP slits, bolts and steel blocks. The test results indicated a possible occurrence of cracks in SFRP nearby the anchor bolts. Although the above-mentioned techniques are proved to be successful in SFRP strengthening, there is still a need to develop a simple and efficient anchoring technique to avoid delamination failure. In the present study, the efficiency of SFRP slits (discussed in detail in section 8.8.2.1.1) was evaluated in shear strengthening of RC deep beams, and it was concluded that SFRP slits were not effective to prevent de-bonding of SFRP from concrete surface. Further, three different types of mechanical anchoring systems were proposed to avoid de-bonding of the SFRP. The proposed anchoring systems were evaluated for different fibre materials (glass and carbon), fibre thickness (3 mm and 5 mm), SFRP configurations (side faces only and both side and bottom faces) and strengths of concrete (low and high strength concrete). The SFRP slits and the proposed anchoring systems are explained in the following section.

#### 8.7.1 SFRP slits

In this study, it is proposed to enhance the bonding by anchoring the SFRP to the specimens by means of slits made on the beam surfaces. The idea of SFRP slit is shown in Figure 8-7. The merit of slit anchoring system was mainly due to the low cost since steel anchoring materials were not utilized. In the specimen *BS-LS-5GA-S*, two slits were made in each shear span by saw cutting into the concrete surface prior to the SFRP application. The SFRP slits were grooved on the beam surface at an angle approximately perpendicular to the potential shear crack direction. During SFRP application, the fibres were first sprayed into slits followed by spraying onto the whole surface of the specimens.

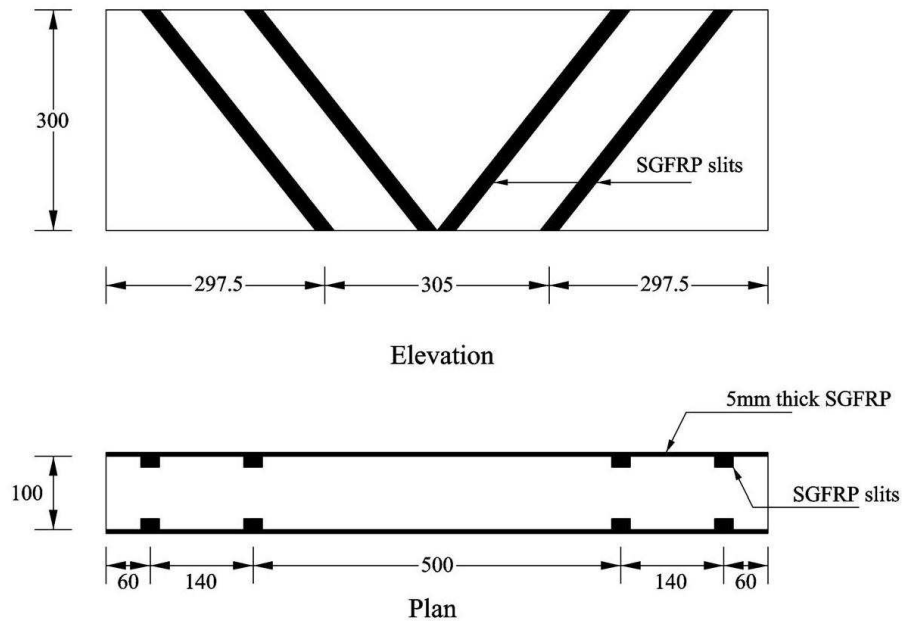


**Figure 8-7: Details of SFRP slits**

### 8.7.2 Proposed anchoring systems

In this study, three anchoring systems were proposed, namely, Through Bolt (TB) anchoring system, Mechanical Expansion Bolt (MB) anchoring system and Epoxy Bolt (EB) anchoring system (Figures 8-8 to 8-10). Anchoring bolts were installed at different horizontal and vertical spacing (i.e., in multiples of shear reinforcement spacing). Horizontal spacing of anchors was selected as being 1.0 and 1.5 times shear reinforcement spacing and vertical spacing of anchors was selected as 0.75 times shear reinforcement spacing. The embedment length of the EB and MB anchors was selected based on the test observation of specimen *BN-LS-5GA-EB* (discussed in detail in section 8.8.2.2.3). The details of spacing and embedment length of the anchors are summarized in Table 8-1. The details of each anchoring system are explained in the following sections.

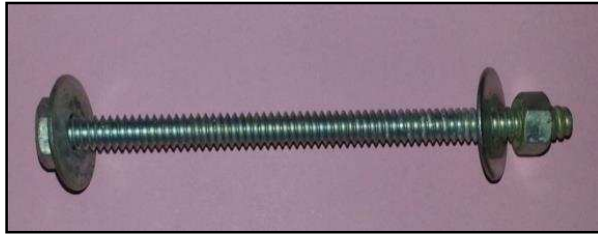


**Figure 8-8: TB anchoring system**



**Figure 8-9: MB anchoring system**



**Figure 8-10: EB anchoring system**

#### 8.7.2.1 TB anchoring system

The TB anchoring system comprised threaded bolts 6 mm diameter and 50 mm long, nuts and washers (Figure 8-8). It was installed in the following steps; 1) holes of 7 mm diameter were drilled through the beam section and SFRP; 2) threaded bolts were inserted into holes; 3) nuts were tightened using washers with an average torque of 8 N.m.

#### 8.7.2.2 MB anchoring system

The MB anchoring system is composed of mechanical expansion anchors (diameter = 7 mm and length = 25 mm), full threaded hex headed bolts (diameter = 4 mm and length = 35 mm), nuts and washers (Figure 8-9). It was installed in the following steps; 1) 8 mm-diameter and 40 mm long holes were drilled perpendicularly to the beam's

side faces at the desired spacing; 2) the drilled holes were cleaned using high pressure water to remove all loose debris and dust; 3) expansion anchors with bolts, nuts and washers were inserted into the holes; 4) expansion anchors were tightened through an average torque of 12 N.m on threaded hex headed bolts; 5) finally, the nuts were tightened by an average torque of 6 N.m.

#### 8.7.2.3 EB anchoring system

The EB anchoring system is composed of threaded rods (diameter = 6 mm and length = 60 mm), nuts and washers (Figure 8-10). It was installed in the following steps; 1) 8 mm diameter and 30 mm long holes were drilled at 120 mm spacing perpendicularly to the beam's side surface through SFRP; 2) holes were cleaned and washed with high pressure water to remove loose debris and dust; 3) epoxy resin prepared as per manufacturer's instructions was filled into the holes; 4) threaded rods wetted with epoxy resin were inserted into the holes; 5) after the epoxy is fully hardened (2-3 hours), nuts were tightened with an average torque of 5 N.m.

### 8.8 Test results and discussions

A comprehensive experimental study was performed to investigate the effect of SFRP strengthening on the ultimate load and deflection of RC deep beams. Different anchoring systems were investigated to prevent the de-lamination of SFRP from concrete surface. The experimental results are summarized in Table 8-3. Most of the strengthened RC deep beams failed by the rupture of SFRP without pull-out of the anchors. This indicated the effectiveness of the proposed anchoring systems. In the following sections, the failure modes and test results are discussed in further detail.

**Table 8-3: Experimental results**

Beam	Ultimate	Increase in	Mid-span	Increase in	Failure modes	
Group	Designation	load, P (kN)	ultimate	deflection	deflection	
			load (%)	(mm)	(%)	
1	BN-LS-CB	122.30	-	1.73	-	Shear failure
	BN-LS-5GA	122.50	0.20	1.68	-	Debonding
	BN-LS-5GA-S	136.30	11	1.78	0.03	Debonding
2	BN-LS-5GA-EB	218.92	79	3.00	73	SFRP rupture
	BN-LS-5GA-EB1	248.50	103	3.40	96	SFRP rupture
	BN-LS-3GA-MB	190.50	56	2.46	42	SFRP rupture
	BN-LS-5GA-MB1	236.60	94	3.13	81	Concrete crushing
	BN-LS-5GA-MB2	239.20	96	3.13	81	SFRP rupture
	BN-LS-5GA-TB	252.20	106	4.13	138	Concrete crushing
3	BN-LS-3CA-MB	221.70	81	2.81	62	SFRP rupture
	BN-LS-5CA-MB	274.70	125	2.63	57	SFRP rupture
4	BN-HS-CB	196.40	-	1.67	-	Shear failure
	BN-HS-3GA-MB	284.60	45	2.23	34	SFRP rupture
	BN-HS-4GA-EB	380.80	94	3.25	94	SFRP rupture
	BN-HS-5GA-MB	444.70	126	3.54	112	SFRP rupture
	BN-HS-5GB-MB	493.20	151	3.06	83	SFRP rupture
	BN-HS-7GB-MB	507.50	158	3.24	94	SFRP rupture



### 8.8.1 Failure modes

A summary of failure modes of all specimens is provided in Table 8-3. The un-strengthened (control) beams of low and high strength concrete failed due to the typical inclined cracks that were formed along the loading and supporting points as shown in Figures 8-11 and 8-12. A similar failure mode was also reported by Islam et al. 2005 [64]. The SGFRP strengthened beam BN-LS-5GA, without any anchoring system, failed due to the de-bonding of the fibres as shown in Figure 8-13. The strengthened specimens with SGFRP slits (BN-LS-5GA-S) was also failed due to the de-bonding of SGFRP (Figure 8-14). However, the specimen BN-LS-5GA-EB anchored with epoxy bolts (EB system) failed by pull-out of the anchored bolts (Figure 8-15). The pull-out failure was supposedly due to the insufficient embedment length of the bolts. This type of failure can be prevented by using bolts with sufficient embedment length. In general, several strengthened specimens failed by the rupture of SFRP as shown in Figures 8-16 to 8-18. However, the failure mode was basically characterized by shear failure since the internal crack in the main body of the strengthened beams was inclined shear crack, similar to the control beams. The rupture failure in SFRP indicated the effectiveness of the anchoring system in fixing the SFRP to the beam surface. Figure 8-19 demonstrated a typical SFRP rupture failure at the mid span of specimens with strengthening configuration A, whereas Figure 8-20 showed the inclined SFRP rupture in specimen BN-HS-5GB-MB with strengthening configuration B. When the thickness of SGFRP was increased to 7 mm as in the beam BN-HS-7GB-MB, the failure was initiated by the pull-out of the expansion anchors and followed by the de-bonding of SGFRP. Other failure modes included concrete crushing at the loading region, which was observed in beams BN-LS-5GA-MB1 and BN-LS-5GA-EB (Figure 8-21). In these two specimens, no de-bonding of SFRP occurred.

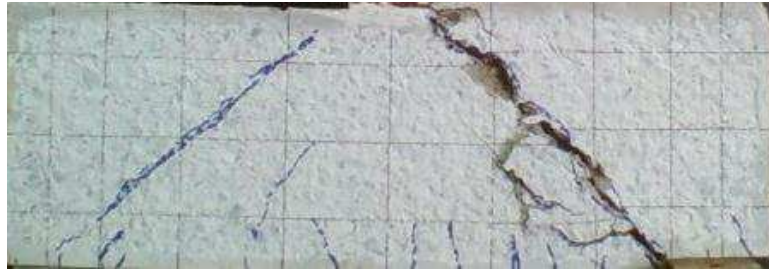


**Figure 8-11: Failure mode of Beam BN-LS-CB**

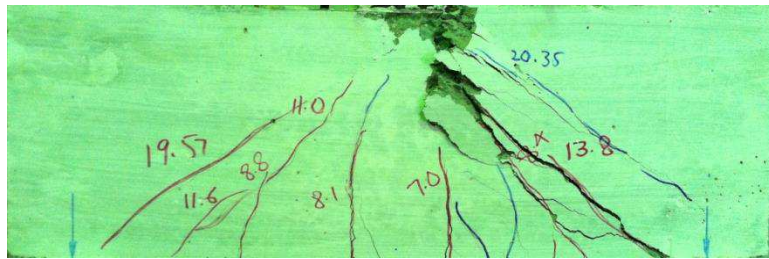


**Figure 8-12: Failure mode of Beam BN-HS-CB**

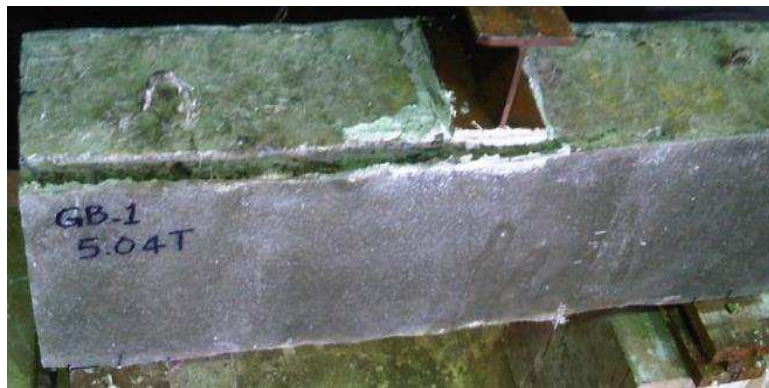


**Figure 8-13: Failure mode of beam BN-LS-5GA**



**Figure 8-14: Failure mode of beam BN-LS-5GA-S**



**Figure 8-15: Failure mode of beam BN-LS-5GA-EB**



**Figure 8-16: Failure mode of Beam BN-LS-5GA-EB1**



**Figure 8-17: Failure mode of Beam BN-LS-5GA-MB2**

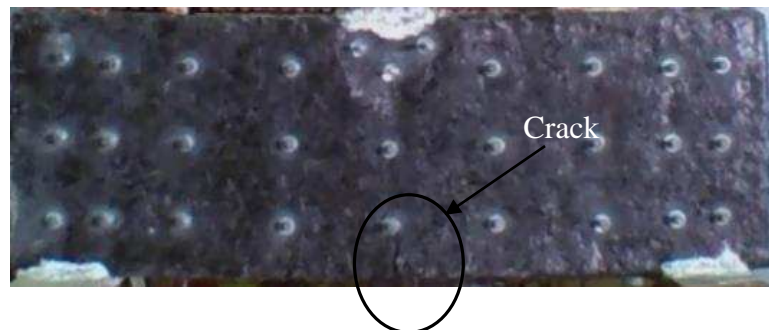


**Figure 8-18: Failure mode of Beam BN-LS-3CA-MB**

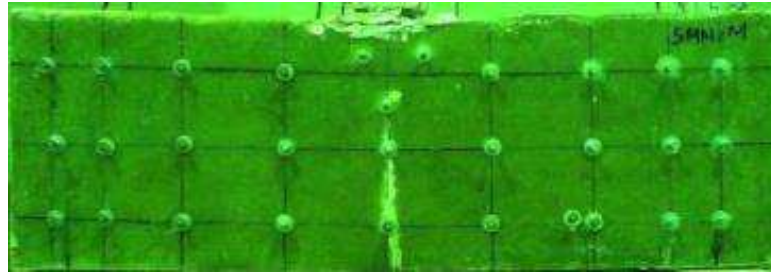


**Figure 8-19: Typical failure mode of beam with SFRP configuration A**

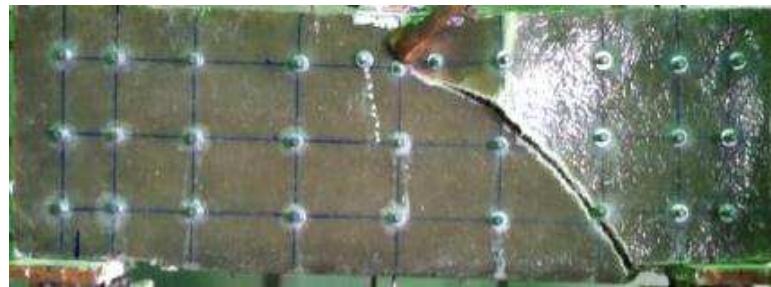


**Figure 8-20: Failure mode of beam BN-HS-5GB-MB with SFRP configuration B**



**Figure 8-21: Typical concrete crushing failure under loading region**

### 8.8.2 Load carrying capacity and mid span deflections

The load-deflection curves of the SFRP-strengthened specimens are shown in Figures 8-22 to 8-29. In each group, the peak load of the control un-strengthened specimen is set as a benchmark, by normalizing its peak load to 100%, and the performance of other specimens is evaluated in terms of the percentage ratio of the ultimate load to that of the control specimen. The comparison is shown in Figures 8-30 and 8-31. This information is valuable to examine the influence of different SFRP parameters on the load carrying capacity and mid span deflection at the peak load. The test results are summarized in Table 8-3 and are discussed in detail in the following sections.

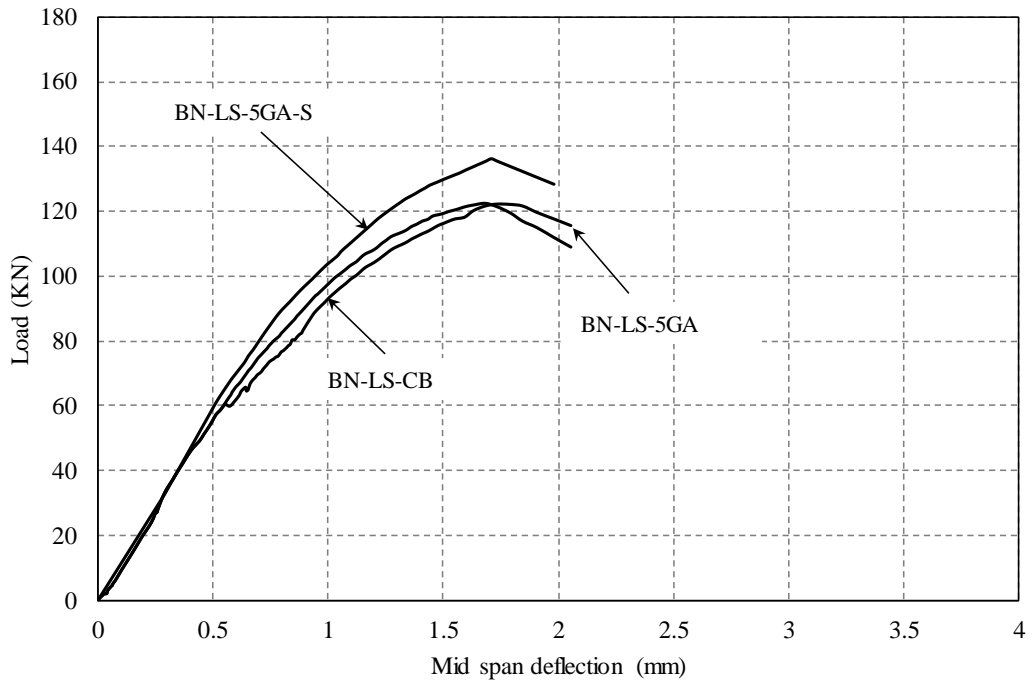


Figure 8-22: Load deflection curves of RC deep beams (effect of SFRP slits)

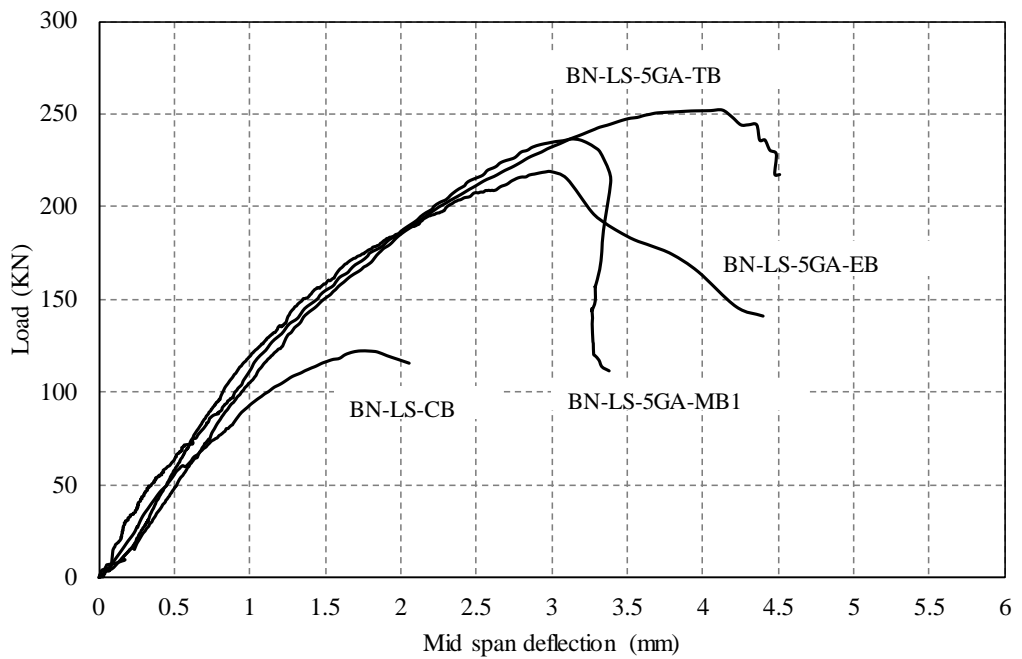


Figure 8-23: Load deflection curves of RC deep beams with different anchoring systems

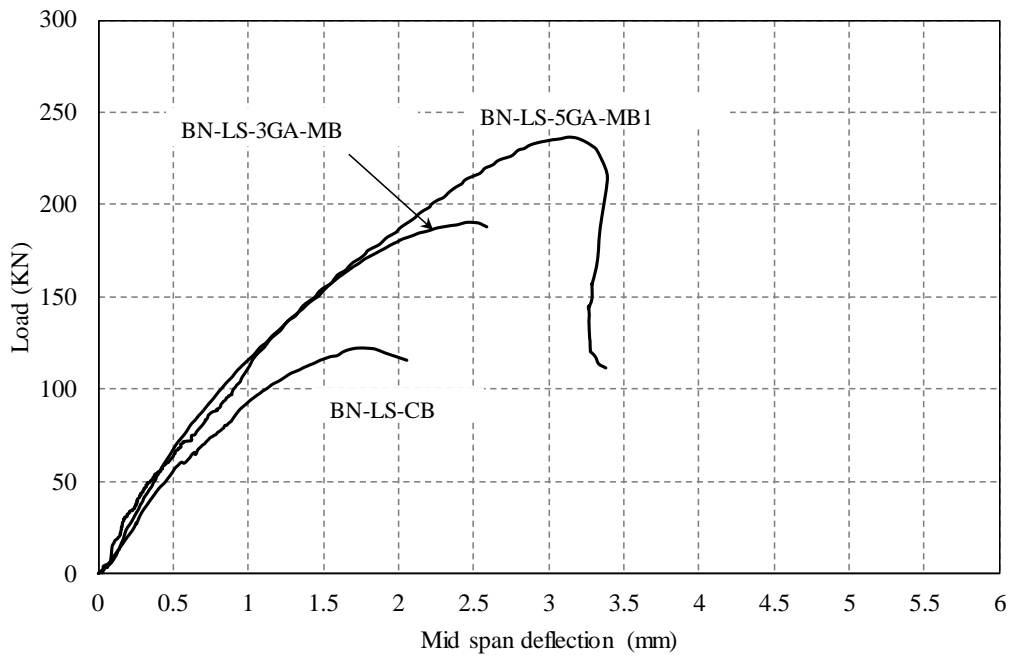


Figure 8-24: Load deflection curves of RC deep beams with different SGFRP thickness

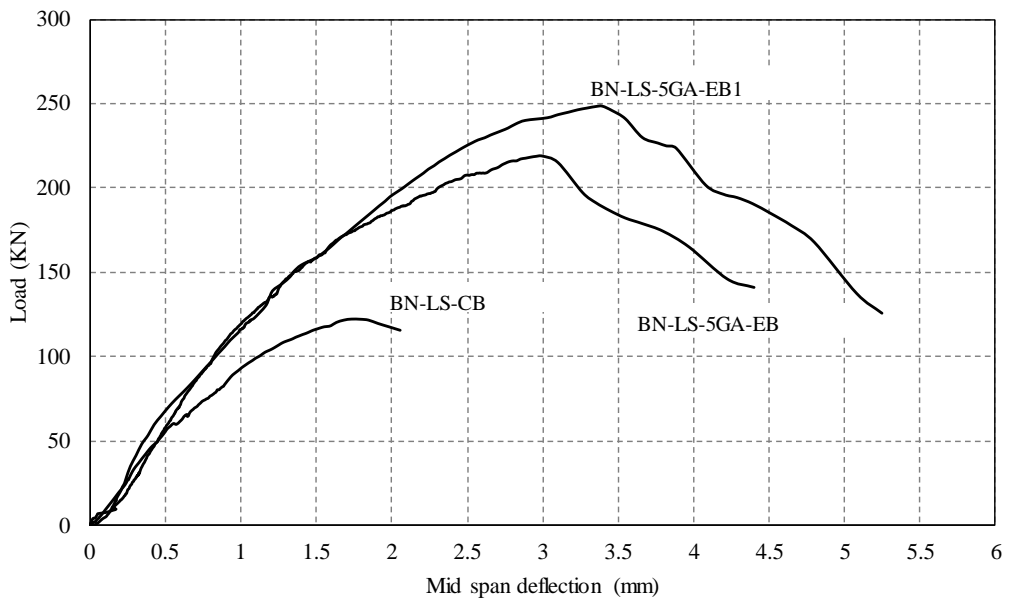


Figure 8-25: Load deflection curves of RC deep beams with different length of bolts

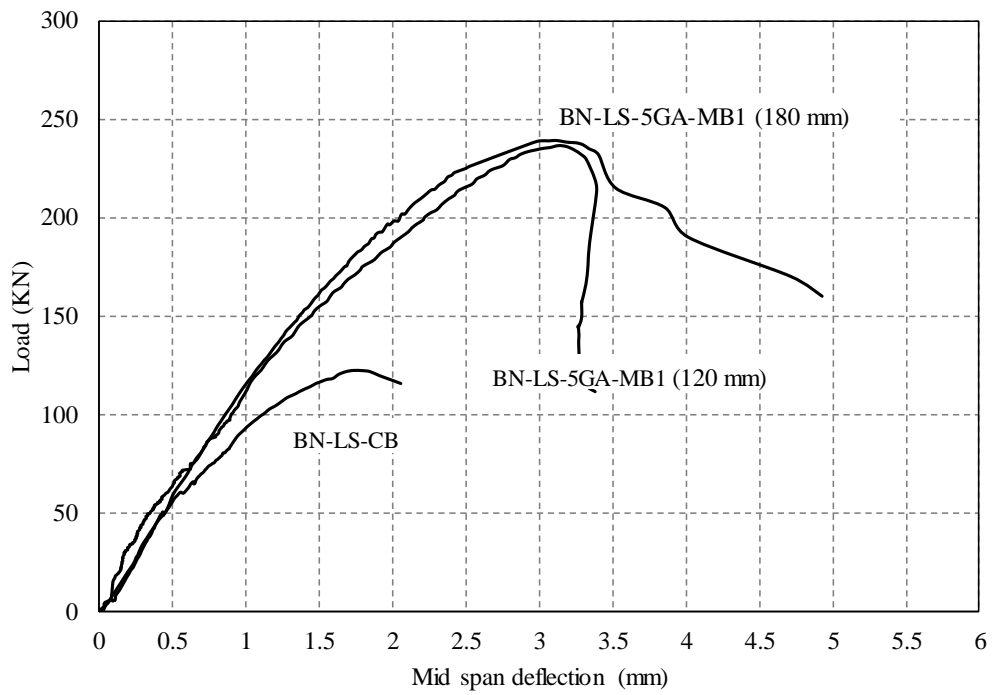


Figure 8-26: Load deflection curves of RC deep beams with different bolt spacing

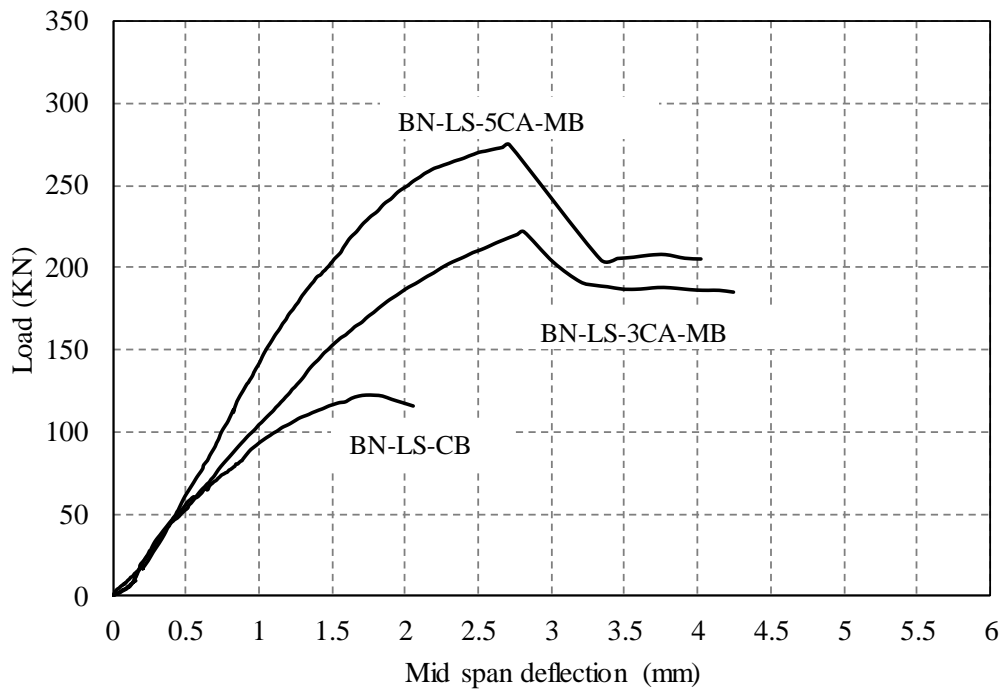


Figure 8-27: Load deflection curves of RC deep beams with different SCFRP thickness

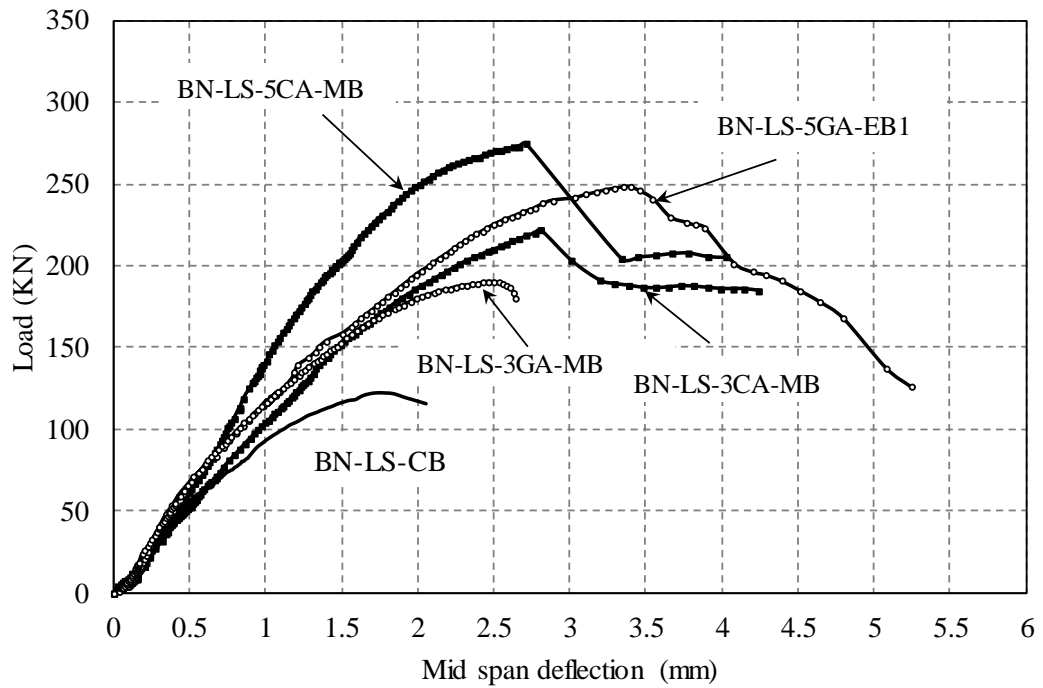


Figure 8-28: Load deflection curves of RC deep beams with different SFRP material (Carbon and Glass)

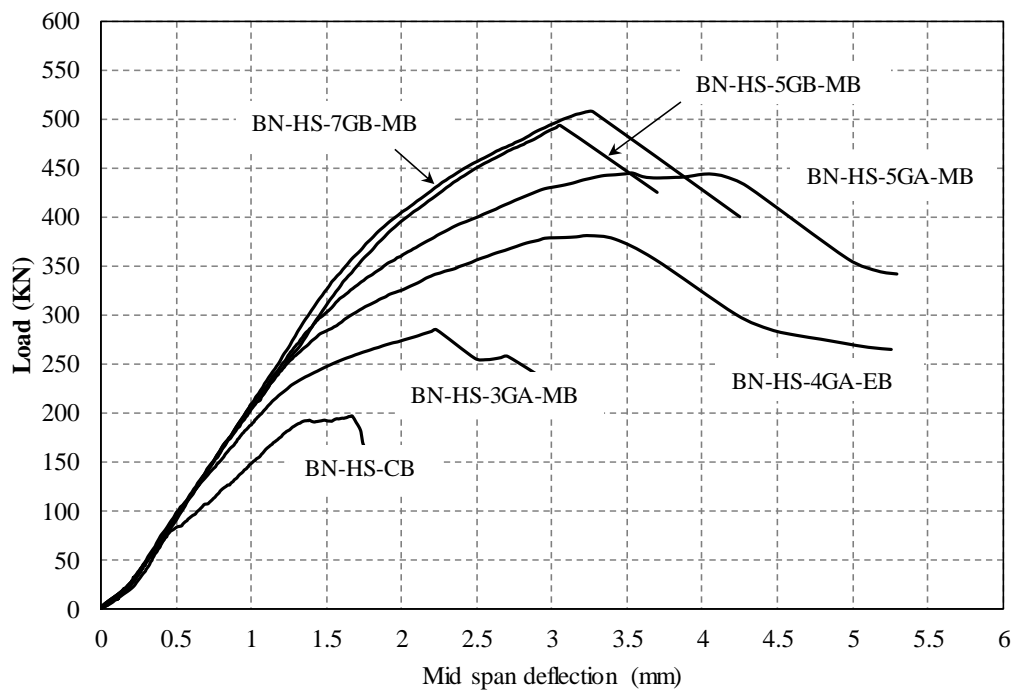


Figure 8-29: Load deflection curves of RC high strength deep beams (group 4)



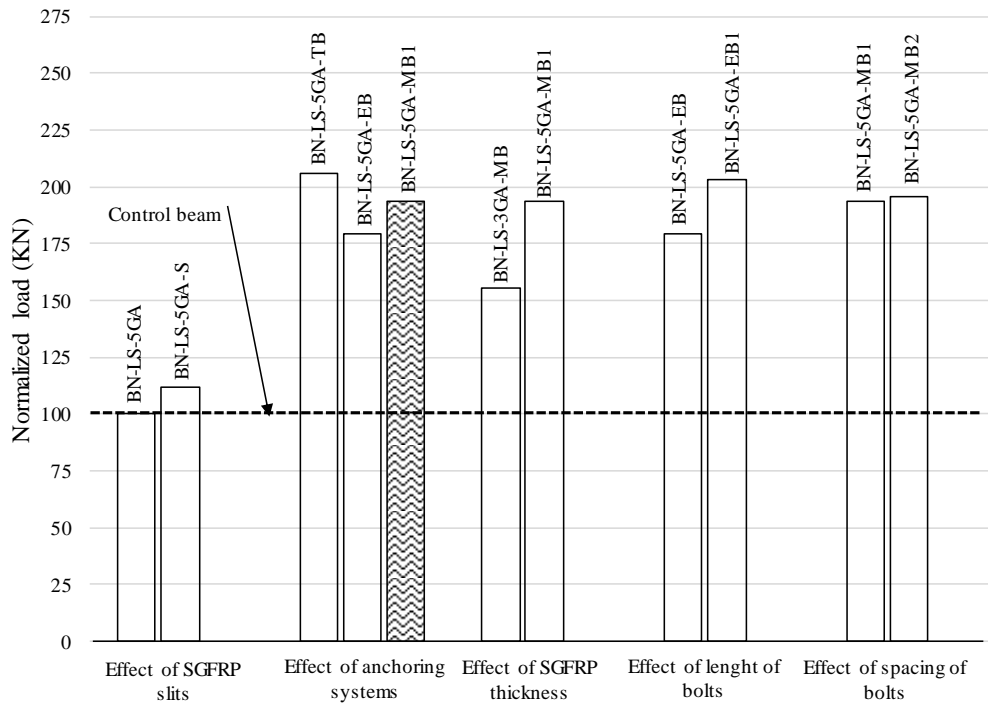


Figure 8-30: Comparison of normalized ultimate loads (Groups 1-3)

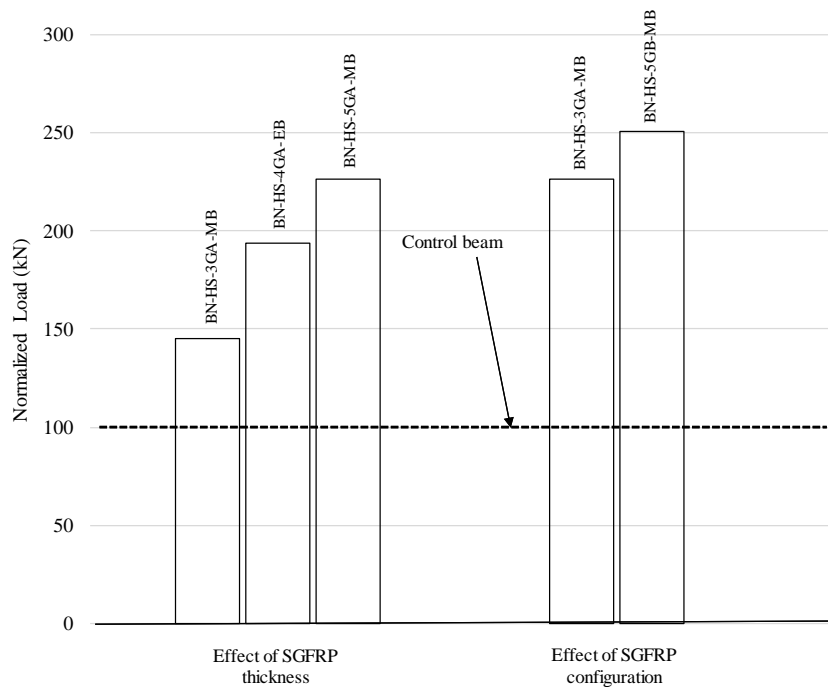


Figure 8-31: Comparison of normalized ultimate loads (Group 4)

### 8.8.2.1 Beam group 1

#### 8.8.2.1.1 Effect of SFRP slits

To study the effect of SFRP slits, the results of three specimens were compared, two of them were strengthened with SGFRP and one was the control beam. The load and deflection curves of these three specimens are shown in Figure 8-22. A comparison of the normalized ultimate loads is displayed in Figure 8-30. The specimen BN-LS-5GA without any anchoring system was used to investigate the bonding performance between SGFRP and concrete surface. As for the specimen BN-LS-5GA-S, SGFRP slits were provided on the side faces as a means to fix SGFRP to the beam surface. In Figures 8-22 and 8-30, it can be seen that the specimen BN-LS-5GA without any anchoring system failed at the same ultimate load and mid-span deflection as that of the control beam. This indicated that the application of SGFRP without anchoring system is ineffective, since the premature delamination of SGFRP led to the propagation of diagonal shear cracks in the beam, bringing about the shear failure similar to the control beam. As for the beam BN-LS-5GA-S with SGFRP slits, the ultimate load was increased by only 11% compared to the control beam. This indicated that the slits contributed only a relatively minor increase in loading capacity, as compared with the proposed anchoring system which can elevate the load capacity by 50-150%. The greater effectiveness of the anchoring system shall be explained in details in the next section.

### 8.8.2.2 Beam group 2

#### 8.8.2.2.1 Effectiveness of the anchoring systems

To study the effectiveness of the anchoring system, three specimens in group 2, namely BN-LS-5GA-EB, BN-LS-5GA-MB1 and BN-LS-5GA-TB were strengthened with the same SGFRP thickness (5 mm) and strengthening configuration (A). However, each beam was anchored with different anchoring systems (i.e., EB, MB and TB systems, respectively) to investigate the efficiency of bolting types in preventing the de-lamination of SFRP from concrete surface. The load and deflection curves of these specimens are shown in Figure 8-23 in comparison with the control specimen BN-LS-CB. A comparison of the normalized ultimate loads is displayed in Figure 8-30. It can be seen that specimen BN-LS-5GA-EB, attained the 79% and 73% increase in the ultimate load and mid-span deflection, respectively, as compared with the control beam.

Specimen BN-LS-5GA-MB1 reached the 94% and 81% higher ultimate load and mid-span deflection, respectively. The TB anchoring system resulted in 106% and 138% increase in the ultimate load and mid-span deflection, respectively. Based on these results, the TB anchoring system has been found to be the most effective anchoring system compared with EB and MB systems.

The failure of beams BN-LS-5GA-MB1 and BN-LS-5GA-TB was due to the crushing of concrete under the loading point (Figure 8-21), which is a typical compression failure for deep beam particularly with the low concrete strength. Deep beam may fail in concrete crushing along the inclined compression strut, or at the loading points. The compression failure illustrated in these specimens indicated that both TB and MB anchoring systems were effective to protect the de-bonding of SGFRP. As a result, a higher increase in the ultimate load and deflection could be obtained. On the other hand, the specimen BN-LS-5GA-EB failed by the pull-out of EB anchoring system at the ultimate load (Figure 8-15). The pull-out of the anchor bolts led to the final delamination of concrete cover, resulting in a lower increase in the ultimate load and deflection as compared to TB and MB anchoring systems. The pull-out failure could be prevented by using a longer embedment length of anchor bolts, which will be additionally discussed in section 8.8.2.2.3.

#### 8.8.2.2.2 Effect of SGFRP thickness

To investigate the effect of SFRP thickness on the ultimate load and deflection of RC deep beam, load deflection curves of specimen BN-LS-3GA-MB (3 mm thick SGFRP) and BN-LS-5GA-MB1 (5 mm thick SGFRP) along with the control beam are shown in Figure 8-24 and the comparison of normalized ultimate load is displayed in Figure 8-30. It can be seen that both ultimate load and mid-span deflection were elevated with an increase in SGFRP thickness. Beam BN-LS-5GA-MB1 and BN-LS-3GA-MB reached 94% and 56% higher ultimate load than the control beam (specimen BN-LS-CB) respectively. It can be seen that the increase in the ultimate load was almost proportional to the thickness of SGFRP. No delamination failure mode was observed in these two specimens. The specimen BN-LS-3GA-MB failed by rupture of SFRP whereas the specimen BN-LS-5GA-MB1 failed by concrete crushing. This implied that the strength increases proportionally to the thickness of SFRP provided that sufficient

anchoring system is installed to prevent delamination failure.

#### 8.8.2.2.3 Effect of anchor bolt length

As discussed in section 8.8.2.2.1, the failure of beam BN-LS-5GA-EB was initiated by the pull-out of the anchor bolts and the following delamination of concrete cover, indicating that the embedment length of the bolts was not sufficient. To further examine the effect of the embedment length, the length of the bolts was increased from 30 mm in specimen BN-LS-5GA-EB to 42 mm in specimen BN-LS-5GA-EB1 while all other parameters were kept similar to the specimen BN-LS-5GA-EB (Table 8-1). The load deflection curves of both specimens BN-LS-5GA-EB and BN-LS-5GA-EB1 along with the control specimen (BN-LS-CB) are shown in Figure 8-25 and the comparison of normalized ultimate load is displayed in Figure 8-30. It can be seen that beam BN-LS-5GA-EB1 achieved the ultimate load of 248.50 kN, which was 14% higher than that of beam BN-LS-5GA-EB (i.e., 218.92 kN). Unlike beam BN-LS-5GA-EB, there was no pull-out of the anchors bolts and the separation of concrete cover in beam BN-LS-5GA-EB1, confirming that the embedment length of the anchor bolts is now adequate to prevent the premature pull-out failure. It should be also noted that the ultimate load of beam BN-LS-5GA-EB1 is now comparable to those of beam BN-LS-5GA-MB1 and beam BN-LS-5GA-TB. This is because the delamination has been prevented and the specimens experience failure caused by either concrete crushing or SFRP rupture instead.

#### 8.8.2.2.4 Effect of anchor bolt spacing

In order to investigate the effect of spacing of anchor bolts on the performance of SFRP strengthening, the horizontal bolt spacing in specimen BN-LS-5GA-MB2 was increased to 180 mm as compared with the 120 mm spacing in the specimen BN-LS-5GA-MB1. The load deflection curves of both beams BN-LS-5GA-MB1 and BN-LS-5GA-MB2 are shown in Figure 8-26 and the comparison of the normalized ultimate load is displayed in Figure 8-30. It can be seen that both beams had almost the same behaviour until the peak load. The increase in the ultimate load was almost the same despite the difference in the spacing of anchor bolts. When considering the failure modes of both specimens (Table 8-3), it was found that specimen BN-LS-5GA-MB1 failed by crushing of concrete at the loading point whereas specimen BN-LS-5GA-

MB2 failed by rupture in SFRP. It can be observed that both failure modes are not relevant to delamination failure, therefore it might be supposed that the 180 mm spacing was sufficient to prevent anchorage failure. Thus, a further decrease in spacing, i.e., 120 mm provided no additional benefits as the failure mode was controlled by either concrete crushing or SFRP rupture.

### 8.8.2.3 Beam group 3

#### 8.8.2.3.1 Effect of SCFRP thickness

In this group, two specimens, namely, BN-LS-3CA-MB and BN-LS-5CA-MB were strengthened with 3 mm and 5 mm thick SCFRP, respectively. The SCFRP was fixed to the specimens by means of MB anchoring system. The load deflection curves of these specimens along with the control specimen (beam BN-LS-CB) are plotted in Figure 8-27 and the comparison of normalized ultimate load is displayed in Figure 8-30. It can be seen that the ultimate load was increased as the thickness of SCFRP increased. The ultimate loads of beams BN-LS-3CA-MB and BN-LS-5CA-MB were found to be 81% and 125% higher than the control beam. As can be seen, the increase in the ultimate load is proportional to the thickness, similar to the case of SGFRP strengthening. The failures of these specimens were caused by rupture in the SCFRP without delamination, thus, the load increase is in proportion to the thickness as expected.

#### 8.8.2.3.2 Effect of SFRP material

In order to investigate the comparative performance of different fibre materials of SFRP, i.e., between SGFRP and SCFRP, the load-deflection curves of specimens BN-LS-3GA-MB, BN-LS-5GA-EB1, BN-LS-3CA-MB and BN-LS-5CA-MB and the control beam BN-LS-CB are shown in Figure 8-28. As can be seen, the SCFRP thickness of 3 mm and 5 mm resulted in a respective increase of 16% and 11% in the ultimate load as compared with the corresponding SGFRP specimens with a similar thickness. As can be seen from Table 5-1, the tensile strength of SCFRP is approximately 13% higher than SGFRP. This material strength is consistent with the observed increase in the ultimate load of the specimens with SCFRP strengthening.

#### 8.8.2.4 Beam group 4

##### 8.8.2.4.1 Effect of SGFRP thickness

The load deflection curves of all tested high-strength beams are shown in Figure 8-29 and the comparison of normalized ultimate load is displayed in Figure 8-31. When comparing between the control low and high strength beam, it can be seen that the high strength beam (specimen BN-HS-CB) failed at the ultimate load of 196.4 kN whereas the low strength one (specimen BN-LS-CB) failed at 122.3 kN. Since both of them have identical dimension and reinforcement detail, the difference in the bearing capacity is basically rooted in the compressive strength of concrete  $f'_c$ , i.e., beam BN-LS-CB is low strength concrete with  $f'_c = 21.45$  MPa whereas beam BN-HS-CB is high strength concrete with  $f'_c = 46.2$  MPa. A similar observation, that is, a higher shear strength in higher strength concrete deep beam, have also been reported Oh and Shin 2001 [78].

As can be seen from Figures 8-29 and 8-31, the SGFRP strengthening technique is also found to significantly enhance the ultimate load and deflection of high strength concrete deep beams, similar to the low strength concrete case. The graphs demonstrate an evident increase in both ultimate load and deflection of strengthened specimens as the thickness of SGFRP was increased. In case of strengthening configuration A, the increase in the ultimate load over the control beam was recorded as 45%, 94%, and 126% in beams BN-HS-3GA-MB, BN-HS-4GA-EB, and BN-HS-5GA-MB with 3, 4 and 5 mm SCFRP thickness, respectively (Figure 8-31). Similarly, for strengthening configuration B, the increase was recorded as 151% and 158% in beams BN-HS-5GB-MB and BN-HS-7GB-MB with 5 and 7 mm SCFRP thickness respectively. It should be noted that the ultimate load of BN-HS-7GB-MB was only slightly increased as compared to the beam BN-HS-5GB-MB. This was supposedly due to the fact that at the ultimate load of BN-HS-7GB-MB, the mechanical expansion bolts were pulled out, followed by a sudden rupture of SGFRP which finally brought about the failure. The premature de-bonding failure of thick SGFRP inhibited the development of rupture strength of SGFRP, and thus limited the increase in the ultimate load. The results here confirmed the importance of providing strong anchoring systems to prevent such de-bonding failures.

#### 8.8.2.4.2 Effect of SGFRP strengthening configuration

In Figure 8-29 and 8-31, it can be seen that beam BN-HS-5GB-MB attained 20% higher increase in the ultimate load as compared with beam BN-HS-5GA-MB. This supported the fact that for the same SGFRP thickness, the strengthening configuration B provided a better performance than configuration A. It was noted that the increase in the ultimate load was not significant, indicating that the SGFRP at the bottom face did not provide a significant direct load bearing mechanism for deep beam. However, it was still beneficial since it could contribute to an enhanced bonding for the SGFRP on the side faces.

## Chapter 9

### SFRP Strengthening of RC Deep Beams with Openings

#### 9.1 Introduction

Reinforced concrete (RC) deep beam is a beam with the depth comparable to the span length. Based on ACI 318-05 [79], an RC beam is defined as a deep beam if the span length-to-depth ratio is less than or equal to four. There are several applications of RC deep beams, such as transfer girders in tall buildings, wall of water tanks, and footings [80, 81]. Rectangular and circular openings of various sizes are sometimes made in the web of the beams to allow for the passage of utilities ducts and conduits for air conditioning and electrical cables. If the web opening is located amidst the load path that joins the support and the loading points, the opening may disturb the flow of the load, resulting in a decrease in the shear capacity. A decrease in shear capacity of RC deep beams with web opening has been demonstrated in previous research works [82-84]. Despite a number of research works on strengthening RC deep beams, a current literature review demonstrated no studies on the use of SFRP to increase the shear strength of deep beams with openings. Furthermore, to our knowledge, no data are available regarding the behavior of SFRP-strengthened RC deep beams with openings. Therefore, the primary goal of this experimental program (Chapter 9) was to evaluate a possible use of the SFRP technique to elevate the shear strength of RC deep beams with openings. Towards this goal, an extensive experimental program has been conducted. Both circular and square openings of different sizes were investigated. Two types of concrete (i.e., low and high strength) were used to cast the specimens. The deep beams with openings were strengthened with a variety of SFRP thicknesses and strengthening configurations. The “MB anchoring system” as discussed in “Chapter 8” was used to avoid de-bonding of the SFRP from the concrete surface.



## 9.2 Experimental program

### 9.2.1 Description of the test specimens and test matrix

A description of the test specimens is shown in Figures 9-1 and 9-2 and summarized in Table 9-1. The test specimens consisted of a total number of 29 RC deep beams with web openings of different shapes and sizes. The entire test matrix was divided into six groups (A, B, C, D, E and F) according to the opening shape and size and the concrete strength (Table 1). Each group consisted of five beams except group F, which had four beams. One specimen in each group was used as a control un-strengthened specimen. The RC deep beams in groups A, B, C and D were made of a low-strength concrete with a cylindrical compressive strength of 24 MPa, whereas the beams in groups E and F were made of a high-strength concrete with a cylindrical compressive strength of 45 MPa. All beams had a constant cross section with the width (T) = 100 mm and total depth (H) = 500 mm. The total span length (L) of the beam was 870 mm, and the shear span length (defined as half of span length between supports) was 435 mm. Two opening shapes (i.e., circular and square) were used with two different sizes for each shape. The size of the square opening was 120 x 120 mm and 180 x 180 mm, and the diameter of circular opening was 100 mm and 160 mm. In all specimens, one opening is made at the centre of each shear span (Figures 9-1 and 9-2). Each beam contained two No.12 bars (deformed bars with a yield strength of 414 MPa) at the bottom face, and top two No. 6 bars (round bars with a yield strength of 290 MPa) at the top face. The web reinforcements consisted of round No. 6 bars placed at 110 mm spacing in both vertical and horizontal directions. Stirrups were used as the vertical web reinforcement, and straight bars were used as the horizontal web reinforcement. Closely spaced vertical stirrups were used at both ends of the beams to avoid premature failure at these locations. The web reinforcements at the opening location were cut, and the circular molds made of plastic pipe were installed prior to the concrete placement. A clear 15 mm thick concrete cover was provided on all sides of beams, and the beams were cast in the horizontal position using molds made of plywood sheets (Figure 9-3). Each specimen was assigned a designation that represented the strength of concrete, the fiber thickness, the strengthening configuration, the shape and size of the opening. As an example, a specimen designation LS-3B-S18 was interpreted as follows: LS = Low-strength concrete, 3B = 3-mm thickness of SFRP with strengthening configuration B

and S18 indicated a square opening with a size of 180 x 180 mm.

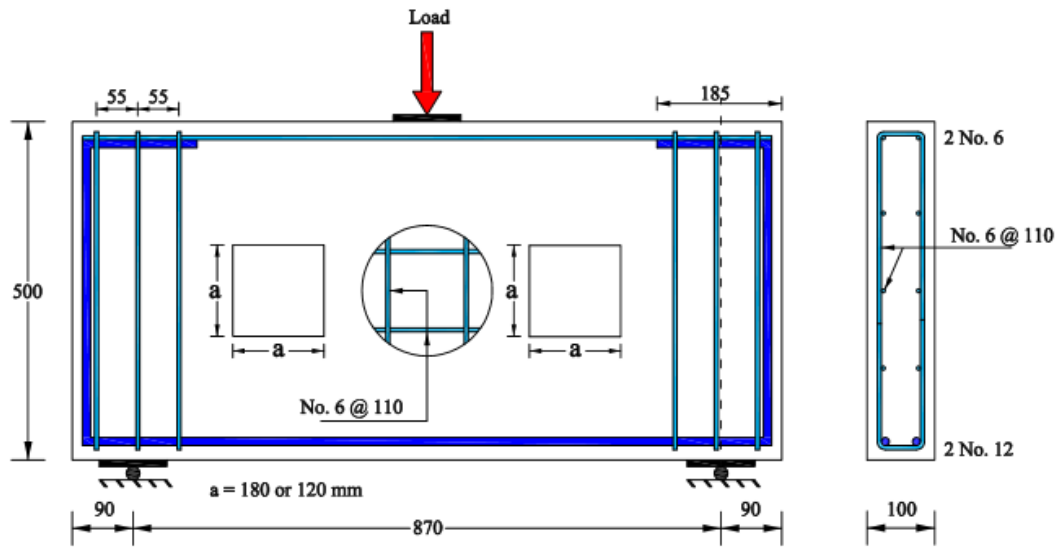


Figure 9-1: Group A, B, E and F beam detailing

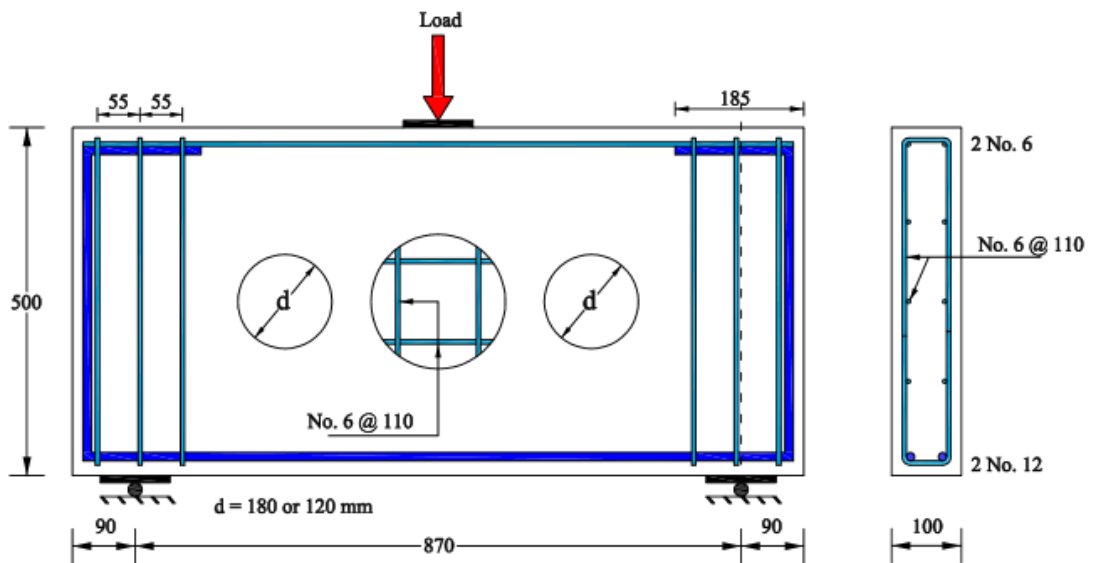


Figure 9-2: Group C and D beam detailing

**Table 9-1: Test matrix**

Group	Beam	Type of opening	Size of opening (mm)	Concrete strength (MPa)	Thickness of fiber (mm)	SGFRP Configuration
A	Control LS-S18	Square	180 x 180	24	-	-
	LS-5A-S18-N*	Square	180 x 180	24	5	A
	LS-3B-S18	Square	180 x 180	24	3	B
	LS-5A-S18	Square	180 x 180	24	5	A
	LS-5B-S18	Square	180 x 180	24	5	B
B	Control LS-S12	Square	120 x 120	24	-	-
	LS-3A-S12	Square	120 x 120	24	3	A
	LS-5A-S12	Square	120 x 120	24	5	A
	LS-5B-S12	Square	120 x 120	24	5	B
	LS-5C-S12	Square	120 x 120	24	5	C
C	Control LS-C16	Circular	160	24	-	-
	LS-3A-C16	Circular	160	24	3	A
	LS-5A-C16	Circular	160	24	5	A
	LS-5B-C16	Circular	160	24	5	B
	LS-5C-C16	Circular	160	24	5	C
D	Control LS-C10	Circular	100	24	-	-
	LS-3A-C10	Circular	100	24	3	A
	LS-5A-C10	Circular	100	24	5	A
	LS-5B-C10	Circular	100	24	5	B
	LS-5C-C10	Circular	100	24	5	C
E	Control HS-S18	Square	180 x 180	45	-	-
	HS-3A-S18	Square	180 x 180	45	3	A
	HS-5A-S18	Square	180 x 180	45	5	A
	HS-5B-S18	Square	180 x 180	45	5	B
	HS-5C-S18	Square	180 x 180	45	5	C
F	Control HS-S12	Square	120 x 120	45	-	-
	HS-3A-S12	Square	120 x 120	45	3	A
	HS-5A-S12	Square	120 x 120	45	5	A
	HS-7A-S12	Square	120 x 120	45	7	A

Note: \*The beam specimen LS-5A-S18-N does not include anchors.



**Figure 9-3: Concrete casting**

### 9.2.2 SGFRP strengthening

In this experimental program, the SFRP strengthening of RC deep beams was performed using glass fibers. The specimens were strengthened with three SGFRP thicknesses (i.e., 3 mm, 5 mm and 7 mm) and three strengthening configurations (i.e., A, B and C) (Table 9-1). For strengthening configuration A, the SGFRP was applied onto side faces of the beam only. For strengthening configuration B, the SGFRP was applied onto the side and bottom faces (Figure 9-4) in the form of U shape. With the SGFRP technique, the fibers are sprayed with resin; therefore, it is easy to vary the thicknesses of SGFRP at desired locations on the sprayed surface. Strengthening configuration C was similar to configuration A, except the thickness of the SGFRP was increased around the openings and at the top and bottom edges of the beams as shown in Figure 9-4. Prior to the SGFRP application, the concrete surfaces were roughened using a hammer and a chisel to enhance bonding with SGFRP (Figure 9-5). The SGFRP was applied onto the specimens by a local contractor using an UltraMax chopper/Saturator unit manufactured by Magnum Venus Plastech (Figure 9-6). After the SGFRP was applied, an aluminum ribbed roller was used to remove any entrapped air and to obtain a uniform thickness of the SGFRP.

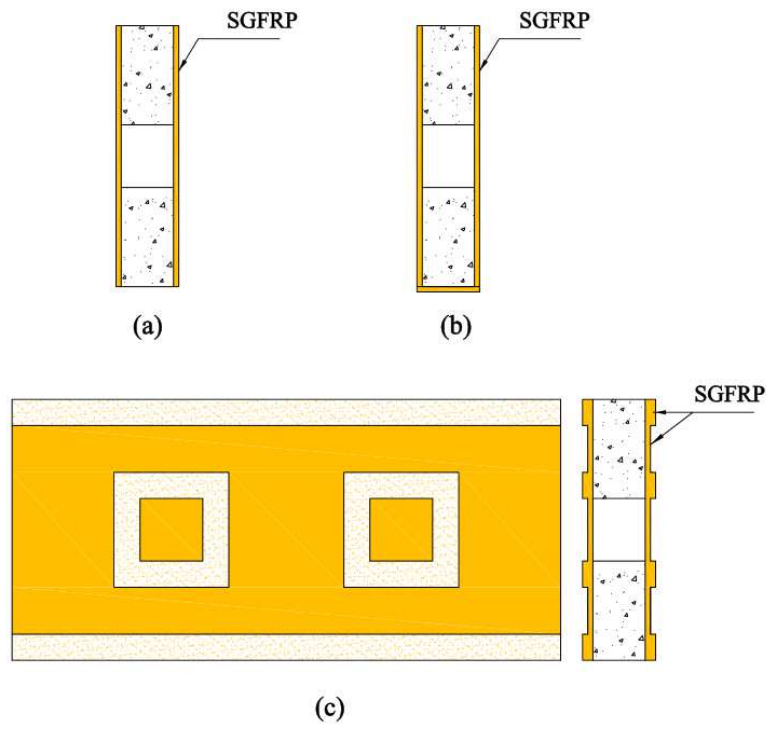


Figure 9-4: SGFRP strengthening configurations a) strengthening configuration A b) strengthening configuration B c) strengthening configuration C



Figure 9-5: Roughened surface of concrete beam



Figure 9-6: SFRP strengthening process of RC deep beams with openings

### 9.2.3 Material properties

The 28-day cylindrical compressive strength of concrete for specimens in groups A through D (low strength concrete, LS) was 24 MPa. The 28-day cylindrical compressive strength of concrete for specimens in groups E and F (high strength concrete, HS) was 45 MPa. The fibers used for the SGFRP was a glass-fiber roving coated with a silicone-based chemicals that enhance the bonding with the resin.

### 9.2.4 Test setup and instrumentation

In this experiment, all specimens were loaded to failure under the condition of a concentrated load applied at the mid span. The testing was performed in a steel reaction frame with a 2000 kN capacity. The load was applied at a constant rate of 10 kN/minute using a hydraulic jack with a 600 kN capacity. At the loading location, a steel plate was placed under the piston of the hydraulic jack to avoid crushing the concrete. A linear variable differential transducer (LVDT) was attached at the mid span to record the deflection. The initiation and propagation of the cracks were marked, and their positions were continuously monitored at different load intervals. Loading set up is shown in Figure 9-7.

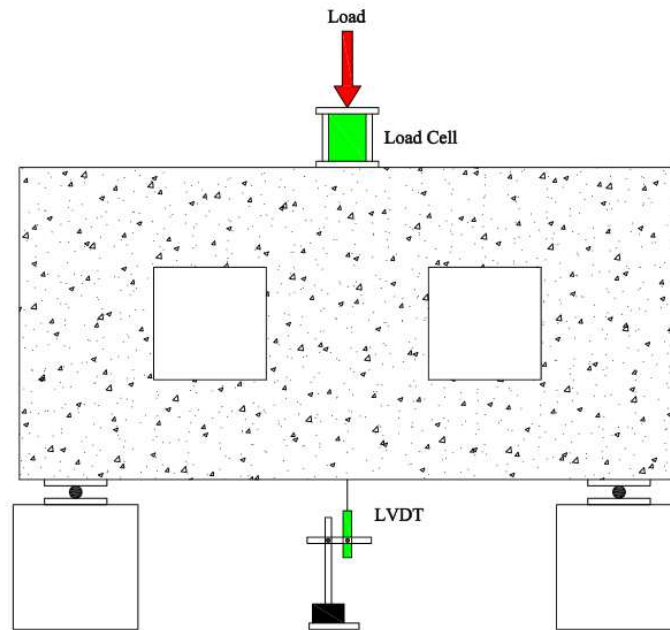


Figure 9-7: Loading set up

### 9.3 MB Anchoring system

The MB anchoring system was installed following the procedure as explained in section 8.7.2.2. A typical installation of the MB anchoring system is shown in Figure 9-8.

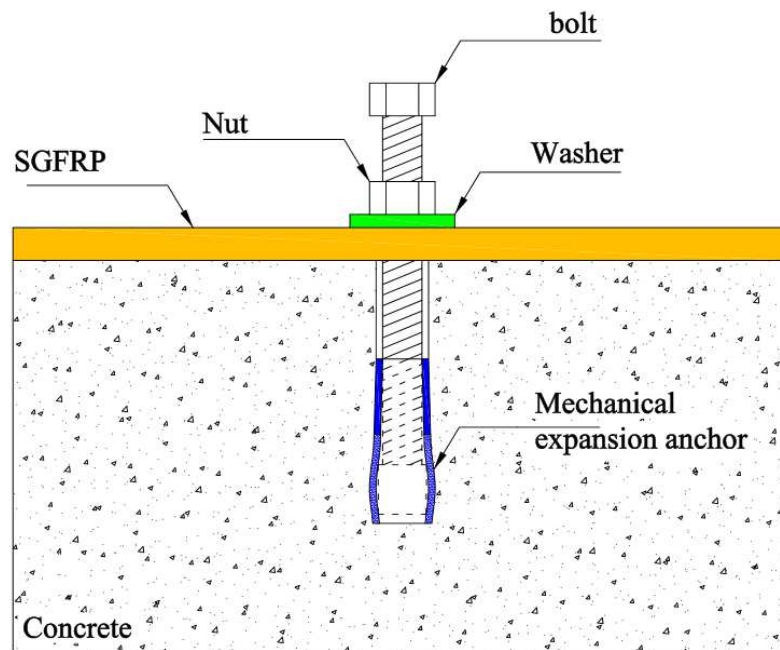


Figure 9-8: MB Anchoring system

## **9.4 Experimental results and discussions**

### **9.4.1 Cracking behavior**

For the control beams in all groups, flexural cracks were observed near the mid-span prior to the appearance of diagonal cracks. The cracking load ranged from 35-50% of the peak load (Table 9-2). As the load increased, diagonal cracks appeared at the opposite corners of the square opening, or at the top and bottom of the circular openings (Figures 9-9 to 9-12). As the load increased, the diagonal cracks widened and propagated in both directions towards the loading and the supporting regions. A further load increase resulted in the widening of diagonal cracks as well as the initiation of new flexural and diagonal cracks. From Table 9-2, it can be seen that the opening size had a great effect on the cracking load. For both square and circular openings, the cracking load was decreased when the opening size was increased. This relationship, a decrease in the cracking load due to an increase in the opening size, has also been reported in literature [66]. As for the SGFRP strengthened specimens, the cracking load could not be recorded because the SGFRP covered the entire surface of the beams' webs, making it impossible to visually observe the crack appearance. However, the rupture of the SGFRP fiber was observed to start at 90-95% of the ultimate load at the opposite corners of the square openings and at the top and bottom of the circular openings (Figures 9-13 and 9-14). As the load increased, the inclined crack rupture in the SGFRP fiber widened, and quickly propagated towards the loading and supporting regions. For all specimens, except HS-7A-S12, the beginning of the cracks and the upcoming ruptures of the SGFRP were similar. In contrast, the specimen HS-7A-S12 failed by anchor pullout and de-bonding of the SGFRP. This shall be discussed later in section 9.4.3.6.



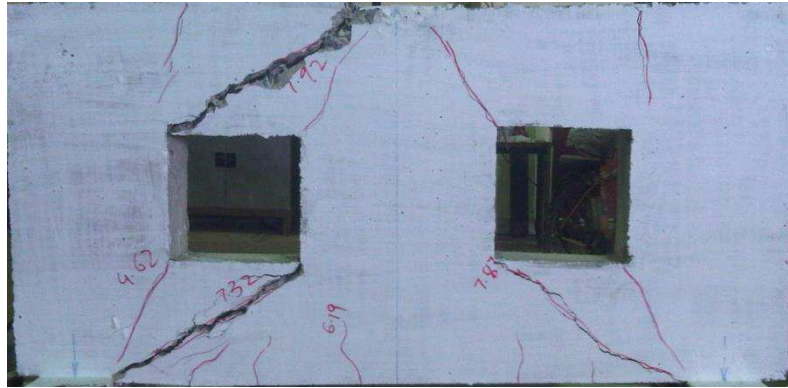


**Figure 9-9: Failure mode of Beam specimen - Control LS-S18**

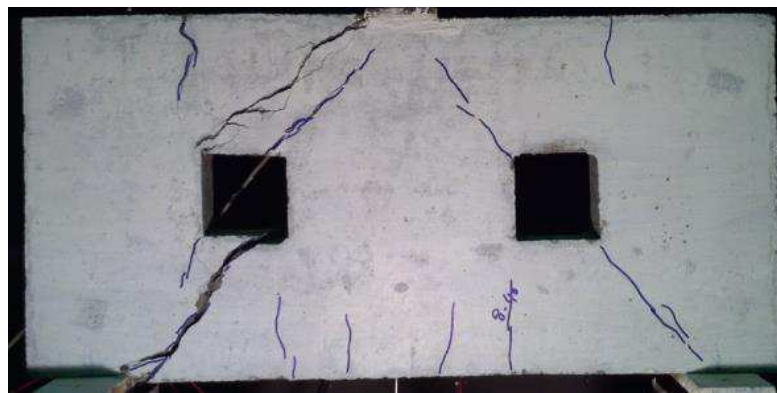


**Figure 9-10: Failure mode of Beam specimen - Control LS-S12**

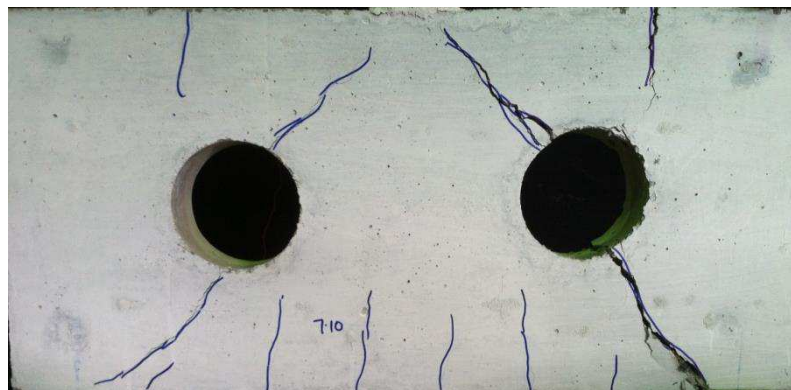


**Figure 9-11: Failure mode of Beam specimen - Control LS-C16**

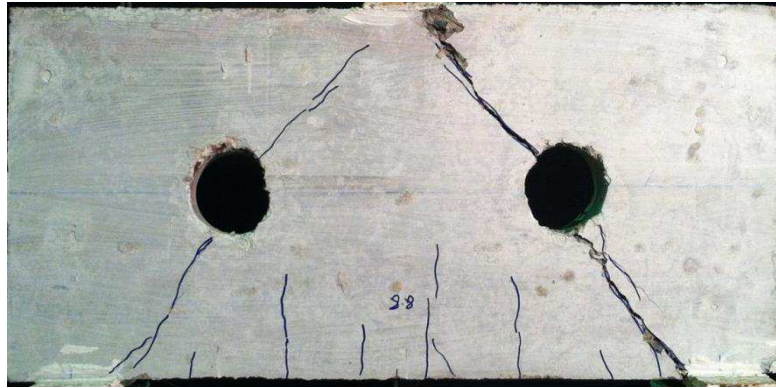


**Figure 9-12: Failure mode of Beam specimen - Control LS-C10**

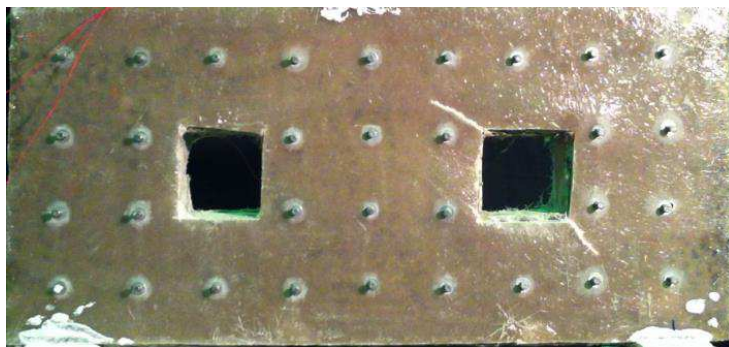


**Figure 9-13: Initiation of diagonal cracks in SFRP beams with square openings**

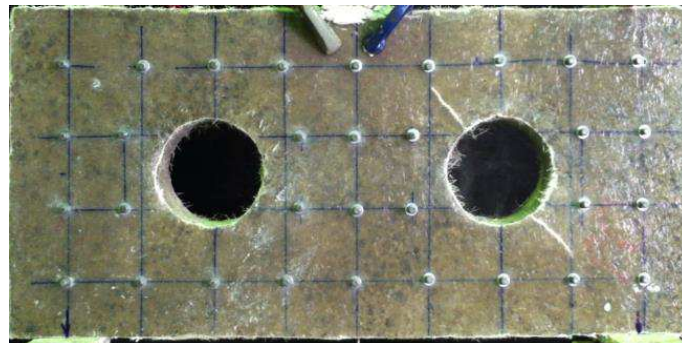


**Figure 9-14: Initiation of diagonal cracks in SFRP beams with circular openings**

**Table 9-2: Experimental test results**

Group	Beam	Cracking load (kN)**	Peak load (kN)	Increased Peak load (%)	Mid span deflection* (mm)	Increased mid span deflection (%)
A	Control LS-S18	50.24	123.22	-	1.78	-
	LS-5A-S18-N	-	202.24	64	1.50	-
	LS-3B-S18	282.57	307.14	149	2.10	18
	LS-5A-S18	285.52	306.35	149	2.61	47
	LS-5B-S18	313.43	342.55	178	2.38	34
B	Control LS-S12	49.50	169.71	-	1.93	-
	LS-3A-S12	302.13	321.41	89	3.72	93
	LS-5A-S12	344.15	368.08	117	3.84	99
	LS-5B-S12	388.08	411.97	143	5.33	176
	LS-5C-S12	377.71	397.17	134	4.07	111
C	Control LS-C16	38.63	181.20	-	2.50	-
	LS-3A-C16	270.80	296.61	64	3.60	44
	LS-5A-C16	328.80	364.52	101	3.51	40
	LS-5B-C16	376.48	411.90	127	4.02	61
	LS-5C-C16	355.89	387.68	114	3.84	54
D	Control LS-C10	44.58	197.40	-	2.34	-
	LS-3A-C10	320.77	348.66	77	3.62	55
	LS-5A-C10	346.28	374.36	90	3.48	49
	LS-5B-C10	422.50	453.81	130	4.52	93
	LS-5C-C10	385.78	412.60	109	3.68	57
E	Control HS-S18	45.37	163.10	-	3.52	-
	HS-3A-S18	215.66	234.41	44	3.34	-
	HS-5A-S18	253.49	271.99	67	4.26	21
	HS-5B-S18	287.35	314.04	93	3.85	9
	HS-5C-S18	271.47	293.80	80	3.68	5
F	Control HS-S12	49.49	187.91	-	2.08	-
	HS-3A-S12	293.89	312.65	66	2.54	22
	HS-5A-S12	348.95	370.83	97	2.56	23
	HS-7A-S12	380.67	405.40	116	2.36	13

*Note: \*Values provided for the mid span deflection are measured at peak load. \*\* For SGFRP strengthened RC deep, the cracking load is onset of initial rupture of SGFRP.*

#### 9.4.2 Failure modes

The un-strengthened control beams of all groups showed a similar failure mode regardless of the shape or size of the openings. In the beams with square openings, the failure occurred when diagonal cracks suddenly formed at the top and bottom corners of the opening (Figures 9-9 and 9-10). Whereas, for the beams with circular openings, the failure occurred when the inclined cracks suddenly formed towards the loading and supporting regions (Figures 9-11 and 9-12). A similar failure mode for RC deep beams with the square and circular openings was reported by [66, 85]. The SGFRP strengthened beam LS-5A-S18-N, which did not have any mechanical anchoring system, failed due to the de-bonding of the fiber as shown in Figure 9-15. However, the SGFRP-strengthened beams that were anchored with expansion bolts failed by the formation of inclined crack ruptures in the fiber at the top and bottom corners of the opening (Figures 9-16 to 9-18). The inclined cracks were initially formed along the load path direction (Figures 9-13 and 9-14) and then progressed rapidly towards the supporting and the loading regions of the beams. When the thickness of SGFRP was increased to 7 mm as in the beam HS-7A-S12, the failure was initiated by the pullout of the expansion anchors and followed by the debonding of SGFRP (Figure 9-19).



**Figure 9-15: Failure mode of SGFRP strengthened beam specimen - LS-5A-S18-N**



Figure 9-16: Typical failure mode of SFRP strengthened beam specimen of group A

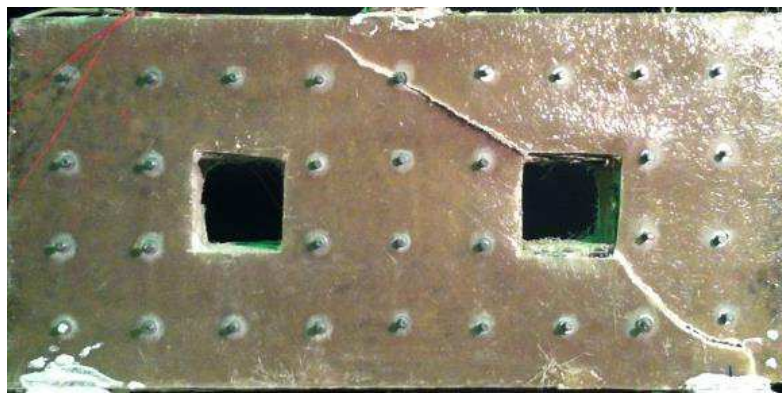


Figure 9-17: Typical failure mode of SFRP strengthened beam specimen of group B

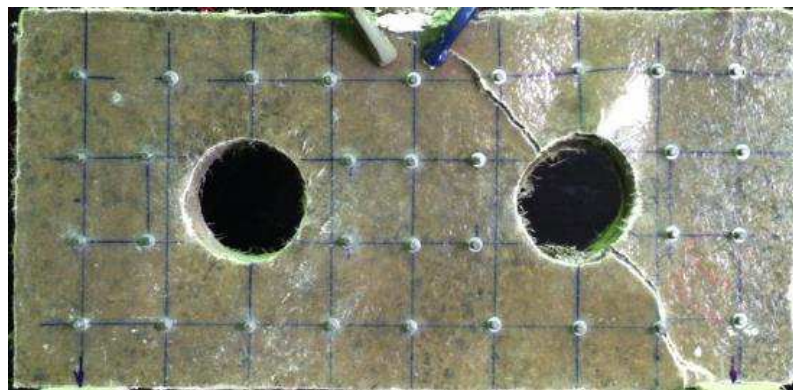


Figure 9-18: Typical failure mode of SFRP strengthened beam specimen of group C



Figure 9-19: Failure mode of SGFRP strengthened beam specimen - HS-7A-S12

#### 9.4.3 Load carrying capacity and mid span deflection

The load-deflection curves of the SGFRP-strengthened RC deep beams with openings are shown in Figures 9-20 to 9-25. This data can be used to evaluate the impact of the SFRP on the load carrying capacity and mid span deflection at the peak load of the beams. The test results are summarized in Table 9-2 and are discussed in detail in the following sections.

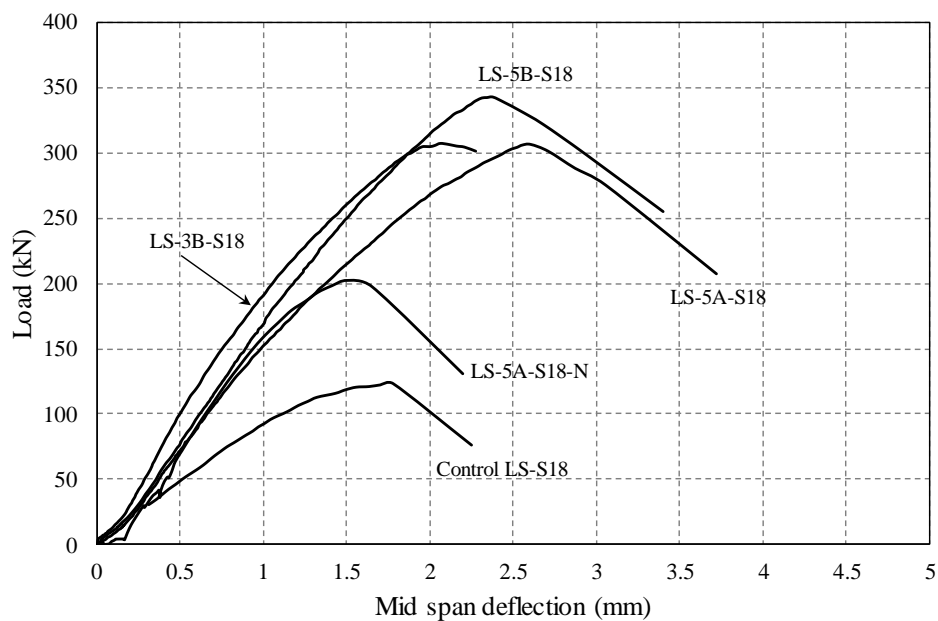


Figure 9-20: Load deflection curves of beams - Group A

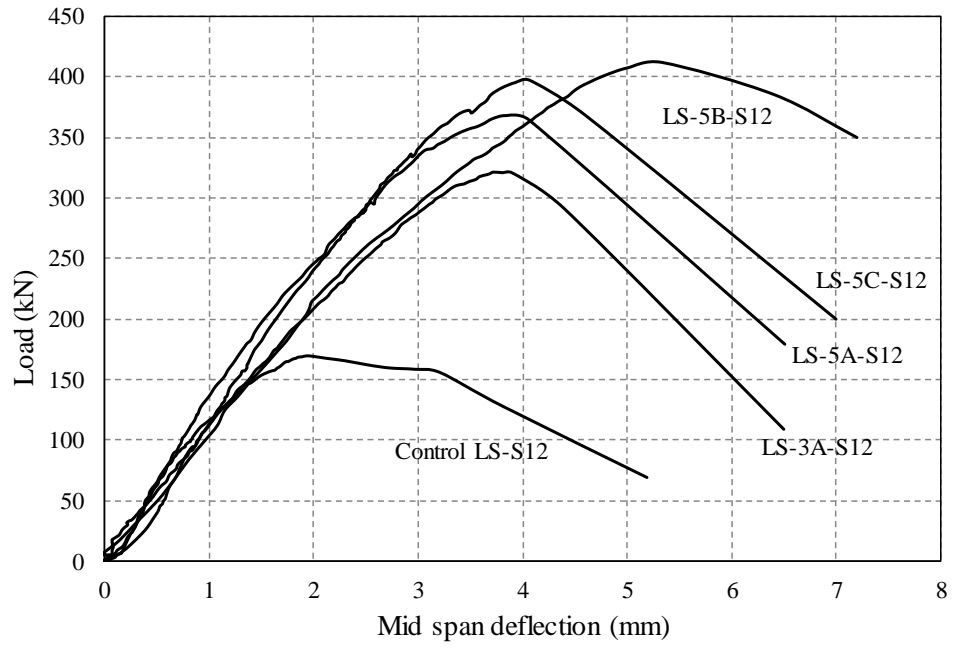


Figure 9-21: Load deflection curves of beams - Group B

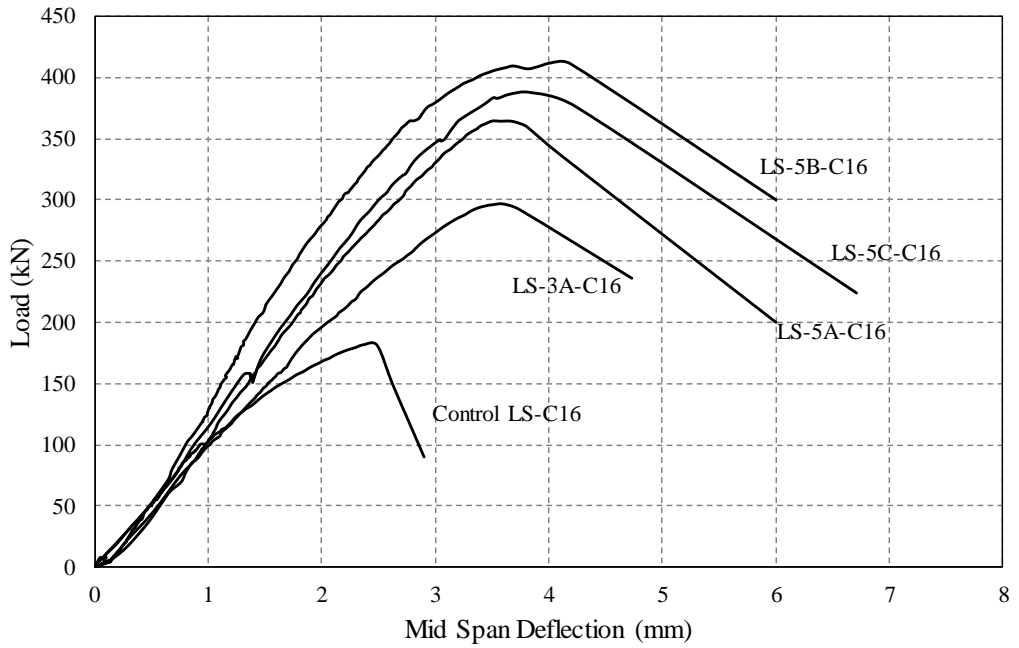
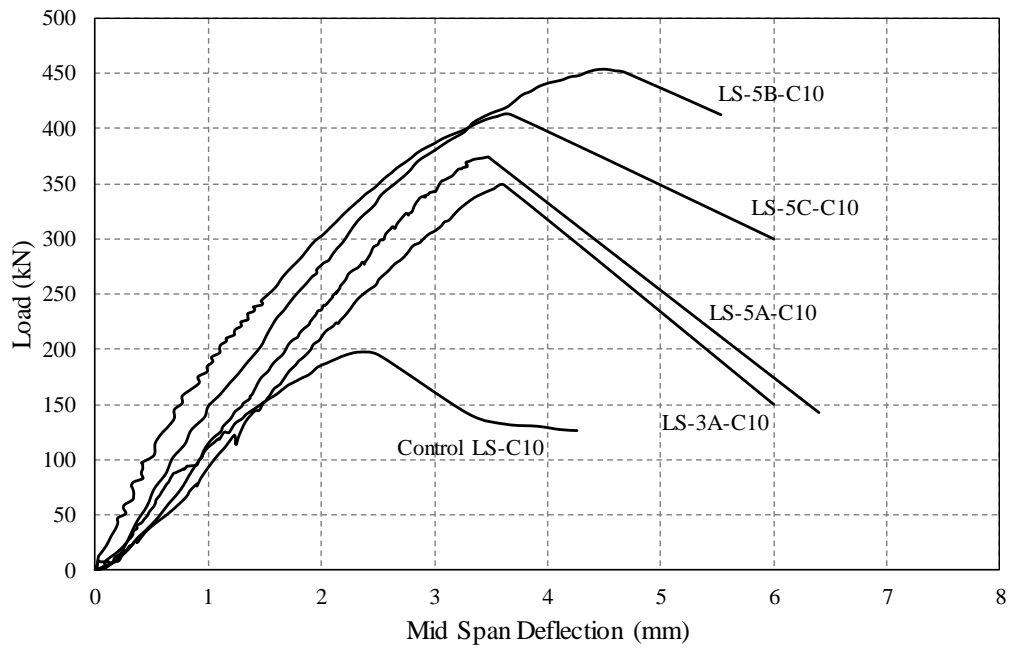
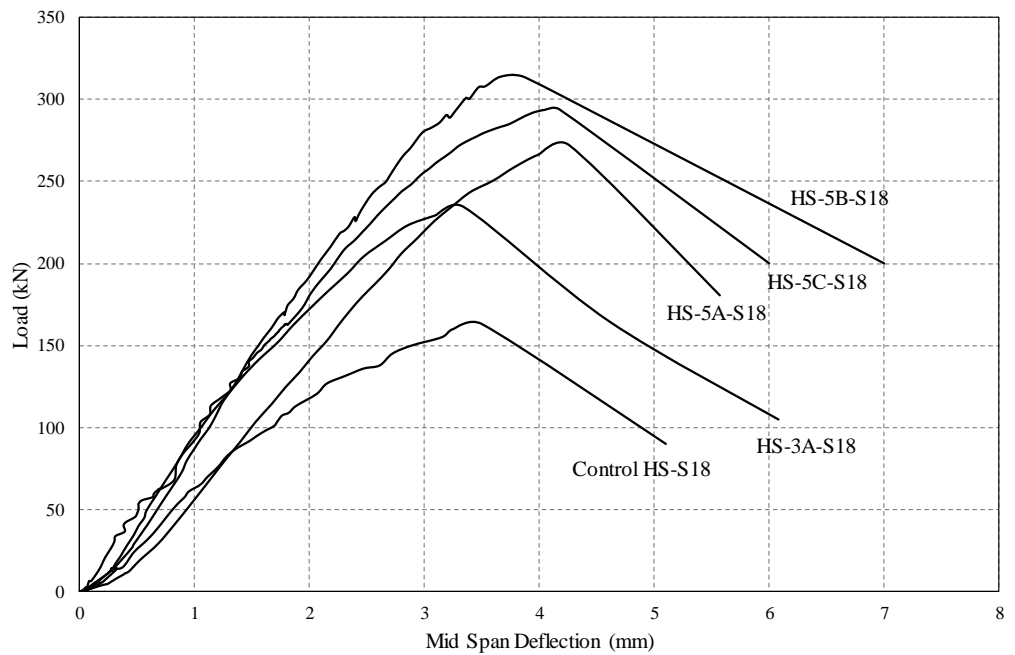


Figure 9-22: Load deflection curves of beams - Group C



**Figure 9-23: Load deflection curves of beams - Group D**



**Figure 9-24: Load deflection curves of beams - Group E**



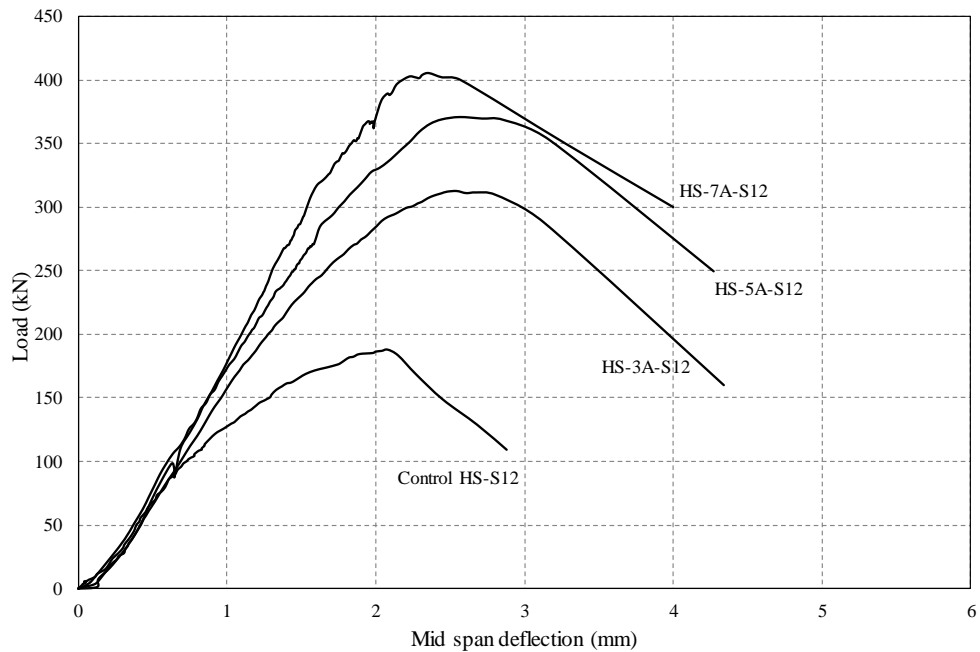


**Figure 9-25: Load deflection curves of beams - Group F**

#### 9.4.3.1 Specimens in group A

Specimens in group A are low strength concrete deep beams with 180 x 180 mm square opening. The load and deflection curves of all specimens are shown in Figure 9-20. The control beam failed at the peak load of 123.22 kN. Among the strengthened specimens, a maximum increase in the peak load of 178% over the control beam was recorded for beam LS-5B-S18, whereas a minimum increase of 64% was measured for beam LS-5A-S18-N without MB anchoring system (Table 9-2). The remaining beams in this group (i.e., LS-3B-S18 and LS-5A-S18) reached peak loads that were 149% greater than the control beam. Similar to the load carrying capacity, the mid-span deflections of the SGFRP-strengthened beams were also increased. A maximum increase in the mid-span deflection was 47%, for beam LS-5A-S18. Beams LS-3B-S18 and LS-5B-S18 reached the peak loads at 18% and 34% enhanced mid-span deflections, respectively.

#### 9.4.3.2 Specimens in group B

Specimens in group B are low strength concrete deep beams with 120 x 120 mm square opening. The load and deflection curves of all specimens are shown in Figure 9-21. The control beam Control LS-S12 failed by a typical shear failure at the peak load of 169.71 kN. This failure load was 38% higher than that of beam Control LS-S18 in

group A with a larger opening size of 180 x 180 mm. The maximum load increase of 143% was measured for the beam LS-5B-S12 with a 5 mm thick SGFRP and with strengthening configuration B. The minimum increase in peak load of 89% was measured for beam LS-3A-S12 with a 3 mm thick SGFRP and with strengthening configuration A. As shown in Figure 9-21, for strengthening configuration A, 89% and 117% increases in peak load were recorded for beams with 3 mm and 5 mm thick SGFRP, respectively. For the same SGFRP thickness (i.e., 5 mm), strengthening configuration B increased the peak load more than configurations C and A, respectively. Similar to group A, the mid-span deflections of the SGFRP-strengthened beams also significantly increased. Increases of 93%, 99%, 176% and 111% were recorded for beams LS-3A-S12, LS-5A-S12, LS-5B-S12, and LS-5C-S12 respectively.

#### 9.4.3.3 Specimens in group C

Specimens in group C are low strength concrete deep beams with 160 mm diameter circular opening. The load and deflection curves of the beams in group C with different SGFRP thicknesses and configurations are shown in Figure 9-22. For the same strengthening configuration (i.e., configuration A), the peak load was elevated by 64% and 101% for the 3 and 5 mm thick SGFRP, respectively. For the same SGFRP thickness (i.e., 5 mm), strengthening configuration B was more effective than configurations A and C. The increases in peak load were 101%, 114% and 127% for the configurations A, C and B respectively. As shown in Figure 9-22, the increases in the mid-span deflections of 44%, 40%, 61% and 54% were recorded for beams LS-3A-C16, LS-5A-C16, LS-5B-C16 and LS-5C-C16, respectively. For a 5-mm thick SGFRP, the highest increase in the mid-span deflection was achieved through configuration B, whereas the lowest increase was obtained with configuration A.

#### 9.4.3.4 Specimens in group D

Specimens in group D are low strength concrete deep beams with 100 mm diameter circular opening. The load and deflection curves of all beams in this group are shown in Figure 9-23. For the same strengthening configuration (i.e., configuration A), the peak load was increased by 77% with the 3 mm thick SGFRP, and by 90% with the 5 mm thick SGFRP. For the same SGFRP thickness (i.e., 5 mm), the strengthening configuration B was the most effective as compared to configurations A and C. The

increases in peak load were 90%, 109% and 130% for strengthening configurations A, C and B, respectively. As shown in Figure 9-23, the increases in the mid-span deflections of 55%, 49%, 93% and 57% were recorded for beams LS-3A-C10, LS-5A-C10, LS-5B-C10 and LS-5C-C10, respectively. For a 5-mm thick SGFRP, the highest increase in mid-span deflection was achieved through strengthening configuration B, whereas the lowest increase was obtained with configuration A.

#### 9.4.3.5 Specimens in group E

Specimens in group E are high strength concrete deep beams with 180 x 180 mm square opening. The load and deflection curves of all beams are shown in Figure 9-24. In this group, the control beam failed at the peak load of 163.10 kN. A maximum increase in peak load was 93% for the beam HS-5B-S18, whereas a minimum increase in peak load was 44% for the beam HS-3A-S18. The remaining beams in this group (i.e., HS-5A-S18 and HS-5C-S18) had the peak loads that were 67% and 80% higher than the control beam, respectively. The mid span deflection at the peak load of strengthened beams was also increased. A maximum increase in the mid-span deflection was 21% for beam HS-5A-S18. Beams HS-5B-S18 and HS-5C-S18 reached the peak loads at 9% and 5% of the enhanced mid-span deflection, respectively.

#### 9.4.3.6 Specimens in group F

Specimens in group F are high strength concrete deep beams with 120 x 120 mm square opening. The load and deflection curves of all beams are shown in Figure 9-25. The control beam Control HS-S12 failed in a typical shear failure at the peak load of 187.91 kN. A maximum increase in the load was recorded for the beam with the thickest SGFRP (i.e., 7 mm). As shown in Figure 9-25, the 66%, 97% and 116% increases in peak load were recorded for the beams with the 3 mm, 5 mm and 7 mm SGFRP thicknesses, respectively. Similar to group E, the mid-span deflections were increased by 22%, 23% and 13% for specimens HS-3A-S12, HS-5A-S12 and HS-7A-S12, respectively.

#### 9.4.4 Effectiveness of the MB anchoring system

In this study, the MB anchoring system as discussed in section 8.7.2.2 was utilized to prevent the de-bonding of SFRP from the concrete surfaces. The beam LS-5A-S18-N, which was tested without any anchoring system, failed by the de-bonding of the SGFRP as shown in Figure 9-15. Thus, an adequate anchoring system is required for the effective performance of the SGFRP strengthening technique. In almost all SGFRP strengthened beams with sufficient anchoring system, no pullout of the anchors was observed prior to the rupture of the fiber; the only exception was beam HS-7A-S12 whose anchors were pulled out and followed by the de-bonding of the SGFRP (Figure 9-19) from the concrete surface. The pullout of the anchors may be associated with the thickness of SGFRP and strengthening configuration. The thickness of SGFRP in the beam HS-7A-S12 was 7 mm, which was higher than other specimens. Since the strength and stiffness of SGFRP composites varied with the thickness, a more critical demand on bonding requirement is imposed at the SGFRP-concrete interface. The de-bonding failure occurred when the bond demand exceeded the anchor pullout capacity. To prevent such failure, anchoring system with greater pullout capacity or more closely-spaced anchors should be provided.

#### 9.4.5 Effect of the opening size and shape

From the experimental results, it was evident that the increase in the opening size, regardless of the shape, led to the reduction in the beam's shear strength. This tendency of strength decrease can be observed in both un-strengthened and strengthened beams. As for the un-strengthened specimens, the comparison of ultimate loads are shown in Figure 9-26 for square and circular openings. It is obvious that the shear strength drops when the opening size becomes larger. It is also of interest to note that the decrease in the ultimate load is more striking in square opening than in circular opening. For the square opening, when the opening size is increased by 1.5 times, i.e., from 120x120 mm to 180x180 mm, the reduction in the peak load was found to be 27.4% and 13.2% for low-strength and high-strength concrete specimens, respectively. However, in case of the circular opening, a 1.6 times increase in the opening size, i.e., from 100 mm diameter to 160 mm diameter resulted in the 8.2% reduction in peak load only.

As for the strengthened specimens, the above observation can be applied too. As can be seen from Figures 9-27 and 9-28, the decrease in the peak load is more highly noticeable in square opening than in circular opening despite the opening size is increased by a lower factor, i.e., 1.5 times increase in square opening versus 1.6 times increase in circular opening. It should also be noted the proportion of the load reduction is rather comparable for both un-strengthened and strengthened specimens made of low-strength concrete. However, in case of the high strength concrete, the reduction in peak load is around 25% in strengthened specimens as compared to only 13.2% in un-strengthened ones. This implied that the efficiency of SGFRP strengthening may be lower in case of high-strength concrete. More details regarding the effect of concrete strength shall be discussed in the following section.

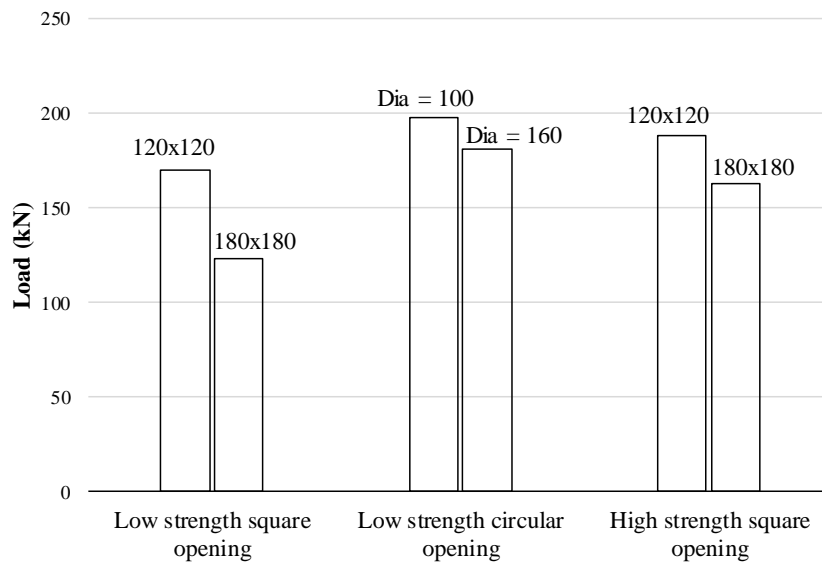


**Figure 9-26: Effect of the openings size and shape (control beams)**

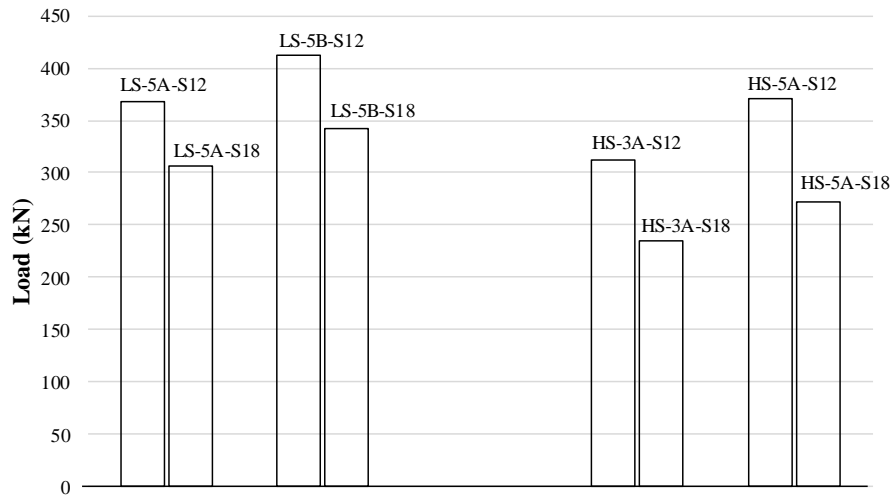


Figure 9-27: Effect of the openings size and shape (SGFRP strengthened beams with square openings)

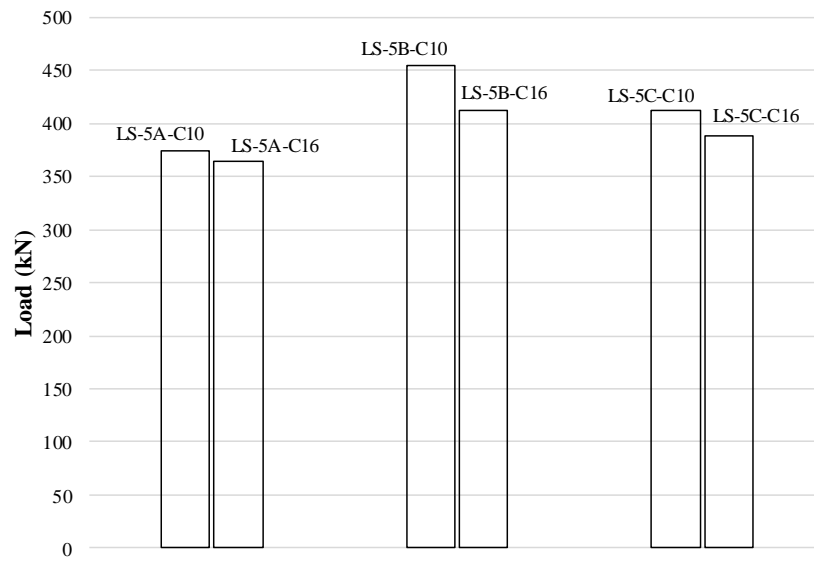
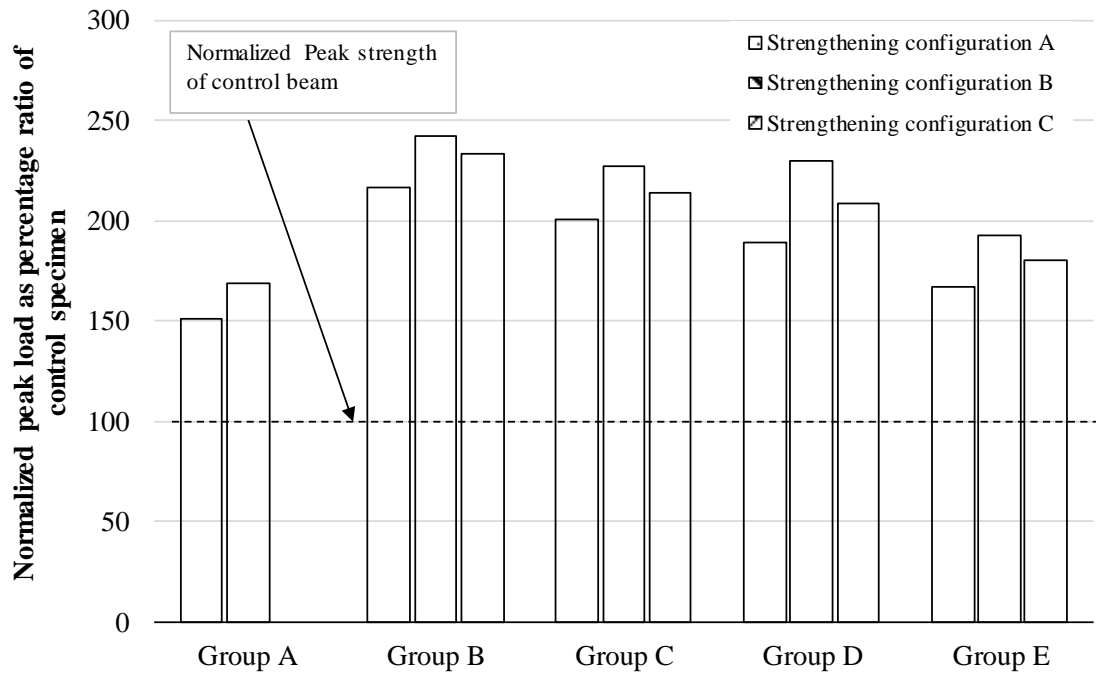


Figure 9-28: Effect of the openings size and shape (SGFRP strengthened beams with circular openings)

#### 9.4.6 Effect of the SGFRP strengthening configuration

In this experiment, three strengthening configurations, namely configurations A, B, C were studied (Figure 9-4). To compare the effectiveness of different strengthening schemes, only the specimens in groups A, B, C, D and E with 5 mm thick SGFRP are selected. Specimens with 3 mm thick SGFRP were excluded since there were only 2 specimens, namely HS-3A-S18 and LS-3B-S18 that had different configurations. Furthermore, these two specimens cannot be appropriately compared as they had different concrete strength. In each group, the peak load of the control unstrengthened specimen is set as a benchmark, by normalizing its peak load to 100%, and the effectiveness of strengthening configurations A, B and C are computed as the percentage ratio of the ultimate load to that of the control specimen. The comparison is shown in Figure 9-29. As can be seen, the strengthening configuration B demonstrates a consistently superior performance over strengthening configurations A and C. This is supposedly due to the U-shape (side and bottom faces) SGFRP configuration that provides better bonding to the concrete surfaces as compared to strengthening configurations A and C with side faces bonding only. In this figure, it is illustrated that the SFRP strengthening can effectively increase the ultimate load by more than two times in case of beams in groups B, C and D. Nevertheless, for the specimens in groups A and E, the increase in the ultimate load is reduced to 1.5-2.0 times. This experimental data indicates that the SGFRP strengthening is more efficient with smaller opening size, circular shape and low-strength concrete.



**Figure 9-29: Effect of the SGFRP-strengthening configuration**

#### 9.4.7 Effect of concrete strength

The test results demonstrated that the SGFRP strengthening effectively increased the ultimate load of the RC deep beams with both low- and the high-strength concrete. However, the percentage increase in peak load was found to be lower in high-strength beams than in low-strength ones. As an example, consider the case of 180 x 180 mm square opening, beam LS-5A-S18 failed at the enhanced peak load of 149%, while the peak load of beam HS-5A-S18 increased by 67% only. Similarly, for SGFRP strengthening configuration B, a 178% increase in the peak load was observed for beam LS-5B-S18, whereas the enhancement was only 93% for beam HS-5B-S18.

As for case of 3 mm SGFRP thickness, the increase in the peak load was 89% for low-strength beam LS-3A-S12 whereas it was only 66% for the high-strength beam HS-3A-S12. A similar trend can also be seen for beams with 5 mm SGFRP thickness, where the peak load was increased by 117% for low-strength concrete beam LS-5A-S12 as compared with 97% for the high-strength concrete beam HS-5A-S12.

It is of interest to examine whether this lower percentage increase in high-strength beam is due to a higher reference load of control high-strength beam over low-strength beam. To verify this assumption, the expected increase in the ultimate load of



the SGFRP strengthened high strength beams are calculated and compared with the actual load increase obtained from the tests. If the effect of strengthening is assumed to be independent of concrete strength, the expected load increase of the high strength concrete beam would be obtained as the sum of 1) the load increase due to the increase in compressive strength,  $\Delta PE_1$  and 2) the load increase due to SGFRP strengthening,  $\Delta PE_2$ . The first part,  $\Delta PE_1$ , may be calculated as;

$$\Delta PE_1 = P_u HS - P_u LS \quad (9)$$

Where  $P_u HS$  and  $P_u LS$  are the peak load of control high strength and low strength beams, respectively

The second part  $\Delta PE_2$  may also be calculated as;

$$\Delta PE_2 = P_u LS - P_u L_{SFRP} \quad (10)$$

Where  $P_u L_{SFRP}$  is the peak load of the SFRP-strengthened low strength concrete beam.

Thus, the expected load increase is  $\Delta PE = \Delta PE_1 + \Delta PE_2$ , whereas the actual load increase may be determined as follows;

$$\Delta PA = P_u H_{SFRP} - P_u L_{SFRP} \quad (11)$$

Where  $P_u H_{SFRP}$  is the peak load of SFRP-strengthened high strength concrete beam.

A comparison of the expected versus the actual load increase is displayed in Figure 9-30. As can be seen, the actual load increase is lower than the expected values. This indicates that the SGFRP strengthening is not as effective in high-strength concrete specimens as in low-strength concrete specimens. The conclusion is in line with the discussions on the effect of size and shape and strengthening configuration in the previous sections. The reason is not yet well understood. However, it is supposed that high-strength concrete, due to its rather brittle cracking characteristics, may induce more numerous cracks that reduce the anchoring capacity of the MB systems. A more detailed study should be carried out to clarify this effect.

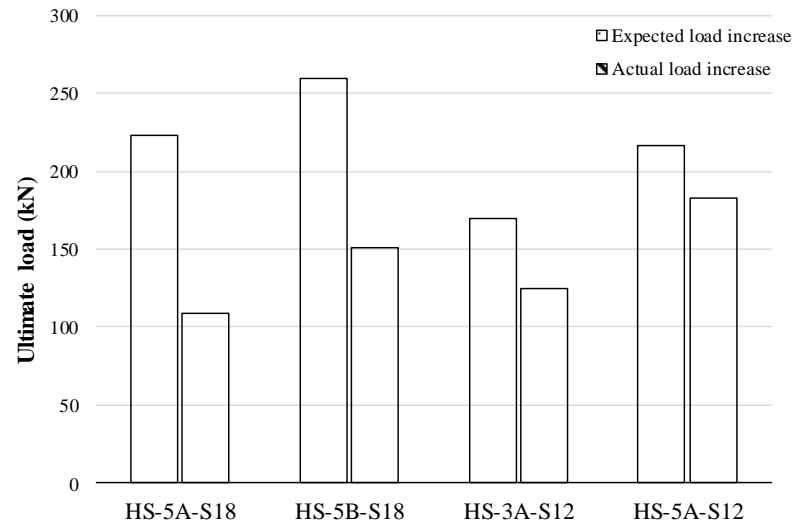


**Figure 9-30: Expected versus actual load increase**

#### 9.4.8 Stiffness of the SGFRP strengthened RC deep beams with openings

The experimental results show that the SGFRP strengthening of the RC deep beams, not only improved the strength and deflection, but also raised the stiffness of the beams. From the load-deflection curves, the secant stiffness at any point may be calculated as the ratio between the load and the corresponding deflection. As shown in Figure 9-31, two values of beam stiffness can be defined, corresponding to two different load levels S1 and S2. The stiffness at S1 is calculated at the peak load whereas the stiffness S2 is calculated at the load equal to the peak load of the corresponding control beam in each group. Thus, for the control beam, the stiffness is calculated only at the peak load (S1) as shown in the Figure 9-31.

The calculated stiffness values for specimens in groups A to F are summarized in Table 9-3. From table 9-3, it can be seen that all three strengthening configurations (i.e., A, B and C) improved the stiffness of the strengthened beams over the control beam. In case of square opening, for the specimens with the same SGFRP thickness, strengthening configuration B renders a higher stiffness as compared with strengthening configuration A. In Table 9-3, for groups A, B and E, the increases in the stiffness at the ultimate load of the beams with strengthening configuration A was calculated to be 70%, 9% and 38%, respectively whereas for beams with the strengthening configuration B, the stiffness increases were 108%, 12% and 76% respectively. However, for RC deep beams with circular opening, both strengthening

configurations A and B resulted in almost similar stiffness increase. Generally, the stiffness improvement of the specimens varied with the increase in the SGFRP thickness.

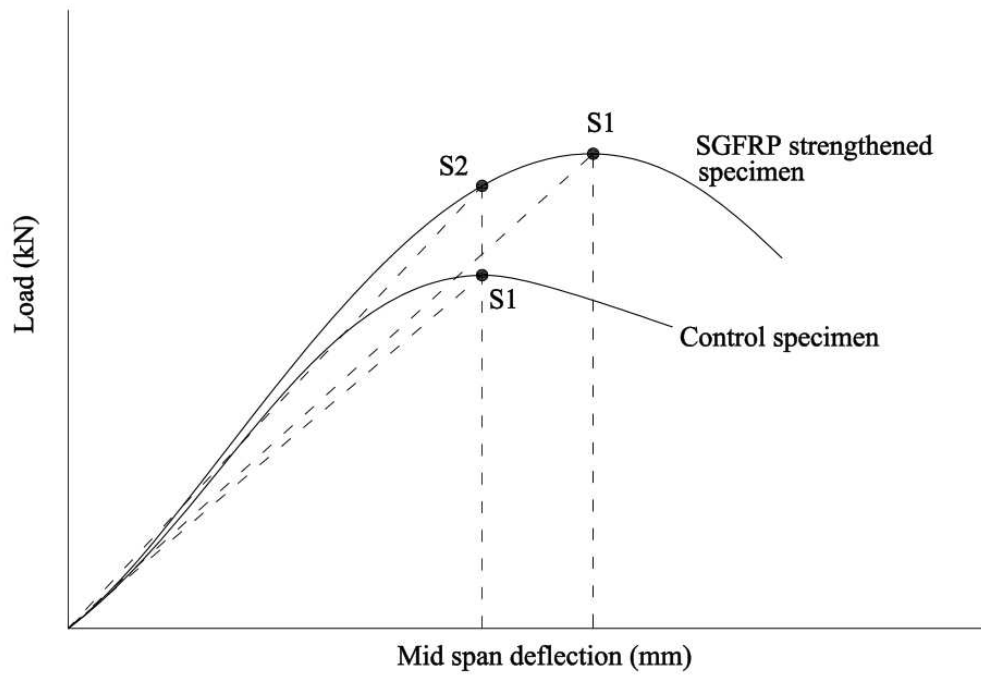


Figure 9-31: Stiffness calculation

**Table 9-13: Stiffness of the RC deep beams with openings**

Group	Beam	Stiffness (S1) (kN/mm)	Increased stiffness (S1) at peak load (%)	Stiffness (S2) - (kN/mm)
A	Control LS-S18	69	-	-
	LS-5A-S18-N	135	95	114
	LS-3B-S18	146	111	173
	LS-5A-S18	117	70	172
	LS-5B-S18	144	108	192
B	Control LS-S12	88	-	-
	LS-3A-S12	86	2	167
	LS-5A-S12	96	9	191
	LS-5B-S12	77	12	213
	LS-5C-S12	98	11	206
C	Control LS-C16	72	-	-
	LS-3A-C16	82	14	119
	LS-5A-C16	104	43	146
	LS-5B-C16	102	41	165
	LS-5C-C16	101	39	155
D	Control LS-C10	84	-	-
	LS-3A-C10	96	14	149
	LS-5A-C10	108	28	160
	LS-5B-C10	100	19	194
	LS-5C-C10	112	33	176
E	Control HS-S18	46	-	-
	HS-3A-S18	70	51	67
	HS-5A-S18	64	38	77
	HS-5B-S18	82	76	89
	HS-5C-S18	80	72	83
F	Control HS-S12	90	-	-
	HS-3A-S12	123	36	150
	HS-5A-S12	145	60	178
	HS-7A-S12	172	90	195

## **Chapter 10**

### **Analytical Analysis of SFRP Strengthened RC Deep Beams**

#### **10.1 Introduction**

The present chapter is primarily focused on the development of nonlinear finite element analysis for RC deep beams strengthened with SFRP. In the first step, the predicted finite element analysis results were compared with experimental results. Further, the finite element analysis is then employed as a tool to investigate the behavior of RC deep beams strengthened with externally bonded SFRP strips.

#### **10.2 Finite element modeling**

Finite element analysis on SFRP strengthened RC deep beams (experimental program as presented in Chapter 8) is performed by using a computer software WCOMD (WCOMD, 1998). In the first step, the predicted finite element analysis results were compared with experimental results. Then, the finite element models were utilized to investigate the behavior of RC deep beams strengthened with different configurations of SFRP strips (vertical and horizontal). A summary of beam specimens, selected from experimental study, for the finite element study is provided in Table 10-1. The RC deep beams are modeled using two dimensional eight-node reinforced concrete planer elements. The smeared cracking approach has been assumed in the modeling of concrete and steel. The SFRP is modeled by planar elements with elastic brittle properties [86]. Since, no de-bonding of SFRP was occurred in RC deep beams strengthened with SFRP, and anchored with bolts (Chapter 8), therefore in finite element analysis SFRP are modeled assuming perfect bonding between SFRP and concrete. The constitute laws of concrete and steel bars, used in finite element analysis are briefly explained in the next section.

**Table 10-1: Summary of experimental program and finite element models**

Specimen	Finite element model	Strength of concrete (MPa)	Fiber	SFRP Thickness	Anchoring system	Strengthening configuration
BN-LS-CB	FEM-LS-CB	21.45	-	-	-	-
BN-LS-3GA-MB	FEM-LS-3GA	21.45	Glass	3	MB	A
BN-LS-5GA-MB1	FEM-LS-5GA	21.45	Glass	5	MB	A
BN-LS-3CA-MB	FEM-LS-3CA	21.45	Carbon	3	MB	A
BN-LS-5CA-MB	FEM-LS-5CA	21.45	Carbon	5	MB	A
BN-HS-CB	FEM-HS-CB	46.20	-	-	-	-
BN-HS-3GA-EB	FEM-HS-4GA	46.20	Glass	3	EB	A
BN-HS-5GA-MB	FEM-HS-5GA	46.20	Glass	5	MB	A
BN-HS-5GB-MB	FEM-HS-5GB	46.20	Glass	5	MB	B

### 10.3 Constitutive models of concrete and reinforcing bars

A detailed description of the general formation of reinforced concrete planar element is available in the literature [87-93]. Here, a brief outline of constitutive models is presented, to show the key material behaviors. Further details can be found in the study [92, 93].

#### 10.3.1 Cracked concrete model

The constitutive model of cracked concrete is shown in Figure 10-1, which is formulated with respect to the crack axis. The model comprised compressive stress model parallel to the crack, tensile stress model orthogonal to crack and shear stress model along the crack face. A single model is formulated by combining tensile and compressive stress models. The relevant constitutive laws are described below.

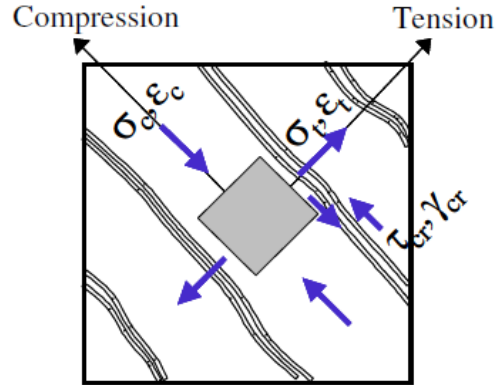


**Figure 10-1: Reinforced concrete planar element with normal and shear stresses**

### 10.3.1.1 Combined tension compression model for normal stress orthogonal and parallel to a crack

The combined tension-compression model for normal stress orthogonal and parallel to a crack is presented in Figure 10-2. On the tension side, the model is essentially linear up to the tensile strength of concrete followed by a constant tensile stress until concrete cracks. The tensile post-cracking behavior can be expressed by the following equation;

$$\sigma_t = f_t \left( \frac{\epsilon_{tu}}{\epsilon_t} \right)^c \quad (12)$$

Where  $\sigma_t$  is tensile stress normal to crack,  $f_t$  is the tensile strength of concrete,  $\epsilon_t$  is tensile strain,  $\epsilon_{tu}$  is cracking strain which can be calculated using expression (13) and parameter  $c$  represents a drop in tensile stress after concrete cracking. In this study; the value of  $c$  is set different for plain and reinforced concrete i.e., 2.0 and 0.4, respectively [93]. The higher value of  $c$  represents a more sudden drop in tensile stress of concrete. The area under the softening curve of the stress–strain law describes a fracture energy required to propagate a crack. It is an important characteristics of concrete for simulating the crack propagation and localized failure.

$$\epsilon_{tu} = 2 \frac{f_t}{E_c} \quad (13)$$

On the compression side, the elsto-plastic fracturing model [92, 93] was used to calculate the compressive stress parallel to a crack. The model is capable of combining

the nonlinearity of plasticity and fracturing damages to account for the permanent deformation and loss of elastic strain energy capacity. The relation between compressive stress and strain can be written as;

$$\sigma_t = \omega K_0 E_{c0} (\varepsilon_t - \varepsilon_p) \quad (14)$$

Where  $\sigma_t$  is the compressive stress parallel to the crack,  $\kappa_0$  is the fracture parameter representing the continuum damage as a result of dispersed cracking in concrete,  $E_{c0}$  is the initial elastic modulus and  $\varepsilon_p$  is the compressive plastic strain. The plastic compressive strain and fracture parameter are empirically formulated [92, 93] as;

$$K_0 = \exp\left(-0.73 \frac{\varepsilon}{\varepsilon'} \left(1 - \exp\left(-1.25 \frac{\varepsilon}{\varepsilon'}\right)\right)\right) \quad (15)$$

$$\varepsilon_p = 2\varepsilon' \left(\frac{\varepsilon}{\varepsilon'} - \frac{20}{7} \left(1 - \exp\left(-0.35 \frac{\varepsilon}{\varepsilon'}\right)\right)\right) \quad (16)$$

An additional damage factor  $\omega$  is incorporated in the model (Equation 14) to consider reduced compressive stress due to transverse tensile strain. Figure 10-2 also shows graphical relation between damage factor  $\omega$  and transverse tensile strain.

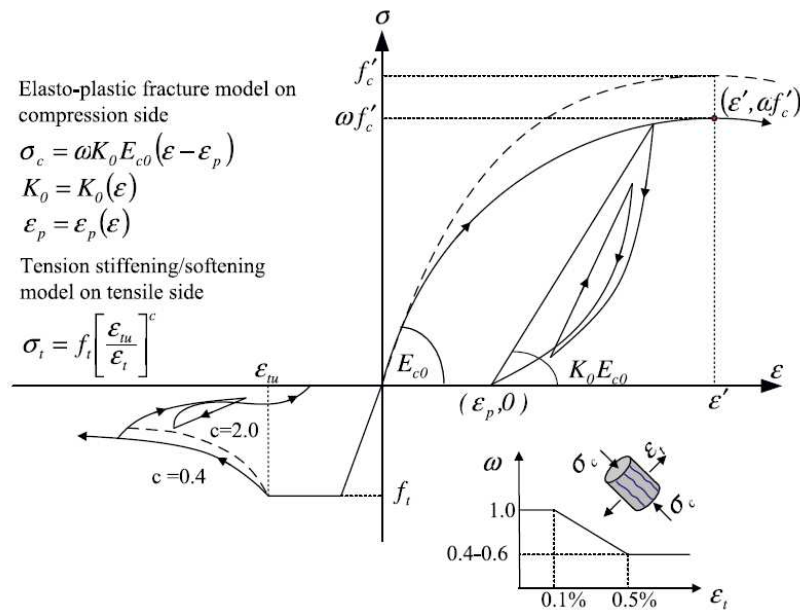


Figure 10-2: Compression-tension model for normal stress parallel and orthogonal to a crack



### 10.3.1.2 Shear stress transfer model

In reinforced concrete, the crack is assumed to form once the principal tensile stress exceeds the tensile strength of concrete. At the instant of cracking, shear stress and strain are zero at the principal planes. As loading proceeds, the principal axes of stress and strain change, thus imposing shear stress and strain on the cracks generated in the previous load step. For computing shear stress transmitted along a crack face, the contact density model [92, 93] is adopted (Figure 10-3). The equation of the shear envelope can be expressed as;

$$\tau_{cr} = 3.8(f'_c)^{1/3} \frac{\beta^2}{1 + \beta^2} \quad (17)$$

Where  $\beta$  is the normalized shear strain which can be defined as;

$$\beta = \frac{\gamma_{cr}}{\varepsilon_t} \quad (18)$$

Where  $\gamma_{cr}$  is the shear strain along cracks and  $\varepsilon_t$  is the tensile strain normal to crack.

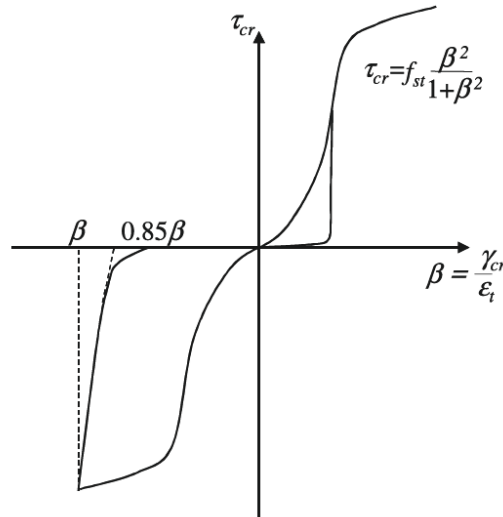


Figure 10-3: Shear stress transfer model

### 10.4 Model of reinforcing steel bar

In this study, the tri-linear model [92, 93] of reinforcing bar is adopted. The model of reinforcing bar is shown in Figure 10-4. In Figure 10-4, the dash line represents the model of bare steel bars. It is assumed that the embedded steel bars will yield at a

stress lower than the nominal tested yield strength of bare bar. This assumption is based on the concept that the behavior of steel bars embedded in concrete is different from bare steel bars, i.e., steel bars embedded in concrete did not yield uniformly at all sections throughout the steel bar. The first yield of an embedded steel bar occurs at crack locations and afterwards yielding extends to other regions. Thus, it can be assumed that the embedded bar yields at an average stress lower than the nominal yield strength. The average yield strength of embedded steel bars can be computed using the following expression [94].

$$\bar{f}_y = f_y - \frac{f_t}{2\rho} \quad (19)$$

$\bar{f}_y$  is the average yield strength of embedded steel bar in concrete,  $f_y$  is the yield strength of bare steel bar,  $f_t$  is the tensile strength of concrete and  $\rho$  is the reinforcement ratio. The middle part of the model is composed of a straight line which joins the average yield point to the  $12\varepsilon_y, 1.1f_y$  point. Whereas the final part of the model follows the model of bar steel bars up to the final steel rupture point.

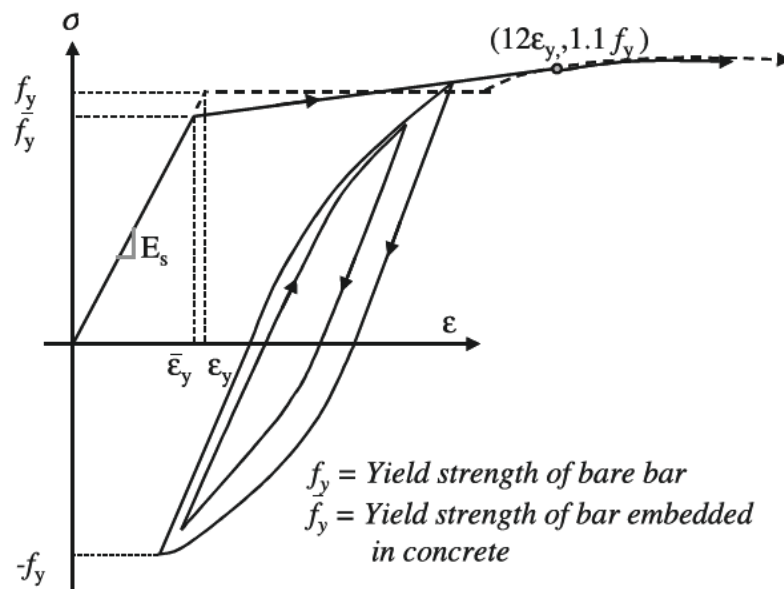


Figure 10-4: Model of steel bar

### 10.5 Constitutive model of SFRP

Pimanmas (2010) [86] has modeled FRP rods by assuming a linear behavior up to tensile strength. The same concept is adopted here and the constitutive model of SFRP is assumed linear up to the tensile strength of SFRP. Once tensile strength is reached, the stress is completely released to zero as shown in Figure 10-5.

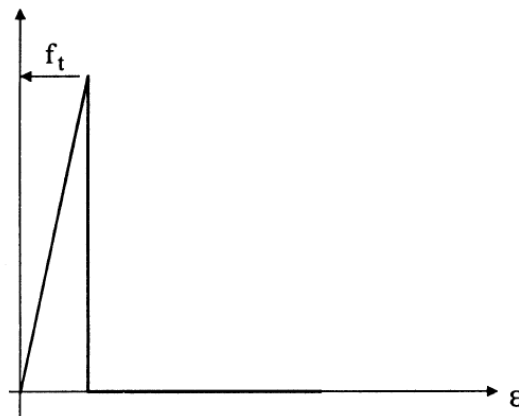


Figure 10-5: SFRP stress strain model

### 10.6 Finite element simulation of test results

The finite element mesh of the RC deep beam is shown in Figures 10-5 to 10-7. The steel plates at the support and loading location were modelled as elastic elements with high stiffness in the finite element model. Support nodes were assigned restraint against vertical movement, whereas loading node was assigned restraint both against vertical and horizontal movement. The finite element analysis results are further discussed in detail in the next section.

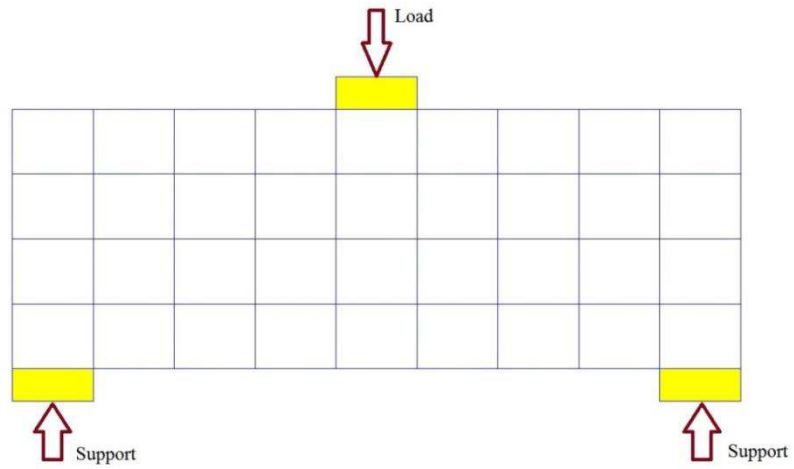


Figure 10-6: Finite element model of control beam FEM-LS-CB

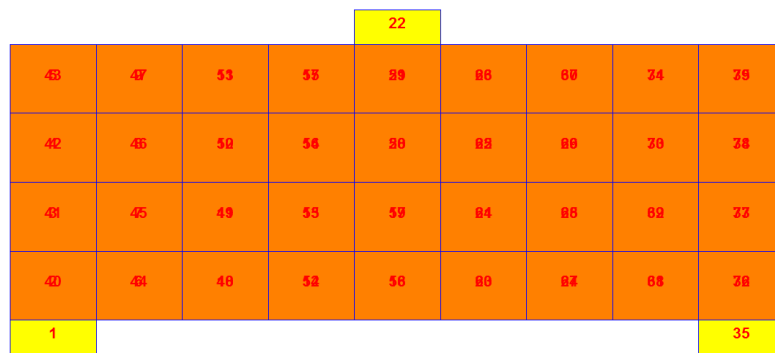


Figure 10-7: Finite element model of SFRP strengthened RC deep beam (Strengthening configuration A)

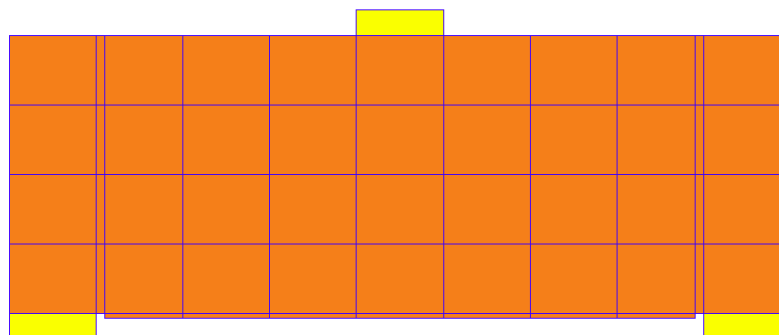
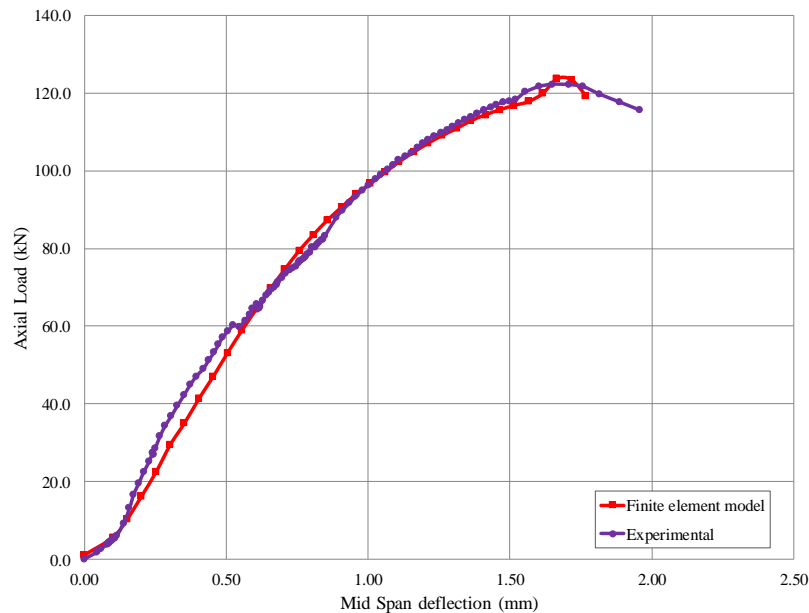


Figure 10-8: Finite element model of SFRP strengthened RC deep beam (Strengthening configuration B)

### 10.6.1 Load capacity and deflection behavior

The predicted load versus mid span deflection curves and cracking patterns are compared with experimental results (Figures 10-9 to 10-17) of selected beam specimens. A detailed summary of predicted finite element results along with the experimental values is presented in Table 10-2. It can be seen that there is an excellent agreement between the experimental and finite element results until failure. The finite element models can accurately predict the behavior of un-strengthened and SFRP strengthened RC deep beams. The predicted load versus mid span deflection curves are also found to be in good agreement, both for low and high strength concrete RC deep beams. The finite element models are also capable of predicting the increase in the ultimate load carrying capacity of SFRP strengthened RC deep beams with an increase in SFRP thickness. Both carbon and glass SFRP strengthened RC deep beams can be well simulated. This clearly validates the accuracy and reliability of finite element models.



**Figure 10-9: Experimental versus finite element model for beam BN-LS-CB and FEM-LS-CB**

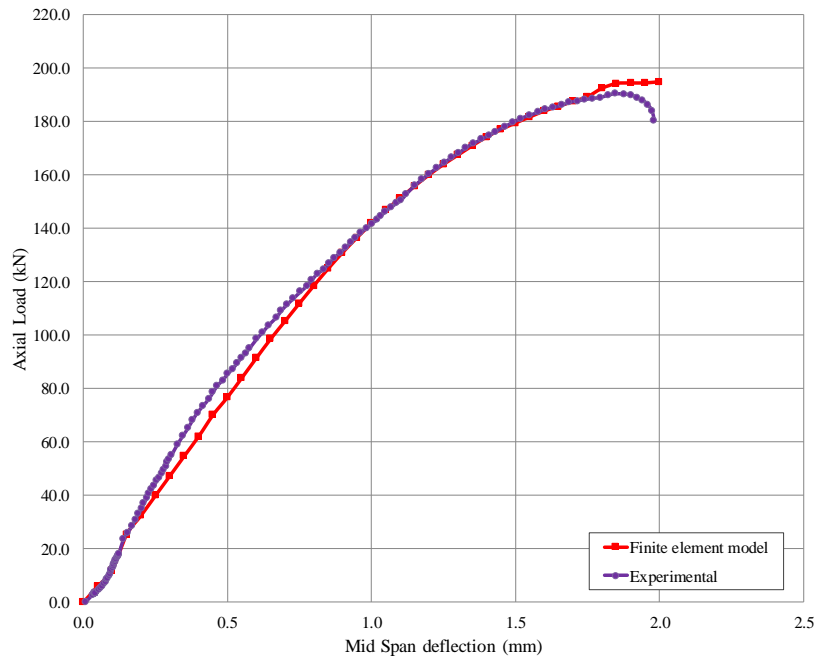


**Figure 10-10: Experimental vs. finite element model for beam BN-LS-3GA-MB and FEM-LS-3GA**

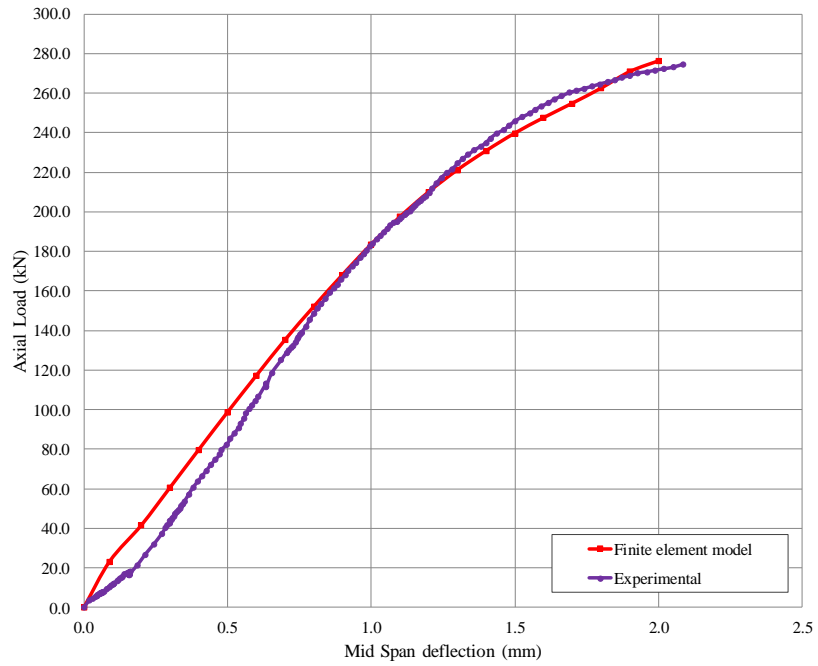


**Figure 10-11: Experimental vs. finite element model for beam BN-LS-5GA-MB1 and FEM-LS-5GA**

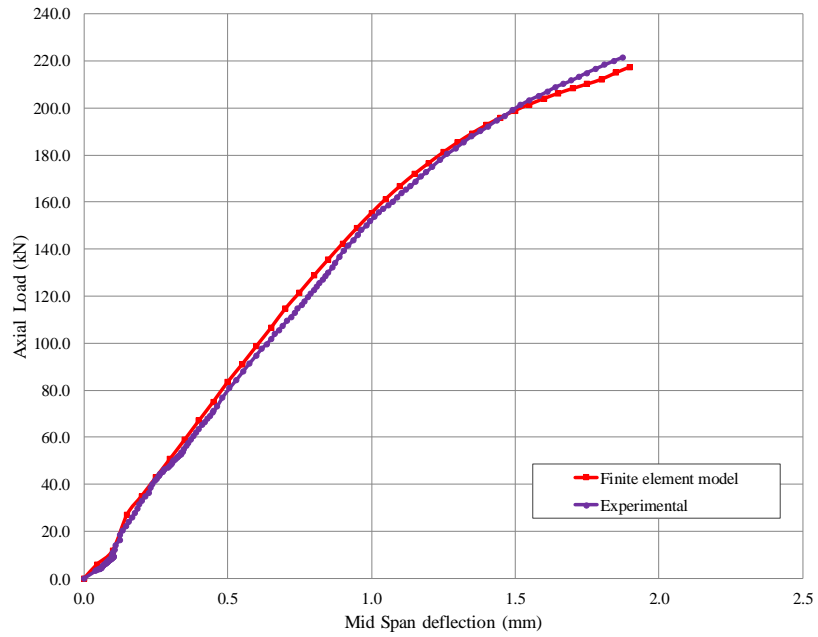


**Figure 10-12: Experimental vs. finite element model for beam BN-LS-3CA-MB and FEM-LS-3CA**

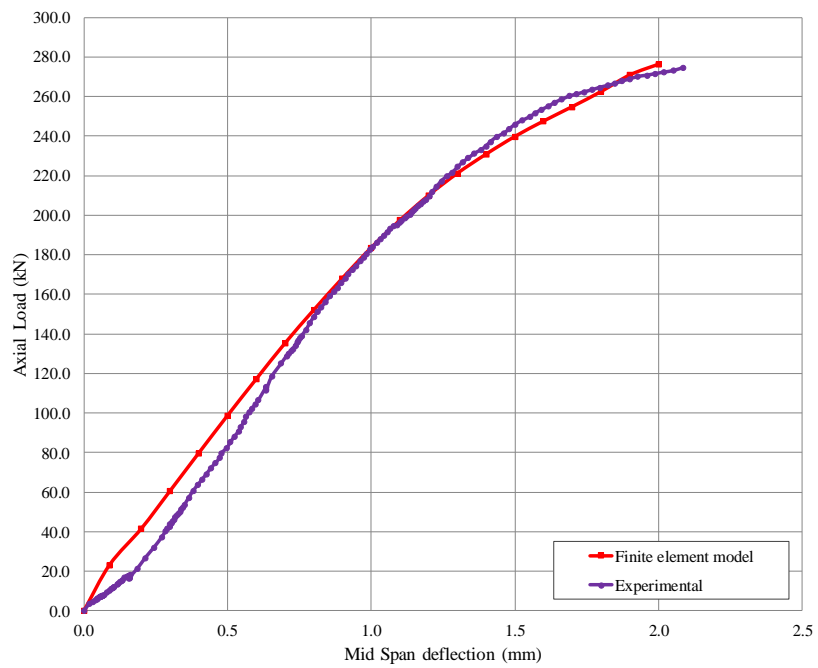


**Figure 10-13: Experimental vs. finite element model for beam BN-LS-5CA-MB and FEM-LS-5CA**

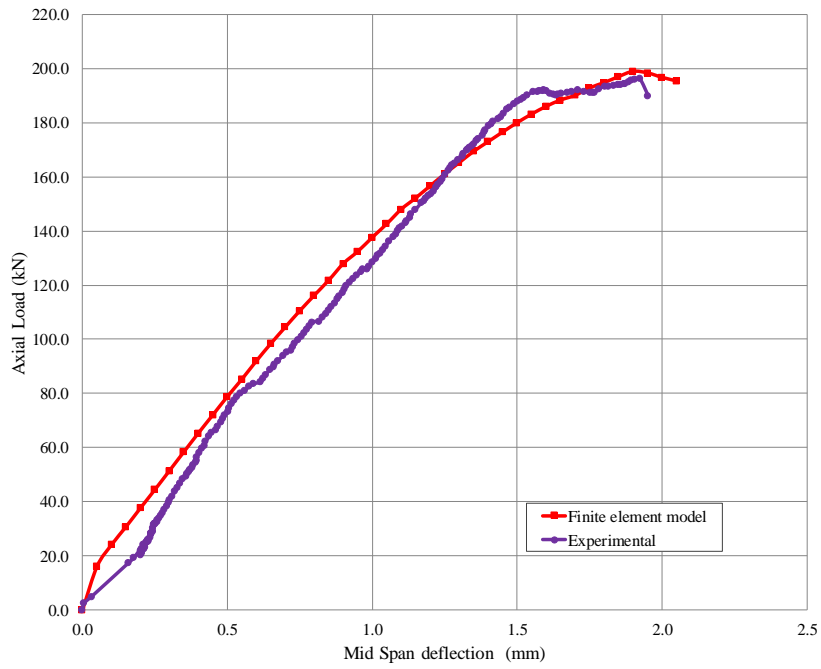


**Figure 10-14: Experimental vs. finite element model for beam BN-HS-CB and FEM-HS-CB**

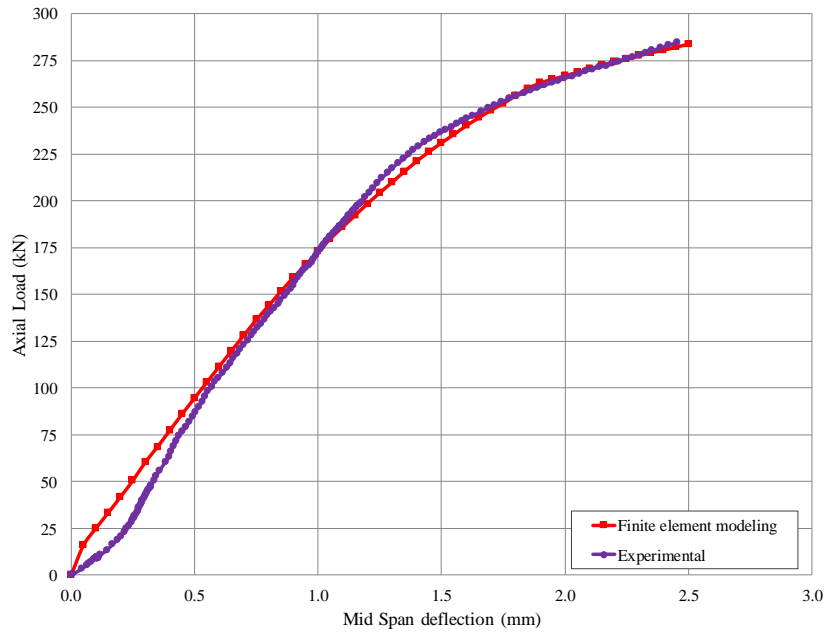


**Figure 10-15: Experimental vs. finite element model for beam BN-HS-3GA-EB and FEM-HS-3GA**



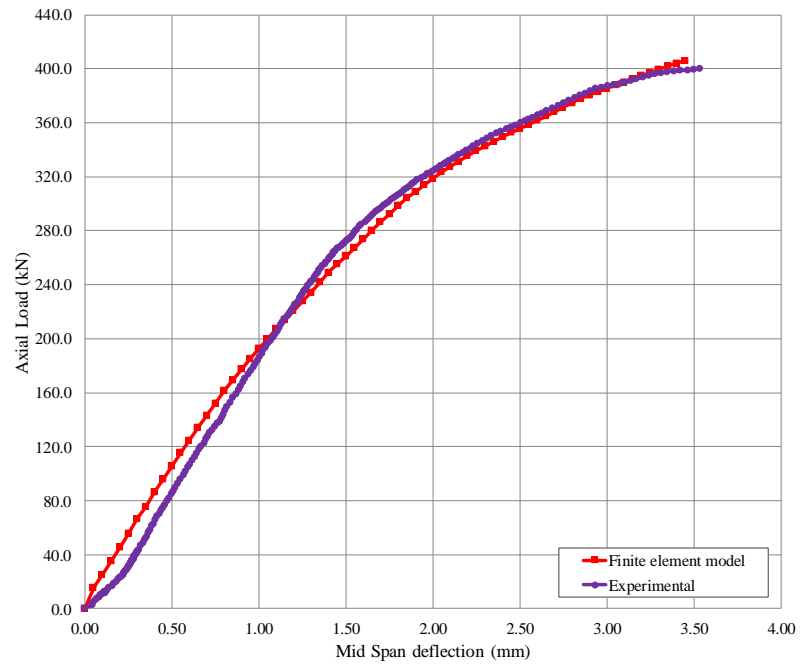


**Figure 10-16: Experimental vs. finite element model for beam BN-HS-5GA-MB and FEM-HS-5GA**

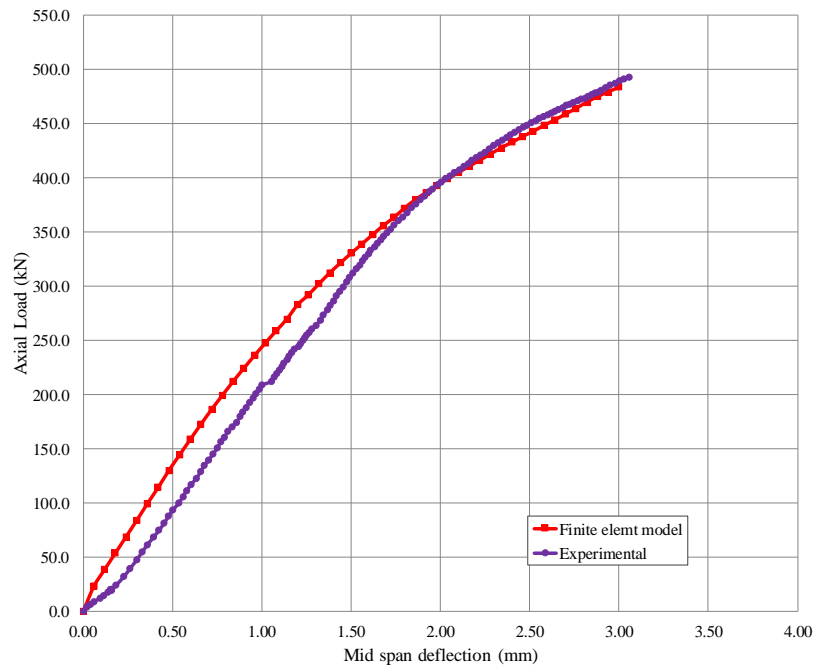


**Figure 10-17: Experimental vs. finite element model for beam BN-HS-5GB-MB and FEM-HS-5GB**

**Table 10-2: Summary of experimental and finite element results**

Finite element model (FEM)	Failure Load (kN)		Percentage Difference	Deflection (mm)		Percentage Difference
	Exp.	FEM		Exp.	FEM	
FEM-LS-CB	122.27	123.70	1.20	1.65	1.67	1.20
FEM-LS-3GA	190.46	195.00	2.40	1.85	2.00	8.10
FEM-LS-5GA	248.53	252.41	1.60	2.34	2.42	3.40
FEM-LS-3CA	221.66	217.50	-1.90	1.90	1.87	-1.60
FEM-LS-5CA	274.7	276.30	0.60	2.10	2.05	-2.40
FEM-HS-CB	196.35	199.10	1.40	1.92	1.90	-1.10
FEM-HS-4GA	284.57	283.50	-0.40	2.45	2.50	2.05
FEM-HS-5GA	400.25	406.16	1.50	3.54	3.45	-2.54
FEM-HS-5GB	493.18	483.95	-1.90	3.06	3.00	-1.96

### 10.6.2 Cracking pattern

The finite element program WCOMD is capable of predicting cracks at every load step. The crack patterns of RC deep beams observed during the experiment and the predicted finite element results are compared in Figures 10-18 to 10-21. A good match between the observed and predicted crack patterns can be seen. Similar to the experimental results, finite element analysis predicts large diagonal shear cracks in the shear span similar to the experiment.

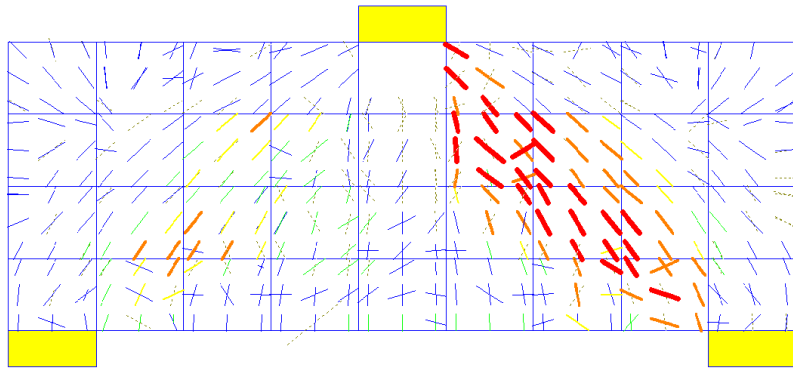


Figure 10-18: Cracking pattern of FEM-LS-CB

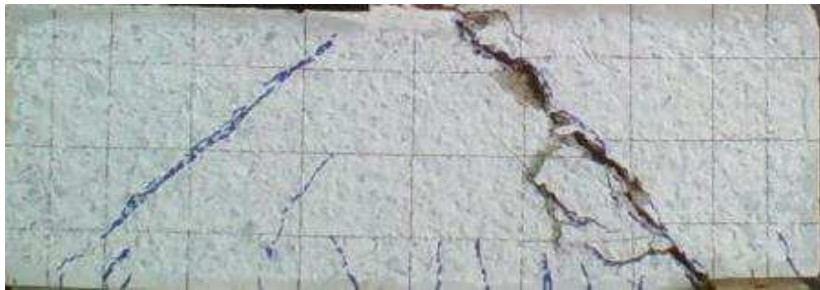


Figure 10-19: Cracking pattern of BN-LS-CB

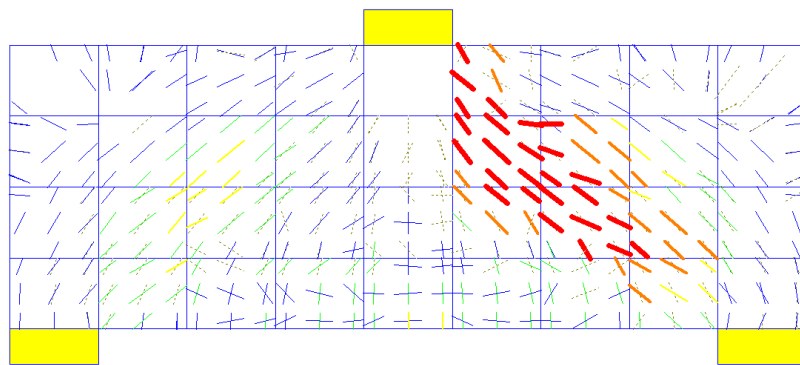


Figure 10-20: Cracking pattern of FEM-HS-CB

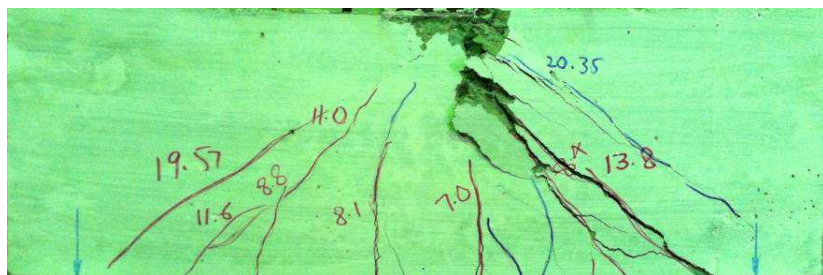


Figure 10-21: Cracking pattern of BN-HS-CB

## **10.7 Discussion on finite element analysis results**

### **10.7.1 Finite element models of un-strengthened low and high strength concrete RC deep beams**

From Table 10-2 and Figures 10-9 to 10-14, it can be seen that finite element models can well predict the ultimate load carrying capacity and mid span deflection of un-strengthened low and high strength RC deep beams, respectively. The ultimate load carrying capacity calculated by the finite element analyses were recorded as 1.20% and 1.40% higher than the measured values for low and high strength beams, respectively. The mid-span deflection of the finite element model FEM-LS-CB was recorded 1.20% higher than the experimental result, whereas the mid span deflection of the finite element model FEM-HS-CB was 1.10% lower than experimental one. A slight difference between the predicted and measured values for both ultimate load and mid span deflections endorse the validity of the finite element models to predict the behavior of un-strengthened RC deep beams.

### **10.7.2 Finite element models for glass SFRP strengthened low strength RC deep beams**

The predicted load versus mid span deflection curves of glass SFRP strengthened RC deep beam models are shown in Figures 10-10 and 10-11 and the results are summarized in Table 10-2. The predicted ultimate load carrying capacities of the finite element models strengthened with glass SFRP were in good agreement with values recorded experimentally. The ultimate load predicted by the finite element models for beams strengthened with 3 mm and 5 mm thick SGFRP was found to be only 2.40% and 1.60% higher than experimentally recorded values, respectively. However, the finite element models of was found to overestimate the mid span deflections. The predicted mid span deflections by the finite element models FEM-LS-3GA and FEM-LS-5GA are found to be 8.10% and 3.40%, respectively, higher than the experimental ones. Although the predicted mid span deflections are slightly higher than the experimentally recorded values, it can be stated that the overall behavior of strengthened specimens can be well simulated by the finite element models.

### 10.7.3 Finite element models for carbon SFRP strengthened low strength RC deep beams

From Table 10-2 and Figures 10-12 and 10-13, it can be seen that the finite element model tended to slightly underestimate the load capacity and mid span deflection of the RC deep beam specimen strengthened with 3 mm thick carbon SFRP. The predicted ultimate load and the mid span deflection of the carbon SFRP strengthened FEM model FEM-LS-3CA were 1.90% and 1.60% lower than those recorded during the experiment. However the finite element slightly overestimates the ultimate load of 5 mm thick carbon SFRP strengthened specimen. The ultimate load was 0.60% higher than the experimental value. Similar to the finite element model FEM-LS-3CA, the predicted mid-span de-flection of the FEM model FEM-LS-5CA was lower than the experimental value, in this case around 2.4%. This difference in the prediction of the ultimate load and deflection is considered to be slight and it can be said that the finite element model can reasonably reproduce the experimental results.

### 10.7.4 Finite element models for glass SFRP strengthened high strength RC deep beams

The comparison of finite element and experimental load versus mid span deflections of high strength RC deep beams strengthened with glass SFRP is illustrated in Figures 10-15 to 10-17. A good comparison can be seen. The ultimate load and mid span deflections can be satisfactorily predicted by the finite element analysis. The ultimate load of the finite element model FEM-HS-5GA was 1.50% higher than the experimental value, whereas only 0.40% and 1.90% decrease in the prediction of the ultimate loads were found for finite element models FEM-HS-4GA and FEM-HS-5GB, respective-ly. The mid span deflection of the model FEM-LS-5GA was only 2.10% higher than the experimentally recorded value, whereas only 2.60% and 1.96% decrease in the prediction of mid span deflection were observed for the finite element models FEM-HS-5GA and FEM-HS-5GB, respectively. Although some small discrepancies were observed between predicted and experimental values, it can be concluded that the presented finite element models are well capable of providing reasonable predictions for glass SFRP strengthened high strength RC deep beams.

### 10.8 Effect of SFRP strips

In the previous section, the finite element analysis was performed for the tested beams and the analytical results were compared with the experimental ones. It can be seen that the present finite element models are capable of efficiently reproduce the load-mid span deflections, crack pattern and the failure modes. In this section, the finite element model has been adopted to further para-metrically examine the behavior of low strength RC deep beams strengthened with various forms SFRP strips.

Extensive research attempts are available to investigate the behavior of RC beams strengthened with externally bonded unidirectional FRP strips for RC beams [64, 65, 95-97]. However, no research activity is found in literature on the behavior of RC deep beams strengthened with SFRP strips. In this finite element analysis, the SFRP strips were applied in both vertical and horizontal directions with different strip widths as shown in Figures 10-22 and 10-25. The finite element models of RC deep beams strengthened with SFRP strips are presented in Figures 10-26 to 10-29. Detailed summary of predicted finite element results is presented in Table 10-3.

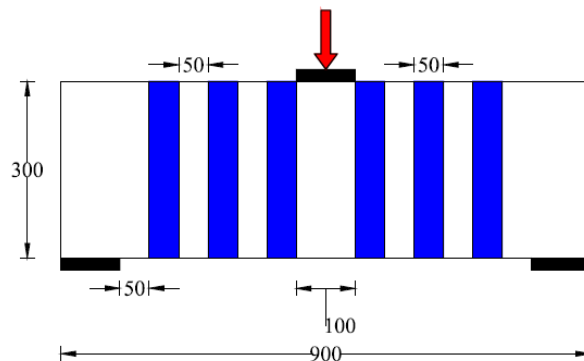


Figure 10-22: Specimen FEM-LS-V01

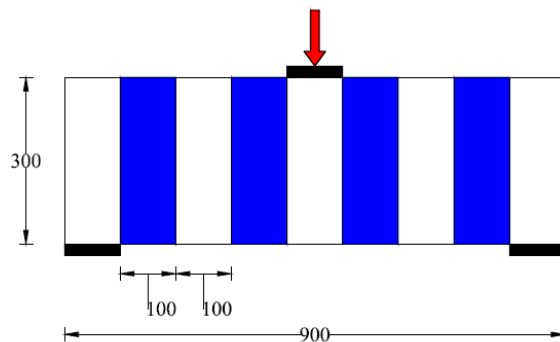


Figure 10-23: Specimen FEM-LS-V02

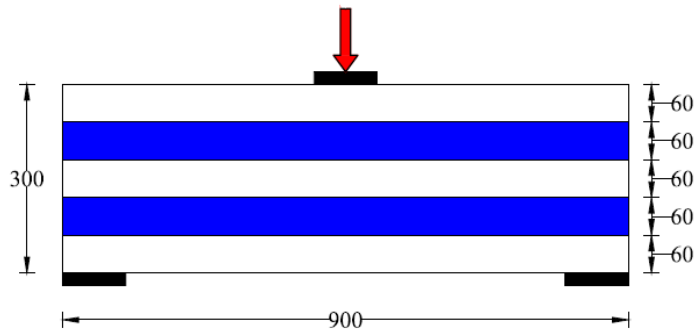


Figure 10-24: Specimen FEM-LS-H01

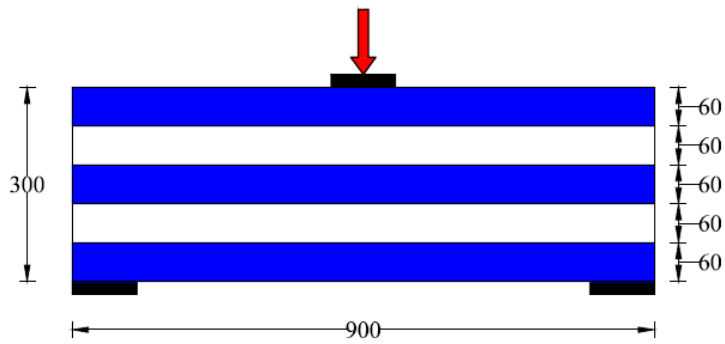
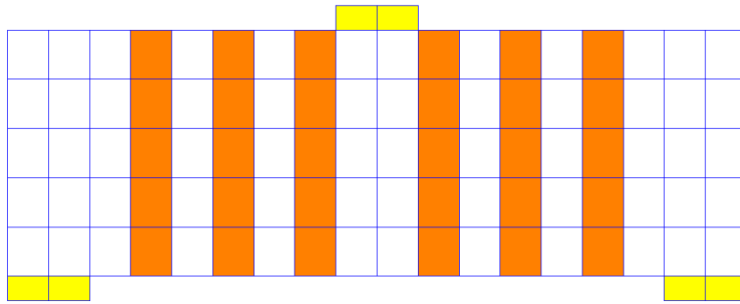


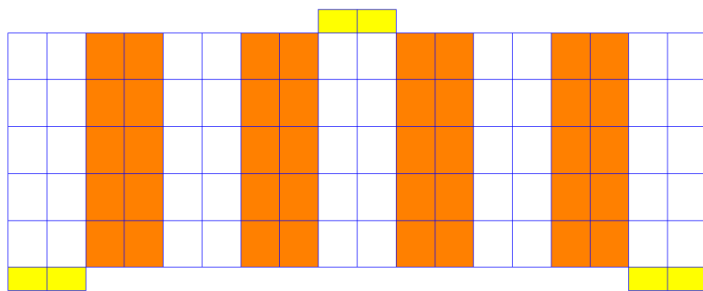
Figure 10-25: Specimen FEM-LS-H02

Table 10-3: Summary of finite element analysis results

Specimen	Failure Load (KN)	Percentage increase	Mid span deflection (mm)	Percentage increase
BN-LS-CB	122.27	-	1.65	-
FEM-LS-V01	143.80	17.60	3.16	91.50
FEM-LS-V02	150.01	22.70	3.16	91.50
FEM-LS-H01	131.77	7.80	1.67	1.21
FEM-LS-H02	144.54	18.20	1.78	7.80



**Figure 10-26: Finite element model FEM-LS-V01**



**Figure 10-27: Finite element model FEM-LS-V02**

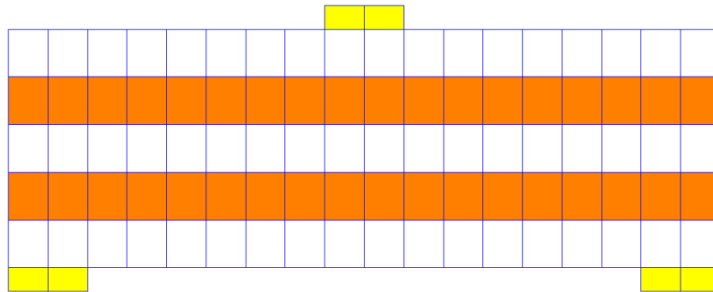


**Figure 10-28: Finite element model FEM-LS-H01**

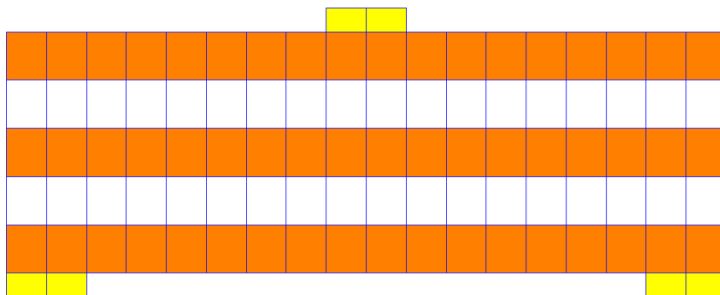


**Figure 10-29: Finite element model FEM-LS-H02**



### 10.8.1 Effect of direction

It has been observed experimentally that externally bonded SFRP are effective to enhance the shear capacity of RC deep beams providing that the SFRP is adequately anchored to the beam surface. Although placing SFRP in strips may pose some strengthening difficulty, however, the application of SFRP in strips may result in a reduced material cost compared with SFRP applied on the full surface of RC beams. The finite element analysis is conducted to examine the influence of the direction of SFRP strips. The comparison of load-mid span deflection of both directions (vertical and horizontal) is shown in Figure 10-30. It can be seen from the analysis results that the vertical SFRP strips are more effective and yields a higher capacity, whereas the beam with horizontal SFRP strips has lower loading capacity and fails by shear failure. This is because the vertical SFRP strips limit the opening of diagonal cracks and finally result in an enhanced shear transfer. The comparison of finite element crack pattern for both SFRP directions is shown in Figures 10-33 and 10-35. In the beam with vertical SFRP strips, the inclined cracks are seen not active in the shear span, whereas in beam with horizontal SFRP strips, the FEM model predicts the inclined cracks concentrated in the shear span. In the beam with vertical SFRP strips, vertical flexure cracks are observed near the mid span instead, indicating the yielding of main flexural steel bars. This demonstrates the efficiency of SFRP vertical strips on the suppression of inclined shear cracks.

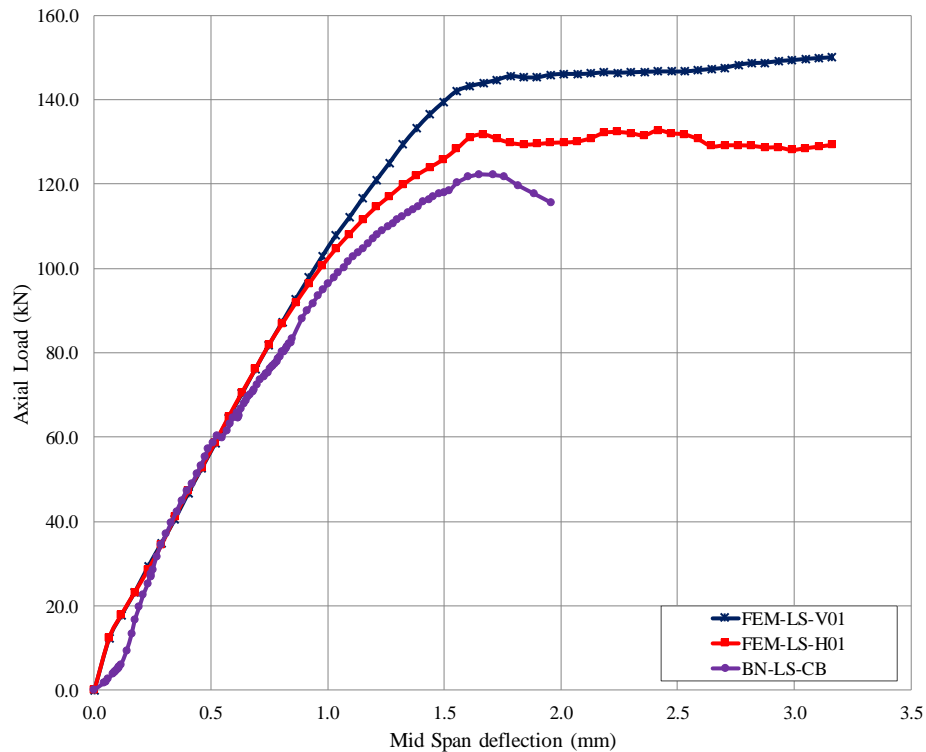


**Figure 10-30: Effect of SFRP strip direction**

### 10.8.2 Effect of vertical SFRP strip width and spacing

This analysis is further conducted to investigate the effect of width of the vertical SFRP strips on the behavior of RC deep beams. The load versus mid span deflection behaviors of both finite element models strengthened with SFRP strips, i.e. FEM-LS-V01 and FEM-LS-V02 along with the control beam are shown in Figure 10-31. A smaller width, but closer spacing of SFRP vertical strips (i.e., model FEM-LS-V01) results in a higher peak load compared with the beam model FEM-LS-V02 with larger strip width but more distant spacing. In Figure 10-31, a 16.60% and 22.70% increase in the ultimate load was found for the finite element models FEM-LS-V01 and FEM-LS-V02, respectively. Since the SFRP strips with smaller widths were more closely spaced over the shear span, thus leaving smaller space for the inclined shear cracks to develop. As a result, inclined shear cracks in the shear span becomes inactive, promoting the development of flexural cracks at the mid span with the higher ultimate load instead (Figure 144). As for the beam model FEM-LS-V02, the space between adjacent strips is larger, allowing the development of some inclined cracks together with the flexural cracks at the mid span (Figure 145). The mid span deflection of both

beams was found to be similar. A 91.50 % increase in the mid span deflection was recorded with both widths of SFRP strips.

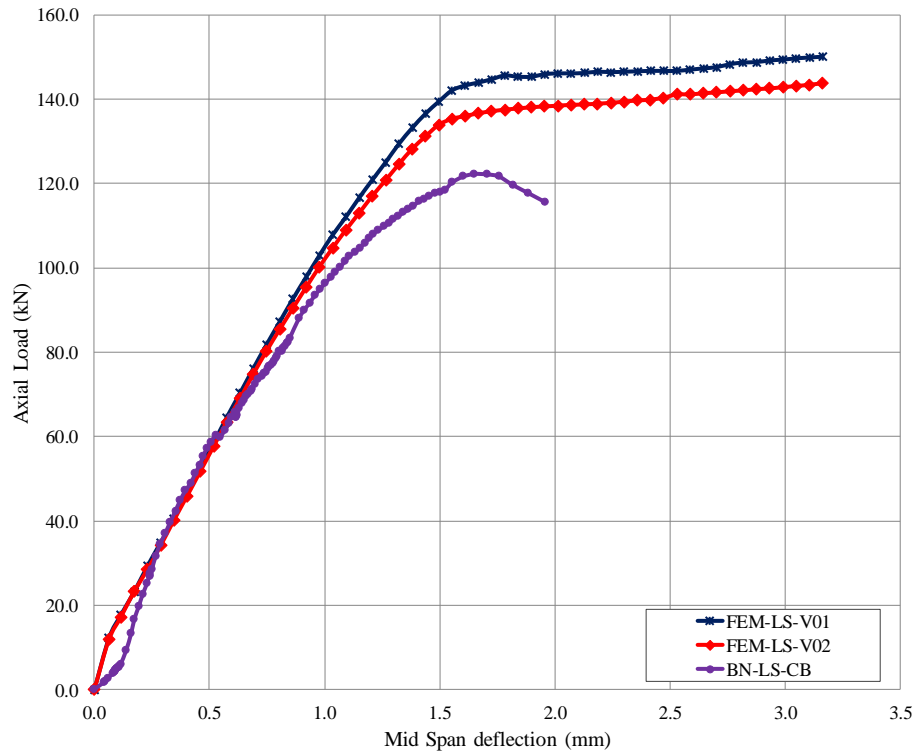


**Figure 10-31: Effect of SFRP strip width and spacing**

### 10.8.3 Effect of position of horizontal SFRP strips

The finite element analysis is also performed to investigate the effect of position of horizontal SFRP strips. Unlike vertical strips, here the width of horizontal SFRP strips was kept constant, but the position was changed and one more strip was added as shown in Figure 10-33. The load versus mid span deflection curves of both beams i.e. FEM-LS-H01 and FEM-LS-H02 are shown in Figure 10-34 along with the control beam BN-LS-CB. It can be observed that the beam FEM-LS-H01 with two horizontal strips results in a lower load carrying capacity than the beam FEM-LS-H02 with three SFRP strips. In Figure 10-34, 7.80% and 18.20% increase in the ultimate load over the control beam were observed for finite element models with two and three SFRP strips, respectively. This result indicates that the area near the centroid of the cross section is essential for the development of inclined shear cracks. In the beam model FEM-LS-H02, this area is covered by the central strip, thus disabling the propagation of shear cracks in this area. As a result, the increase in the ultimate is higher than beam model FEM-LS-H01 where there is no horizontal SFRP strip covering this area.

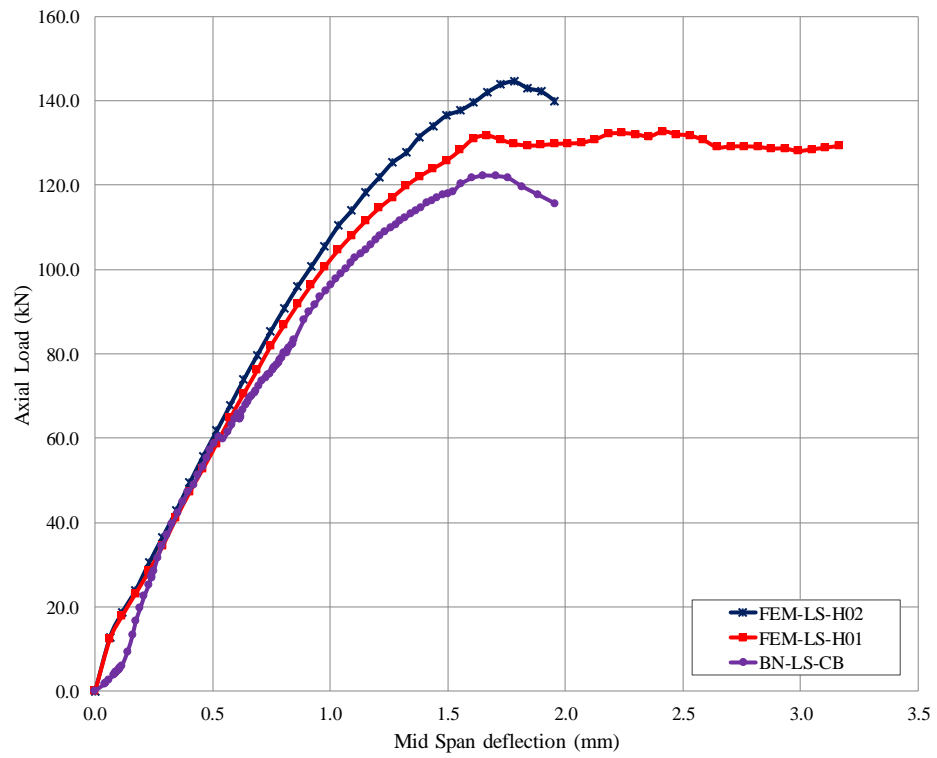


**Figure 10-32: Effect of SFRP strip position**

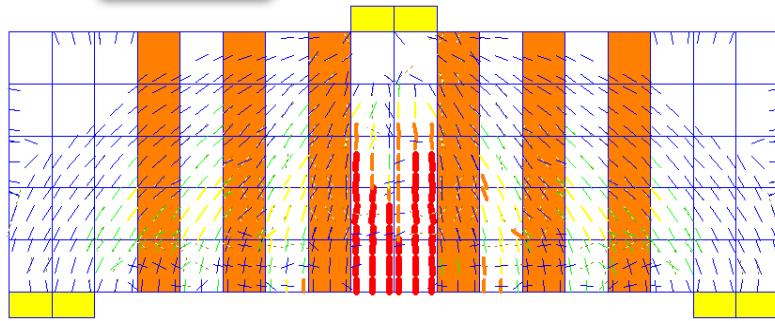


Figure 10-33: Cracking pattern of FEM-LS-V01

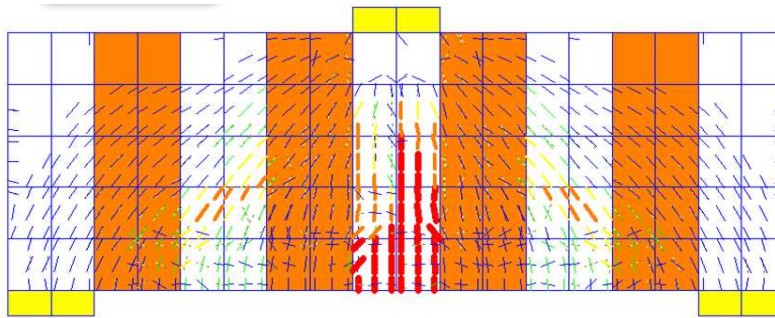


Figure 10-34: Cracking pattern of FEM-LS-V02

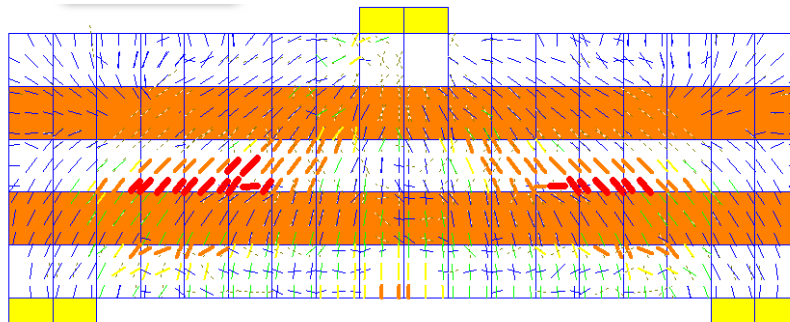


Figure 10-35: Cracking pattern of FEM-LS-H01

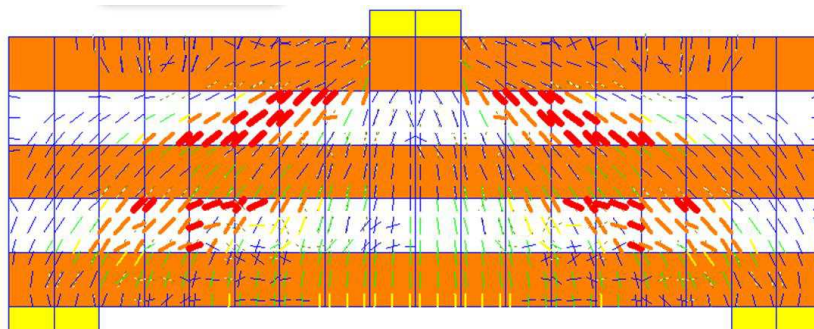


Figure 10-36: Finite element model FEM-LS-H02

## **Chapter 11**

### **Analytical Analysis of SFRP Strengthened RC Deep Beams with openings**

#### **11.1 Introduction**

Chapter 11 is primarily focused on the development of nonlinear finite element analysis for RC deep beams with web openings strengthened using externally bonded SFRP. In the first step, the predicted finite element analysis results were compared with experimental results. Further, the finite element models were utilized to investigate the behavior of RC deep beams with openings, located at different locations and results are compared with RC deep beam without opening.

#### **11.2 Finite element modeling**

Finite element analysis on SFRP strengthened RC deep beams with web openings (experimental program as presented in Chapter 9) is performed by using a computer software WCOMD (WCOMD, 1998). In the first step, the predicted finite element analysis results were compared with experimental results. Then, the finite element models were utilized to investigate the behavior of RC deep beams with openings, located at different locations and results are compared with RC deep beam without opening. A summary of beam specimens, selected from experimental study, for the finite element study is provided in Table 11-1. The RC deep beams are modeled using two dimensional eight-node reinforced concrete planer elements. The smeared cracking approach has been assumed in the modeling of concrete and steel. The SFRP is modeled by planar elements with elastic brittle properties. Since, no de-bonding of SFRP was occurred in RC deep beams with openings strengthened using SFRP, and anchored with MB bolts (Chapter 9), therefore in finite element analysis SFRP are modeled assuming perfect bonding between SFRP and concrete. The constitute laws of concrete and steel bars, used in finite element analysis are discussed in chapter 10 (Section 10.3-10.5).

**Table 11-1: Summary of experimental program and finite element models**

Group	Beam	Finite element model
A	Control LS-S18	FEM-Con- LS-S18
	LS-3B-S18	FEM-LS-3B-S18
	LS-5A-S18	FEM-LS-5A-S18
	LS-5B-S18	FEM-LS-5B-S18
B	Control LS-S12	FEM-Con-LS-S12
	LS-3A-S12	FEM-LS-3A-S12
	LS-5A-S12	FEM-LS-5A-S12
	LS-5B-S12	FEM-LS-5B-S12
	LS-5C-S12	FEM-LS-5C-S12
C	Control LS-C16	FEM-Con-LS-C16
	LS-3A-C16	FEM-LS-3A-C16
	LS-5A-C16	FEM-LS-5A-C16
	LS-5B-C16	FEM-LS-5B-C16
	LS-5C-C16	FEM-LS-5C-C16
D	Control LS-C10	FEM-Con-LS-C10
	LS-3A-C10	FEM-LS-3A-C10
	LS-5A-C10	FEM-LS-5A-C10
	LS-5B-C10	FEM-LS-5B-C10
	LS-5C-C10	FEM-LS-5C-C10
E	Control HS-S18	FEM-Con-HS-S18
	HS-3A-S18	FEM-HS-3A-S18
	HS-5A-S18	FEM-HS-5A-S18
	HS-5B-S18	FEM-HS-5B-S18
	HS-5C-S18	FEM-HS-5C-S18
F	Control HS-S12	FEM-Con-HS-S12
	HS-3A-S12	FEM-HS-3A-S12
	HS-5A-S12	FEM-HS-5A-S12

### 11.3 Finite element simulation of test results

The finite element mesh of the RC deep beams with openings is shown in Figures 11-1 to 11-12. The steel plates at the support and loading location were modelled as elastic elements with high stiffness in the finite element model. Support nodes were assigned restraint against vertical movement, whereas loading node was assigned restraint both against vertical and horizontal movement. The finite element analysis results are further discussed in detail in the next section.

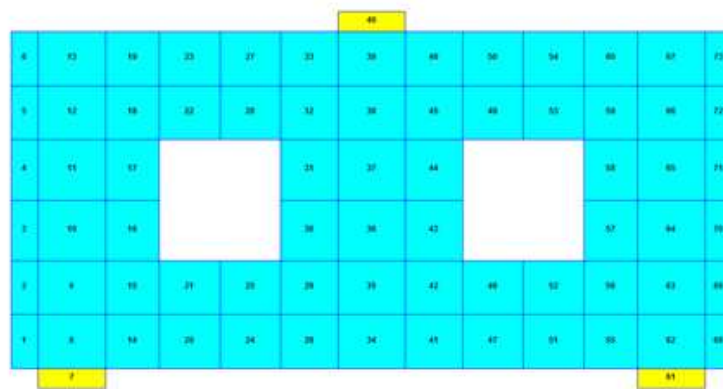


Figure 11-1: FEM-Con-LS-S18 and FEM-Con-HS-S18

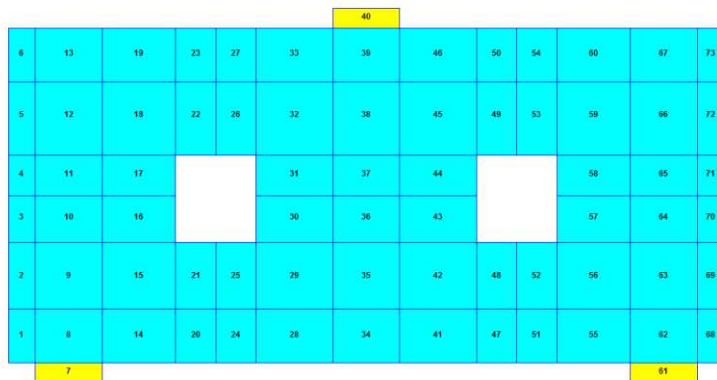


Figure 11-2: FEM-Con-LS-S12 and FEM-Con-HS-S12



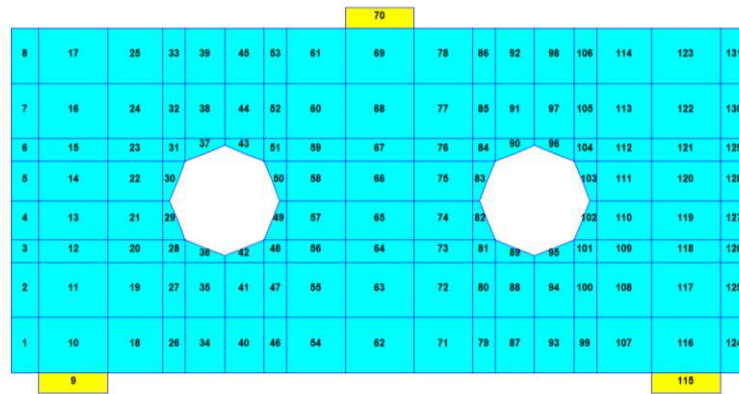


Figure 11-3: FEM-Con-LS-C16

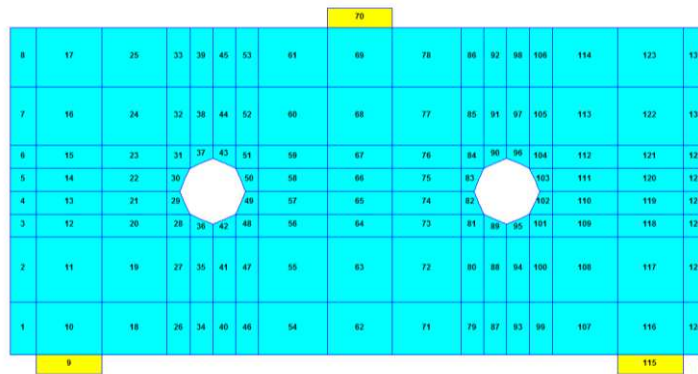


Figure 11-4: FEM-Con-LS-C10



Figure 11-5: FEM-LS-5A-S18, FEM-HS-3A-S18 and FEM-HS-5A-S18

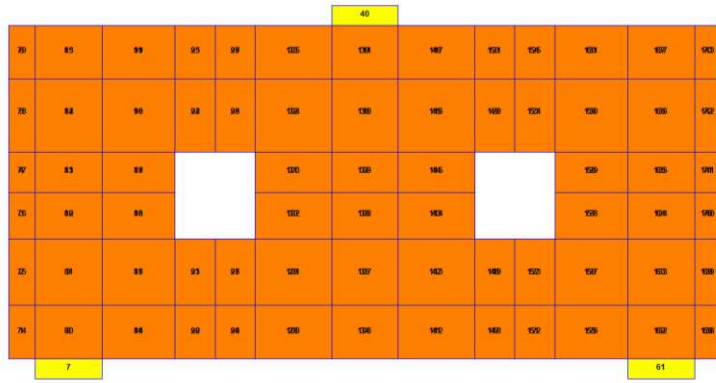


Figure 11-6: FEM-LS-3A-S12, FEM-LS-5A-S12, FEM-HS-3A-S12 and FEM-HS-5A-S12

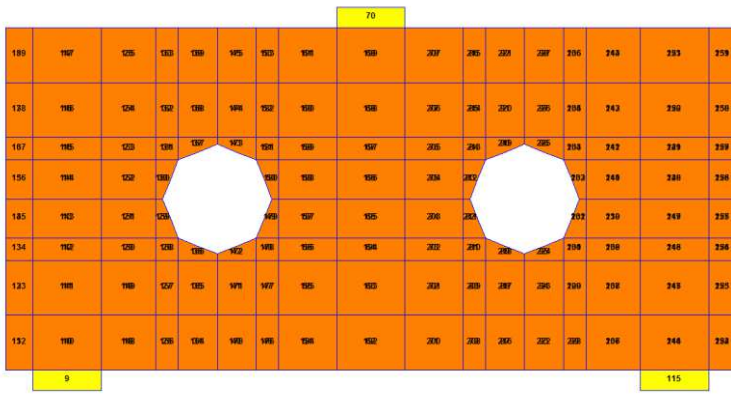


Figure 11-7: FEM-LS-3A-S12 and FEM-LS-5A-S12

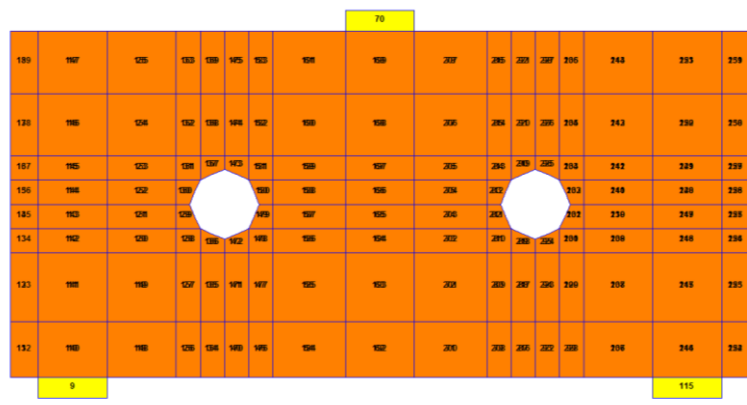


Figure 11-8: FEM-LS-3A-C10, FEM-LS-5A-C10

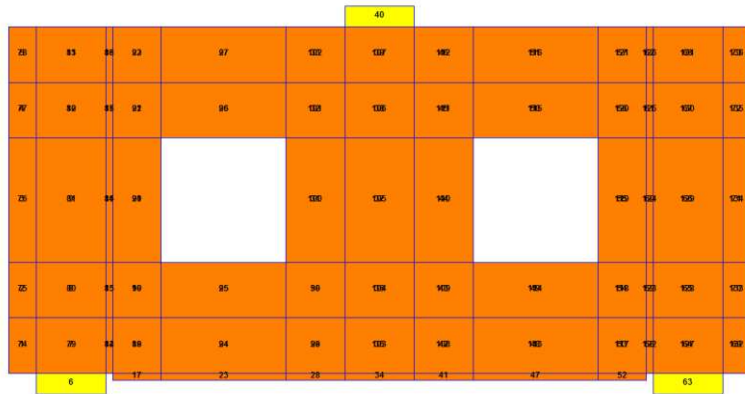


Figure 11-9: FEM-LS-5B-S18 and FEM-HS-5B-S18

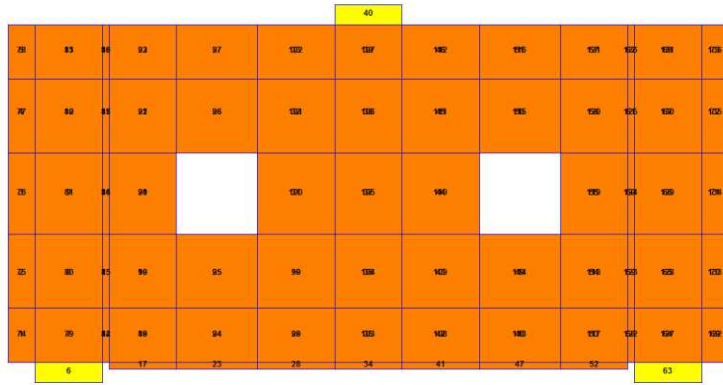


Figure 11-10: FEM-LS-5B-S12

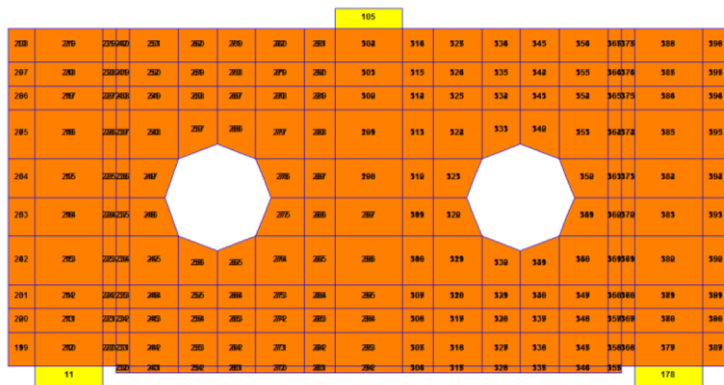


Figure 11-11: FEM-LS-5B-S12

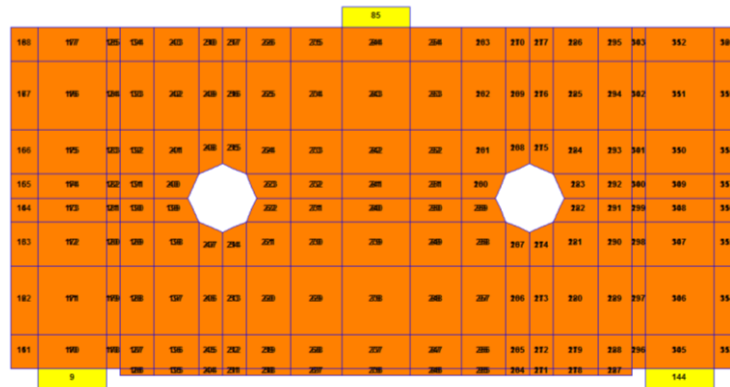


Figure 11-12: FEM-LS-5B-S12

### 11.3.1 Load capacity and deflection behavior

The predicted load versus mid span deflection curves compared with experimental results (Figures 11-13 to 11-39) of selected beam specimens. A detailed summary of predicted finite element results along with the experimental values is presented in Table 11-2. It can be seen that there is an excellent agreement between the experimental and finite element results until failure. The finite element models can accurately predict the behavior of un-strengthened and SGFRP strengthened RC deep beams. The predicted load versus mid span deflection curves are also found to be in good agreement, both for low and high strength concrete RC deep beams with openings. The finite element models are also capable of predicting the increase in the ultimate load carrying capacity of SFRP strengthened RC deep beams with an increase in SGFRP thickness for both circular and square openings. This clearly validates the accuracy and reliability of finite element models.

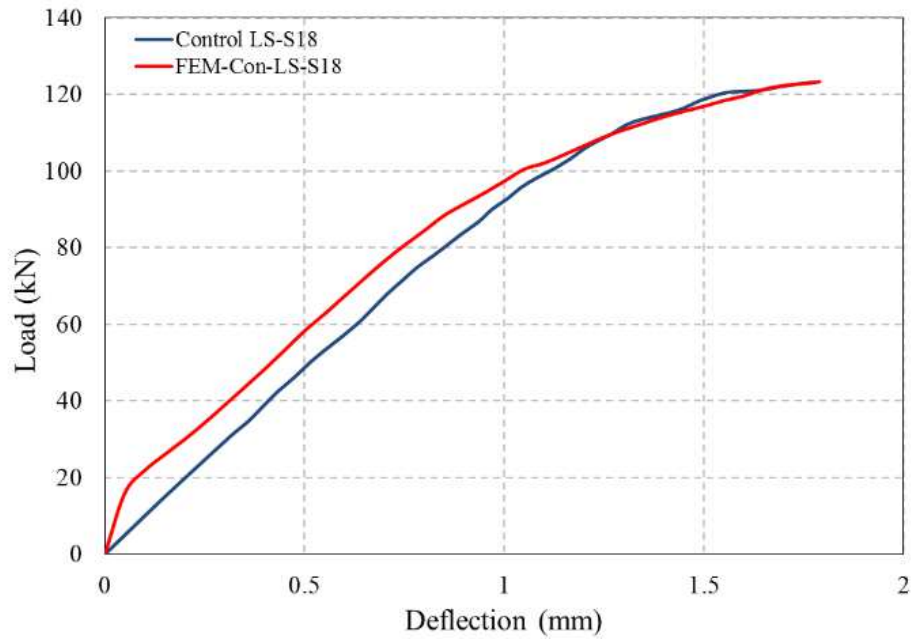


Figure 11-13: Control LS-S18 vs. FEM-Con- LS-S18

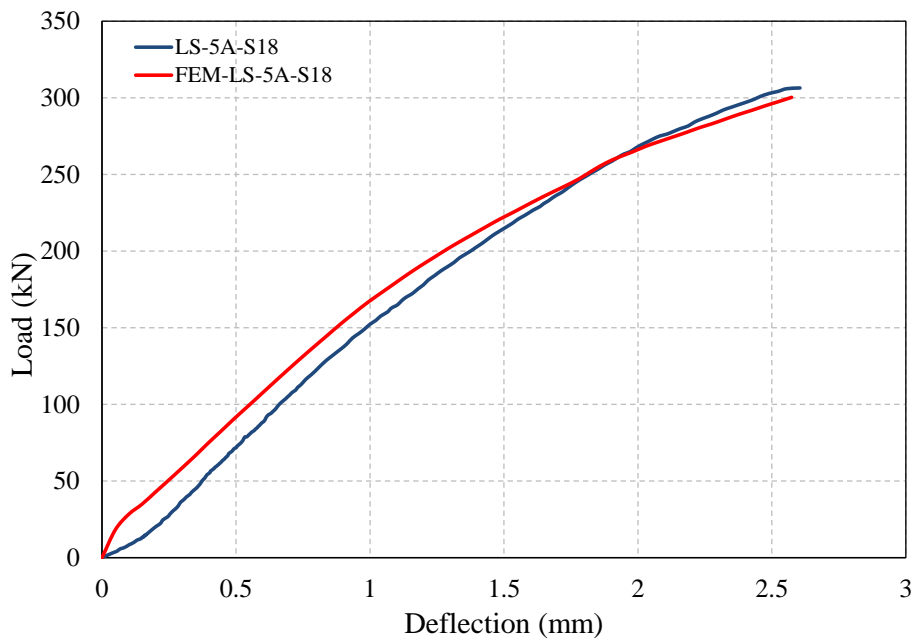


Figure 11-14: LS-5A-S18 vs. FEM-LS-5A-S18

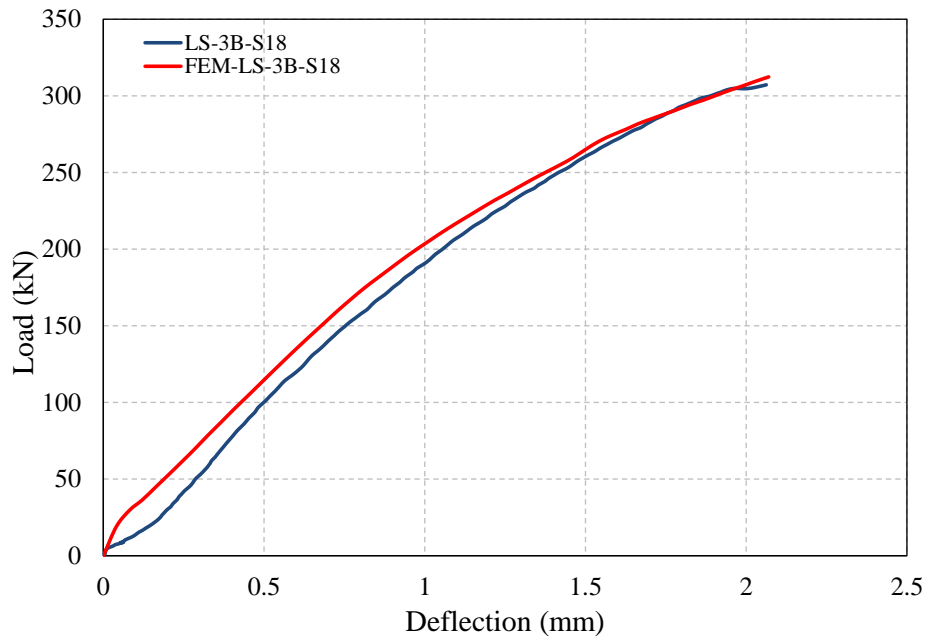


Figure 11-15: LS-3B-S18 vs. FEM-LS-3B-S18

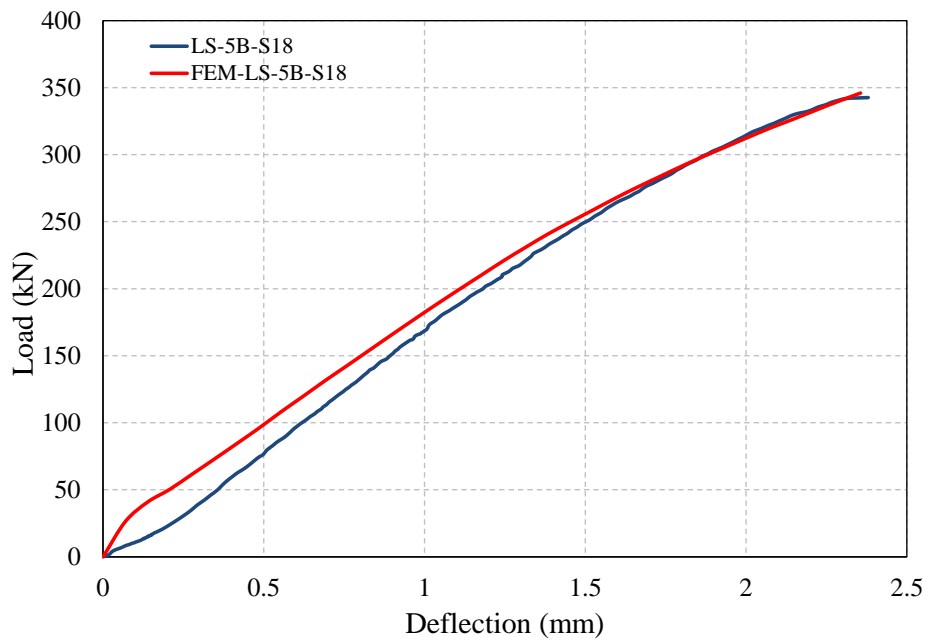


Figure 11-16: LS-5B-S18 vs. FEM-LS-5B-S18

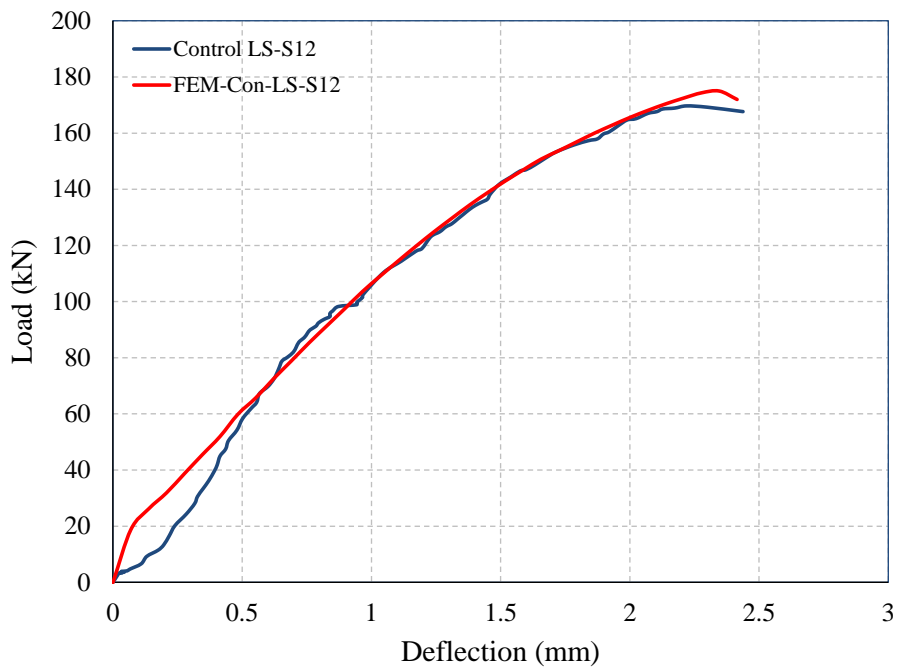


Figure 11-17: Control LS-S12 vs. FEM-Con-LS-S12

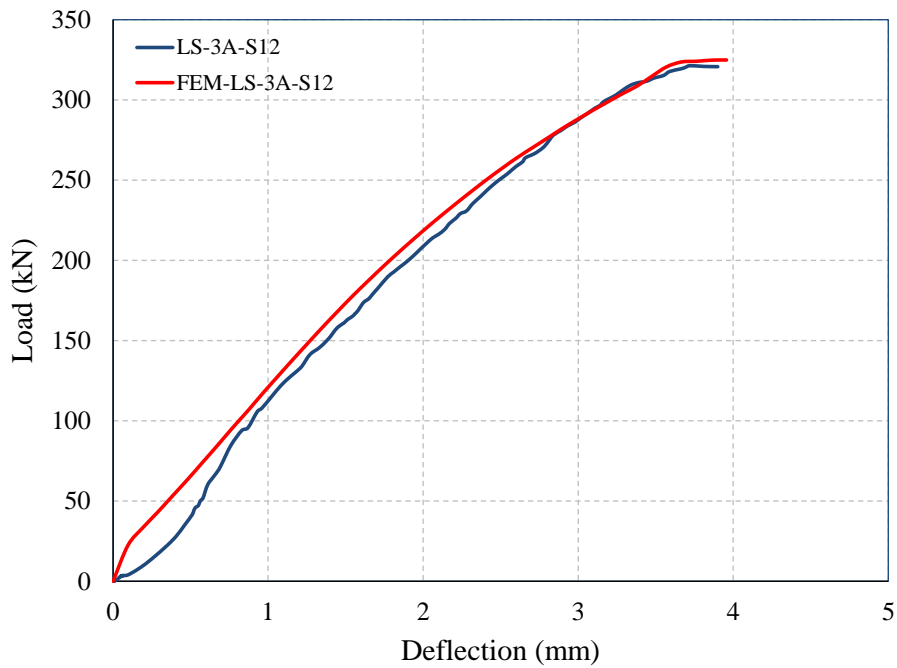


Figure 11-18: LS-3A-S12 vs. FEM-LS-3A-S12

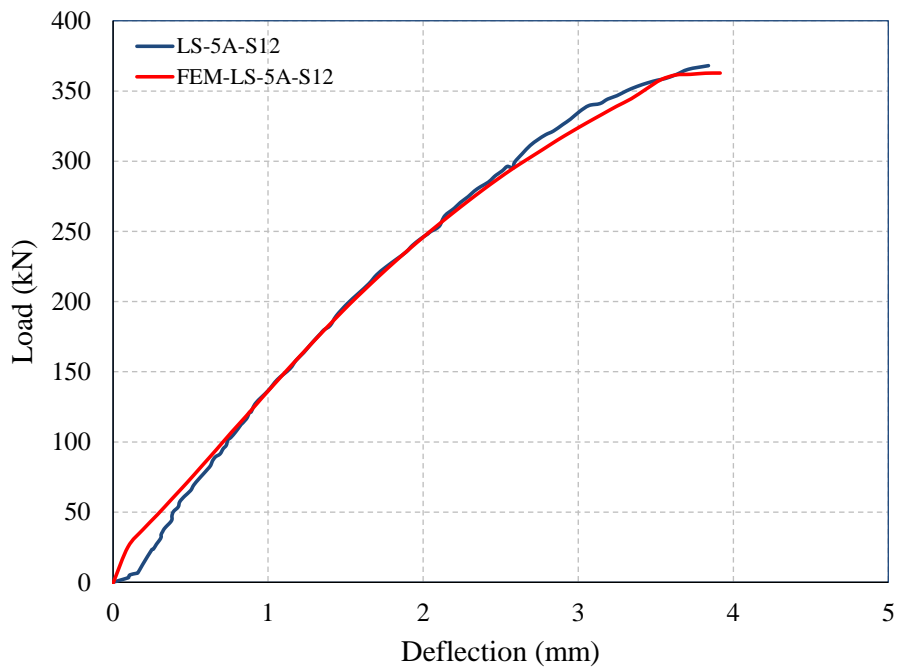


Figure 11-19: LS-5A-S12 vs. FEM-LS-5A-S12

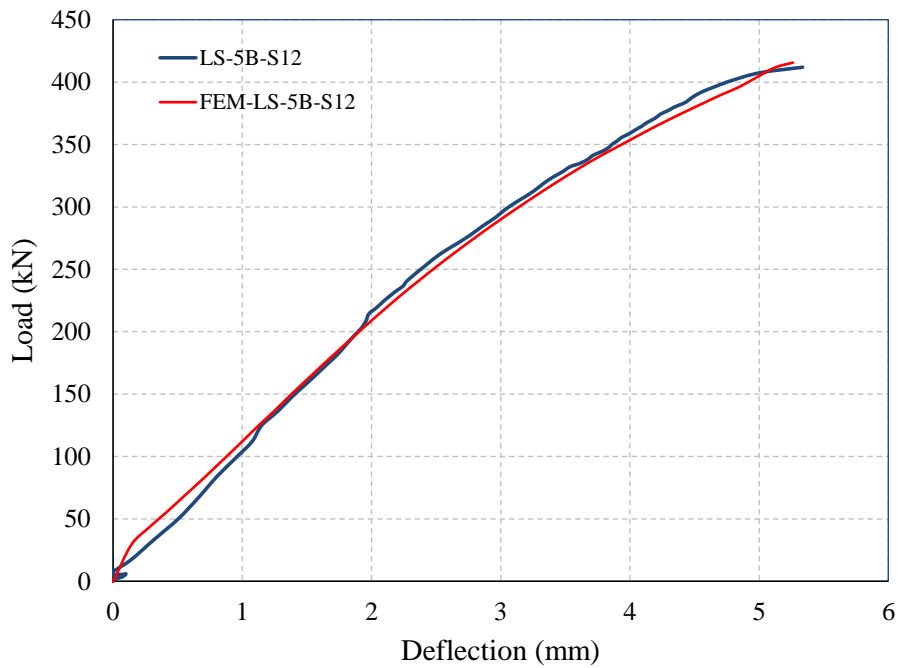


Figure 11-20: LS-5B-S12 vs. FEM-LS-5B-S12



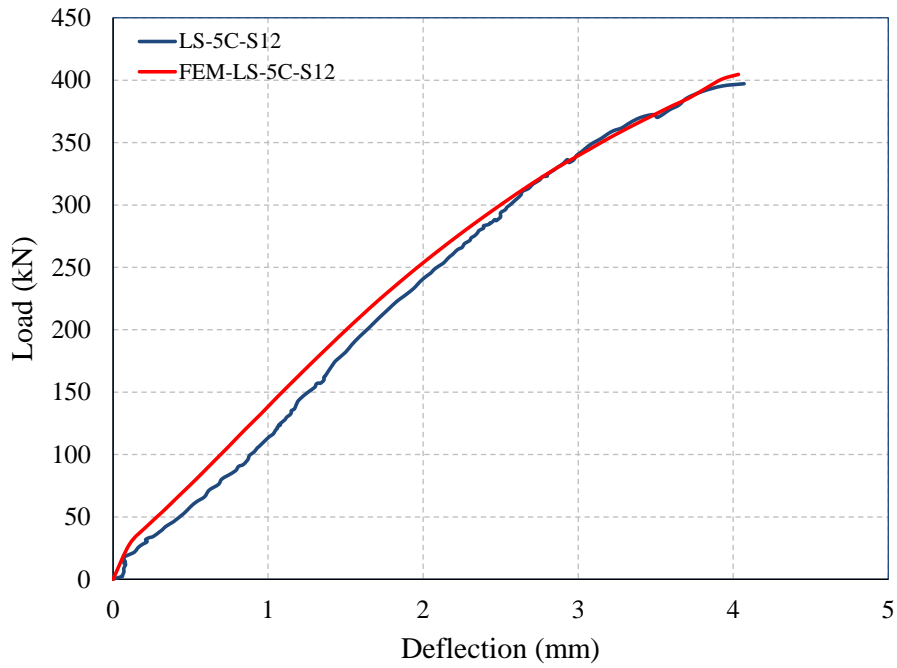


Figure 11-21: LS-5C-S12 vs. FEM-LS-5C-S12

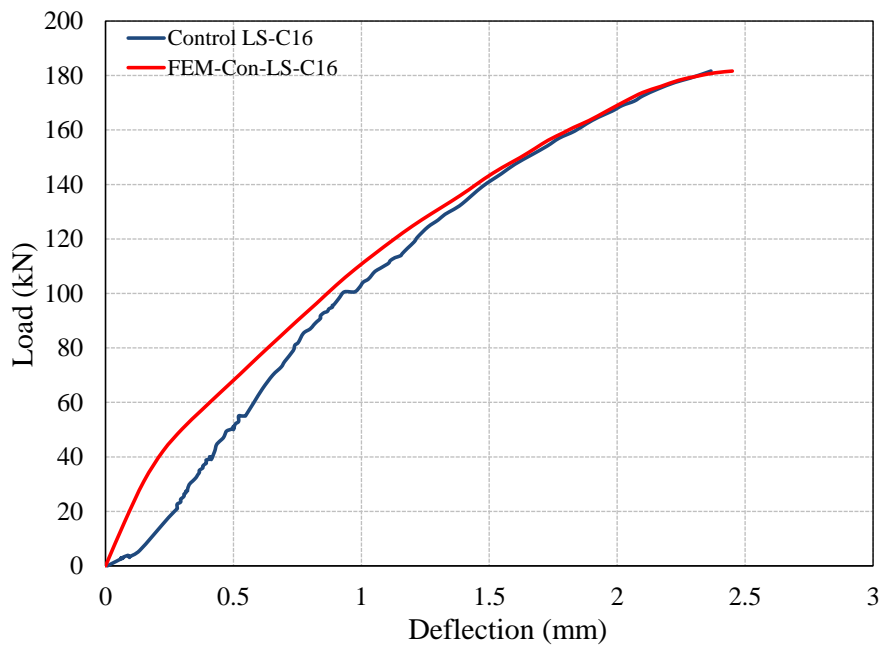


Figure 11-22: Control LS-C16 vs. FEM-Con-LS-C16

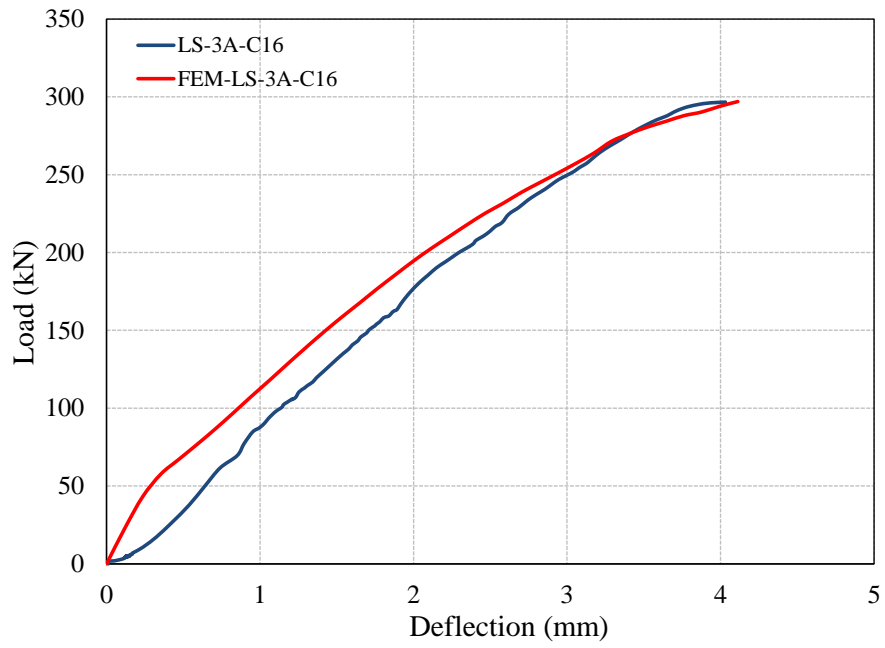


Figure 11-23: LS-3A-C16 vs. FEM-LS-3A-C16

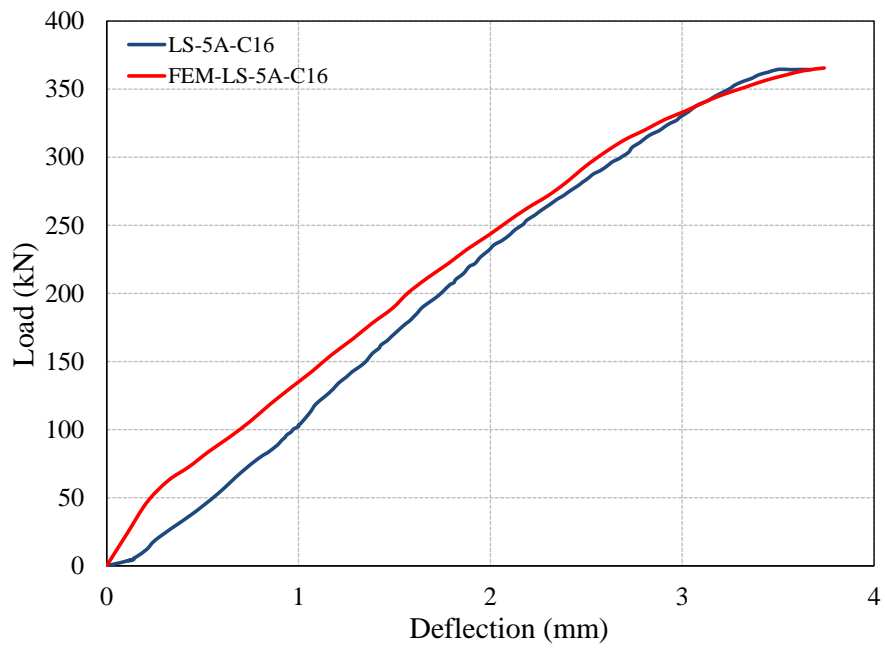


Figure 11-24: LS-5A-C16 vs. FEM-LS-5A-C16

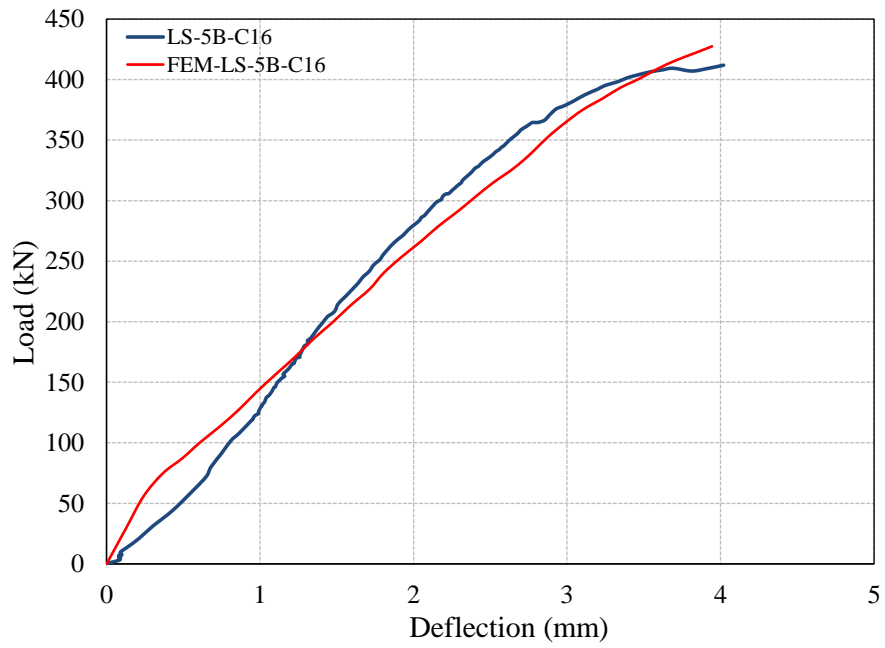


Figure 11-25: LS-5B-C16 vs. FEM-LS-5B-C16

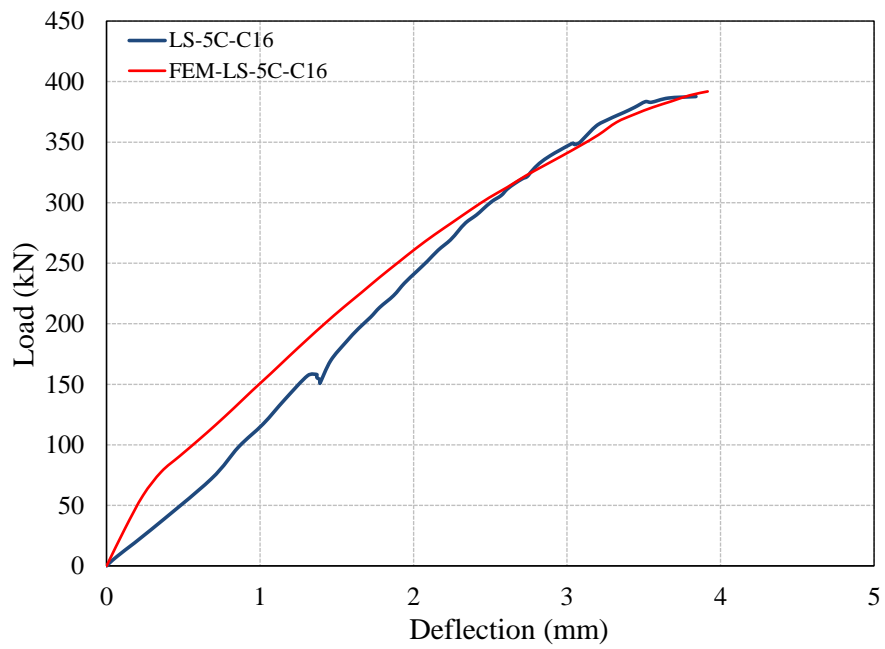


Figure 11.26: LS-5C-C16 vs. FEM-LS-5C-C16

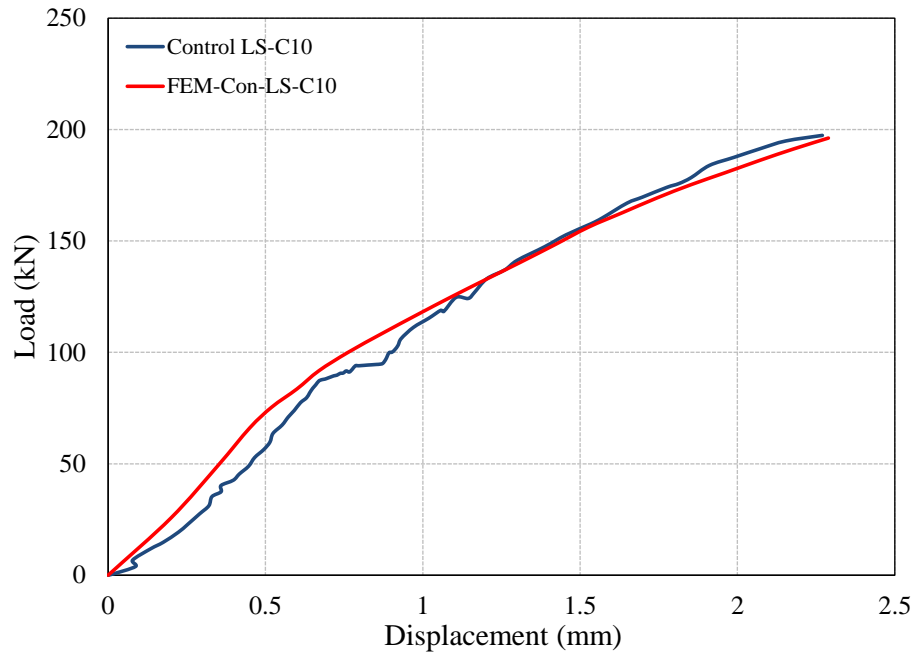


Figure 11-27: Control LS-C10 vs. FEM-Con-LS-C10

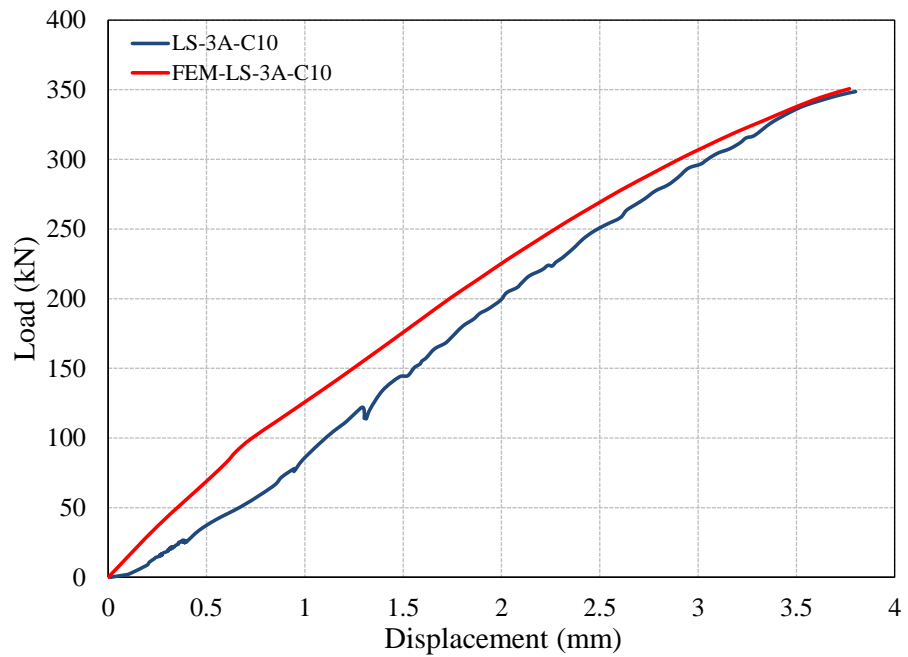
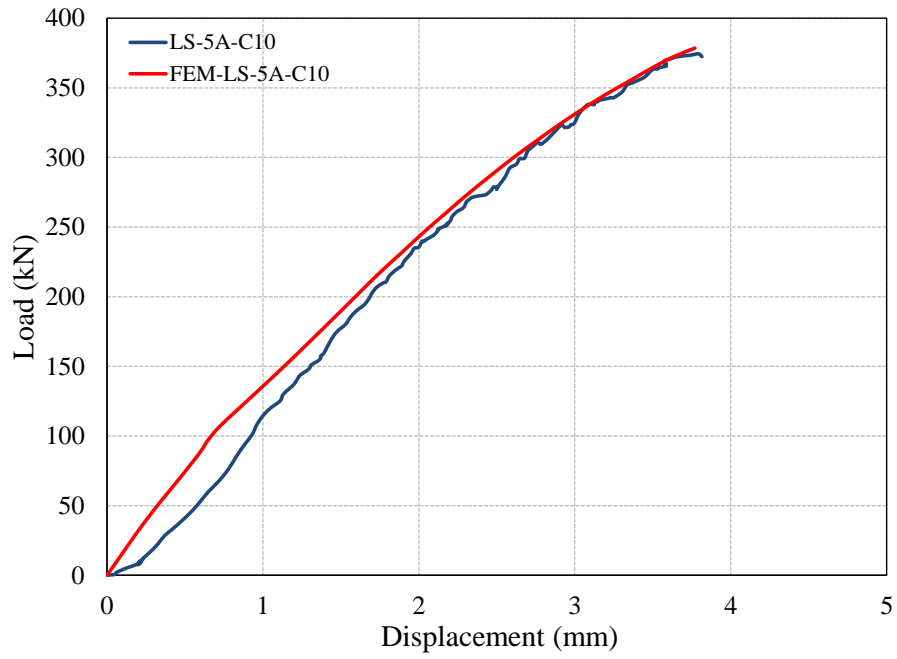
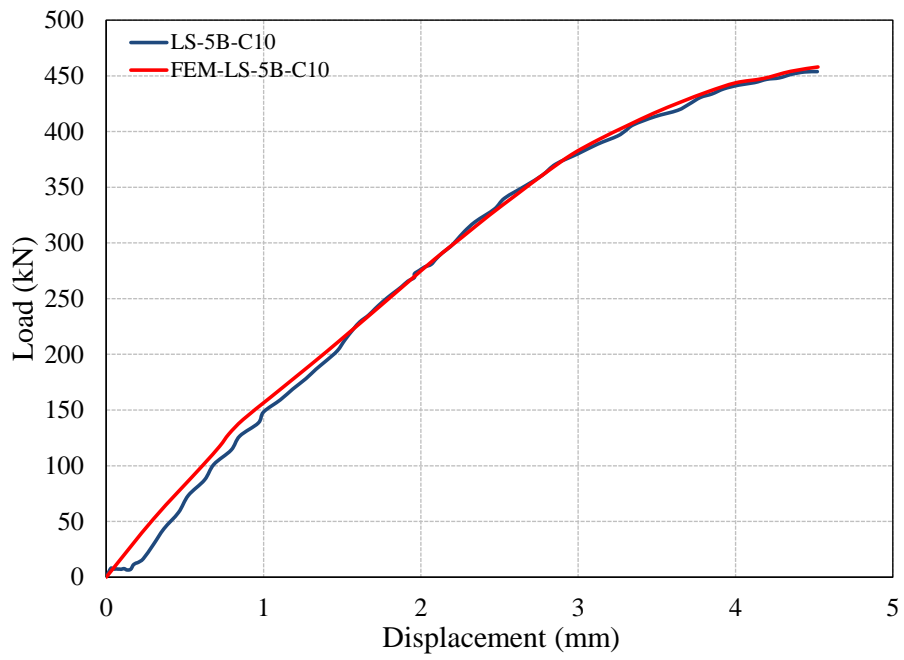


Figure 11-28: LS-3A-C10 vs. FEM-LS-3A-C10



**Figure 11-29: LS-5A-C10 vs. FEM-LS-5A-C10**



**Figure 11-30: LS-5B-C10 vs. FEM-LS-5B-C10**

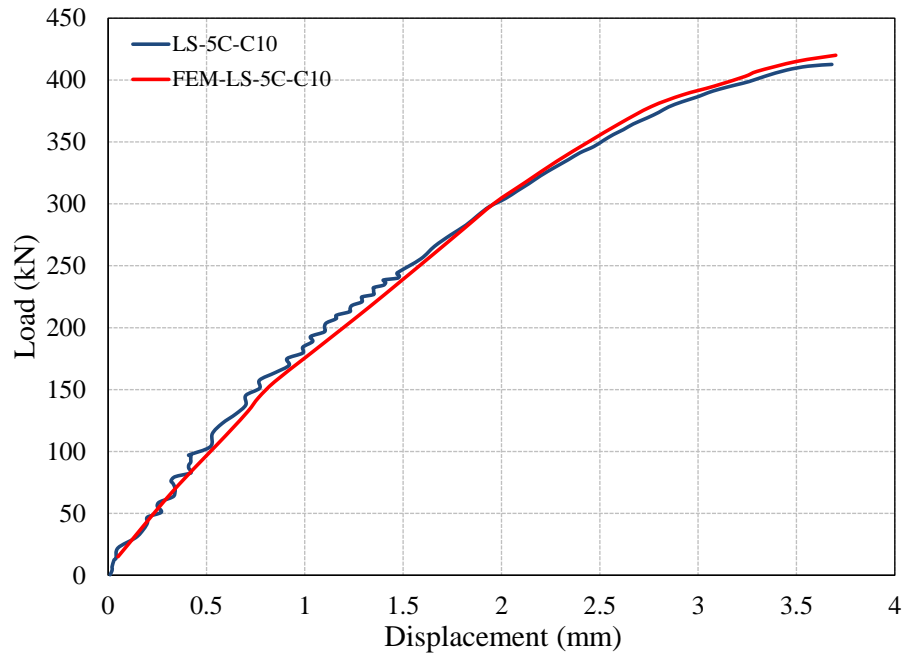


Figure 11-31: LS-5C-C10 vs. FEM-LS-5C-C10

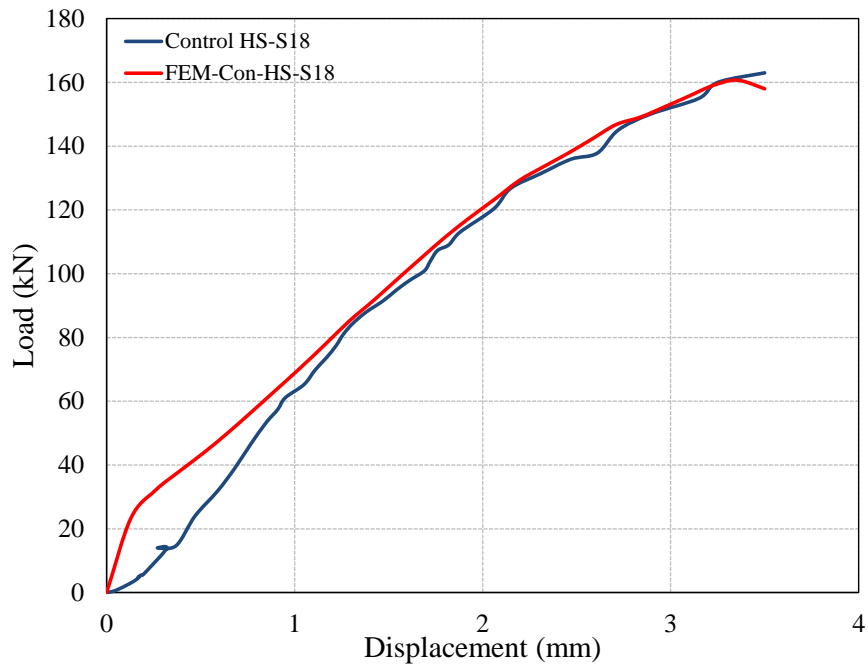
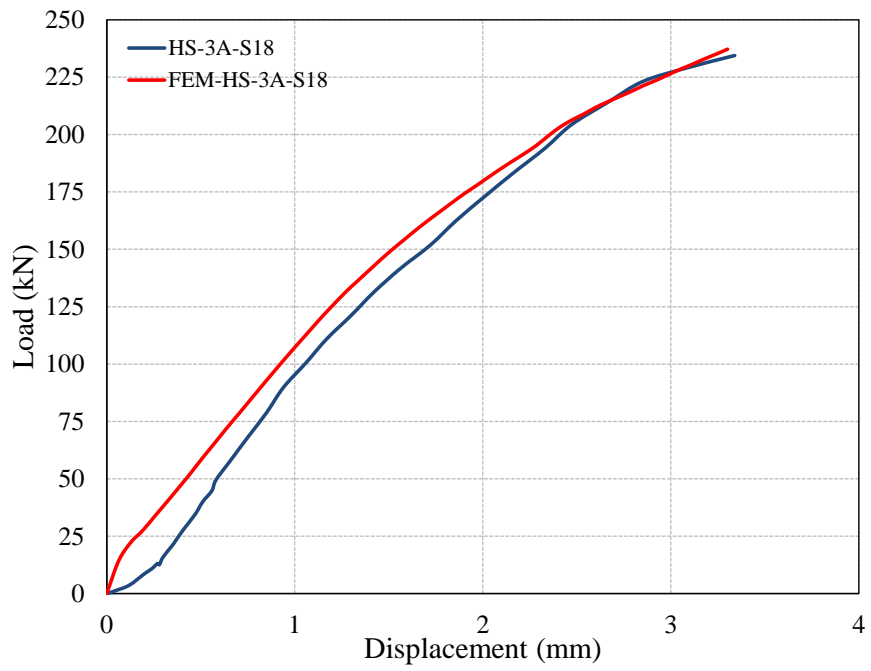
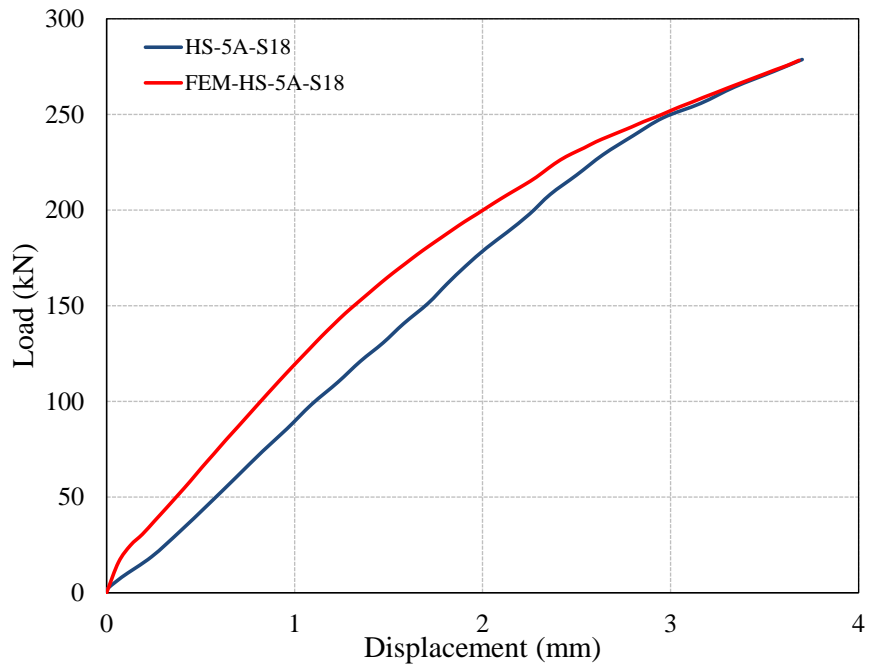


Figure 11-32: Control HS-S18 vs. FEM-Con-HS-S18



**Figure 11-33: HS-3A-S18 vs. FEM-HS-3A-S18**



**Figure 11-34: HS-5A-S18 vs. FEM-HS-5A-S18**

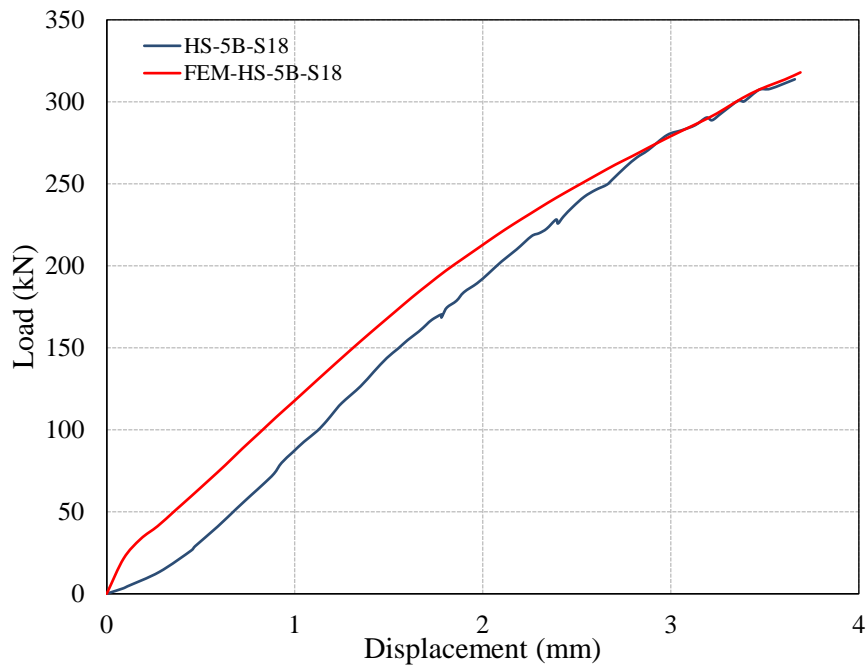


Figure 11-35: HS-5B-S18 vs. FEM-HS-5B-S18

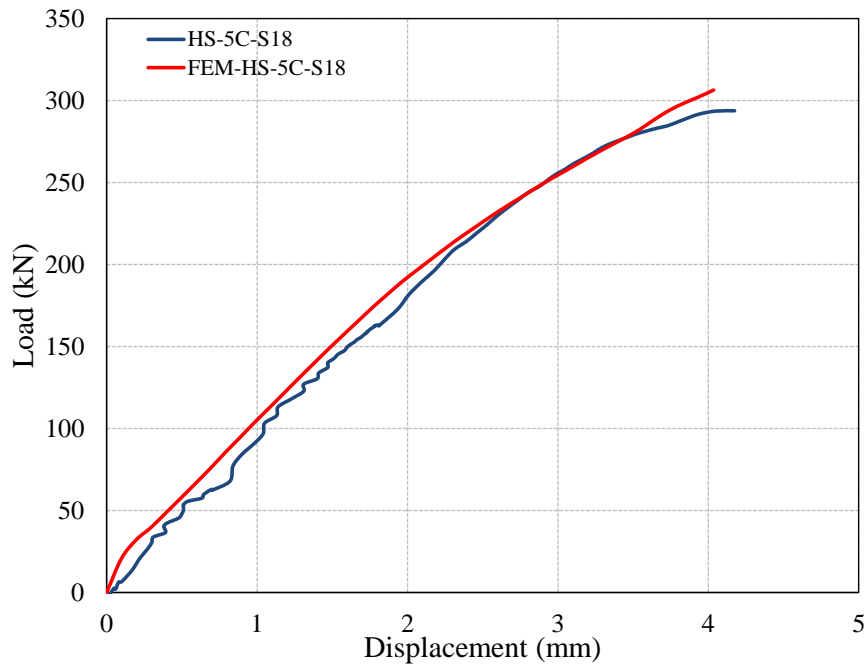


Figure 11-36: HS-5C-S12 vs. FEM-HS-5C-S12



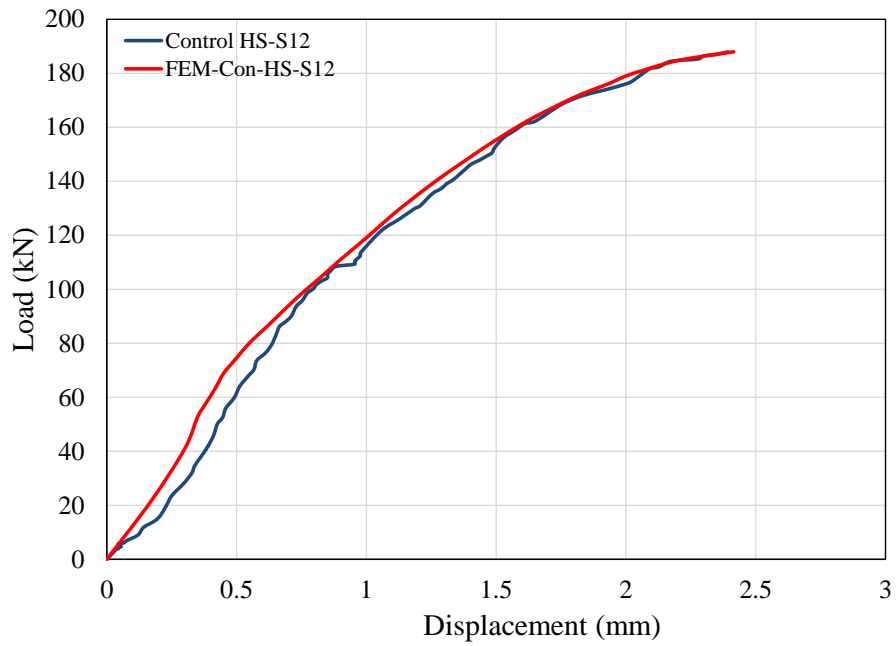


Figure 11-37: Control HS-S12 vs. FEM-Con-HS-S12

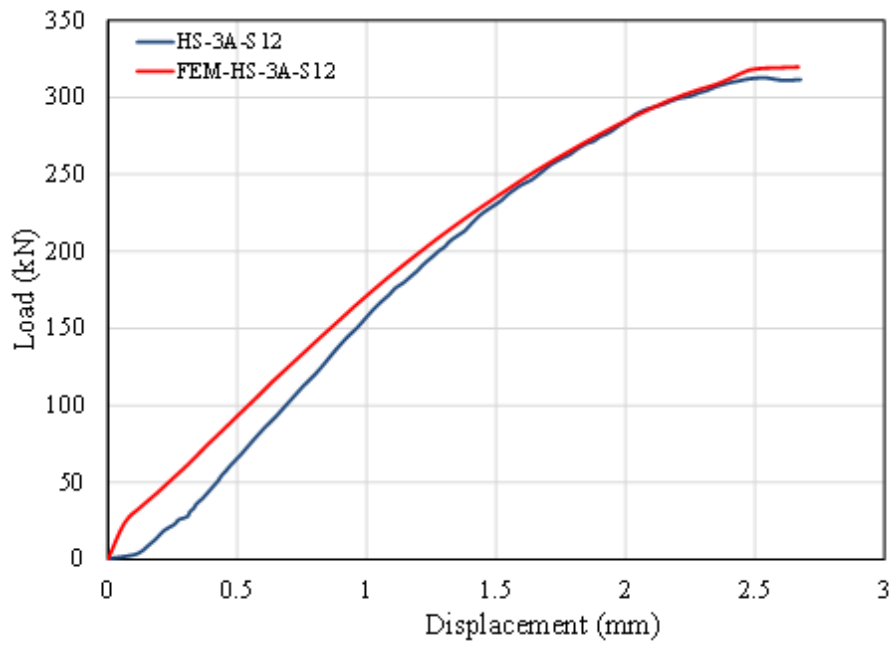
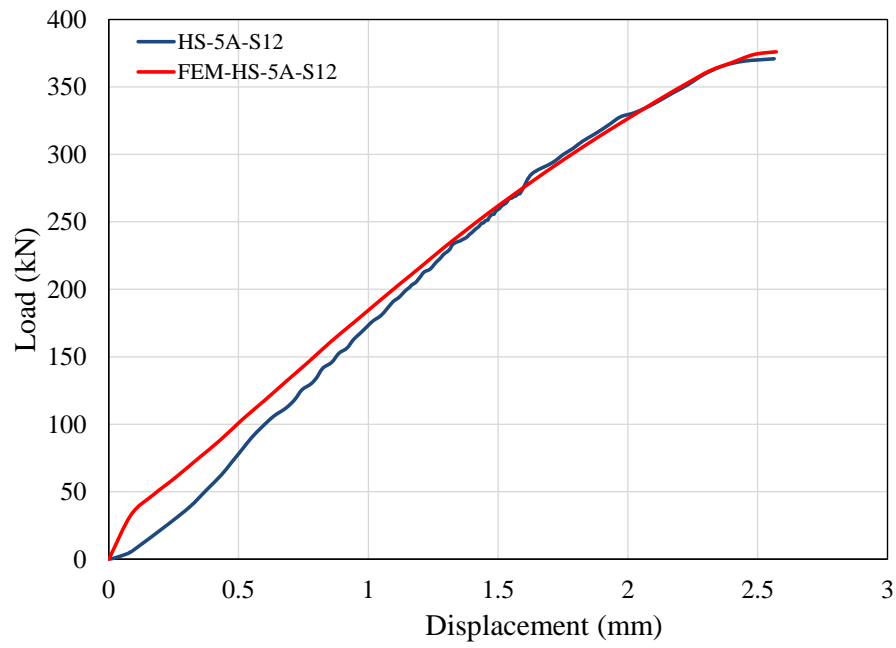


Figure 11-38: HS-3A-S12 vs. FEM-HS-3A-S12



**Figure 11-39: HS-5A-S12 vs. FEM-HS-5A-S12**

**Table 11-2: Summary of experimental and finite element results**

Group	Finite element model	Failure load (kN)		Percentage	Displacement (mm)		Percentage
		Exp.	FEM	Difference	Exp.	FEM	Difference
A	FEM-Con- LS-S18	123.22	123.33	0.08	1.78	1.79	0.56
	FEM-LS-3B-S18	306.35	300.25	-2.03	2.61	2.57	-1.20
	FEM-LS-5A-S18	307.14	312.30	1.65	2.06	2.07	0.37
	FEM-LS-5B-S18	342.55	345.93	0.98	2.38	2.36	-1.01
B	FEM-Con-LS-S12	167.67	172.00	2.52	2.44	2.42	-0.95
	FEM-LS-3A-S12	320.78	324.95	1.28	3.90	3.96	1.43
	FEM-LS-5A-S12	368.08	362.81	-1.45	3.84	3.92	1.93
	FEM-LS-5B-S12	411.97	415.68	0.89	5.34	5.26	-1.41
	FEM-LS-5C-S12	397.17	404.68	1.86	4.07	4.03	-0.90
C	FEM-Con-LS-C16	181.65	181.63	-0.01	2.37	2.45	3.40
	FEM-LS-3A-C16	296.61	296.98	0.12	4.03	4.11	1.96
	FEM-LS-5A-C16	364.25	365.49	0.34	3.67	3.74	1.87
	FEM-LS-5B-C16	411.90	427.46	3.64	4.02	3.94	-1.91
	FEM-LS-5C-C16	387.68	391.89	1.07	3.84	3.92	1.95
D	FEM-Con-LS-C10	197.40	196.20	-0.61	2.27	2.29	0.84
	FEM-LS-3A-C10	348.66	350.72	0.59	3.80	3.77	-0.82
	FEM-LS-5A-C10	372.40	378.47	1.60	3.82	3.77	-1.19
	FEM-LS-5B-C10	453.81	457.95	0.90	4.52	4.52	0.09
	FEM-LS-5C-C10	412.60	420.00	1.76	3.68	3.70	0.54
E	FEM-Con-HS-S18	163.00	158.00	-3.16	3.50	3.48	-0.57
	FEM-HS-3A-S18	234.41	237.17	1.16	3.34	3.30	-1.15
	FEM-HS-5A-S18	278.71	278.26	-0.16	3.70	3.68	-0.46
	FEM-HS-5B-S18	313.72	317.92	1.32	3.66	3.69	0.81
	FEM-HS-5C-S18	293.80	306.43	4.12	4.18	4.04	-3.46
F	FEM-Con-HS-S12	187.91	186.00	-1.03	2.39	2.42	0.95
	FEM-HS-3A-S12	311.52	319.74	2.57	2.68	2.67	-0.31
	FEM-HS-5A-S12	370.83	376.00	1.38	2.56	2.47	-0.31

### 11.3.2 Cracking pattern

The finite element program WCOMD is capable of predicting cracks at every load step. The crack patterns of RC deep beams observed during the experiment and the predicted finite element results are compared in Figures 11-40 to 11-47. A good match between the observed and predicted crack patterns can be seen. Similar to the experimental results, finite element analysis predicts large diagonal shear cracks in the shear span similar to the experiment in both types of openings i.e. circular and square.

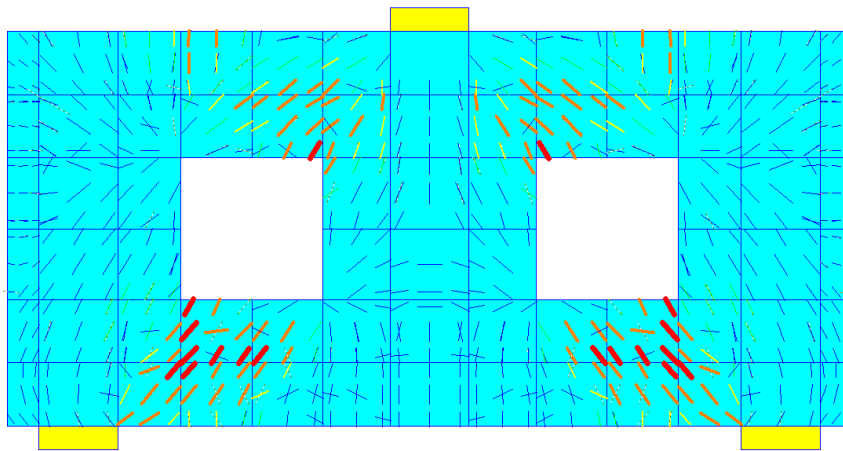


**Figure 11-40: FEM-Con- LS-S18**

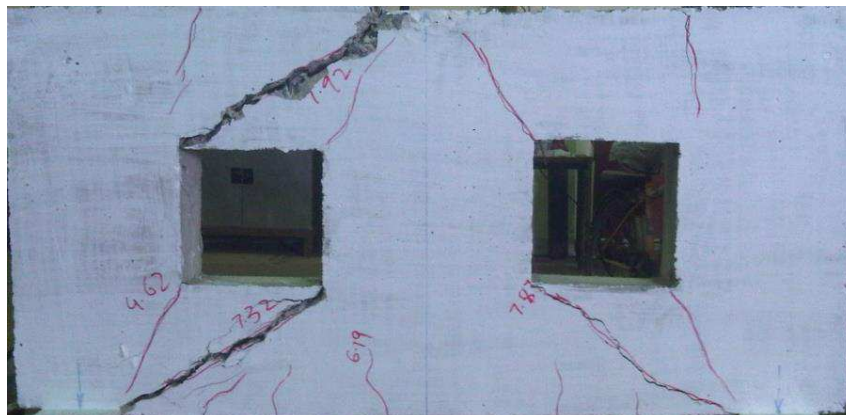


**Figure 11-41: Control LS-S18**

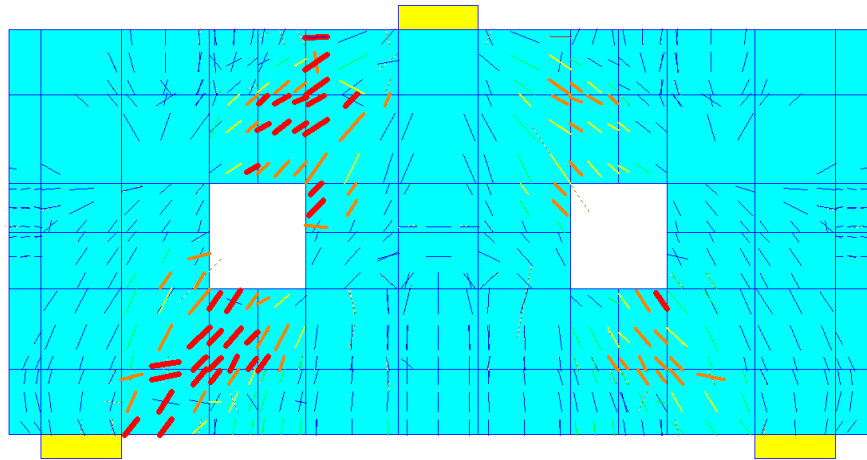


Figure 11-42: FEM-Con-LS-S12

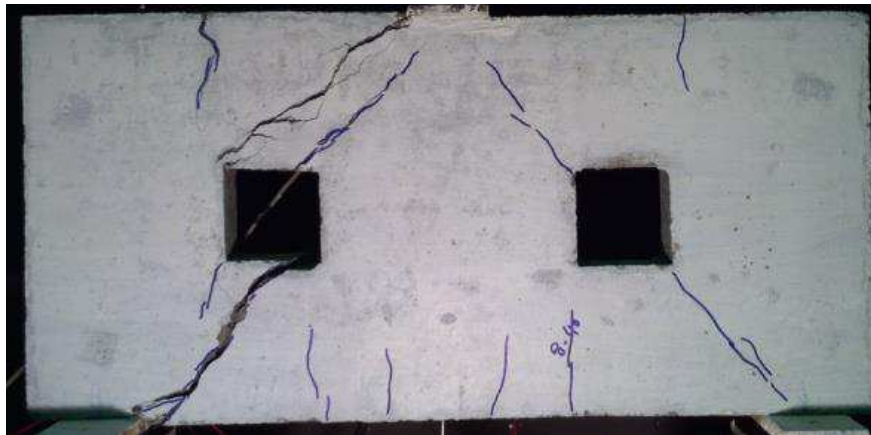
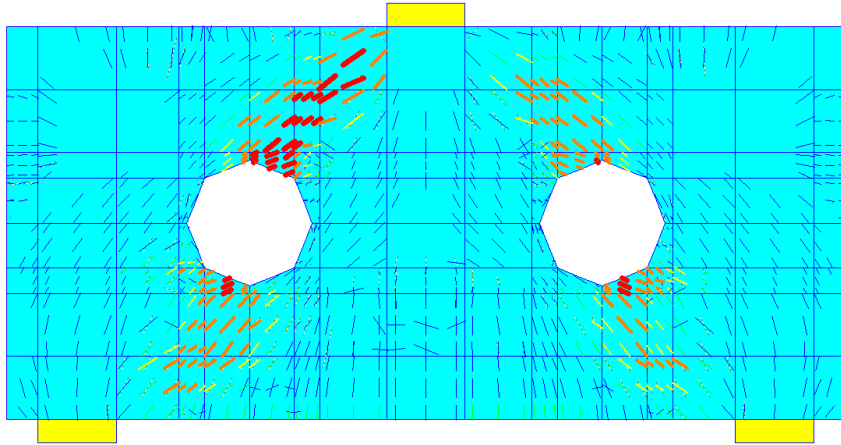
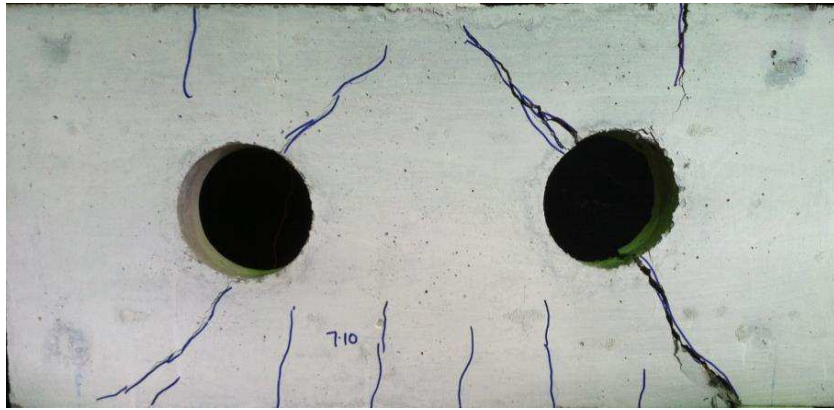


Figure 11-43: Control LS-S12



**Figure 11-44: FEM-Con-LS-C16**



**Figure 11-45: Control LS-C16**

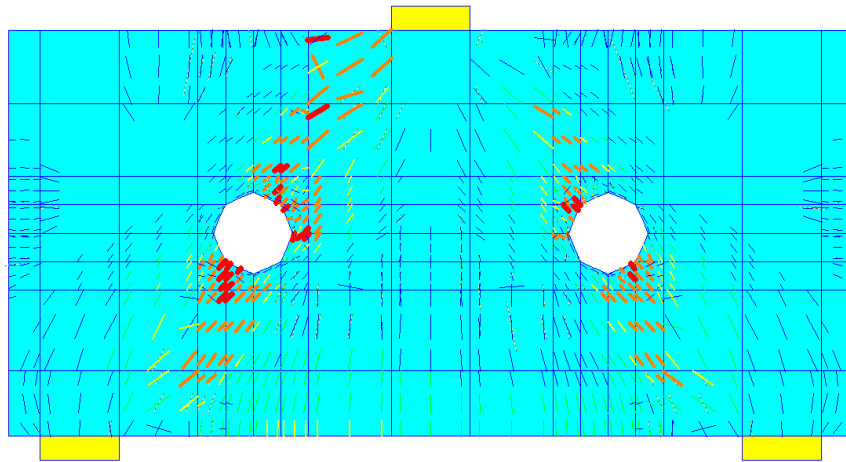


Figure 11-46: FEM-Con-LS-C10

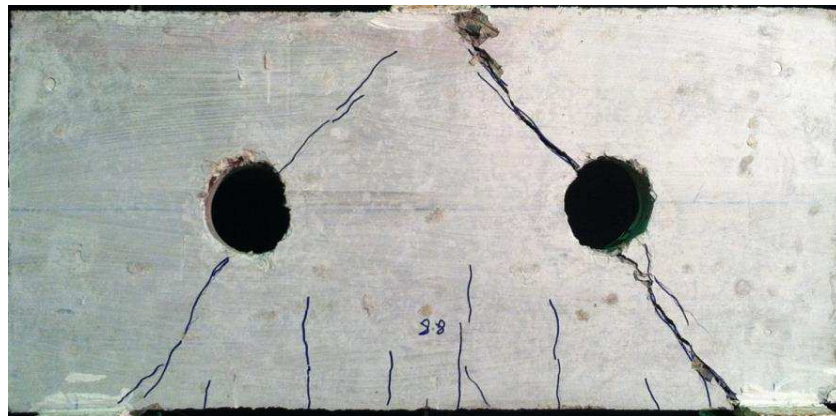


Figure 11-47: Control LS-C10

## **11.4 Discussion on finite element results**

### **11.4.1 Finite element models of un-strengthened RC deep beams with openings**

From Table 11-2 and Figures 11-13, 11-17, 11-22, 11-27, 11-32 and 11-37, it can be seen that finite element models can well predict the ultimate load carrying capacity and mid span deflection of un-strengthened low and high strength RC deep beams with openings. In low strength groups (A to B) RC deep beams with openings, overall, load carrying capacity calculated by finite element analysis is recorded higher than experimental ones for square opening and lower than experimental ones for circular openings. The ultimate load carrying capacity calculated by the finite element analyses were recorded as 0.08% and 2.52% higher than the finite element models i.e., FEM-Con-LS-S18 and FEM-Con-LS-S12, respectively. The mid-span deflection of the finite element model FEM-Con-LS-S18 was recorded 0.56% higher than the experimental result, whereas the mid span deflection of the finite element model FEM-Con-LS-S12 was 0.95% lower than experimental one. The ultimate load carrying capacity calculated by the finite element analyses were recorded as 0.01% and 0.61% lower than the measured values for circular openings of 160 mm Dia. (Group C) and circular openings of 100 mm Dia. (Group D), respectively. The mid-span deflection of the finite element model FEM-Con-LS-C16 was recorded 3.40% higher than the experimental result, whereas the mid span deflection of the finite element model FEM-Con-LS-S12 was 0.84% higher than experimental one. Unlike RC deep beams with square opening of low strength concrete, In high strength concrete groups (E and F), the ultimate load carrying capacity calculated by the finite element analyses were recorded as 3.16% and 1.03% lower than the measured values for square openings of 180x180 mm and square openings of 120x120 mm, respectively. The mid-span deflection of the finite element model FEM-Con-HS-S18 was recorded 0.57% lower than the experimental result, whereas the mid span deflection of the finite element model FEM-Con-LS-S12 was 0.95% higher than experimental one. A slight difference between the predicted and measured values for both ultimate load and mid span deflections endorse the validity of the finite element models to predict the behavior of un-strengthened RC deep beams with openings.



## 11.4.2 Finite element models for SGFRP strengthened RC deep beams with openings

### 11.4.2.1 Group A

The predicted load versus mid span deflection curves of SFRP strengthened RC deep beams with openings are shown in Figures 11-14 to 11-16 and the results are summarized in Table 11-2. The predicted ultimate load carrying capacities of the finite element models strengthened with SFRP were in good agreement with values recorded experimentally. The ultimate load of the finite element model FEM-LS-3B-S18 was 2.03% lower than the experimental value, whereas only 1.65% and 0.98% increase in the prediction of the ultimate loads were found for finite element models FEM-LS-5A-S18 and FEM-LS-5B-S18, respectively. However, the finite element models were found to underestimate the mid span deflections. The predicted mid span deflections by the finite element models FEM-LS-3B-S18 and FEM-LS-5B-S18 are found to be 1.20% and 1.01%, respectively, lower than the experimental ones. A slight increase of 0.37% in mid span deflection is observed for finite element model FEM-LS-5A-S18 compared with experimental one. Although the predicted mid span deflections are slightly lower than the experimentally recorded values, it can be stated that the overall behavior of strengthened specimens can be well simulated by the finite element models.

### 11.4.2.2 Group B

From Table 11-2 and Figures 11-18 to 11-21, it can be seen that the finite element model tended to slightly overestimate the load capacity and mid span deflection of the RC deep beams with openings. The ultimate load of the finite element models FEM-LS-3A-S12, FEM-LS-5B-S12 and FEM-LS-5C-S12 was 1.28%, 0.89% and 1.86% higher, than the experimental value, respectively, whereas only 1.45% decrease in the prediction of the ultimate load was found for finite element model FEM-LS-5A-S12. The mid span deflection of the models FEM-LS-3A-S12 and FEM-LS-5A-S12 was only 1.43 and 1.93% higher than the experimentally recorded value, respectively, whereas only 1.41% and 0.90% decrease in the prediction of mid span deflection were observed for the finite element models FEM-LS-5B-S12 and FEM-LS-5C-S12, respectively.

#### 11.4.2.3 Group C

From Table 11-2 and Figures 11-23 to 11-26, it can be seen that the finite element models tended to slightly overestimate the load capacity and mid span deflection of the RC deep beams with openings. The ultimate load of the finite element models FEM-LS-3A-C16, FEM-LS-5A-C16, FEM-LS-5B-C16 and FEM-LS-5C-C16 was 0.12%, 0.34%, 3.64% and 1.07% higher, than the experimental value, respectively. The mid span deflection of the models FEM-LS-3A-C16, FEM-LS-5A-C16 and FEM-LS-5C-C16 was only 1.96, 1.87 and 1.95% higher than the experimentally recorded value, respectively, whereas only 1.91% decrease in the prediction of mid span deflection were observed for the finite element model FEM-LS-5B-C16.

#### 11.4.2.4 Group D

The predicted load versus mid span deflection curves of SGFRP strengthened RC deep beams with openings (Group D) are shown in Figures 11-28 to 11-31 and the results are summarized in Table 11-2. The predicted ultimate load carrying capacities of the finite element models strengthened with SGFRP were in good agreement with values recorded experimentally. However there is found a slight overestimate in the prediction of ultimate load carrying capacity. The ultimate load of the finite element models FEM-LS-3A-C10, FEM-LS-5A-C10, FEM-LS-5B-C10 and FEM-LS-5C-C10 was 0.59%, 1.60%, 0.90% and 1.76% higher, than the experimental value, respectively. The predicted mid span deflections by the finite element models FEM-LS-3A-C10 and FEM-LS-5A-C10 are found to be 0.82% and 1.19%, respectively, lower than the experimental ones. A slight increase of 0.09% and 0.54% in mid span deflection is observed for finite element model FEM-LS-5B-C10 and FEM-LS-5C-C10 compared with experimental ones, respectively. This difference in the prediction of the ultimate load and de-flection is considered to be slight and it can be said that the finite element model can reasonably reproduce the experimental results.

#### 11.4.2.5 Group E

From Table 11-2 and Figures 11-33 to 11-36, it can be seen that the finite element model tended to slightly overestimate the load capacity and mid span deflection of the RC deep beams with openings. The ultimate load of the finite element models FEM-HS-3A-S18, FEM-HS-5B-S18 and FEM-HS-5C-S18 was 1.16%, 1.32% and

4.12% higher, than the experimental value, respectively, whereas only 0.16% decrease in the prediction of the ultimate loads were found for finite element models FEM-HS-5A-S18. The mid span deflection of the models FEM-HS-3A-S18, FEM-HS-5A-S18 and FEM-HS-5C-S18 was only 1.15%, 0.46% and 3.46 lower than the experimentally recorded value, respectively, whereas only 0.81% increase in the prediction of mid span deflection were observed for the finite element model FEM-HS-5B-S18.

#### 11.4.2.6 Group F

From Table 11-22 and Figures 11-38 and 11-39, it can be seen that the finite element model tended to slightly overestimate the load capacity and mid span deflection of the RC deep beams with openings. The ultimate load of the finite element models FEM-HS-3A-S12 and FEM-HS-5A-S12 was 2.57% and 1.38% higher, than the experimental value, respectively. A slight decrease of 0.31% in mid span deflection is observed for finite element models FEM-HS-3A-S12 and FEM-HS-5A-S12 compared with experimental one. Although the predicted mid span deflections are slightly lower than the experimentally recorded values, it can be stated that the overall behavior of strengthened specimens can be well simulated by the finite element models.

#### 11.4.2.7 Strengthening configurations

Finite element analysis results revealed that mostly ultimate load carrying capacity of SFRP strengthened RC deep beams with SFRP configurations A, B and C, recorded from finite element results is higher than experimental ones. The exception i.e. low ultimate load carrying compared with experimental one is observed only in few beams such as FEM-LS-5A-S12 and with strengthening configuration A. Similar behavior i.e. higher mid span deflections are recorded from finite element analysis compared with experimental ones with few exceptions.

### **11.5 Effect of openings size and location**

In the previous section, the finite element analysis was performed for the tested beams and the analytical results were compared with the experimental ones. It can be seen that the present finite element models are capable of efficiently reproduce the load-mid span deflections, crack pattern and the failure modes. In this section, the finite element model has been adopted to further parametrically examine the behavior of low strength RC deep beams with openings. The parameters included the opening size,

opening shape, location, and the thickness of the SFRP sheets. In the finite element analysis, RC deep beam without opening is also considered to investigate the effect of presence of opening on shear strength of RC deep beams.

Extensive research attempts are available to investigate the behavior of RC beams with openings, located at different locations and strengthened with externally bonded unidirectional FRP for RC beams [66]. However, no research activity is found in literature on the behavior of RC deep beams with openings, located at different locations and strengthened with SFRP. In this finite element analysis, the RC deep beams with openings, located at different locations were strengthened with different thickness of SFRP to investigate the effect of SFRP strengthening on shear strength of RC deep beams with openings. The details of RC deep beams are shown in Figures 11-48 to 11-54 and summarized in Table 11-3. Finite element models of these beams are shown in Figures 11-55 to 11-61.

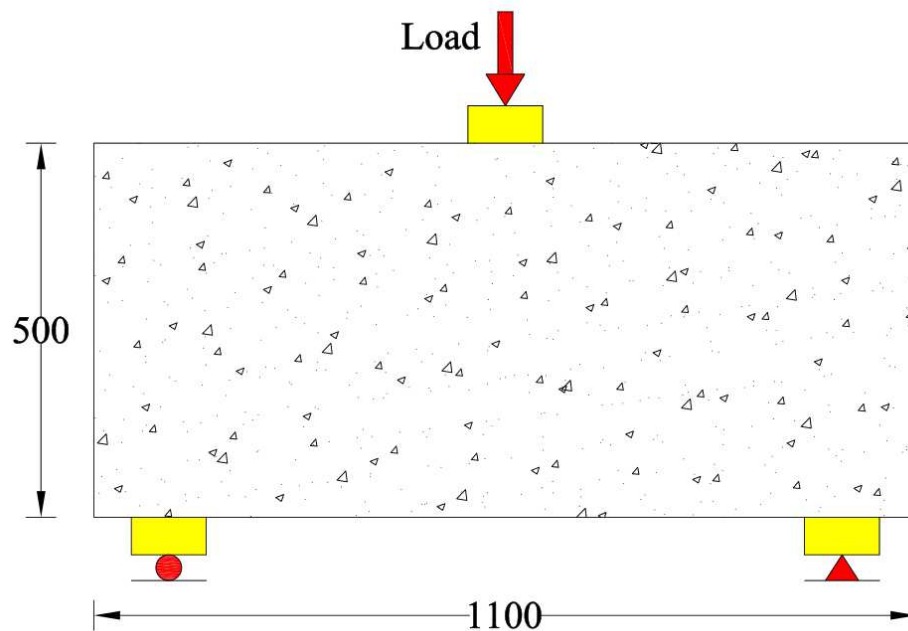


Figure 11-48: Beam N-C

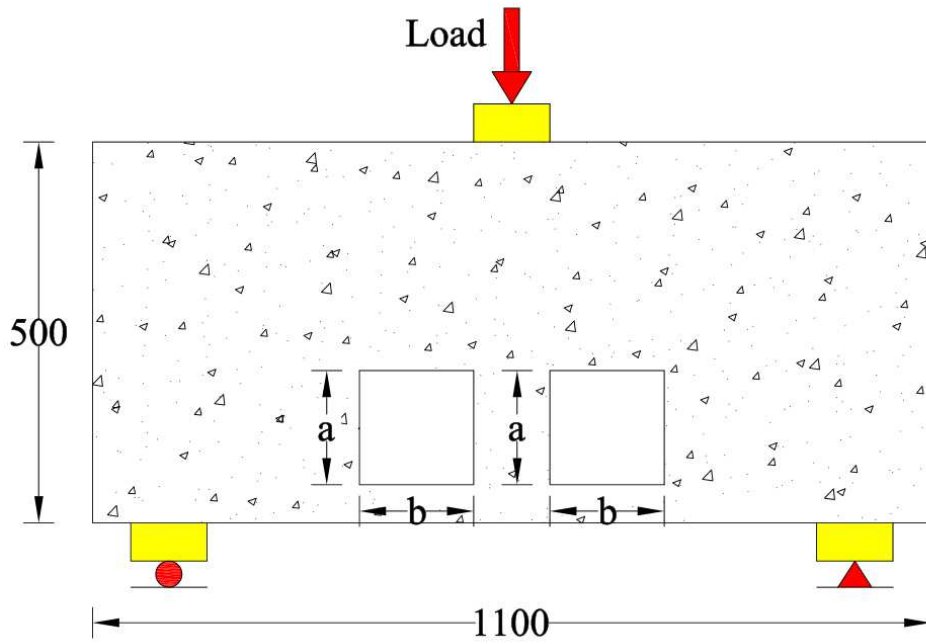


Figure 11-49: Beam N-S-B

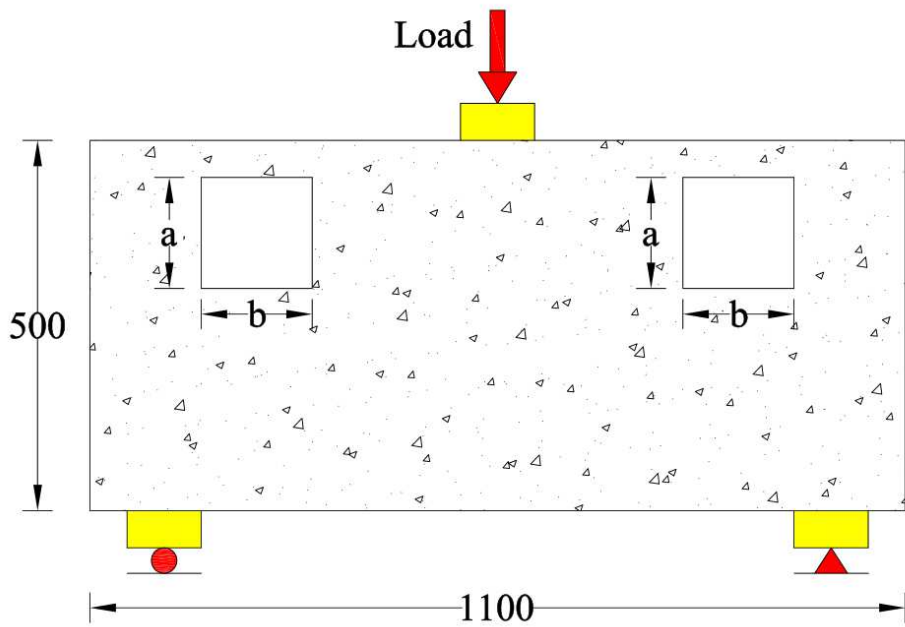


Figure 11-50: Beam N-S-T

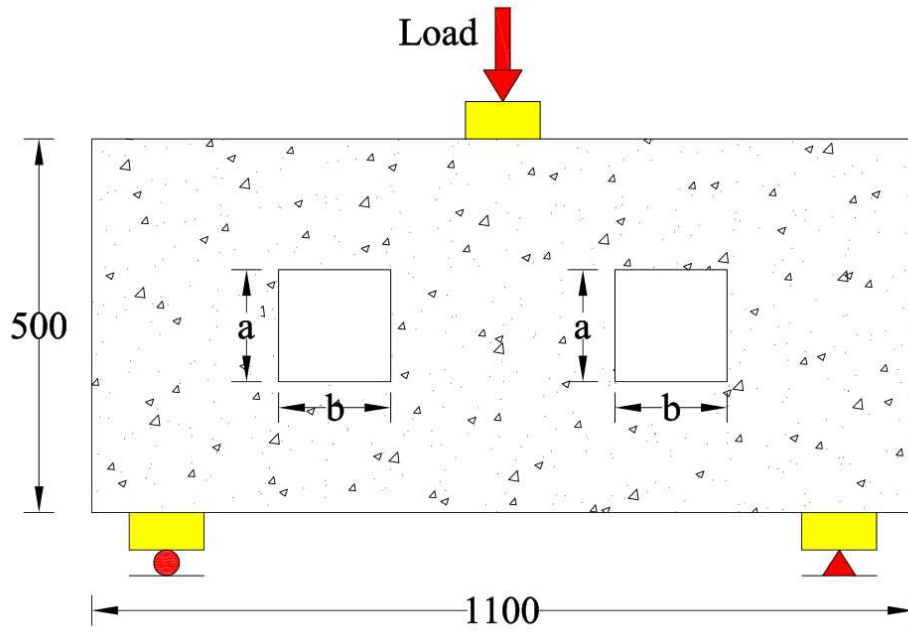


Figure 11-51: Beam N-S-C

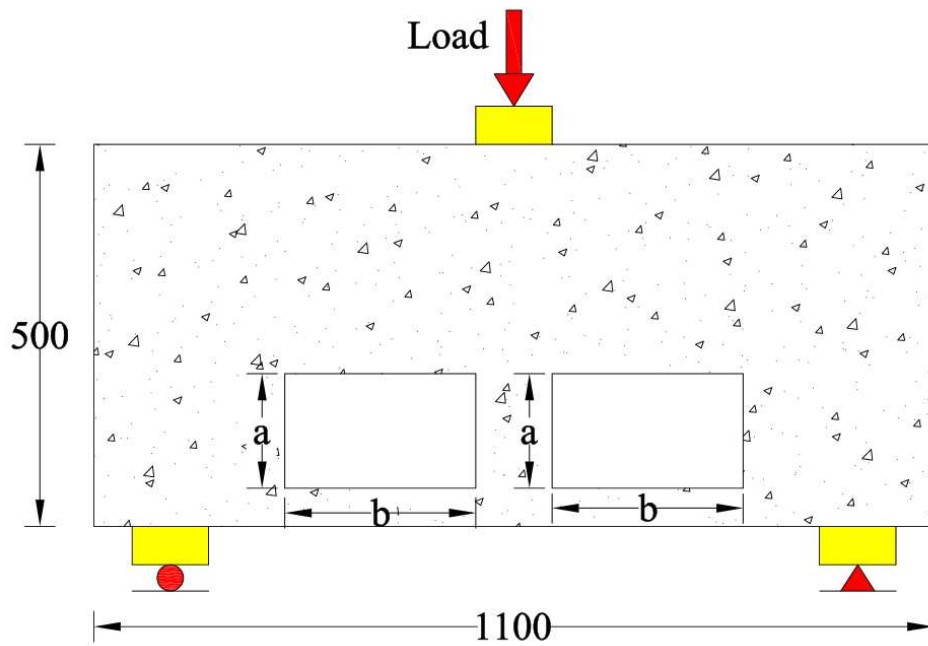


Figure 11-52: Beam N-R-B

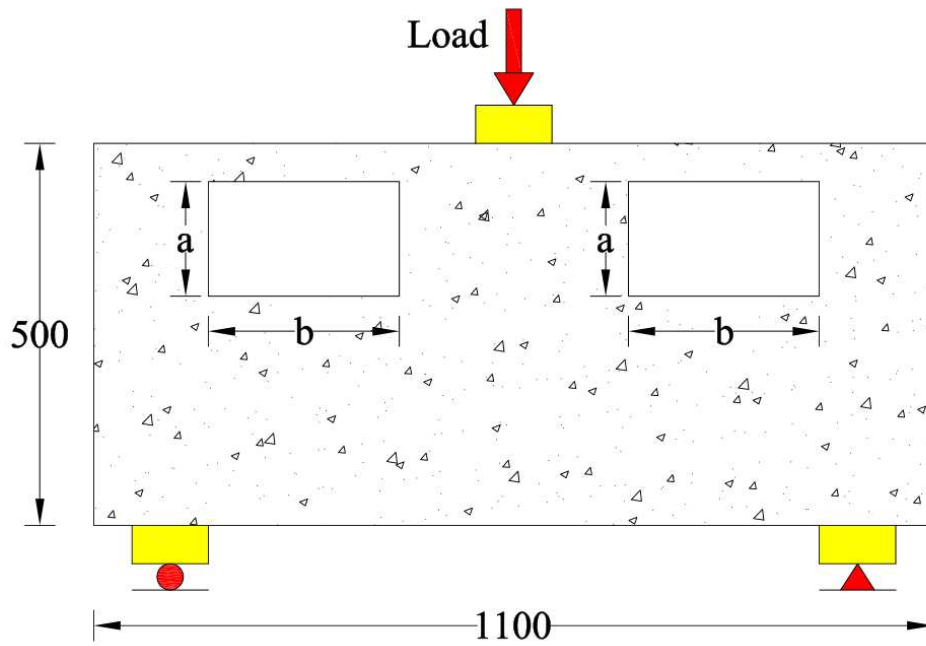


Figure 11-53: Beam N-R-T

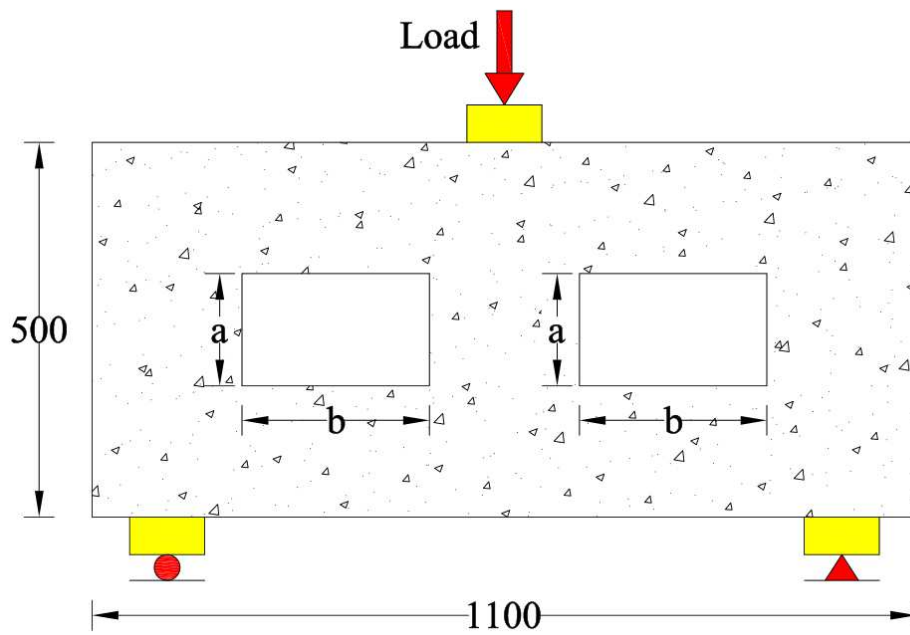
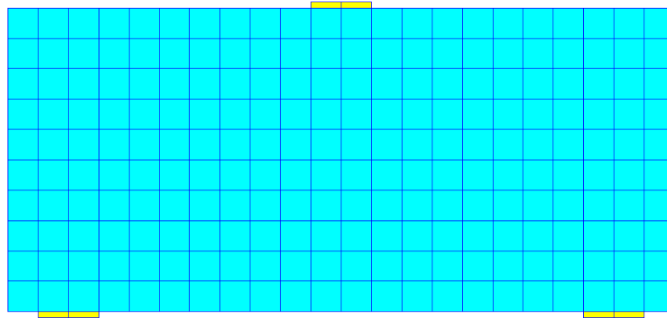


Figure 11-54: Beam N-R-C

**Table 11-3: Details of finite element models**

Group	Finite element model	Opening shape	Opening size	Location of opening	SFRP
					Thickness (mm)
A	N-C	No opening	-	-	No
B	N-S-B	Sqaure	a = 150, b = 150	Bottom of shear span	No
	F-S-B-3	Sqaure	a = 150, b = 150	Bottom of shear span	3
	F-S-B-5	Sqaure	a = 150, b = 150	Bottom of shear span	5
	N-R-B	Rectangular	a = 150, b = 250	Bottom of shear span	No
	F-R-B-3	Rectangular	a = 150, b = 250	Bottom of shear span	3
	F-S-B-5	Rectangular	a = 150, b = 250	Bottom of shear span	5
C	N-S-T	Sqaure	a = 150, b = 150	Top of shear span	No
	F-S-T-3	Sqaure	a = 150, b = 150	Top of shear span	3
	F-S-T-5	Sqaure	a = 150, b = 150	Top of shear span	5
	N-R-T	Rectangular	a = 150, b = 250	Top of shear span	No
	F-R-T-3	Rectangular	a = 150, b = 250	Top of shear span	3
	F-S-T-5	Rectangular	a = 150, b = 250	Top of shear span	5
D	N-S-C	Sqaure	a = 150, b = 150	Centre of shear span	No
	F-S-C-3	Sqaure	a = 150, b = 150	Centre of shear span	3
	F-S-C-5	Sqaure	a = 150, b = 150	Centre of shear span	5
	N-R-C	Rectangular	a = 150, b = 250	Centre of shear span	No
	F-R-C-3	Rectangular	a = 150, b = 250	Centre of shear span	3
	F-S-C-5	Rectangular	a = 150, b = 250	Centre of shear span	5





**Figure 11-55: Finite element model N-C**

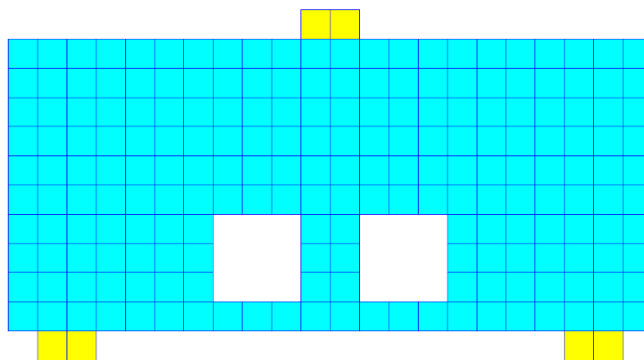


**Figure 11-56: Finite element model N-S-B**

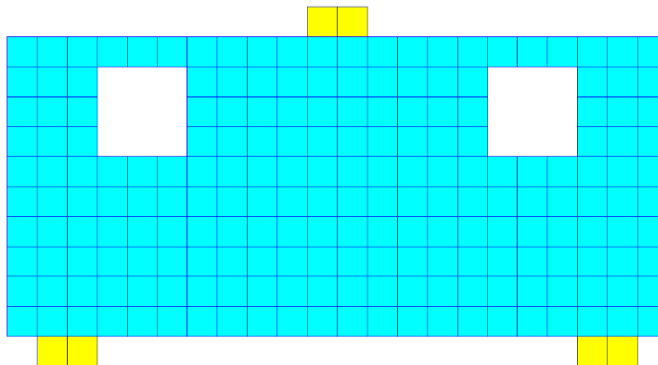


**Figure 11-57: Finite element model N-S-T**

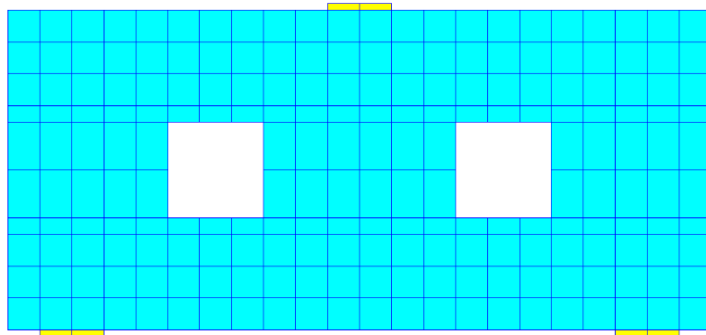


**Figure 11-58: Finite element model N-S-C**

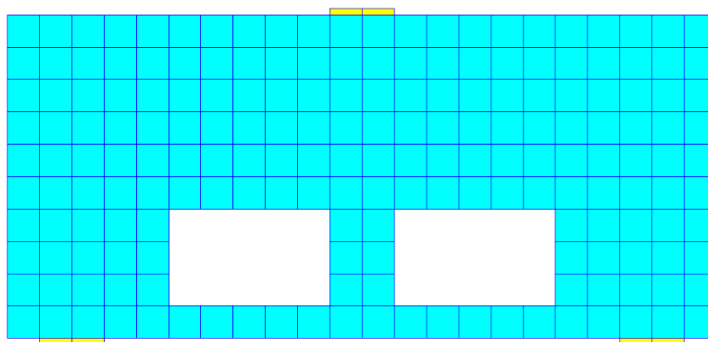


**Figure 11-59: Finite element model N-R-B**

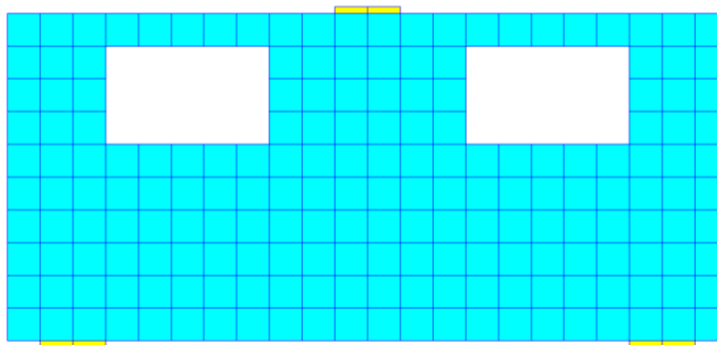


**Figure 11-60: Finite element model N-R-T**

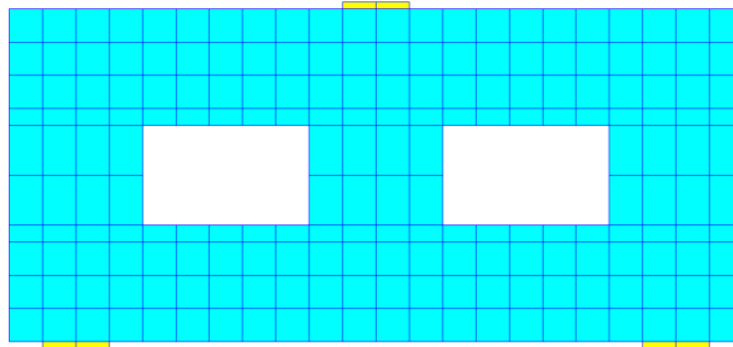


Figure 11-61: Finite element model N-R-C

## 11.6 Finite element analysis results

### 11.6.1 Effect of openings location

The finite element results for un-strengthened RC deep beams without opening and with openings located at different locations are summarized in Table 11-4. The load versus mid span deflection plots are shown in Figures 11-62 and 11-63, comparison of ultimate load between different beams is given in the Figure 11-642 and crack patterns are shown in Figures 11-65 to 11-71. As it can be seen that there is considerable decrease in ultimate load carrying capacity of the RC deep beams for both square and rectangular openings. For square opening, a maximum decrease of 34.0% is observed when openings provided at the center of shear span and a minimum decrease of 3.0% is observed when square openings were located at the bottom. A decrease of 10% is observed for square openings located at top of the shear span. Similar to the square openings, decrease in ultimate load is also observed for rectangular openings. However percentage decrease is higher than square openings as shown in figure 11-62. 51%, 47% and 29% decrease in ultimate load carrying capacity is observed for rectangular openings located at center, top and bottom, respectively.

**Table 11-4: Details of finite element models**

Beam	Ultimate load (kN)	Mid span deflection (mm)	Percentage decrease in ultimate load (%)
N-C	186.98	1.36	-
N-S-B	181.09	1.44	3.00
N-S-T	167.65	1.20	10.0
N-S-C	122.33	1.92	34.0
N-R-B	132.73	1.52	29.0
N-R-T	98.39	1.20	47.0
N-R-C	91.30	2.08	51.0

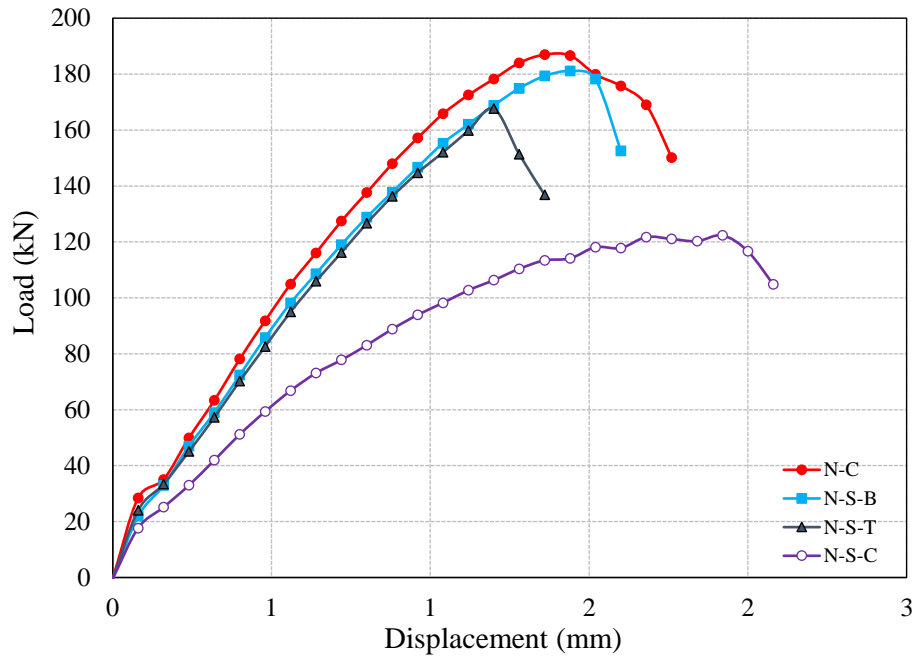


**Figure 11-62: RC deep beams without opening and with square openings**

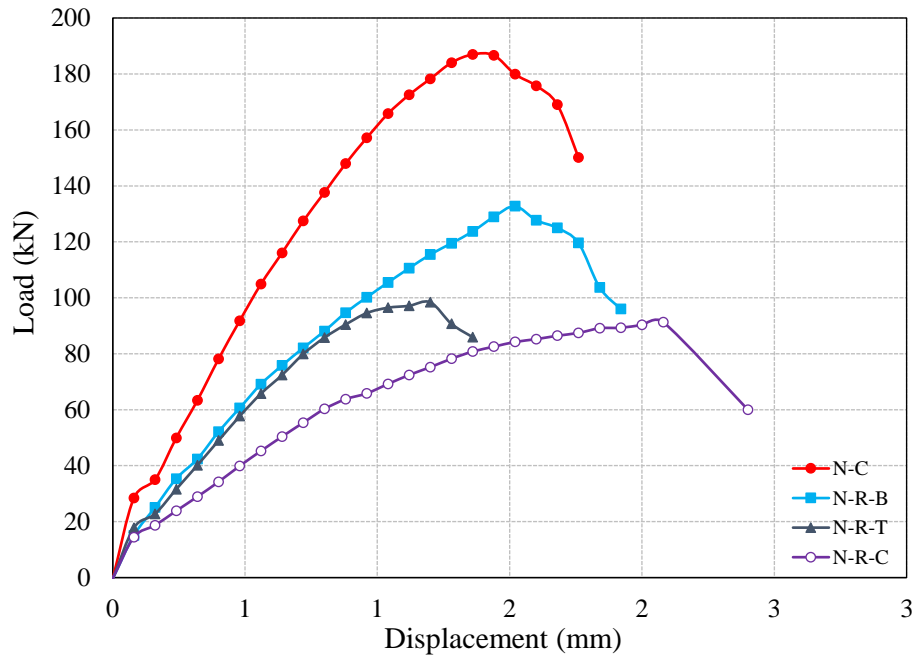


Figure 11-63: RC deep beams without opening and with rectangular openings

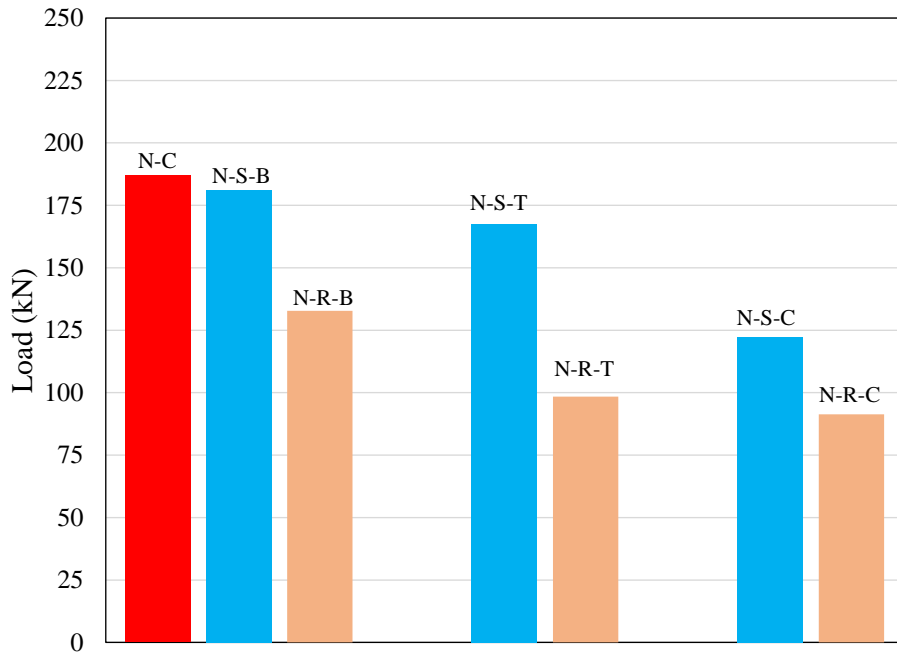
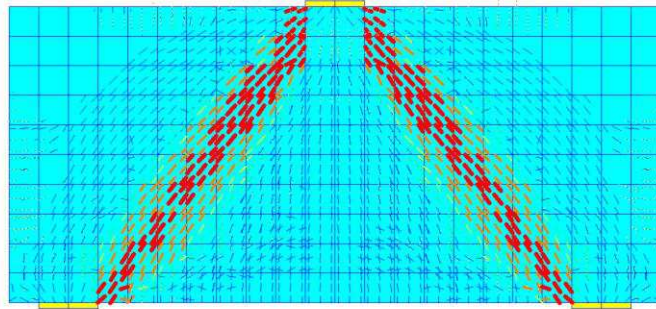
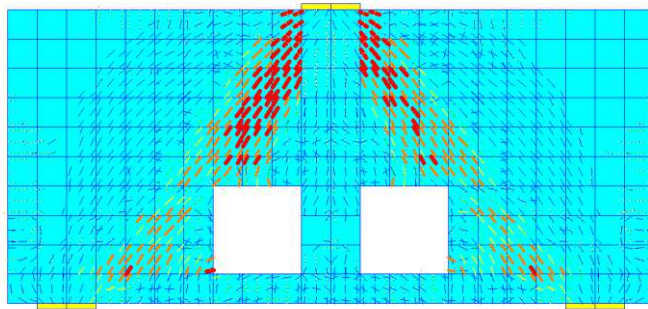


Figure 11-64: Comparison of ultimate load



**Figure 11-65: Finite element model N-R-C**



**Figure 11-66: Finite element model N-S-B**

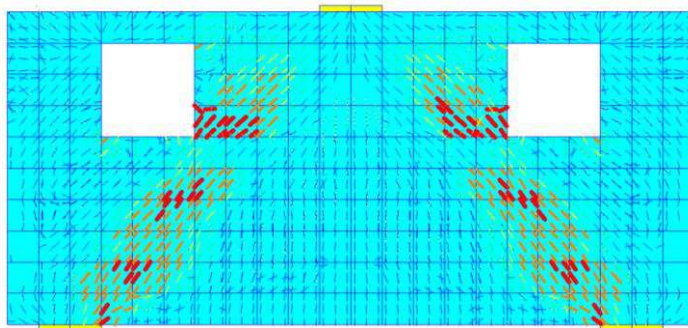


**Figure 11-67: Finite element model N-S-T**

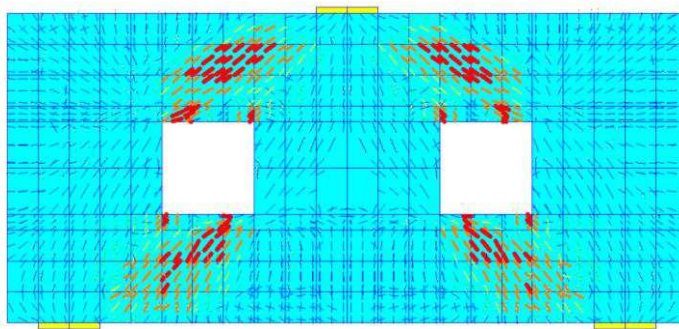


**Figure 11-68: Finite element model N-S-C**

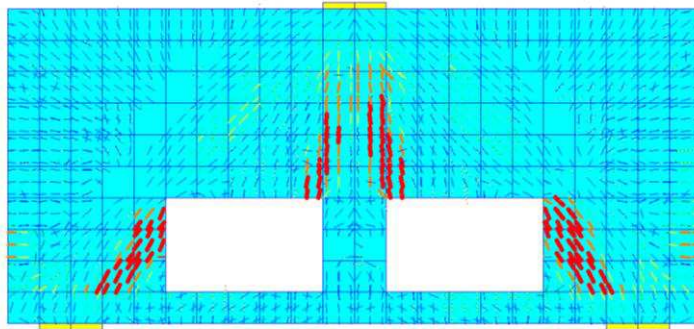


Figure 11-69: Finite element model N-R-B

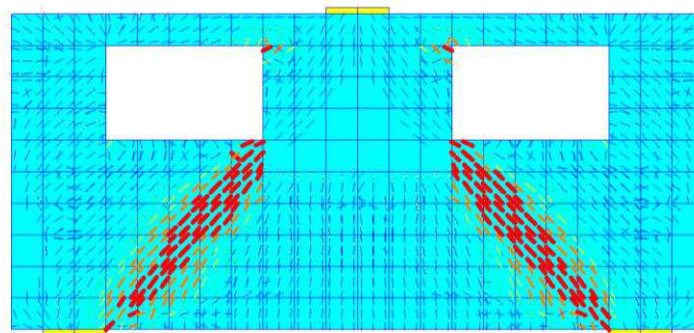


Figure 11-70: Finite element model N-R-T

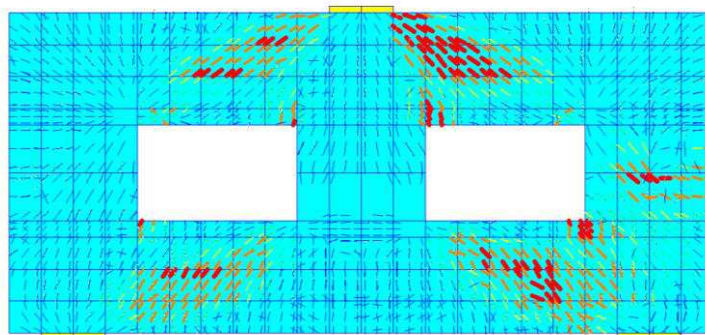


Figure 11-71: Finite element model N-R-C

### 11.6.2 Effect of SGFRP strengthening

The finite element analysis results for SGFRP strengthened RC deep beams with openings along with unstrengthened beams are summarized in Table 11-5. The load versus mid span deflection plots are shown in Figures 11-72 to 11-77 and comparison of ultimate load between different beams is given in the Figures 11-78 and 11-79. According to finite element analysis results, it can be seen that the control finite element model N-S-B failed at the ultimate load of 181.09 kN. Whereas; finite element models F-S-B-3 and F-S-B-5, strengthened by 3 mm and 5 mm of SFRP, failed at the ultimate load of 264 kN and 305.30 kN, respectively. The loading capacity of finite element models F-S-B-3 and F-S-B-5 was increased up to 46% and 69% compared to the control specimen. The control finite element model N-R-B exhibited an ultimate load of 132.73 kN. Whereas, 71% and 91% increases in peak load were observed with the specimens of 3 mm and 5 mm GFRP thickness (finite element models F-R-B-3, F-R-B-5), respectively. By changing the opening location to the top, the peak load of the control finite element model with square openings (N-S-T) was 167.65 kN. Whereas; finite element models F-S-T-3 and F-S-T-5, strengthened by 3 mm and 5 mm of GFRP, failed at the ultimate load of 275.66 kN and 324.61 kN, respectively. The reference finite element model N-R-T exhibited an ultimate load of 98.39 kN. The loading capacity of finite element models F-R-T-3 and F-R-T-5 increased up to 71% and 122% compared to the control finite element model. The un-strengthened finite element model N-S-C exhibited a load of 121.74kN. The increase of 87% and 129% increases in peak load were observed with the specimens of 3 mm and 5 mm GFRP thickness (F-S-C-3, F-S-C-5), respectively. By increasing the width of the opening, the control finite element models with rectangular opening was failed at the lowest ultimate load of 97.30kN. An increase of 81% and 121% of the peak load were achieved from beams model with 3mm and 5mm of GFRP fiber to the beam webs, respectively.

It was observed from the FEM analysis results that the ultimate loads of the beams with the rectangular openings were lower than that of the beams with square openings. Applying the fiber compo-sites to the web of beams lead to increase the ultimate loading capacity. It is also noticed from the FEM results that in all opening location investigated, it is more effective to strengthen the beams with rectangular openings than that with



square openings. In case of openings at the center, the fiber composites have less contribution to the loading capacity of the beams. It is maybe due to the less amount of fiber at the critical zone. Fiber thickness also has an effect on the capacity of the beams. Increase the fiber thickness from 3mm to 5mm lead to increase the loading capacity from 87% to 129% for specimen having a square openings at the center of shear span.

**Table 11-5: Summary of finite element analysis**

Group	Finite element model	Ultimate load (kN)	% Increase in ultimate load	Displacement (mm)	% Increase in displacement
B	N-S-B	181.09	-	1.44	-
	F-S-B-3	264.00	46.0	1.68	17.0
	F-S-B-5	305.30	69.0	1.84	28.0
	N-R-B	132.73	-	1.52	-
	F-R-B-3	226.81	71.0	1.84	21.0
	F-S-B-5	253.49	91.0	1.91	26.0
C	N-S-T	167.65	-	1.20	-
	F-S-T-3	275.66	64.0	1.76	47.0
	F-S-T-5	324.61	94.0	1.84	53.0
	N-R-T	98.39	-	1.20	-
	F-R-T-3	168.54	71.0	1.36	13.0
	F-S-T-5	219.35	122.0	1.76	47.0
D	N-S-C	121.74	-	1.68	-
	F-S-C-3	228.00	87.00	1.84	10.0
	F-S-C-5	278.60	129.0	1.92	14.0
	N-R-C	97.30	-	2.96	-
	F-R-C-3	175.90	81.0	2.40	-
	F-S-C-5	214.74	121.0	2.56	-

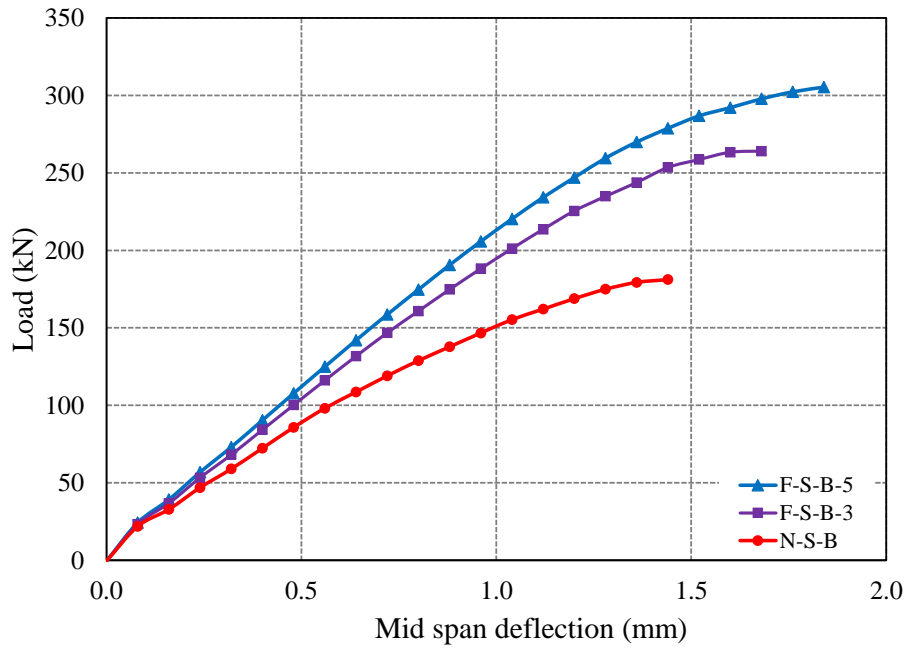


Figure 11-72: Square openings located at bottom

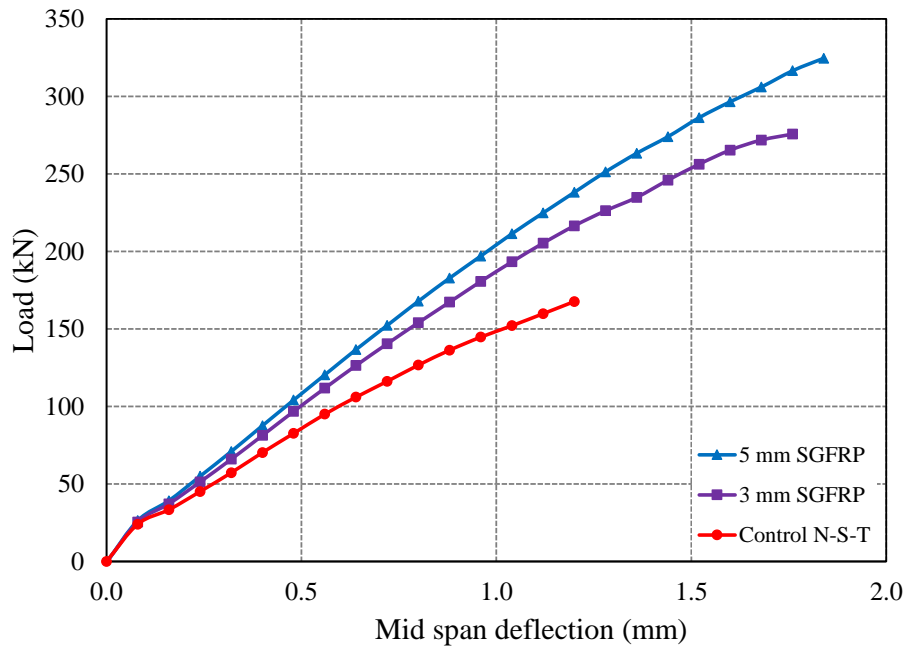


Figure 11-73: Square openings located at top

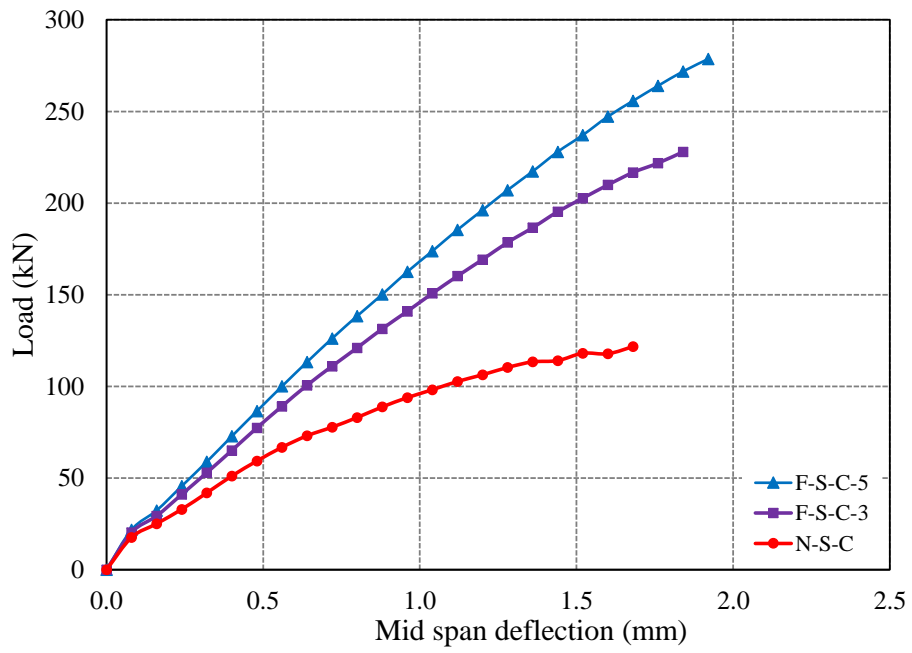


Figure 11-74: Square openings located at center

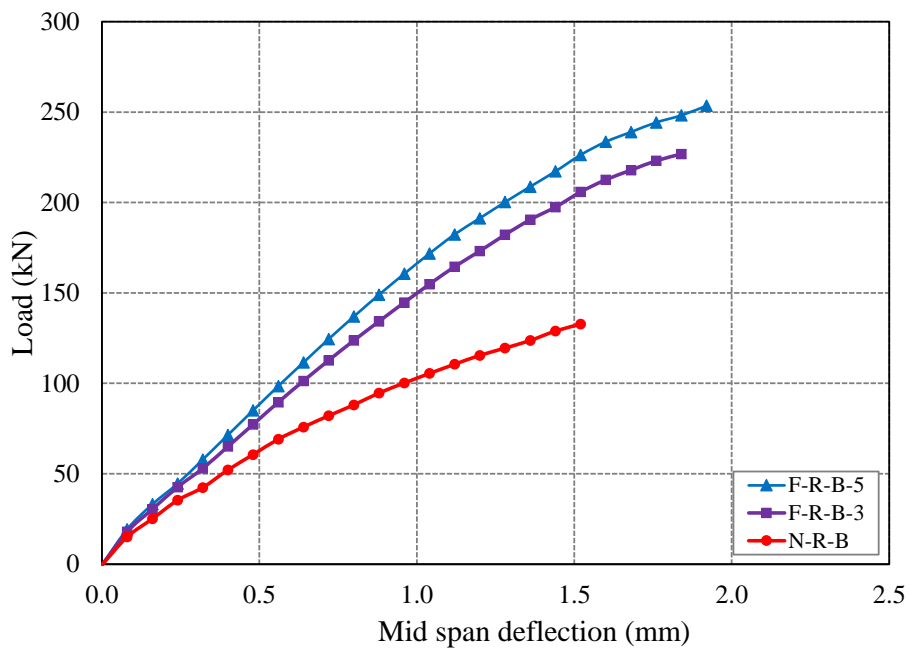


Figure 11-75: Rectangular openings located at bottom

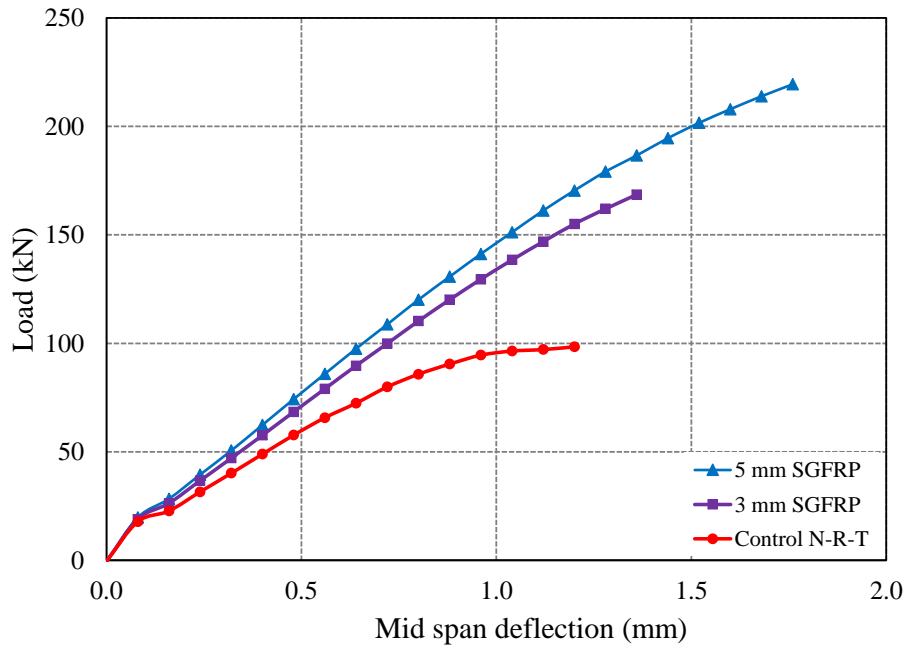


Figure 11-76: Rectangular openings located at top

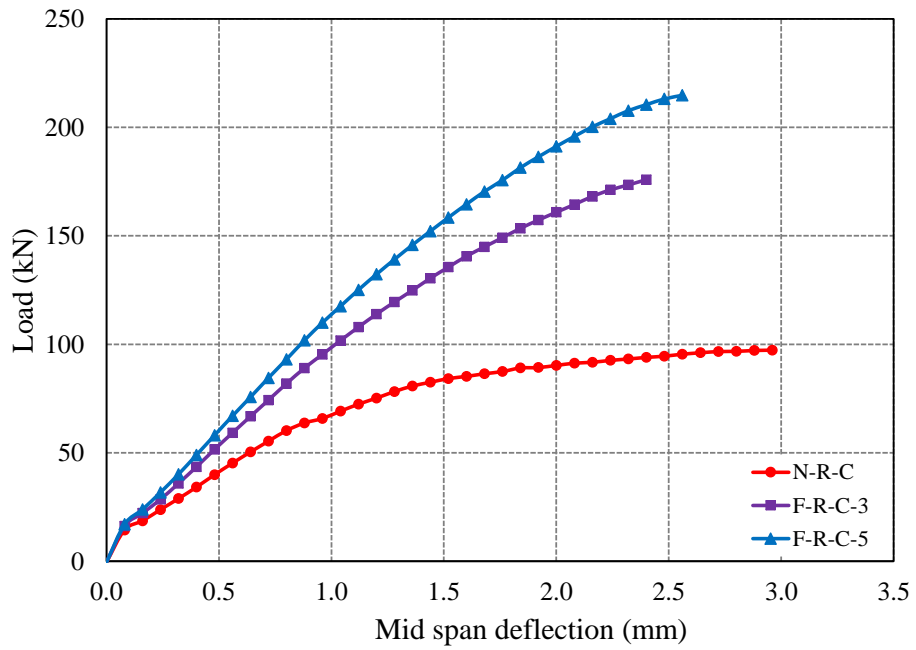
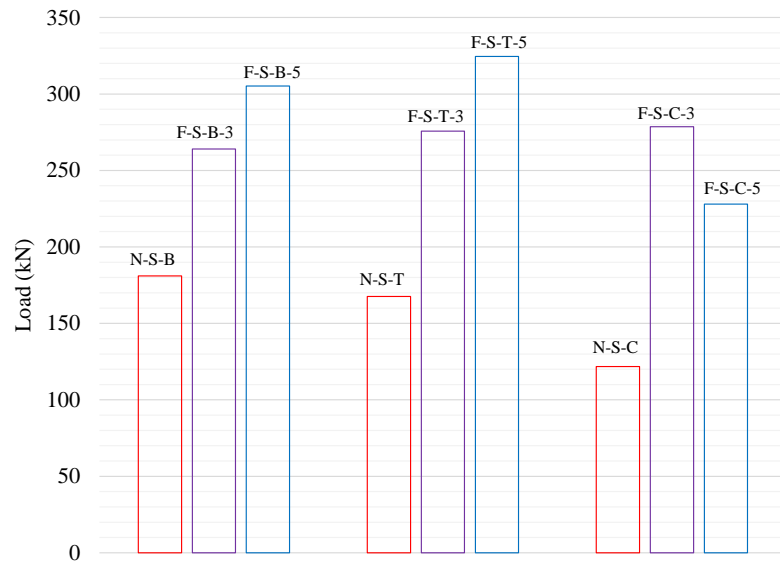
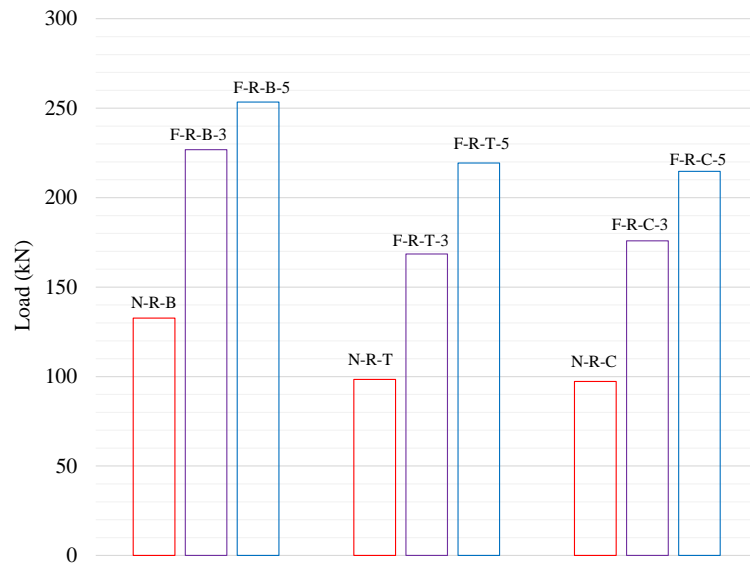


Figure 11-77: Rectangular openings located at center



**Figure 11-78: Comparison of ultimate load (Square openings)**



**Figure 11-79: Comparison of ultimate load (Rectangular openings)**

## Chapter 12

### SFRP Strengthening of Large Sized RC Columns

#### 12.1 Introduction

Seismic record in the past have shown that most of the buildings during earthquakes were collapsed due to the failure of vertical members (i.e. Columns). In the low seismic areas, buildings are usually designed for gravity loads only, which are vulnerable to damage during earthquakes. A recent survey of existing reinforced concrete buildings in Thailand revealed that most columns are designed against gravity loads only and seismic design provisions are not generally regulated. The significant detailing deficiencies typically found are the use of widely spaced stirrup and the use of lap splices in potential plastic hinge area [98]. These columns are referred as non-ductile columns in available literature [99]. The seismic behavior of RC columns is notably improved with conventional unidirectional FRP jacketing in the existing studies [100-107]. Despite of successful application of the conventional uni-directional FRP to improve the seismic behavior of RC columns, the ultimate failure of the conventional FRP jacketed RC columns is often governed by the FRP rupture in weak direction and bulging [107-110] which may be accompanied by rapid buckling of longitudinal steel bars [111].

However, in existing literature, limited research efforts are available on behavior of concrete confined with SFRP [21]. A detailed review of existing literature showed that so far no research effort is conducted to explore the performance of SFRP to enhance the strength and ductility of non-ductile RC columns. Therefore, the present experimental program (Chapter 12) is mainly conducted to investigate the behavior of non-ductile RC columns (representing reinforcement detailing of those structures which were designed against gravity loads only or constructed prior to the development of modern seismic codes) strengthened using SFRP. Three types of RC columns (i.e. shear, flexure-shear and flexure dominated) were strengthened using SFRP jackets and tested under lateral cyclic loading. A constant axial load was also applied along with lateral cyclic loading. In SFRP, two types of fiber materials (i.e. glass and carbon) were used for seismic strengthening of RC columns.

## 12.2 Experimental program

In this experimental program a total of five RC column specimens with same cross sectional dimensions but different heights were constructed and strengthened with SFRP composite. The results of SFRP strengthened RC columns were compared with control or un-strengthened RC columns in the existing study [99]. The details of constructed RC columns are shown in Figure 12-1. All columns were reinforced with continuous longitudinal reinforcement and similar cross section of 250 x 350 mm. Two of the columns were flexure-dominated cantilevers with a height to the point of application of the load (shear span) of 2.10 m and two column specimens were shear dominated cantilevers with shear span of 1.10 m. The remaining one RC column was flexure-shear dominated cantilever with shear span of 1.60 m. All columns were designed as non-ductile column representative of typical detailing of midrise buildings in Thailand. The names and details of test specimens are presented in Table 12-1. The RC columns were fixed into 0.5 m deep heavily reinforced and high strength concrete block (Figure 12-1). The longitudinal steel bars were anchored with 90 degree hooks at the bottom of concrete block. RC columns were reinforced longitudinally with steel bars of 16 mm in diameter (deformed bars) and transversely with round steel bars of 6 mm in diameter in accordance with the control or un-strengthened specimens. The yield and ultimate strength of the longitudinal steel bars was 410 MPa and 530 MPa, respectively. The corresponding values for the round steel bars used for stirrups were 390 MPa and 450 MPa. The casting of RC columns was performed following field practice. In first step the base concrete block was casted with ready-mixed high strength concrete (50 MPa) and in second step (on two consecutive days) RC columns were casted. The compressive strengths of concrete measured on standard cylinders (diameter = 150 mm and height = 300 mm) on the day of testing of columns are presented in Table 1. The notation of RC column specimens is assigned to represent curvature behavior and strengthening material. For example, the meaning of column designation FSD-CARB was as follows: FSD = flexure-shear dominated RC column and CARB was designated a column strengthened with Sprayed Carbon Fiber Reinforced Polymer composites (SCFRP). Test matrix is summarized in Table 12-1.

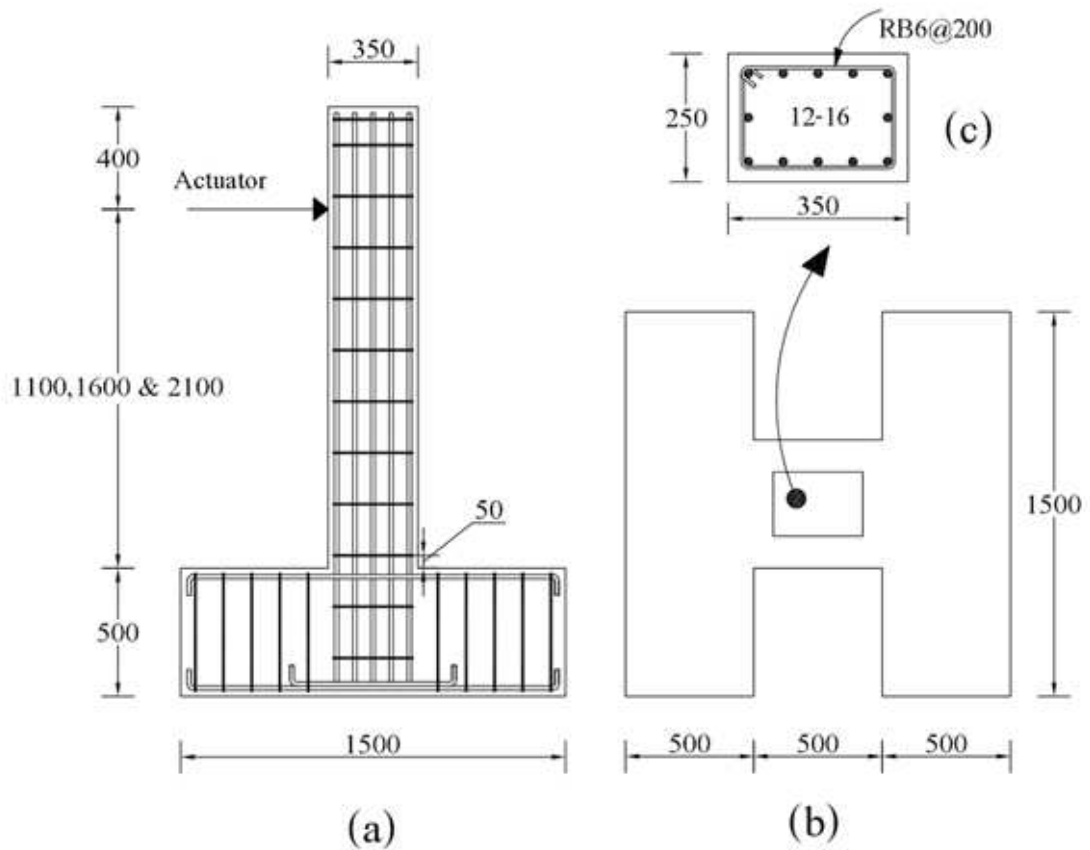


Figure 12-1: Detailing of RC columns (units in mm)

Table 12-1: Details of test specimens

Sr. No	Specimen	Shear span (m)	Strength of concrete (MPa)	SFRP material	Thickness of SFRP (mm)
1	SD-CON*	1.10	28	-	-
2	FSD-CON*	1.60	33	-	-
3	FD-CON*	2.10	30	-	-
4	SD-CARB	1.10	29	Carbon	10
5	SD-GLAS	1.10	29	Glass	10
6	FSD-CARB	1.60	32	Carbon	10
7	FD-CARB	2.10	30	Carbon	10
8	FD-GLAS	2.10	30	Glass	10

\*The control specimens are taken from available literature [99]



### 12.3 Strengthening of RC columns

RC columns were strengthened with SFRP composites. The location and height of SFRP jackets were selected based on observed failure modes and crushing of concrete in un-strengthened RC columns [99]. The SFRP jacketing was applied in the plastic hinge region in all three types of columns (i.e., shear, flexure-shear and flexure dominated). The SFRP was applied up to the height of 0.50 m from the base of the column as shown in Figure 12-2. The SFRP strengthening of RC columns was performed using Sprayed Carbon Fiber Reinforced Polymer composites (SCFRP) and Sprayed Glass Fiber Reinforced Polymer composites (SGFRP). Throughout in this study a single fiber length of 26 mm was used for SCFRP and SGFRP. The thickness of SFRP was kept constant equal to 10 mm for both SGFRP and SCFRP strengthened RC columns. Prior to the SFRP application, the concrete surfaces of the RC columns were roughened using a hammer and a chisel to improve the bond between SFRP and concrete (Figure 12-3). In the next step, RC columns were rounded with a corner radius of 25 mm in strengthening zone to avoid pre-mature rupture of SFRP at the corners (Figure 12-4). The roughened concrete surfaces were washed with high water pressure to remove dust and loose debris. The SFRP was applied onto the specimens using an UltraMax chopper/Saturator unit as shown in Figure 12-4. The thickness of the SFRP was continuously monitored and controlled by experienced technicians during spraying fibers. After the SFRP was applied, an aluminum ribbed roller was used to remove any entrapped air and to obtain uniform thickness for the SFRP (Figure 12-5). Prior to the testing, the SFRP over the required height and footing block were removed using an electric cutter (Figure 12-6). Since the SFRP was applied in 10 mm thickness, at larger drift ratio there were chances of high bearing pressure in SFRP jacket at the column ends (i.e. at the intersection of column and footing). Therefore, SFRP jacketed RC columns were additionally wrapped with 3 layers of CFRP sheet (width of sheet = 3 cm) at the bottom end of columns to avoid pre-mature rupture of SFRP. Typical SCFRP and SGFRP strengthened RC columns are shown in (Figure 12-7).

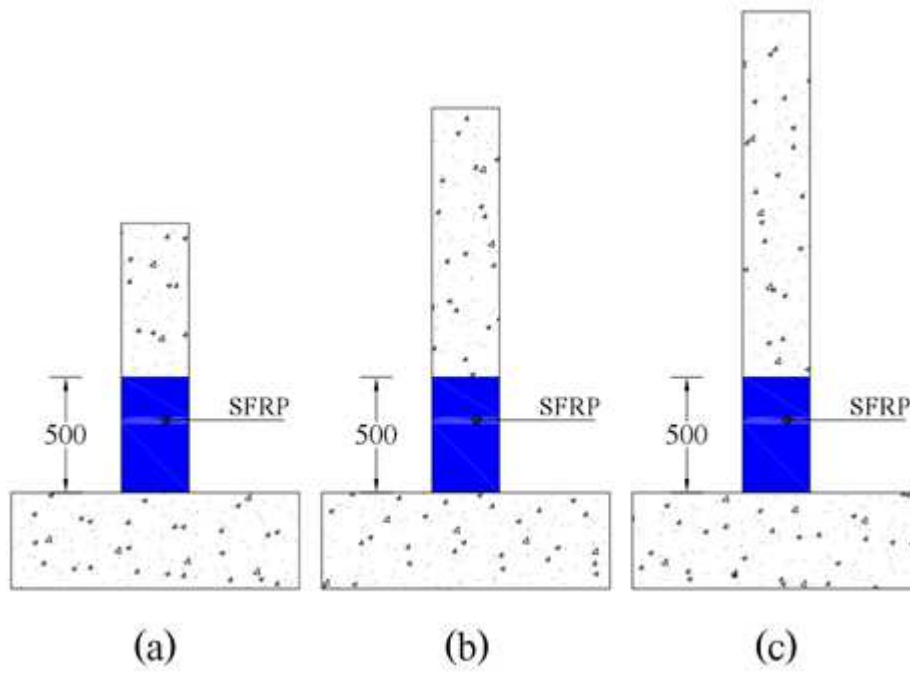


Figure 12-2: Details of SFRP strengthening



Figure 12-3: Roughened concrete surface of column



**Figure 12-4: SFRP application process**



**Figure 12-5: Surface preparation using ribbed aluminum roller**



**Figure 12-6: SFRP cutting process**



**Figure 12-7: SFRP strengthened RC Columns**

## 12.4 Instrumentation and testing procedure

The RC column specimens were well instrumented to record the required necessary data at different deformation steps. A large number of strain gauges with a gauge length of 5 mm were fixed to the longitudinal and transverse steel bars in each specimen to measure the strains. The strain gauges were installed prior to the casting of concrete at different locations as shown in (Figure 12-8). The location of the strain gauges for longitudinal bars was chosen to estimate the strain in the steel bars at the onset of buckling i.e. either middle height between the column base and first stirrup or middle of two stirrups. Eight linear variable differential transducers (LVDTs) were used (four on each side of the RC column) to obtain displacement, rotation and curvatures during test. The LVDTs were installed at different heights equal to 100 mm, 350, 600 and 850 mm from column base. The shear deformation was captured by installing additional six LVDTs. One LVDT was installed directly at the top of the RC column to monitor axial deformation. Typical installation of LVDTs at different locations is shown in Figure 12-9. During the test, the lateral and axial loads were recorded using pre-calibrated load cells. The RC columns were subjected to combine reversed cyclic load and constant axial load. The axial compressive load (equal to 400 kN representing axial load ratio of 14-16%) was applied prior to the lateral load began using a hydraulic jack. Axial load was kept constant and monitored continuously throughout the test. The lateral load was applied using a horizontally installed 250kN-hydraulic actuator to simulate the seismic demand. The loading set up is show in the Figure 12-10. RC column specimens were subjected to reversed cyclic loads using a target percent drift of  $\pm 0.25$ ,  $\pm 0.5$ ,  $\pm 0.75$ ,  $\pm 1.0$ ,  $\pm 1.5$ ,  $\pm 2.0$ ,  $\pm 2.5$ ,  $\pm 3.0$  and etc., for convenient. The hydraulic actuator was operated manually in a displacement control mode. In lateral loading program, 2 cycles per drift level was applied up to the 8% drift and beyond this drift level, 1 cycle per drift was applied. The lateral loading history is shown in the Figure 12-11.

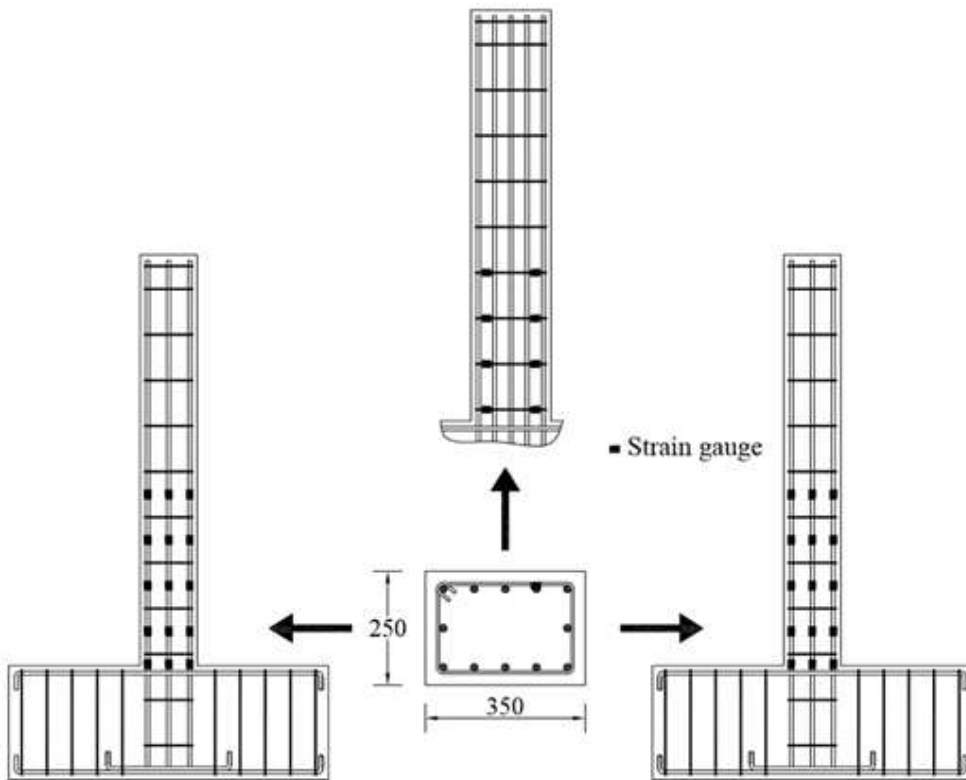


Figure 12-8: Details of strain gauges

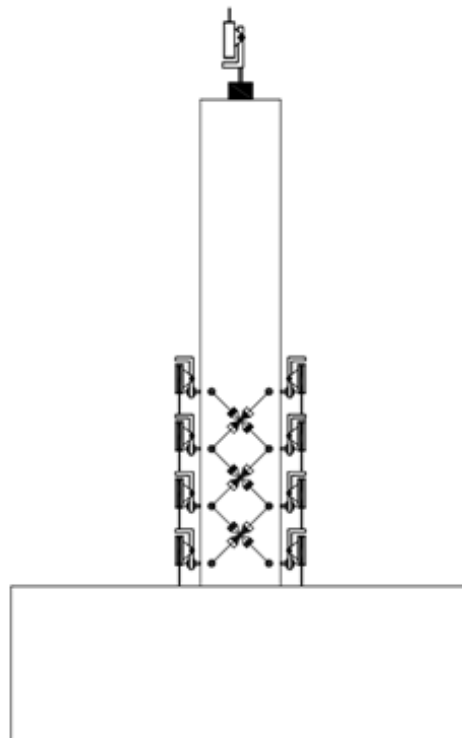


Figure 12-9: Details of LVDTs installation

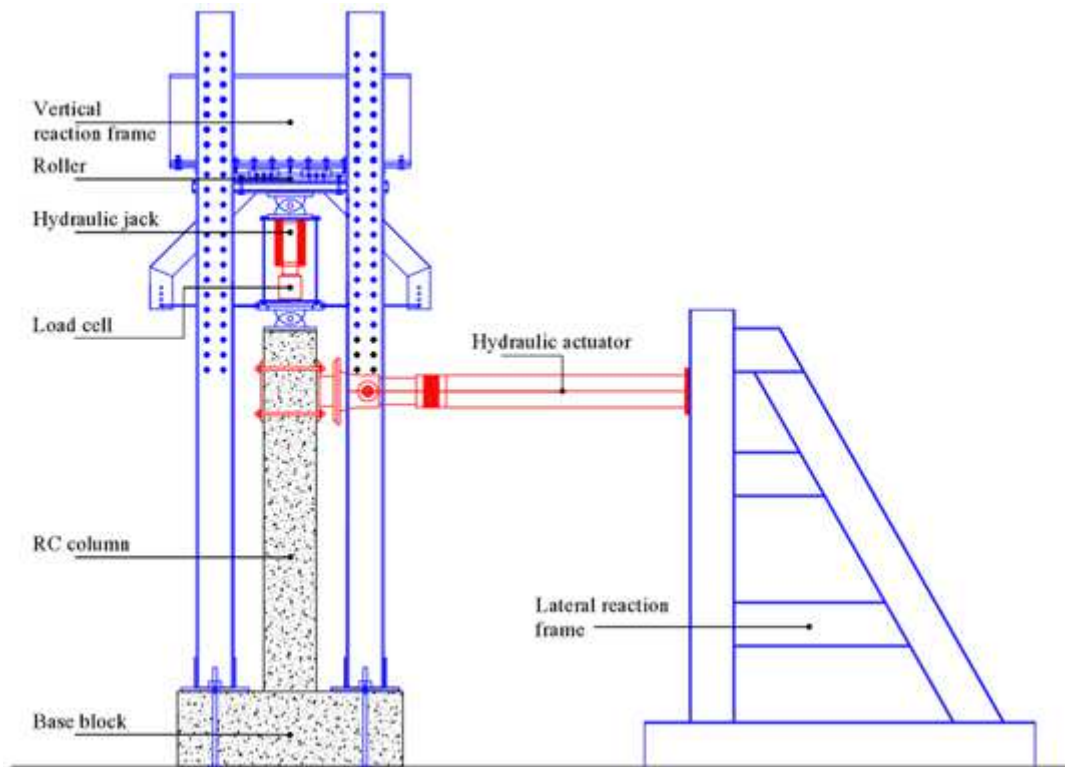


Figure 12-10: Loading setup

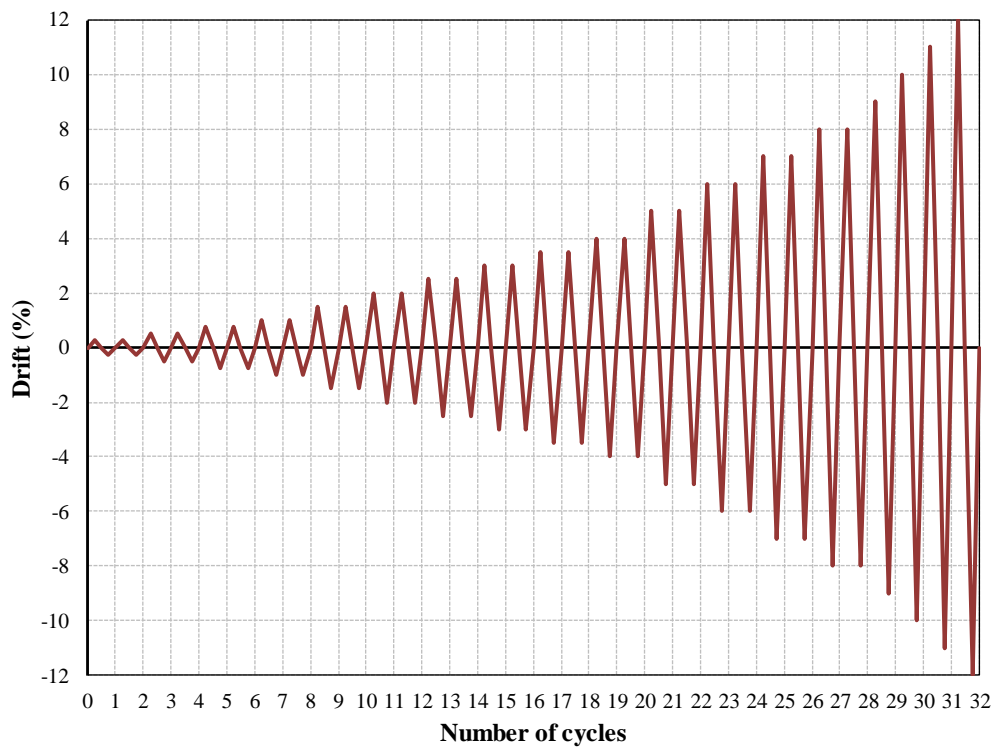


Figure 12-11: Lateral loading protocol

## 12.5 Results and discussion

The experimental response of SFRP strengthened RC columns along with reference or un-strengthened RC columns is given in Figures 12-12 to 12-19 in the form of lateral load versus drift ratio. The drift ratio is calculated by dividing the top end displacement with the column's height (distance between the base and point of application of lateral load). The envelop curves of the corresponding columns are also presented in Figures 12-20 to 12-22. Experimental results in term of lateral load and displacement at first yield ( $P_y$  and  $\delta_y$ ), the maximum load ( $P_{max}$ ), the ultimate displacement ( $\delta_u$ ), the displacement ductility factor ( $\mu_\epsilon$ ) and failure modes in term of buckling or rupture of longitudinal reinforcement are summarized in Table 12-2. The ultimate displacement ( $\delta_u$ ) was defined as that at which a drop of the load from  $P_{max}$  to  $P_{80\%}$  was observed and displacement ductility factor ( $\mu_\epsilon$ ) is considered as ratio between ultimate displacement and first yield displacement. On the lateral load versus drift ratio graphs, the yielding point of longitudinal reinforcement, the yielding point of transverse reinforcement and buckling of longitudinal reinforcement are marked as 1, 2, and 3, respectively. A dotted line is drawn to indicate the ultimate displacement point. Test results are discussed in detail in the following sections.

**Table 12-2: Summary of test results**

Specimen	Test results					
	$P_y$	$\delta_y$	$P_{max}$	$\delta_u$	$\mu_\epsilon = \delta_u / \delta_y$	Failure modes
SD-CON*	120.0	1.00	162.8	2.0	2.00	Buckling of longitudinal bars
FSD-CON*	90.00	1.50	119.5	3.5	2.33	Buckling of longitudinal bars
FD-CON*	80.00	1.50	86.80	4.0	2.67	Buckling of longitudinal bars
SD-CARB	205.6	1.50	242.1	8.0	5.33	Buckling of longitudinal bars
SD-GLAS	204.7	1.50	237.8	8.0	5.33	Buckling of longitudinal bars
FSD-CARB	91.35	1.50	144.5	7.0	4.70	Buckling of longitudinal bars
FD-CARB	95.80	1.50	105.3	8.0	5.33	-
FD-GLAS	92.30	1.50	105.9	7.0	4.70	Rupture of longitudinal bars

\*The details were taken from available literature [3]



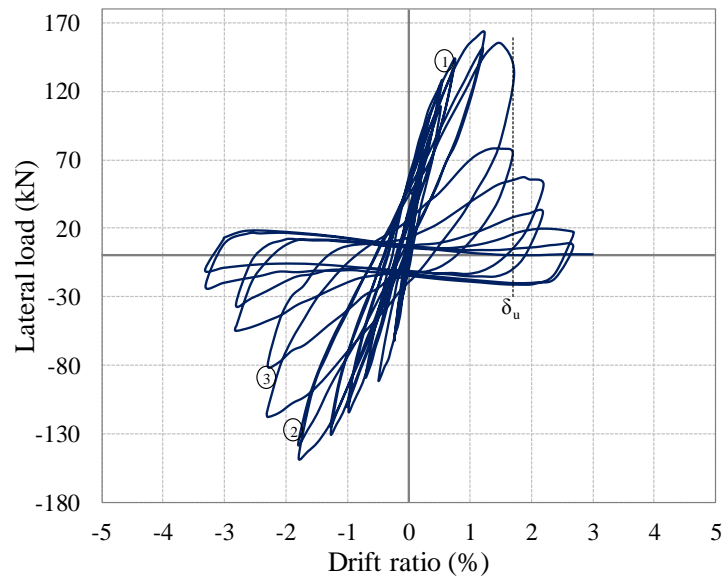


Figure 12-12: Load-displacement hysteretic response of column SD-CON [99]

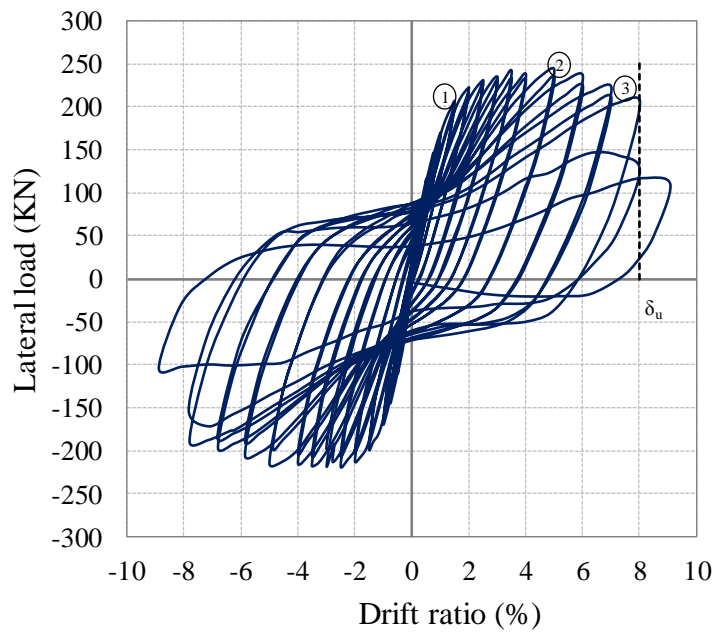
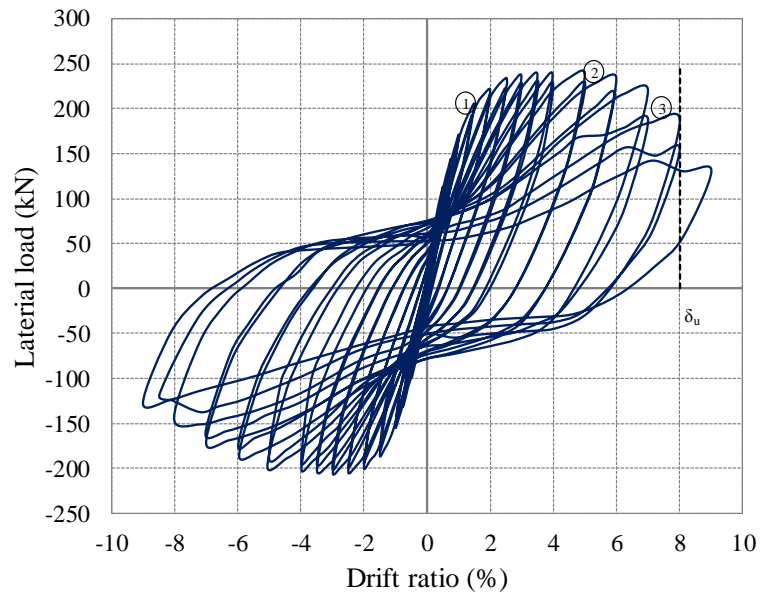
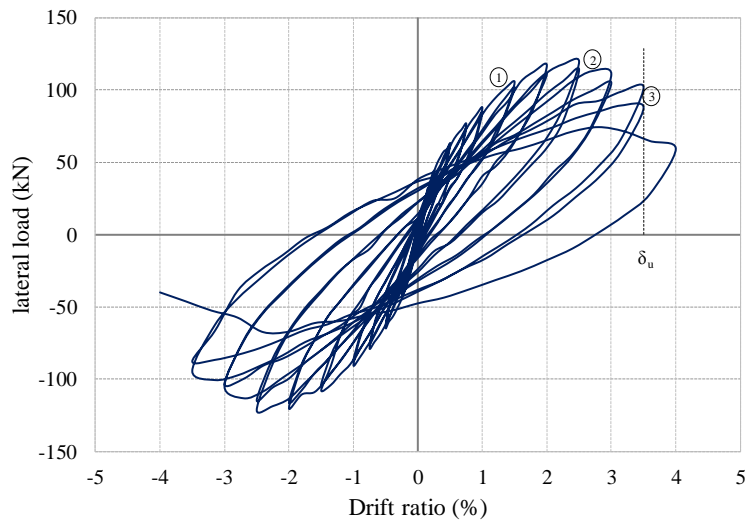


Figure 12-13: Load-displacement hysteretic response of column SD-CARB



**Figure 12-14: Load-displacement hysteretic response of column SD-GLAS**



**Figure 12-15: Load-displacement hysteretic response of column FSD-CON**

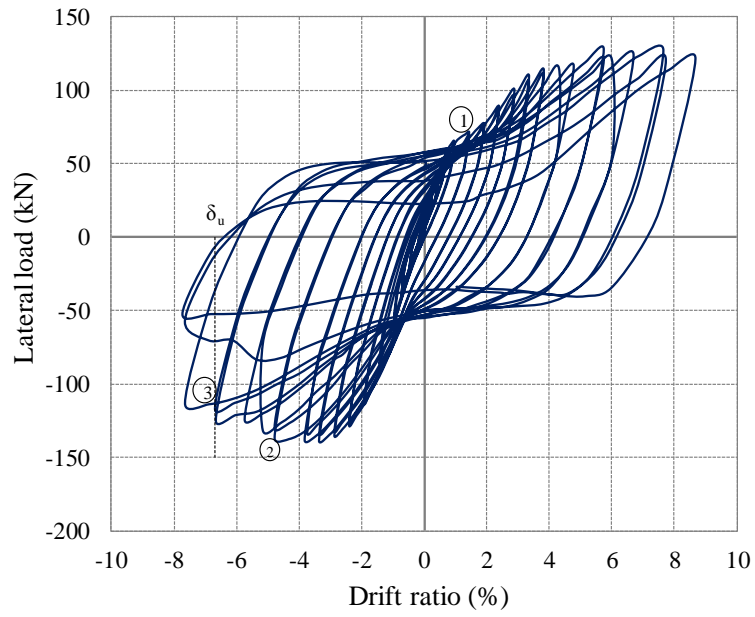


**Figure 12-16: Load-displacement hysteretic response of column FSD-CARB**

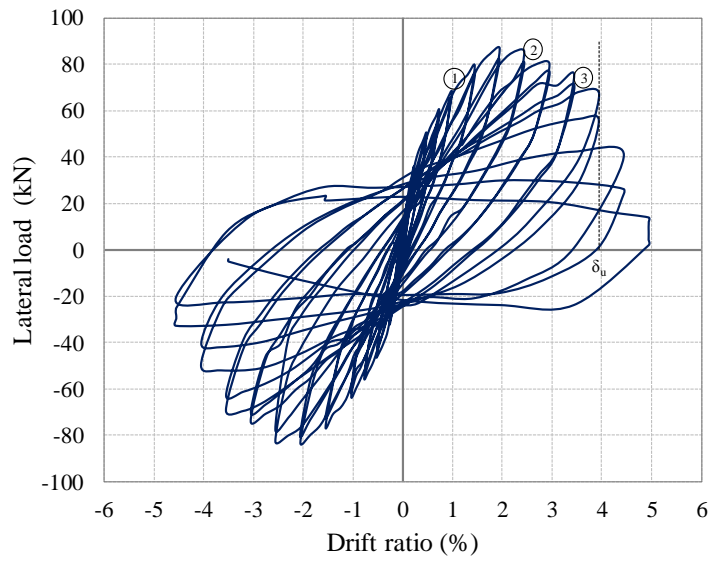


**Figure 12-17: Load-displacement hysteretic response of column FD-CON**

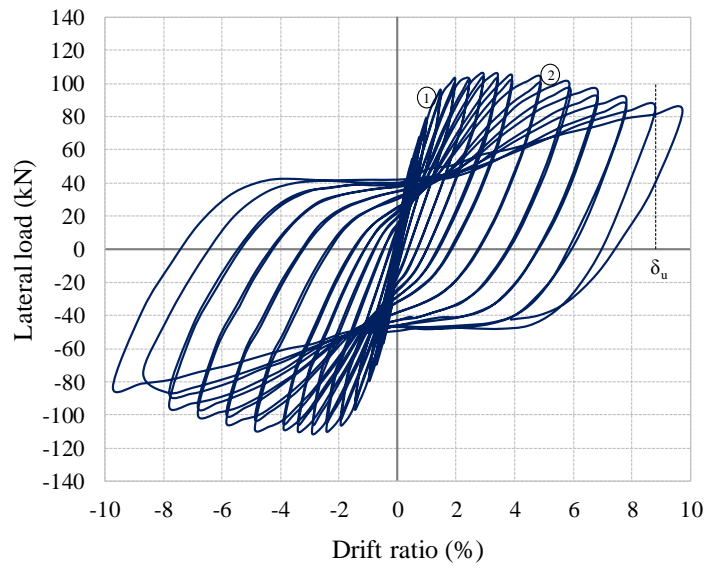


**Figure 12-18: Load-displacement hysteretic response of column FD-CARB**

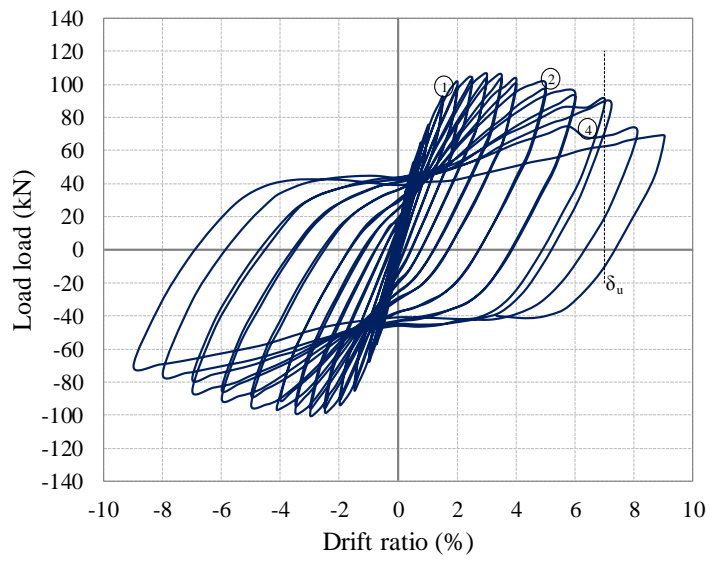


**Figure 12-19: Load-displacement hysteretic response of column SD-GLAS**

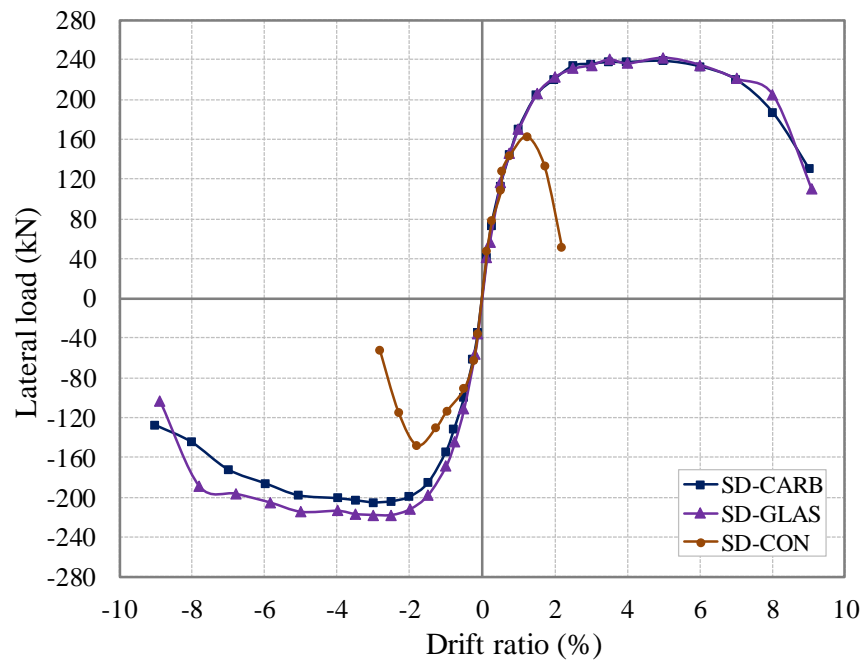


Figure 12-20: Shear dominated RC columns

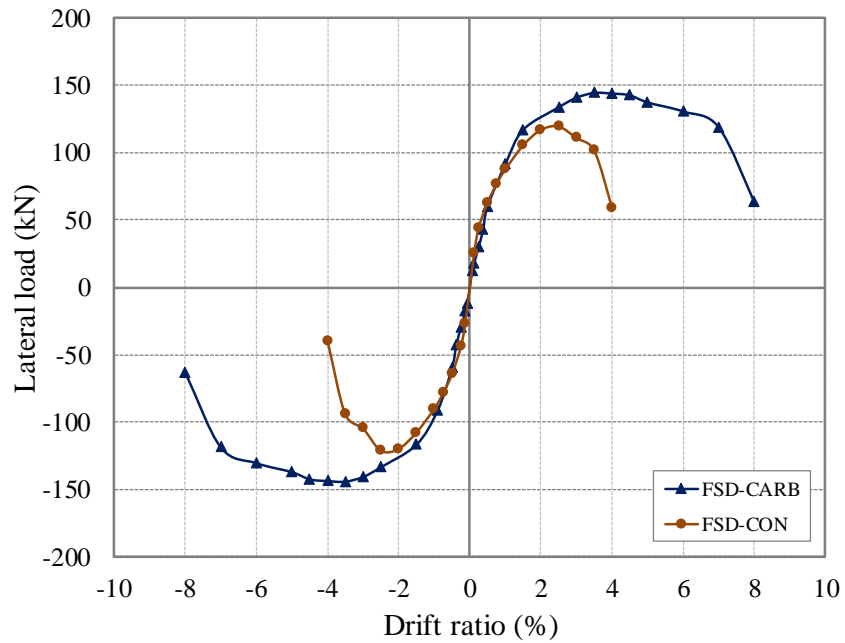


Figure 12-21: Flexure-shear dominated RC columns

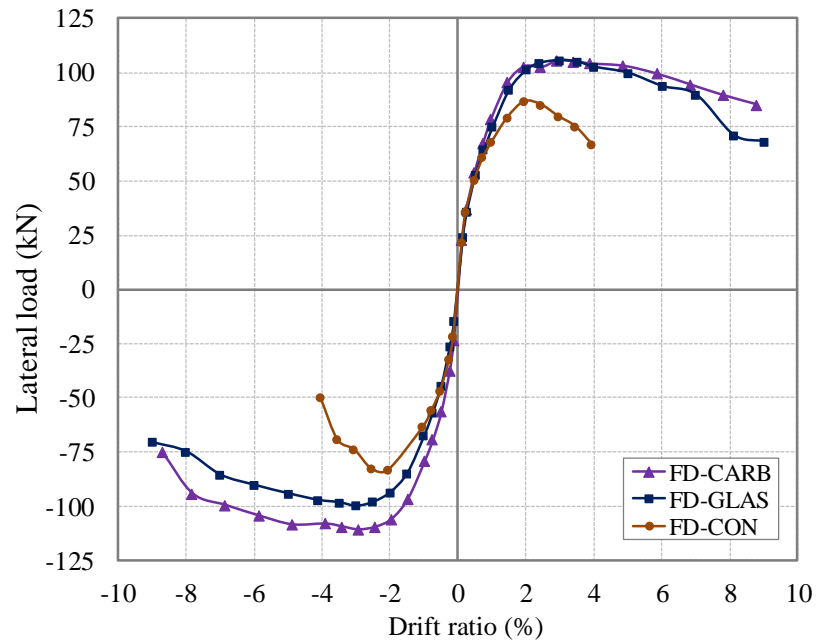


Figure 12-22: Flexure dominated RC columns

### 12.5.1 Shear dominated RC columns

In the shear dominated control specimen SD-CON, Initial cracking was observed at 0.50% lateral drift at 150 mm and 200 mm height from the pedestal. These cracks increased in number as the lateral drifts increased. At 1.5% specimen reached its peak lateral strength. At this stage (1.5% lateral drift) an inclined shear crack was observed. At 2% lateral drift another large shear crack appears from other side. 20% of peak lateral strength dropped at 2% drift. With increasing drift beyond 2% it was observed that shear plan penetrating downward and increase in axial deformation was observed. The shear crack increased in width as the lateral drift increased. At 2.5% drift buckling of longitudinal reinforcement was observed from strain variation at 400-500 mm height from the pedestal. At 3.5 % lateral drift ultimate gravity load collapse occurred due to excessive core crushing as shown in the Figure 12-23 [99].

The SFRP strengthened shear dominated RC columns exhibited excellent performance up to drift ratio more than 8. In the both specimens (i.e. SD-GLAS and SD-CARB) there were no flexural cracks observed up to the lateral drift of 1.5%. Few flexural cracks were start appearing at 2.0% lateral drift at about 100-200 mm above the top level of SFRP. Further during the whole experiment no more cracks were observed with

no cover concrete spalling. At 5.0% (230% higher lateral drift compared with control specimen) lateral drift peak lateral strength was reached in both SFRP strengthened shear dominated specimens (i.e. SD-CARB and SD-GLAS). At 8% lateral drift (second cycle) buckling of the longitudinal reinforcement started, and 20% drop in peak lateral strength reached. Overall for both SFRP strengthened shear dominated specimens, the SFRP jackets enhanced 46-48% strength and also improved the displacement ductility considerably (166%) compared with un-strengthened specimen. Figure 12-24 shows an image of the SFRP strengthened specimens SD-GLAS at 9% lateral drift. Tests were stopped at 9% lateral drift due to the limitations of test setup and to avoid any damage to the test equipment.



**Figure 12-23: Failure mode of column SD-CON at 3.5% lateral drift**



**Figure 12-24: Failure mode of column SD-GLAS at 9% lateral drift**

### 12.5.2 Flexure-shear dominated RC columns

In the flexure-shear dominated control specimen FSD-CON, initial flexural cracking were observed at 0.50% lateral drift, at location of 250mm and 350mm from above the pedestal level. These cracks increase in number as the lateral drift increased. At 2.5% lateral drift the peak lateral strength was achieved. At 2.5% lateral drift cover concrete started spalling. At lateral drift of 3.5% a shear crack was observed which was later widened in width and length and at the same stage transverse reinforcement yielded. Lateral strength dropped to 20% of peak lateral strength at 3.5% drift. At 4% lateral drift longitudinal steel was visible with large crushing of the concrete as shown in the Figure 12-25 [99].

Compared to the reference specimen (FSD-CON), the behavior of the SCFRP strengthened specimen (FSD-CARB) was more ductile. Initial flexural cracking were observed at 1% lateral drift at about 100-300 mm above the top level of SCFRP. These



cracks increase slightly in number as the lateral drift increased. At 5% lateral drift (100% higher lateral drift compared with control specimen) the peak lateral strength was achieved. At 7% lateral drift buckling of the longitudinal reinforcement started, and 20% drop in peak lateral strength reached. The strength and ductility of the SCFRP strengthened specimen FSD-CARB was recorded almost 20% and 102%, respectively, higher than un-strengthened specimens FSD-CON. Figure 12-26 shows an image of the SCFRP strengthened specimen FSD-CARB at 9% lateral drift. Test was stopped at 9% lateral drift due to the limitations of test setup and to avoid any damage to the test equipment.



**Figure 12-25: Failure mode of column FSD-CON at 4% lateral drift**



**Figure 12-26: Failure mode of column FSD-CARB at 9% lateral drift**

### 12.5.3 Flexure dominated RC columns

In the flexure dominated control specimen FD-CON, Visible flexural crack start appearing at 0.5% lateral drift at about 150mm, 450mm and 550mm above the pedestal level. With increasing the lateral drift number of flexural cracks goes on increasing. At 1.5% lateral drift cover concrete start spalling at about 150 mm where the maximum moment occurred. This spalling of cover concrete increases as lateral drift increases. At 2.0% lateral strength peak lateral strength reached. At 2% lateral drifts cracks along the corner reinforcement start appearing, these cracks increased in length and width as the strain in this region goes on increasing with increasing lateral drift. At 4% buckling of the longitudinal reinforcement started, and 20% drop in peak lateral strength reached (Figure 12-27) [99].

For SFRP strengthened specimens (FD-GLAS and FD-CARB), the results showed that the SFRP jackets improved the flexural strength and flexural ductility. The behavior of SFRP strengthened specimen FD-GLAS and FD-CARB was observed similar irrespective of strengthening material type (i.e. glass and carbon). Initial flexural

cracking were observed at 0.75% lateral drift at about 50-500 mm above the top level of SFRP. These cracks increased in number as the lateral drift was increased. At 3.0% (50% higher lateral drift compared with control specimen) lateral drift, peak lateral strength was reached in both SFRP strengthened flexure dominated specimens (i.e. FD-CARB and FD-GLAS). In SGFRP strengthened RC column FD-GLAS, rupture of longitudinal reinforcement was observed at 7% lateral drift thus resulting into sudden 20% drop in peak lateral strength. Whereas in SCFRP strengthened RC column FD-CARB, no signs of buckling or rupture of reinforcement were observed up to 9% lateral drift and test was stopped due to limitations of the test setup to avoid any damage to the test equipment. Figure 12-28 shows an image of the SFRP strengthened RC column specimens at 9% lateral drift.



**Figure 12-27: Failure mode of column FD-CON at 4.5% lateral drift**

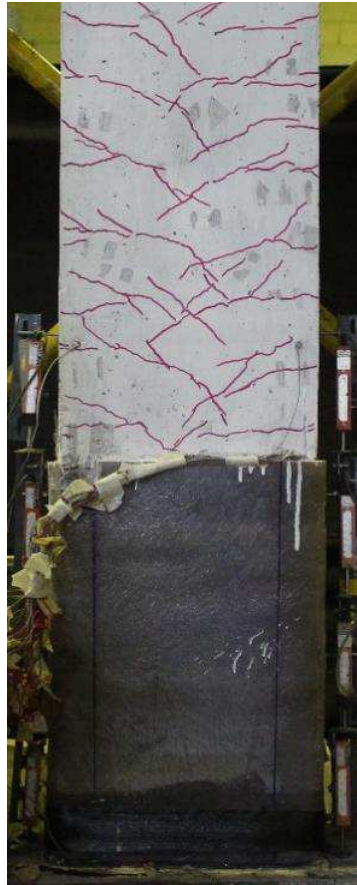


**Figure 12-28: Failure mode of column FD-GLAS at 9% lateral drift**

## 12.6 Ductility

The displacement ductility ratio  $\mu_\epsilon$  is here defined as the ratio between ultimate displacement and yielding displacement. Those specimens with larger displacement ductility ratio had better ductility. The displacement ductility ratio of all RC column specimens is given in the Table 12-2. A comparison of the skeleton curves of the SFRP strengthened and control specimens is shown in Figures 12-20 to 12-22. As it can be observed from Table 12-2 and Figures 12-20 to 12-22, the ductility of the un-strengthened specimens is lower and the ductility of the both SCFRP and SGFRP strengthened RC columns is greatly improved. However the initial stiffness of the SFRP strengthened specimens is almost same as the un-strengthened ones.

The displacement ductility ratio of un-strengthened specimen SD-CON is 2.0, and that of the SFRP strengthened specimens SD-CARB and SD-GLAS is 5.33. Both strengthening fiber materials (i.e. carbon and glass) resulted into similar increased ductility compared with un-strengthened specimens. The displacement ductility ratio of un-strengthened specimen FSD-CON is 2.33, and that of the SCFRP strengthened specimens FSD-CARB is 4.70. Whereas, the displacement ductility ratio of un-strengthened specimen FD-CON is 2.67, and that of the SFRP strengthened specimens FD-CARB and FD-GLAS is 5.33 and 4.70, respectively. Here in case of flexure dominated RC columns, the SCFRP strengthening performs better than SGFRP strengthening. Since the breakage of the longitudinal bars is observed in the FD-GLAS at lateral drift ratio of 7.0%, thus resulting into sudden loss of load carrying capacity and lower ductility ratio.

## 12.7 Development of strain in steel bars

The strains in the longitudinal reinforcement were measured using strain gauges installed on the bars at the center of the flexural faces. Whereas; strains in the transverse reinforcement were measured using strain gauges installed at the centers of the stirrups as shown in Figure 12-8. Hysteretic responses of the longitudinal and transverse steel bars are shown in Figures 12-29 to 12-36. The strain variation in the longitudinal reinforcement of SCFRP strengthened RC columns (i.e. shear and flexure dominated) is shown in Figure 12-39. The yielding of longitudinal reinforcement and transverse

reinforcement along with buckling of longitudinal reinforcement captured from the hysteretic load-strain responses are marked as 1, 2 and 3 respectively in Figures 12-29 to 12-38. It can be seen that yielding of longitudinal and transverse reinforcement always resulted in a rapid increase in the tensile strains of longitudinal and transverse reinforcement. However, the buckling of the longitudinal reinforcement did not change much the responses of the transverse reinforcement. It can be observed from Figures 12-12 to 12-19 (Lateral load versus drift ratio) that the yield of transverse steel reinforcement occurred at lateral displacements of approximately 3%-5% for all SFRP strengthened RC columns. It is noticeable that for reference specimens (SD-CON, FSD-CON and FD-CON) the ultimate state was reached immediately after the buckling of longitudinal reinforcement. However for the SFRP strengthened specimens the buckling of longitudinal reinforcement did not lead to an immediate degradation of the load carrying capacity.

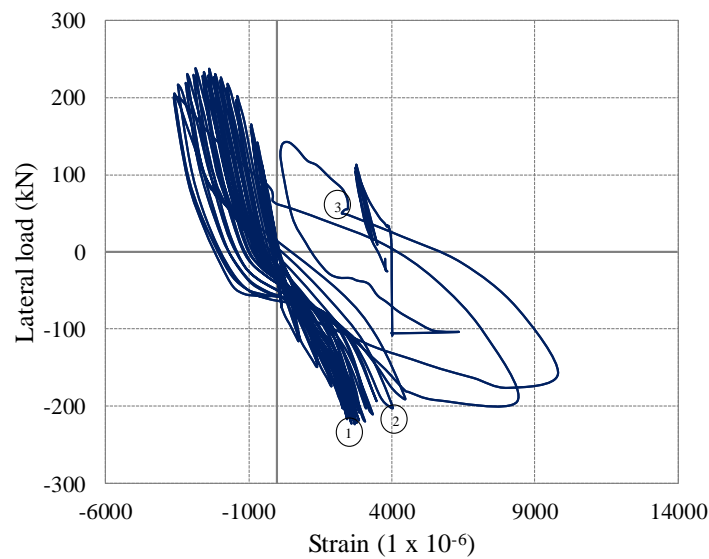


**Figure 12-29: Strain in longitudinal reinforcement (SD-CARB)**

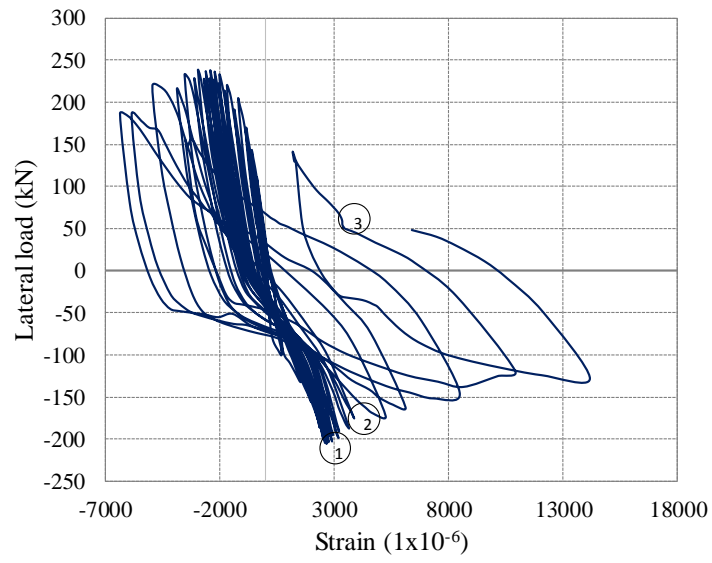


**Figure 12-30: Strain in longitudinal reinforcement (SD-GLAS)**

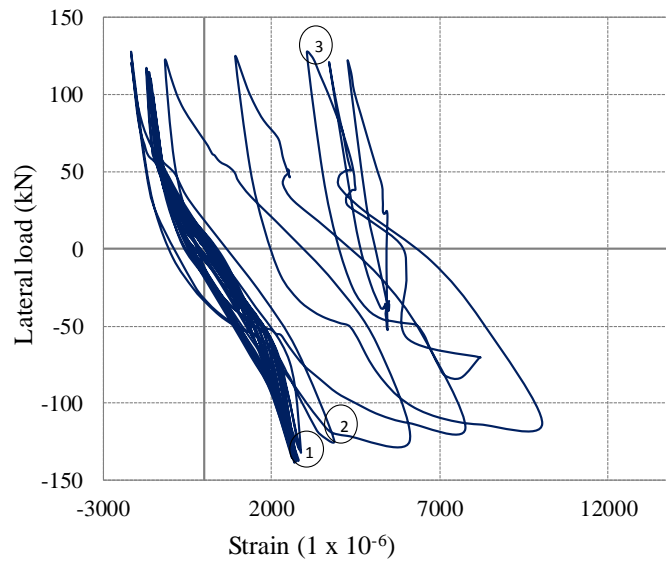


**Figure 12-31: Strain in longitudinal reinforcement (FSD-CARB)**

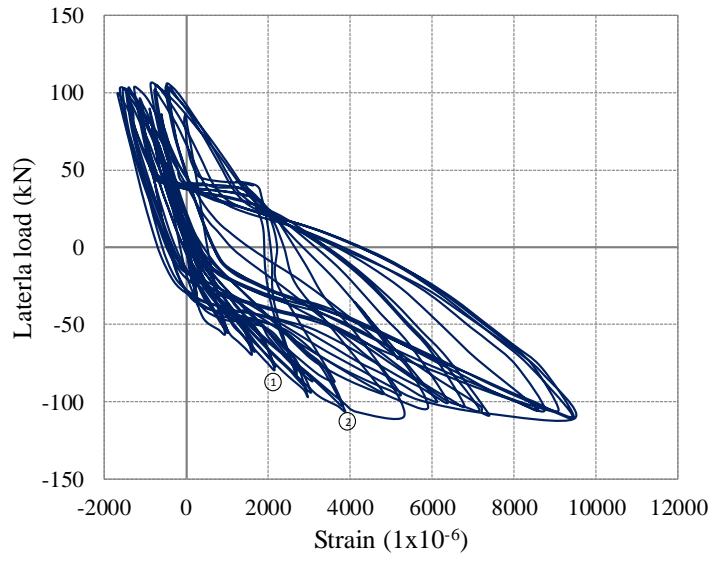


**Figure 12-32: Strain in longitudinal reinforcement (FD-CARB)**

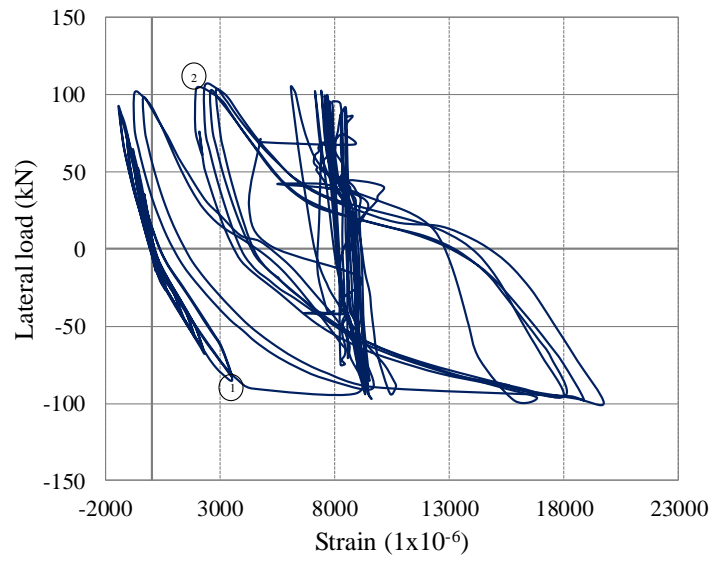


**Figure 12-33: Strain in longitudinal reinforcement (FD-GLAS)**



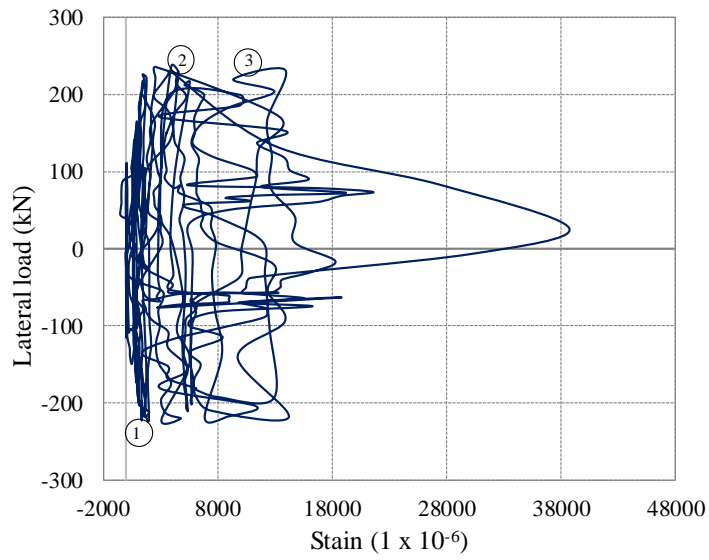


**Figure 12-34: Strain in Transverse reinforcement (SD-CARB)**

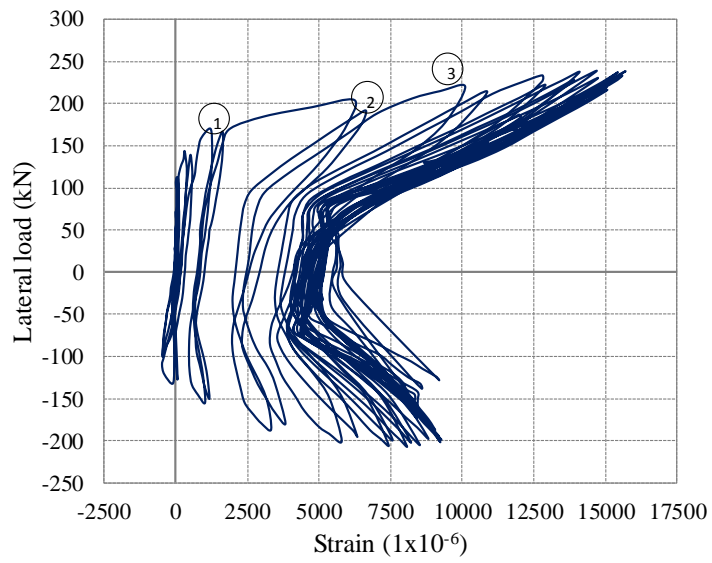


**Figure 12-35: Strain in Transverse reinforcement (SD-GLAS)**

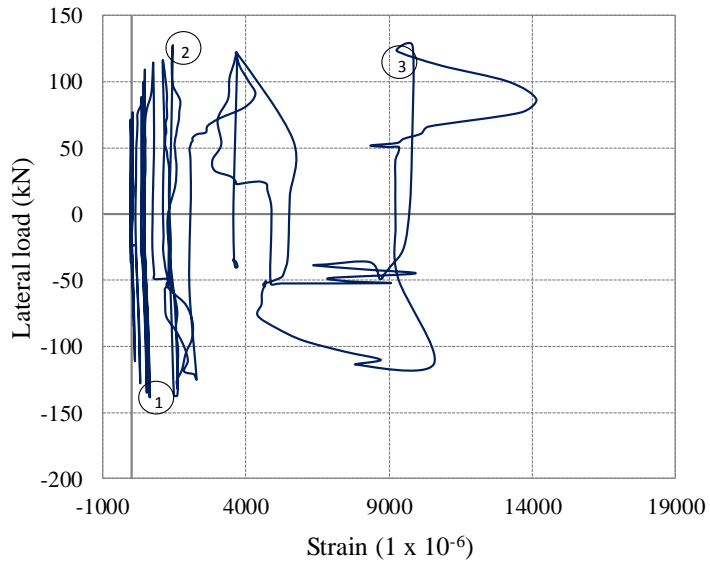


**Figure 12-36: Strain in Transverse reinforcement (FSD-CARB)**

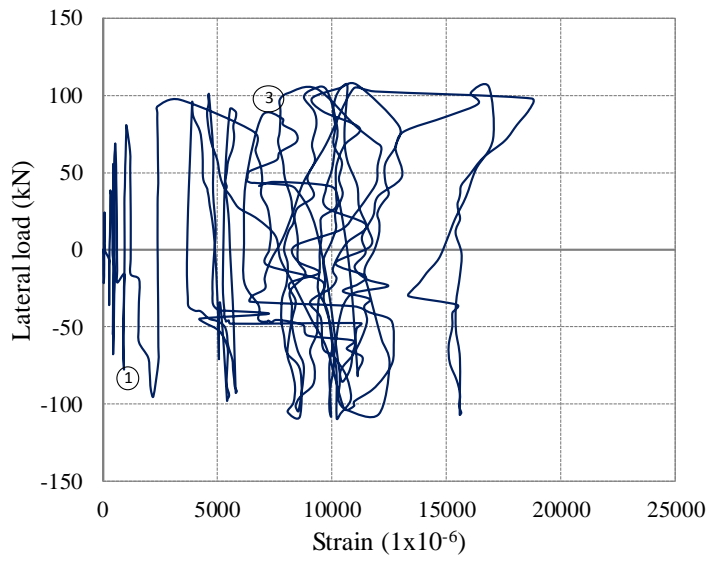


**Figure 12-37: Strain in Transverse reinforcement (FD-CARB)**

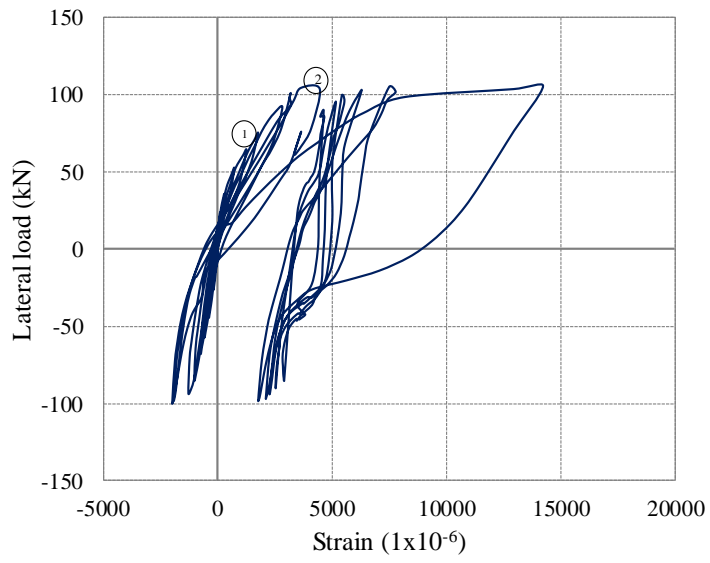
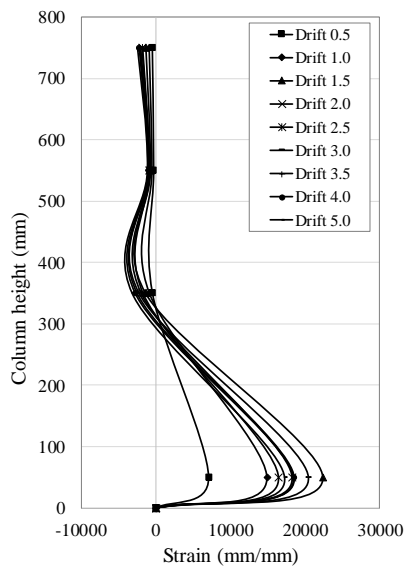
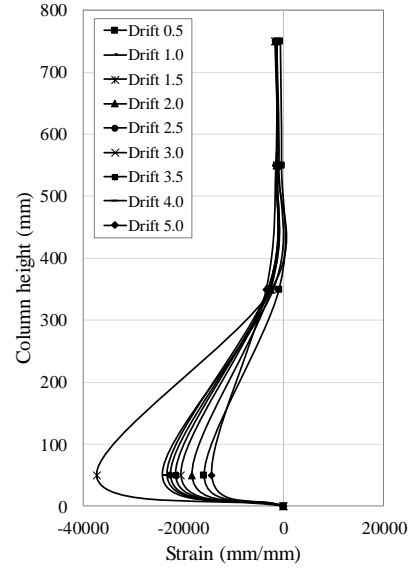


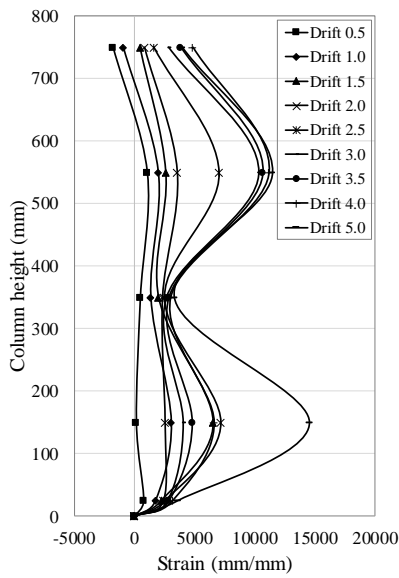
**Figure 12-38: Strain in Transverse reinforcement (FD-GLAS)**



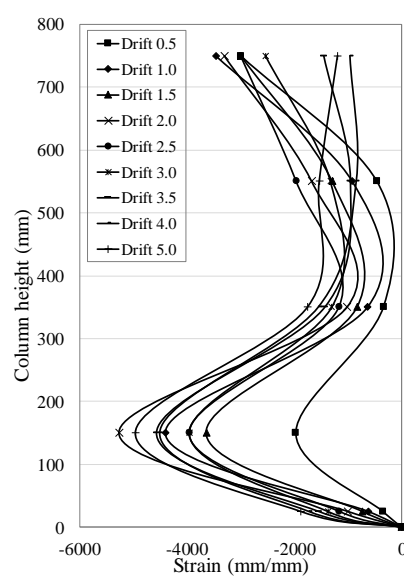
(a) SD-CARB (Tension)



SD-CARB (Compression)



(b) FD-CARB (Tension)



FD-CARB (Compression)

**Figure 12-39: Strain distribution along longitudinal reinforcement**

## 12.8 Stiffness

To evaluate further the effectiveness of SFRP strengthening versus unstrengthened specimens, the stiffness curves (instantaneous secant stiffness at a certain displacement) are plotted in Figures 12-40 to 12-42. On these figures, a positive value of cycle number corresponds to a loading cycle involving upward lateral displacement, and negative values are related to cycles involving downward displacement. The initial stiffness of all un-strengthened RC columns is lower compared with SFRP strengthened specimens but there is no significant different in terms of initial stiffness between two strengthening material (i.e. carbon and glass). Moreover, from Figures 12-40 to 12-42, it can be observed that the SFRP strengthening is resulted into improved stiffness of RC columns irrespective of their aspect ratio (i.e. shear, flexure-shear and flexure dominated).

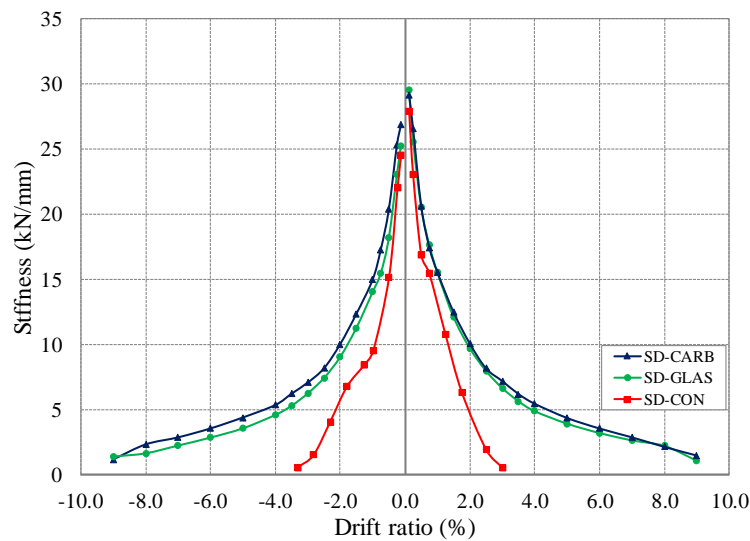


Figure 12-40: Stiffness degradation curves of shear dominated RC columns

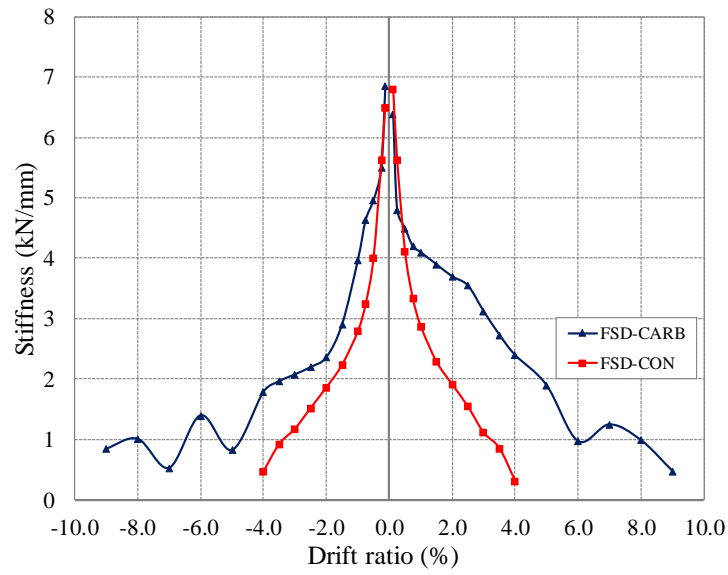


Figure 12-41: Stiffness degradation curves of flexure-shear dominated RC columns

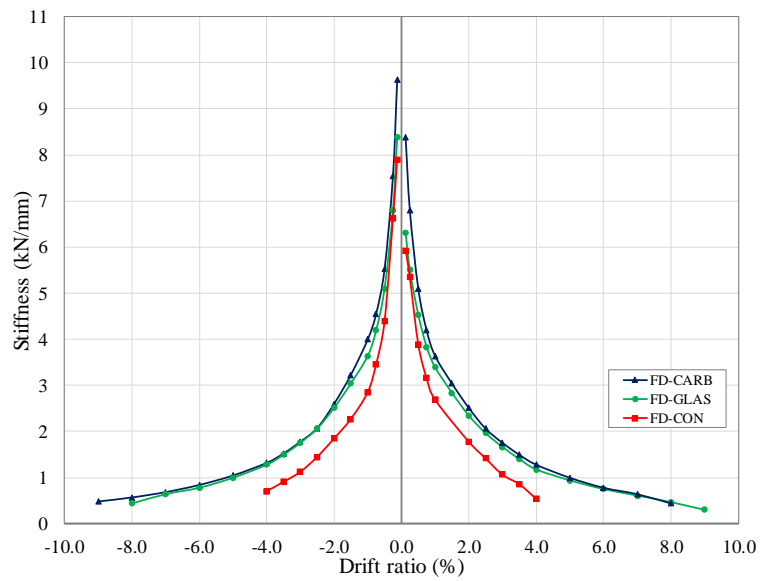


Figure 12-42: Stiffness degradation curves of flexure dominated RC columns

## 12.9 Cumulative dissipated energy

The cumulative hysteretic dissipation energy was evaluated for all the tests, considering the area of each loading cycle in the X and Y direction and then the total energy was calculated as the sum of these two parts. The cumulative energy dissipation versus the lateral drift ratio is presented in Figures 12-43 to 12-45. It can be seen that SFRP strengthened RC columns permits to dissipate more energy compared with un-strengthened specimens. This is mainly due to the plastic hinge zone confinement provided by the SFRP jackets. The RC columns confined with SFRP in the plastic hinge zone can experience bigger deflections. However if we see on the first part of graphs (i.e. until failure of SD-CON, FSD-CON, and FD-CON), there is no significant difference between the curves of strengthened and un-strengthened specimens. Further, it can be observed that there is no noticeable difference between the two strengthening materials (i.e. carbon and glass) in terms of energy absorption capacity. For a same displacement path, the same energy dissipation occurred in both SCFRP and SGFRP strengthened RC columns.

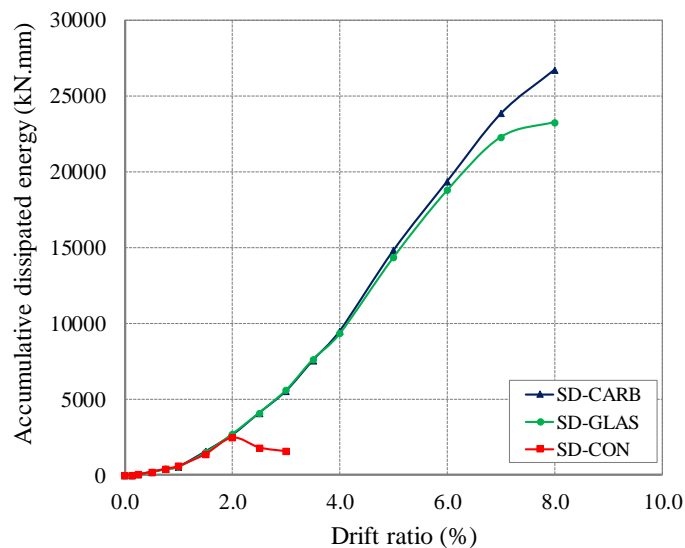


Figure 12-43: Cumulative dissipated energy of shear dominated RC columns

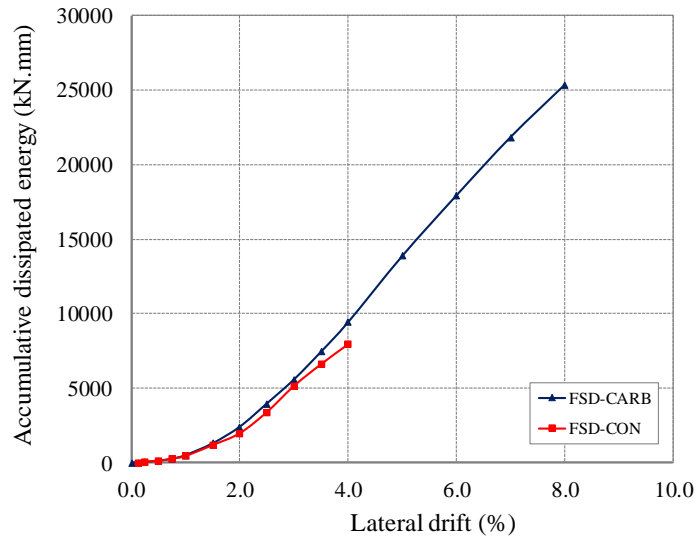


Figure 12-44: Cumulative dissipated energy of flexure-shear dominated RC columns

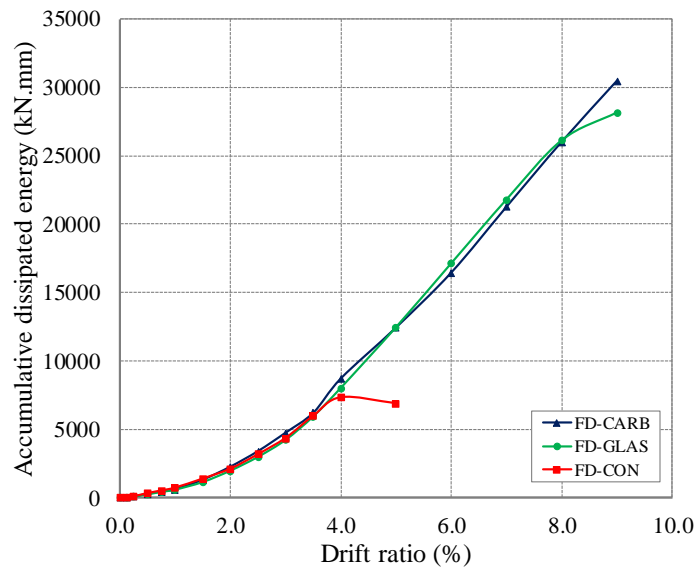
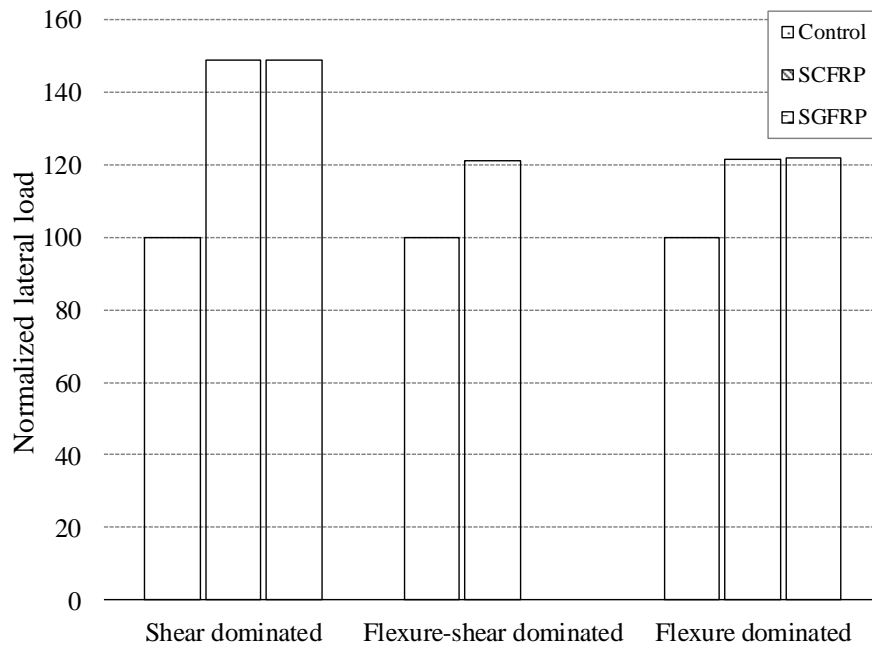


Figure 12-45: Cumulative dissipated energy of flexure dominated RC columns



### 12.10 Effect of aspect ratio

From Table 12-2, it can be seen that all un-strengthened RC columns were failed due to the crushing of concrete and buckling of steel bars within the plastic hinge region with ductility of 2.30-2.67. Whereas, SFRP strengthened RC columns exhibited excellent performance up to ductility of 4.70-5.33. The comparison of normalized lateral load and normalized displacement ductility ratio of SFRP strengthened and un-strengthened specimens is presented in Figure 12-46 and 12-47, respectively. In each group of RC columns, the maximum lateral load and displacement ductility ratio of the control un-strengthened specimen is set as a benchmark, by normalizing its maximum lateral load and ductility 100%, and the effectiveness of SFRP is computed as the percentage ratio of the lateral load and ductility to that of the control specimen. From Figure 12-46, it can be seen that efficiency of SFRP strengthening in terms of maximum lateral load is higher for shear dominated columns compared with flexure-shear and flexure dominated columns. Overall, 48%, 20% and 21% increases in maximum lateral load is observed for shear, flexure-shear and flexure dominated SFRP strengthened RC columns, respectively. Similar to the maximum lateral load, increase in ductility due to SFRP jacketing is found higher for shear dominated columns compared with others. In Figure 12-46, 166%, 101% and 99% increases in ductility is observed for SCFRP strengthened RC columns SD-CARB, FSD-CARB and FD-CARB, respectively. Whereas, 166% and 76% increases in ductility is recorded for SD-GLAS and FD-GLAS, respectively.



**Figure 12-46: Comparison of maximum lateral load**

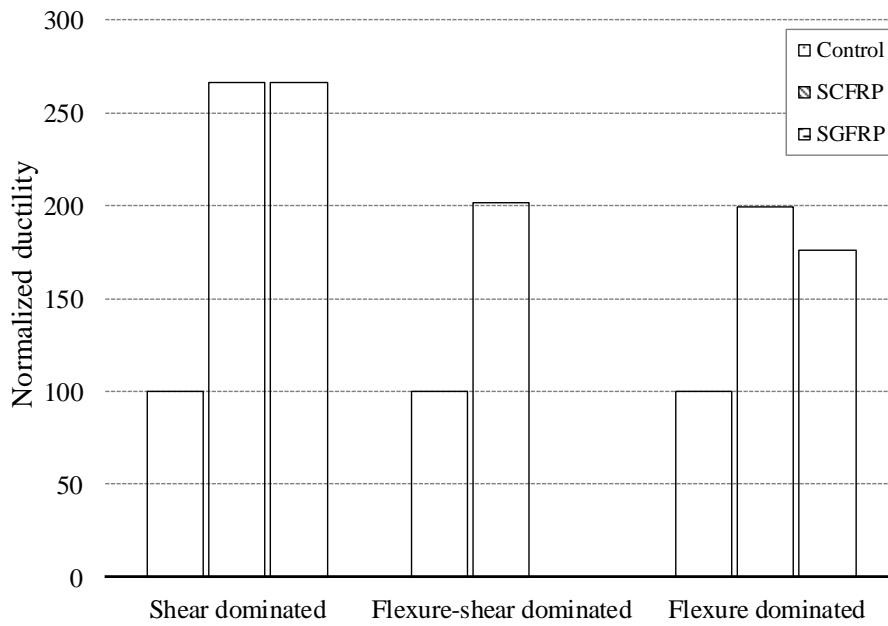


**Figure 12-47: Comparison of ductility**

### **12.11 Effect of SFRP material**

RC columns strengthened with SCFRP and SGFRP exhibited excellent performance in terms of strength and ductility enhancement compared with un-strengthened specimens. SCFRP and SGFRP jacketing is resulted into similar increase of maximum lateral load for shear and flexure dominated RC columns as shown in the Figure 12-46. For both strengthening materials, 48% and 22% increases in maximum lateral load was observed for shear and flexure dominated RC columns, respectively. In accordance with strength increase, SCFRP and SGFRP strengthening materials also resulted into similar increase in ductility. 166% increases in ductility is recorded for RC columns specimens SD-CARB and SD-GLAS. However, in flexure dominated RC columns, the SGFRP strengthened RC column FD-GLAS is resulted into lower ductility compared with SCFRP strengthened RC column FD-CARB. 125% and 76% increases in ductility is recorded for specimens SD-CARB and SD-GLAS, respectively. This exception may can be associated with rupture of the longitudinal reinforcement which was observed in RC column SD-GLASS. The behavior of both strengthening materials is also found similar in terms of stiffness and cumulative energy dissipation as shown in Figures 12-40 to 12-45.

### **12.12 Bulging of concrete**

In RC columns retrofitted with conventional unidirectional FRP, failure of FRP jacketing is reported as bulging out of the concrete and FRP near column ends following the fracture in the FRP wrap in the hoop direction as shown in the Figure 12-48 [34, 104, 112]. However, in All SFRP strengthened RC columns, no bulging out of concrete and SFRP were observed (Figures 12-24, 12-26 and 12-28). This is indicating the effectiveness of SFRP to confine concrete. Since SFRP are comprised of randomly distributed fibers, the tensile strength of composite is uniform in both directions thus avoiding rupture in hoop direction. In addition, SFRP are low price compared with unidirectional FRP and can be sprayed with large thickness. RC columns were strengthened with 10 mm thickness of SFRP. Since the strength and stiffness of SFRP composite varied with thickness, a stiffer SFRP jacket is more helpful to avoid outward bulging of concrete.



Figure 12-48: Rupture of FRP strap in hoop direction in FRP strengthened RC Column [34]

### 12.13 Observed failure modes

In un-strengthened RC column specimens, a higher rate of lateral strength degradation was observed, especially after yielding of stirrups, rate of lateral strength degradation has been found increased significantly. Difference of rate of lateral strength degradation for FSD-CON and FD-CON is marginal owing to small change in shear demand. In specimen SD-CON, pre-mature buckling of longitudinal reinforcement was observed at an early stage after developing large shear cracks. In case of flexure-shear dominated and flexure dominated RC columns (FSD-CON, FD-CON) longitudinal reinforcement buckled at 100 mm from the bottom where the maximum moment occurred. Overall all un-strengthened RC columns were failed due to excessive crushing of concrete and buckling of longitudinal reinforcement in the plastic hinge region [3]. In contrast to the un-strengthened specimens, SFRP strengthened columns showed excellent performance up to lateral drift ratio more than 8 due to the confinement effect of SFRP. Rate of lateral strength degradation is observed very gradual in SFRP strengthened RC columns compared with un-strengthened RC columns. No buckling of longitudinal steel bars were observed in flexure dominated RC columns owing to confinement effect of SFRP in plastic hinge area. Whereas buckling of longitudinal reinforcement in medium and short columns started very late (after 6% lateral drift). In SFRP

strengthened RC columns, minor cracking was observed in parts above the SFRP, however the width and number of cracks was found very less due to low moment seismic demand in upper part of columns.

## Chapter 13

### Conclusions and Recommendations

#### 13.1 Conclusions

In general, the experimental results obtained in this study, support the hypothesis that Sprayed glass fiber reinforced polymers and sprayed carbon fiber reinforced polymers do have the potential to become a feasible alternative to existing strengthening techniques for reinforced concrete members.

The sprayed fiber technique used in this research is capable of producing a reliable fiber reinforced polymer composites which exhibit tow dimensionally isotropic strength properties. With the shopper/spray equipment use for study, glass and carbon fiber reinforced polyester matrix was produced. These materials exhibited maximum composite strength of 92 and 104 MPa for glass and carbon SFRP, respectively. Material strength properties are highly depended upon fiber length and fiber material.

The application process of SFRP is very easy and straightforward which requires a minimal amount of operator training. Thickness of SFRP material is directly controlled and managed by the operator, resulting in more flexibility in the design process compared with conventional unidirectional FRPs. One salient feature of the SFRP is their ability to easily bend around much sharper corners than unidirectional continuous fiber fabrics.

SFRP is effective to enhance the strength and deformability of concrete for both circular and square sections. The increase in the compressive strength and deformability varies with the SFRP shell thickness for both circular and square sections. The fiber length of 26 mm was found to be superior to 13 mm, both in terms of ultimate strength and deformability enhancement. The efficiency of SFRP for providing the external confinement and the resulting increase in strength and ductility is greater in circular columns than in square columns.

It was found that almost all strength models (developed for conventional unidirectional FRP) are conservative to predict the experimental compressive strength of SFRP-confined concrete. New strength models propose for SFRP confined concrete are capable to predict the compressive strength of SFRP confined concrete columns.

The SFRP was shown to be capable of significantly increasing both the strength and stiffness of RC deep beams with and without web openings. However, the application of SFRP without anchoring system was not effective to enhance the ultimate load and deflection. The sole application of SFRP produces almost the same performance as the unstrengthened beam due to the premature SFRP debonding failure that inhibited the development of the usable SFRP strength. SFRP slits made on the beam surfaces provided a little increase in the ultimate load. The slits could not prevent the debonding of SFRP from concrete surface. The beneficial effect of SFRP slits was low, in comparison to other proposed anchoring systems. Three proposed anchoring systems (i.e. TB, MB and EB systems) are found to be effective to prevent the delamination of SFRP. Provided that they are installed at close spacing and with enough embedment length, they could effectively inhibit the debonding failure and brought about more favourable failures such as concrete crushing and SFRP rupture that could mobilise higher strength. The effectiveness of these anchoring systems depends on the thickness of SFRP. The thicker SFRP requires a stronger anchoring system to firmly fix it with the specimens. Among the three anchoring systems, TB system is found to be the most effective technique to hold the SFRP. The thickness of SFRP has a great impact on the increase in the ultimate load and deflection of deep beams, both for low- and high- strength concrete. The increase in the ultimate load was in proportion to the thickness provided that sufficient anchoring system is installed to prevent premature debonding failure. Both strengthening configurations A and B were found to be efficient to increase the ultimate load and deflection of RC deep beams. Strengthening configuration B resulted in a little higher increase in the ultimate load as compared to strengthening configuration A due to the additional benefits on the bonding enhancement at the bottom face. SCFRP resulted in a higher increase in the ultimate load than SGFRP. The load increase was supposedly due to the higher tensile strength of carbon fibres over the glass fibres.

The externally bonded SFRP was remarkably effective to increase the ultimate load of the RC deep beams with both the square and circular openings and both low- and high-strength concrete beams. The mechanical Expansion Bolt (MB) anchoring system was effective to prevent the de-bonding failure of the SGFRP from concrete surface. In this study, no pullout of the expansion bolts and de-bonding failure was

observed for beams with MB anchoring system, except for the specimen HS-7A-S12 which was strengthened with a 7 mm thick SFRP. All strengthening configurations (A, B and C) enhanced the shear strength of the RC deep beams with openings by a factor of 1.5-2.4. The strengthening configuration B was superior to configurations A and C. The increase in the ultimate load of RC deep beams with opening varied with the thickness of SFRP. The higher the SFRP thickness, the higher the increase in the ultimate load. The efficiency of the SGFRP strengthening and MB anchoring system was lower for the high-strength concrete specimens as compared with the low-strength specimens. The SGFRP-strengthened RC deep beams with sufficient anchoring system failed by the inclined crack rupture in the SGFRP, whereas the failure was pullout of anchors and accompanying SGFRP de-bonding when the anchoring system was not sufficient.

The finite element analysis results are found to be in good agreement with experimental results for both low and high strength concrete RC deep beams with and without web openings. The finite element models are also capable of simulating the behavior of RC deep beams strengthened with glass and carbon fibers. The analytical models successfully show the crack propagation and failure modes of RC deep beams.

The SFRP was shown to be capable of significantly increasing both the strength and stiffness of RC Columns, while at the same time dramatically improving their energy absorption characteristics. SFRP strengthening is found effective for different types of columns (i.e. shear, flexure-shear and flexure dominated) to increase strength and ductility. However, percentage increase in strength and ductility is found higher for shear dominated RC columns compared with flexure-shear and flexure dominated RC columns.

### **13.2 Recommendations for future research work**

Probably the most obvious suggestion for continued research into SFRP technique is to investigate the feasibility of implementing this technique in the field. The design of the apparatus used in this process appears to be well adapted for such use since it is completely portable and requires minimal support equipment. However, in its current configuration on site use would be very difficult since the spraying of overhead surfaces is virtually impossible without modifications to equipment design.



Future studies should examine a wider range of geometry, SFRP material thickness, SFRP material properties and they should also be concerned with a more systematic comparison between the specimens strengthened with SFRP and conventional unidirectional FRP with equivalent jacket stiffness.

## References

- [1] S. Qazi, L. Michel, and E. Ferrier, "Experimental investigation of CFRP anchorage systems used for strengthening RC joints," *Composite Structures*, vol. 99, pp. 453-461, 2013.
- [2] S. M. A. a. J. O. Jirsa, "Strength of reinforced concrete frame connections rehabilitated by jacketing," *ACI Structural Journal*, vol. 90, 1993.
- [3] E. Julio, F. Branco, and V. Silva, "Structural rehabilitation of columns with reinforced concrete jacketing," *Progress in Structural Engineering and Materials*, vol. 5, pp. 29-37, 2003.
- [4] E. N. Julio and F. A. Branco, "Reinforced Concrete Jacketing--Interface Influence on Cyclic Loading Response," *ACI Structural Journal*, vol. 105, 2008.
- [5] Y. Xiao and H. Wu, "Retrofit of reinforced concrete columns using partially stiffened steel jackets," *Journal of Structural Engineering*, vol. 129, pp. 725-732, 2003.
- [6] E. Choi, J. Park, T.-H. Nam, and S.-J. Yoon, "A new steel jacketing method for RC columns," *Magazine of Concrete Research*, vol. 61, pp. 787-796, 2009.
- [7] A. Ghobarah, T. S. Aziz, and A. Biddah, "Rehabilitation of reinforced concrete frame connections using corrugated steel jacketing," *ACI Structural Journal*, vol. 94, 1997.
- [8] L. C. Bank, *Composites for construction: structural design with FRP materials*: John Wiley & Sons, 2006.
- [9] A. J. Boyd, "Rehabilitation of reinforced concrete beams with sprayed glass fiber reinforced polymers," 2000.
- [10] Y. Xiao and H. Wu, "Compressive behavior of concrete confined by carbon fiber composite jackets," *Journal of Materials in Civil Engineering*, vol. 12, pp. 139-146, 2000.
- [11] V. M. Karbhari and Y. Gao, "Composite jacketed concrete under uniaxial compression-verification of simple design equations," *Journal of materials in civil engineering*, vol. 9, pp. 185-193, 1997.
- [12] P. Rochette and P. Labossiere, "Axial testing of rectangular column models confined with composites," *Journal of Composites for Construction*, vol. 4, pp. 129-136, 2000.
- [13] J.-G. Dai, Y.-L. Bai, and J. Teng, "Behavior and modeling of concrete confined with FRP composites of large deformability," *Journal of Composites for Construction*, vol. 15, pp. 963-973, 2011.
- [14] R. Irwin and A. Rahman, "FRP strengthening of concrete structures--design constraints and practical effects on construction detailing," *Available: Science Direct, www.sciencedirect.com.[Accessed September, 2009]*, 2002.
- [15] N. Banthia, C. Yan, and N. Nandakumar, "Sprayed Fiber Reinforced Plastics (FRPs) for Repair of Concrete Structures," in *PROCEEDINGS OF THE 2ND INTERNATIONAL CONFERENCE ON ADVANCED COMPOSITE MATERIALS IN BRIDGES AND STRUCTURES, ACMBS-II, MONTREAL 1996*, 1996.

- [16] H. Lee and L. Hausmann, "Structural repair and strengthening of damaged RC beams with sprayed FRP," *Composite structures*, vol. 63, pp. 201-209, 2004.
- [17] H. Lee, R. Hausmann, and W. Seaman, "Effectiveness of retrofitting damaged concrete beams with sprayed fiber-reinforced polymer coating," *Journal of Reinforced Plastics and Composites*, vol. 27, pp. 1269-1286, 2008.
- [18] S. M. Soleimani, "Sprayed glass fiber reinforced polymers in shear strengthening and enhancement of impact resistance of reinforced concrete beams," 2006.
- [19] N. Banthia and A. Boyd, "Sprayed fibre-reinforced polymers for repairs," *Canadian Journal of Civil Engineering*, vol. 27, pp. 907-915, 2000.
- [20] H. Lee, W. Suaris, and L. Hausmann, "Experimental study on structural enhancement of sprayed fiber-reinforced composites for retrofit/strengthening of concrete beams," *Composites Part B: Engineering*, 2003.
- [21] K. Y. Kwon, D. Y. Yoo, S. C. Han, and Y. S. Yoon, "Strengthening effects of sprayed fiber reinforced polymers on concrete," *Polymer Composites*, 2014.
- [22] H. Lee, "Effectiveness of anchorage in concrete beams retrofitted with sprayed fiber-reinforced polymers," *Journal of reinforced plastics and composites*, vol. 23, pp. 1285-1300, 2004.
- [23] S. Ross, A. Boyd, M. Johnson, R. Sexsmith, and N. Banthia, "Potential retrofit methods for concrete channel beam bridges using glass fiber reinforced polymer," *Journal of Bridge Engineering*, vol. 9, pp. 66-74, 2004.
- [24] T. Cristina, "FIBER REINFORCED PLASTICS (SFRP's) for REPAIR and STRENGTHENING of CONCRETE BRIDGE STRUCTURES: AN ANALYSIS."
- [25] T. Kanakubo, T. Furuta, K. Takahashi, and T. Nemoto, "SPRAYED FIBER-REINFORCED POLYMERS FOR STRENGTHENING OF CONCRETE STRUCTURES," ed: Japan, 2010.
- [26] B. Scholefield, "Rehabilitation of reinforced concrete columns by various methods," M. Sc. thesis. University of Calgary, Calgary, Alta, 2003.
- [27] E. Shaheen and N. Shrive, "Sprayed glass fibre reinforced polymer masonry columns under concentric and eccentric loading This article is one of a selection of papers published in this Special Issue on Masonry," *Canadian Journal of Civil Engineering*, vol. 34, pp. 1495-1505, 2007.
- [28] H. Lee, G. Avila, and C. Montanez, "Numerical study on retrofit and strengthening performance of sprayed fiber reinforced polymer," *Engineering structures*, vol. 27, pp. 1476-1487, 2005.
- [29] Y. Xiao, "Applications of FRP composites in concrete columns," *Advances in Structural Engineering*, vol. 7, pp. 335-343, 2004.
- [30] A. C. D.-o. P. S. D. 70.01, "Standard Test Methods for Density and Specific Gravity (Relative Density) of Plastics by Displacement," 1991.
- [31] A. Standard, "Standard test method for ignition loss of cured reinforced resin," *West Conshohocken (PA): ASTM*, vol. 100.
- [32] A. Standard, "Standard test method for tensile properties of plastics," *ASTM International. Designation: D*, vol. 638, 2003.
- [33] A. Michael, H. Hamilton III, and M. Ansley, "Concrete Confinement Using Carbon Fiber Reinforced Polymer Grid," *ACI Struct J*, vol. 230, pp. 991-1010, 2005.

- [34] H. Saadatmanesh, M. R. Ehsani, and M.-W. Li, "Strength and ductility of concrete columns externally reinforced with fiber composite straps," *ACI Structural journal*, vol. 91, 1994.
- [35] J. B. Mander, M. J. Priestley, and R. Park, "Theoretical stress-strain model for confined concrete," *Journal of structural engineering*, vol. 114, pp. 1804-1826, 1988.
- [36] M. Samaan, A. Mirmiran, and M. Shahawy, "Model of concrete confined by fiber composites," *Journal of structural engineering*, 1998.
- [37] 細谷学, 川島一彦, and 星隈順一, "A Stress-Strain Model for Concrete Cylinders Confined by Carbon Fiber Sheets," *土木学会論文集*, pp. 37-52, 1998.
- [38] I. A. Shehata, L. A. Carneiro, and L. C. Shehata, "Strength of short concrete columns confined with CFRP sheets," *Materials and Structures*, vol. 35, pp. 50-58, 2002.
- [39] M. N. Youssef, M. Q. Feng, and A. S. Mosallam, "Stress-strain model for concrete confined by FRP composites," *Composites Part B: Engineering*, vol. 38, pp. 614-628, 2007.
- [40] T. Jiang and J. Teng, "Analysis-oriented stress-strain models for FRP-confined concrete," *Engineering Structures*, vol. 29, pp. 2968-2986, 2007.
- [41] A. C150, "Standard Specification of Portland Cement," ed: ASTM International West Conshohocken, PA, 2012.
- [42] J. Berthet, E. Ferrier, P. Hamelin, G. Al Chami, M. Thériault, and K. Neale, "Modelling of the creep behavior of FRP-confined short concrete columns under compressive loading," *Materials and structures*, vol. 39, pp. 53-62, 2006.
- [43] F. E. Richart, A. Brandtzaeg, and R. L. Brown, "A study of the failure of concrete under combined compressive stresses," *University of Illinois Bulletin*; v. 26, no. 12, 1928.
- [44] M. N. Fardis and H. Khalili, "Concrete encased in fiberglass-reinforced plastic," in *ACI Journal Proceedings*, 1981.
- [45] A. Committee, "Guide for the design and construction of concrete reinforced with FRP bars," 2001.
- [46] K. MIYAUCHI, "Estimation of strengthening effects with carbon fiber sheet for concrete column," in *Proceedings of the 3rd International Symposium on Non-Metallic (FRP) Reinforcement for Concrete Structures*, 1997, pp. 217-224.
- [47] M. Saafi, H. Toutanji, and Z. Li, "Behavior of concrete columns confined with fiber reinforced polymer tubes," *ACI Materials Journal*, vol. 96, 1999.
- [48] H. Toutanji, "Stress-strain characteristics of concrete columns externally confined with advanced fiber composite sheets," *ACI Materials Journal*, vol. 96, 1999.
- [49] A. Ilki and N. Kumbasar, "Behavior of damaged and undamaged concrete strengthened by carbon fiber composite sheets," *Structural Engineering and Mechanics*, vol. 13, pp. 75-90, 2002.
- [50] L. Lam and J. Teng, "Strength models for fiber-reinforced plastic-confined concrete," *Journal of Structural Engineering*, vol. 128, pp. 612-623, 2002.

- [51] R. Benzaid, H. Mesbah, and N. E. Chikh, "FRP-confined concrete cylinders: axial compression experiments and strength model," *Journal of Reinforced plastics and composites*, vol. 29, pp. 2469-2488, 2010.
- [52] M. R. Spoelstra and G. Monti, "FRP-confined concrete model," *Journal of composites for construction*, vol. 3, pp. 143-150, 1999.
- [53] A. Mirmiran and M. Shahawy, "Behavior of concrete columns confined by fiber composites," *Journal of Structural Engineering*, 1997.
- [54] G. Campione and N. Miraglia, "Strength and strain capacities of concrete compression members reinforced with FRP," *Cement and concrete composites*, vol. 25, pp. 31-41, 2003.
- [55] R. Kumutha, R. Vaidyanathan, and M. Palanichamy, "Behaviour of reinforced concrete rectangular columns strengthened using GFRP," *Cement and concrete composites*, vol. 29, pp. 609-615, 2007.
- [56] Y. Al-Salloum, "Experimental and analytical investigation of compressive strength of FRP-confined concrete," *Final Rep. King Saud University. Kingdom of Saudi Arabia*, 2007.
- [57] L. Lam and J. Teng, "Design-oriented stress-strain model for FRP-confined concrete in rectangular columns," *Journal of Reinforced Plastics and Composites*, vol. 22, pp. 1149-1186, 2003.
- [58] J. Restrepo and B. DeVino, "Enhancement of the axial load carrying capacity of reinforced concrete columns by means of fiberglass-epoxy jackets," in *PROCEEDINGS OF THE 2ND INTERNATIONAL CONFERENCE ON ADVANCED COMPOSITE MATERIALS IN BRIDGES AND STRUCTURES, ACMBS-II, MONTREAL 1996*, 1996.
- [59] P. J. Fanning and O. Kelly, "Ultimate response of RC beams strengthened with CFRP plates," *Journal of Composites for Construction*, vol. 5, pp. 122-127, 2001.
- [60] J. Teng, S. T. Smith, J. Yao, and J. Chen, "Intermediate crack-induced debonding in RC beams and slabs," *Construction and building materials*, vol. 17, pp. 447-462, 2003.
- [61] F. Ceroni, A. Prota, and M. Pecce, "Analysis of the behaviour of concrete beams with FRP laminates," in *Third Middle East Symposium on Structural Composites for Infrastructure Applications, Aswan, Egypt December, 2002*, pp. 17-20.
- [62] F. Ceroni and M. Pecce, "Design provisions for crack spacing and width in RC elements externally bonded with FRP," *Composites Part B: Engineering*, vol. 40, pp. 17-28, 2009.
- [63] S. Matthys, "Structural behaviour and design of concrete members strengthened with externally bonded FRP reinforcement," Ghent University, 2000.
- [64] M. Islam, M. Mansur, and M. Maalej, "Shear strengthening of RC deep beams using externally bonded FRP systems," *Cement and Concrete Composites*, vol. 27, pp. 413-420, 2005.
- [65] Z. Zhang, C.-T. T. Hsu, and J. Moren, "Shear strengthening of reinforced concrete deep beams using carbon fiber reinforced polymer laminates," *Journal of Composites for Construction*, vol. 8, pp. 403-414, 2004.

- [66] T. El Maaddawy and S. Sherif, "FRP composites for shear strengthening of reinforced concrete deep beams with openings," *Composite Structures*, vol. 89, pp. 60-69, 2009.
- [67] J. Chen and J. Teng, "Shear capacity of FRP-strengthened RC beams: FRP debonding," *Construction and Building Materials*, vol. 17, pp. 27-41, 2003.
- [68] J. Chen and J. Teng, "Anchorage strength models for FRP and steel plates bonded to concrete," *Journal of Structural Engineering*, vol. 127, pp. 784-791, 2001.
- [69] A. Bousselham and O. Chaallal, "Mechanisms of shear resistance of concrete beams strengthened in shear with externally bonded FRP," *Journal of Composites for Construction*, vol. 12, pp. 499-512, 2008.
- [70] O. Chaallal, M. Shahawy, and M. Hassan, "Performance of reinforced concrete T-girders strengthened in shear with carbon fiber-reinforced polymer fabric," *ACI Structural Journal*, vol. 99, 2002.
- [71] G. Chen, J. Teng, and J. Chen, "Shear strength model for FRP-strengthened RC beams with adverse FRP-steel interaction," *Journal of Composites for Construction*, vol. 17, pp. 50-66, 2012.
- [72] A. Khalifa and A. Nanni, "Improving shear capacity of existing RC T-section beams using CFRP composites," *Cement and Concrete Composites*, vol. 22, pp. 165-174, 2000.
- [73] A. C. S. Tests, "Conform to ASTM C31 and ASTM C39," *One set of four cylinders for each*, vol. 50.
- [74] A. Standard, "C39, 2005," "Standard Test Method for Compressive Strength of Cylindrical Concrete Specimens," ASTM International, West Conshohocken, PA, 2005, DOI: 10.1520/C0039\_C0039M-05E01," ed.
- [75] J. R. Casas and J. Pascual, "Debonding of FRP in bending: Simplified model and experimental validation," *Construction and Building Materials*, vol. 21, pp. 1940-1949, 2007.
- [76] H. Thomsen, E. Spacone, S. Limkatanyu, and G. Camata, "Failure mode analyses of reinforced concrete beams strengthened in flexure with externally bonded fiber-reinforced polymers," *Journal of composites for construction*, vol. 8, pp. 123-131, 2004.
- [77] Z.-M. Wu, C.-H. Hu, Y.-F. Wu, and J.-J. Zheng, "Application of improved hybrid bonded FRP technique to FRP debonding prevention," *Construction and Building Materials*, vol. 25, pp. 2898-2905, 2011.
- [78] J.-K. Oh and S.-W. Shin, "Shear strength of reinforced high-strength concrete deep beams," *ACI Structural Journal*, vol. 98, 2001.
- [79] A. Committee, "Building code requirements for structural concrete (ACI 318-05) and commentary (ACI 318R-05)," 2005.
- [80] G. Russo, R. Venir, and M. Pauletta, "Reinforced concrete deep beams-shear strength model and design formula," *ACI Structural Journal*, vol. 102, 2005.
- [81] S. Soliman, "Behavior and analysis of reinforced concrete deep beams," MS thesis, Menoufiya University, Egypt, 2003.
- [82] F. Kong and G. Sharp, "Structural idealization for deep beams with web openings," *Magazine of Concrete Research*, vol. 29, pp. 81-91, 1977.

- [83] M. Mansur and W. Alwis, "Reinforced fibre concrete deep beams with web openings," *International Journal of Cement Composites and Lightweight Concrete*, vol. 6, pp. 263-271, 1984.
- [84] A. F. Ashour and G. Rishi, "Tests of reinforced concrete continuous deep beams with web openings," *ACI Structural Journal*, vol. 97, 2000.
- [85] H. Kumar, "Experimental and numerical studies on behaviour of FRP strengthened deep beams with openings," MSc Thesis, National Institute of Technology, Rourkela, 2012.
- [86] A. Pimanmas, "Strengthening R/C beams with opening by externally installed FRP rods: Behavior and analysis," *Composite Structures*, vol. 92, pp. 1957-1976, 2010.
- [87] Y. Rashid, "Ultimate strength analysis of prestressed concrete pressure vessels," *Nuclear engineering and design*, vol. 7, pp. 334-344, 1968.
- [88] R. De Borst and P. Nauta, "Non-orthogonal cracks in a smeared finite element model," *Engineering Computations*, vol. 2, pp. 35-46, 1985.
- [89] Z. P. Bazant and J. Planas, *Fracture and size effect in concrete and other quasibrittle materials* vol. 16: CRC press, 1997.
- [90] F. J. Vecchio, "Nonlinear finite element analysis of reinforced concrete membranes," *ACI Structural Journal*, vol. 86, 1989.
- [91] H. R. Riggs and G. H. Powell, "Rough crack model for analysis of concrete," *Journal of Engineering Mechanics*, vol. 112, pp. 448-464, 1986.
- [92] H. Okamura and K. Maekawa, "Nonlinear analysis and constitutive models of reinforced concrete," *Gihodo, Tokyo*, vol. 10, 1991.
- [93] K. Maekawa, H. Okamura, and A. Pimanmas, *Non-linear mechanics of reinforced concrete*: CRC Press, 2003.
- [94] H. Salem and K. Maekawa, "Spatially averaged tensile mechanics for cracked concrete and reinforcement in highly inelastic range," *Concrete library of JSCE*, vol. 34, pp. 151-169, 1999.
- [95] J. Dong, Q. Wang, and Z. Guan, "Structural behaviour of RC beams externally strengthened with FRP sheets under fatigue and monotonic loading," *Engineering Structures*, vol. 41, pp. 24-33, 2012.
- [96] J. Teng, G. Chen, J. Chen, O. Rosenboom, and L. Lam, "Behavior of RC beams shear strengthened with bonded or unbonded FRP wraps," *Journal of Composites for Construction*, vol. 13, pp. 394-404, 2009.
- [97] S. H. Alsayed and N. A. Siddiqui, "Reliability of shear-deficient RC beams strengthened with CFRP-strips," *Construction and Building Materials*, vol. 42, pp. 238-247, 2013.
- [98] C. Suesuttajit, P. Warnitchai, W. Kanok-Nukulchai, and R. Sahamitmongkol, "A SURVEY OF CONFIGURATION IRREGULARITIES IN TYPICAL MULTI-STORY CONCRETE BUILDINGS IN THAILAND 3. Author."
- [99] K. Rodsin, P. Warnitchai, and T. Awan, "Ultimate Drift at Gravity Load Collapse of Non-ductile RC Columns," 2010.
- [100] H. Saadatmanesh, M. R. Ehsani, and L. Jin, "Seismic strengthening of circular bridge pier models with fiber composites," *ACI Structural Journal*, vol. 93, 1996.

- [101] F. Seible, M. N. Priestley, G. A. Hegemier, and D. Innamorato, "Seismic retrofit of RC columns with continuous carbon fiber jackets," *Journal of composites for construction*, vol. 1, pp. 52-62, 1997.
- [102] M. A. Haroun, A. S. Mosallam, M. Q. Feng, and H. M. Elsanadedy, "Experimental investigation of seismic repair and retrofit of bridge columns by composite jackets," *Journal of reinforced Plastics and Composites*, vol. 22, pp. 1243-1268, 2003.
- [103] Y. Mo, Y.-K. Yeh, and D. Hsieh, "Seismic retrofit of hollow rectangular bridge columns," *Journal of Composites for Construction*, vol. 8, pp. 43-51, 2004.
- [104] R. Sause, K. A. Harries, S. L. Walkup, S. Pessiki, and J. M. Ricles, "Flexural behavior of concrete columns retrofitted with carbon fiber-reinforced polymer jackets," *ACI Structural Journal*, vol. 101, 2004.
- [105] H. M. Elsanadedy and M. A. Haroun, "Seismic design guidelines for squat composite-jacketed circular and rectangular reinforced concrete bridge columns," *ACI structural journal*, vol. 102, 2005.
- [106] K. K. Ghosh and S. A. Sheikh, "Seismic upgrade with carbon fiber-reinforced polymer of columns containing lap-spliced reinforcing bars," *ACI Structural Journal*, vol. 104, 2007.
- [107] O. Ozcan, B. Binici, and G. Ozcebe, "Improving seismic performance of deficient reinforced concrete columns using carbon fiber-reinforced polymers," *Engineering Structures*, vol. 30, pp. 1632-1646, 2008.
- [108] J.-G. Dai, L. Lam, and T. Ueda, "Seismic retrofit of square RC columns with polyethylene terephthalate (PET) fibre reinforced polymer composites," *Construction and Building Materials*, vol. 27, pp. 206-217, 2012.
- [109] M. J. Masia and N. G. Shrive, "Carbon fibre reinforced polymer wrapping for the rehabilitation of masonry columns," *Canadian Journal of Civil Engineering*, vol. 30, pp. 734-744, 2003.
- [110] D. D'Ayala, A. Penford, and S. Valentini, "Use of FRP fabric for strengthening of reinforced concrete beam-column joints," in *Proceedings of the 10th International conference on structural faults and repair, London*, 2003.
- [111] T. Ogata and K. Osada, "Seismic retrofitting of expressway bridges in Japan," *Cement and Concrete Composites*, vol. 22, pp. 17-27, 2000.
- [112] K. Galal, A. Arafa, and A. Ghobarah, "Retrofit of RC square short columns," *Engineering Structures*, vol. 27, pp. 801-813, 2005.